FINAL REPORT

Computational and Experimental Investigation of Contaminant Plume Response to DNAPL Source Zone Architecture and Depletion in Porous and Fractured Media

SERDP Project ER-1610

September 2013

Edward Sudicky
Walter Illman
Shaun Frape
University of Waterloo

Tian-Chyi Jim Yeh
University of Arizona

SERDP
DOD ▪ EPA ▪ DOE

REPORT DOCUMENTATION PAGE

Form Approved
OMB No. 0704-0188

1. REPORT DATE *(DD-MM-YYYY)*	**2. REPORT TYPE**	**3. DATES COVERED** *(From - To)*
08-08-2013	Final	Jun 2008 – September 2013

4. TITLE AND SUBTITLE
Computational and Experimental Investigation of Contaminant Plume Response to DNAPL Source Zone Architecture and Depletion in Porous and Fractured Media

5a. CONTRACT NUMBER
W912HQ-08-C-0018

5b. GRANT NUMBER

5c. PROGRAM ELEMENT NUMBER

6. AUTHOR(S)
Edward A. Sudicky, Walter A. Illman, and Shaun K. Frape

5d. PROJECT NUMBER
ER-1610

5e. TASK NUMBER

5f. WORK UNIT NUMBER

7. PERFORMING ORGANIZATION NAME(S) AND ADDRESS(ES)
University of Waterloo
200 University Ave W
Waterloo, Ontario, N2L 3G1
Canada

8. PERFORMING ORGANIZATION REPORT NUMBER

9. SPONSORING / MONITORING AGENCY NAME(S) AND ADDRESS(ES)

10. SPONSOR/MONITOR'S ACRONYM(S)

11. SPONSOR/MONITOR'S REPORT NUMBER(S)

12. DISTRIBUTION / AVAILABILITY STATEMENT

13. SUPPLEMENTARY NOTES

14. ABSTRACT: a. Objectives: Dense Non-Aqueous Phase Liquid (DNAPL) source zones can contribute to long-term groundwater contamination, thus remediation and management are of high importance. In spite of efforts towards understanding the fundamental processes affecting the fate of DNAPLs spilled or released in heterogeneous unconsolidated geologic materials, it is widely recognized that few, if any, sites contaminated by DNAPLs have been remediated with respect to either dissolved contaminants contained in the aqueous phase or removal of the DNAPL source. Further, there remains a paucity of knowledge on the behavior of DNAPLs spilled in fractured geologic media. The main objectives of this research are: (1) to develop computational tools for predicting aqueous-phase plume response to DNAPL source zone architecture and depletion for both porous and fractured geologic media; (2) to conduct a suite of numerical experiments to investigate the relationship between DNAPL source-zone characteristics and dissolve-phase plume migration in porous and fractured media; (3) to develop a stochastic information fusion (SIF) technology to define the DNAPL source and its characteristics by exploiting available hydraulic head and concentration data as well as signatures of stable isotope data of chlorinated solvents; (4) to conduct laboratory experiments to validate the proposed computational approaches; and (5) to apply the technique at a well-characterized fractured rock site at Smithville, Ontario, Canada.
b. Technical Approach: A data analysis environment has been developed through modification of an existing numerical model, CompFlow, to account for discrete fractures and stable isotope fractionation. Information that can be included in the data analysis environment include geologic information, well hydrographs, contaminant concentration data and isotopic signatures, and hydraulic property measurements.
c. Results: The project has yielded robust, yet practical tools for predicting contaminant transport in porous and fractured geologic media that should be useful to the DoD and its consultants. Key conclusions from the various components to this project are summarized below in a Table. In particular, the CompFlow model has been modified to include the effects of isotope fractionation and discrete fractures. Numerical simulations provide important new insights on the utility of isotopes in revealing contaminant transport and reaction processes. Simulations have also revealed that DNAPL concentration and mass flux downstream and source depletion (dissolution) are strongly related. In addition, DNAPL source architecture and the partitioning of the source between the fracture and matrix domains are mainly functions of statistics of fracture network geometry and hydraulic characteristics of fracture/matrix. The downstream mass flux, however, is extremely difficult to be lowered under a certain level with a very small portion of remaining source in most fractured porous media. Laboratory adsorption and desorption experiments indicate higher fractionation of 37Cl isotopes than 13C isotopes. Additional laboratory experiments with a rock block showed that Transient Hydraulic Tomography based on the SIF technology is a promising technology in mapping the spatial distributions of hydraulic conductivity, specific storage, and their uncertainty estimates. A field study at the Smithville site showed that isotopic and chemical data support the fact that biodegradation of TCE is occurring at the Smithville site. In addition, numerical simulation studies of TCE plume transport suggest that the stability of the plume is due to first-order degradation. The dominant process is most likely reductive dechlorination of TCE. Model results support earlier estimates that indicated that the pump-

15. SUBJECT TERMS: Dense Nonaqueous Phase Liquid sources zones and plumes, numerical modeling, hydraulic tomography, fractured rocks, heterogeneity, plume mass flux, compound specific isotope analysis

16. SECURITY CLASSIFICATION OF:			17. LIMITATION OF ABSTRACT	18. NUMBER OF PAGES	19a. NAME OF RESPONSIBLE PERSON
a. REPORT	b. ABSTRACT	c. THIS PAGE			19b. TELEPHONE NUMBER *(include area code)*

Contributors:
This project supported the following graduate students, post-doctoral researchers and research associates from the University of Waterloo and University of Arizona. Their names are given in alphabetical order: Tapesh Ajmera, Justin Clark, Hyoun-Tae Hwang, Deqiang Mao, Joanna M. Niemi, Young-Jin Park, Rubiat Sharmeen, Orfan Shouakar-Stash, Randy Stotler, Fatemeh Valkili, Xiao Min Wang, Ken Walton.

Abreviations:
BTCs **B**reak-**t**hrough **c**urves
CMM **C**omposite **M**ulti-component **M**odel
CWML **C**hemical **W**aste **M**anagement, **L**td
DCE **D**i**c**hloro**e**thylene
DNAPL **D**ense **N**on**a**queous **P**hase **L**iquids
IRMS **I**sotope **R**atio **M**ass **S**pectrometry
MOE Ontario **M**inistry **o**f the **E**nvironment
PCE **P**er**c**hloro**e**thylene (tetrachloroethylene)
PCB **P**oly**c**hlorinated **b**iphenyl
PDF **P**robability **D**ensity **F**unction
SIF **S**tochastic **I**nformation **F**usion
SMOC **S**tandard **M**ean **O**cean **C**hloride
SSLE **S**equential **S**uccessive **L**inear **E**stimator
SUPG **S**treamline-**U**pwind **P**etrov-**G**arlekin
TCE **T**ri**c**hloro**e**thylene
TCB **T**ri**c**hloro**b**enzene
VC **V**inyl **C**hloride
VOCs **V**olatile **O**rganic **C**ompounds

Table of Contents

List of Tables

List of Figures

1. Abstract

a. Objectives: Dense Non-Aqueous Phase Liquid (DNAPL) source zones can contribute to long-term groundwater contamination, thus remediation and management are of high importance. In spite of efforts towards understanding the fundamental processes affecting the fate of DNAPLs spilled or released in heterogeneous unconsolidated geologic materials, it is widely recognized that few, if any, sites contaminated by DNAPLs have been remediated with respect to either dissolved contaminants contained in the aqueous phase or removal of the DNAPL source. Further, there remains a paucity of knowledge on the behavior of DNAPLs spilled in fractured geologic media. The main objectives of this research are: (1) to develop computational tools for predicting aqueous-phase plume response to DNAPL source zone architecture and depletion for both porous and fractured geologic media; (2) to conduct a suite of numerical experiments to investigate the relationship between DNAPL source-zone characteristics and dissolve-phase plume migration in porous and fractured media; (3) to develop a stochastic information fusion (SIF) technology to define the DNAPL source and its characteristics by exploiting available hydraulic head and concentration data as well as signatures of stable isotope data of chlorinated solvents; (4) to conduct laboratory experiments to validate the proposed computational approaches; and (5) to apply the technique at a well-characterized fractured rock site at Smithville, Ontario, Canada.

b. Technical Approach: A data analysis environment has been developed through modification of an existing numerical model, CompFlow, to account for discrete fractures and stable isotope fractionation. Information that can be included in the data analysis environment include geologic information, well hydrographs, contaminant concentration data and isotopic signatures, and hydraulic property measurements.

c. Results: The project has yielded robust, yet practical tools for predicting contaminant transport in porous and fractured geologic media that should be useful to the DoD and its consultants. Key conclusions from the various components to this project are summarized below in a Table. In particular, the CompFlow model has been modified to include the effects of isotope fractionation and discrete fractures. Numerical simulations provide important new insights on the utility of isotopes in revealing contaminant transport and reaction processes. Simulations have also revealed that DNAPL concentration and mass flux downstream and source depletion (dissolution) are strongly related. In addition, DNAPL source architecture and the partitioning of the source between the fracture and matrix domains are mainly functions of statistics of fracture network geometry and hydraulic characteristics of fracture/matrix. The downstream mass flux, however, is extremely difficult to be lowered under a certain level with a very small portion of remaining source in most fractured porous media. Laboratory adsorption and desorption experiments indicate higher fractionation of ^{37}Cl isotopes than ^{13}C isotopes. Additional laboratory experiments with a rock block showed that Transient Hydraulic Tomography based on the SIF technology is a promising technology in mapping the spatial distributions of hydraulic conductivity, specific storage, and their uncertainty estimates. A field study at the Smithville site showed that isotopic and chemical data support the fact that biodegradation of TCE is occurring at the Smithville site. In addition, numerical simulation studies of TCE plume transport suggest that the stability of the plume is due to first-order degradation. The dominant process is most likely reductive dechlorination of TCE. Model results support earlier estimates that indicated that the pump-and-treat system has only recovered a small volume of TCE. It also suggests that the pump-and-treat system has been ineffective in controlling the plume and the stability of the plume is due to first-order degradation.

d. Benefits: The developed data analysis environment will improve our understanding of contaminant plume response to DNAPL source zone architecture and depletion in porous and fractured media. Thus, effective remediation strategies can be designed, which reduce the uncertainty and the cost of DNAPL source zone remediation (SERDP, 2006).

Summary Conclusion Table for ER-1610.

Summary Conclusion	Key Considerations
DNAPL-Involved Compound Specific Isotopic Analysis Modeling	We have presented a model that can simulate multiphase and multi-component flow and transport with isotope fractionation. The model is verified for DNAPL-aqueous phase equilibrium partitioning, aqueous phase multi-chain and multi-component reactive transport, and aqueous phase multi-component transport with isotope fractionation. Results from numerical simulations clearly indicate that the isotope signature can be significantly influenced by multiphase flow. It is also illustrated that degradation and isotope enrichment compete with dissolution to determine the isotope signatures in the source zone: isotopic ratios remain the same as those of the source if dissolution dominates the reaction, while heavy isotopes are enriched in reactants along flow paths when degradation becomes dominant.
Modeling Flow in Fractured Media	Node bisection technique is effective in creating a mesh with fewer nodes than traditional discretization schemes.
Semi-analytical Contaminant Transport Model Subject to Chain-Decay Reactions	A set of new, semi-analytical solutions to simulate three-dimensional contaminant transport subject to first-order chain-decay reactions and equilibrium sorption have been developed. The analytical solutions can treat the transformation of contaminants into daughter products by first-order decay and the increasing concentrations of transformation species, leading to decay chains consisting of multiple contaminant species and various reaction pathways. The solutions in their current forms are capable of accounting for up to seven species and four decay levels and have been verified with a numerical model. The ability of this model to consider decay chains consisting of multiple contaminant species, various reaction pathways, unique branching ratios, and retardation factors for different members makes it ideal for use in these screening studies.
Numerical Simulations of Source Mass Depletion in Fractured Porous	TCE concentration and mass flux downstream and source depletion (dissolution) are strongly related With increase in matrix permeability, NAPL TCE can migrate further vertically and aqueous TCE can transport further downstream. It is concluded from the results that DNAPL source architecture and the

Media	partitioning of the source between the fracture and matrix domains are mainly functions of statistics of fracture network geometry and hydraulic characteristics of fracture/matrix; source depletion and the rate of DNAPL migration to downstream are closely related; and the downstream mass flux, however, is extremely difficult to be lowered under a certain level with a very small portion of remaining source in most fractured porous media.
Compound Specific Hydrogen Analysis	New method shows high accuracy and precision; quantification limit as low as 400 ug/L.
Sorption Effects on Isotopic Fractionation	Results for adsorption and desorption experiments indicate higher fractionation of ^{37}Cl isotopes than ^{13}C isotopes.
Biodegradation Effects on Isotopic Fractionation	cis-DCE production started to increase once TCE concentration decreased to about 120 mg/L The type of bacteria responsible for degrading TCE to cis-DCE survived in the oxic environment, but the type of bacteria responsible for degrading cis-DCE to VC and subsequently ethene was sensitive to oxygen and killed in the period when Oxidation Reduction Potential (ORP) became positive. This is an ongoing project and the conclusions should be considered to be tentative.
Transient Hydraulic Tomography (THT) in Fractured Media	It is possible to delineate permeable fracture zones, their pattern and connectivity through the THT analysis of multiple pumping tests along with the inverse code SSLE developed by Zhu and Yeh [2005]. From the estimated K and S_s tomograms obtained from THT analysis of synthetic and laboratory data, it is evident that THT captured the fracture pattern quite well and they became more distinct with additional pumping tests. The results were validated using different methods. In particular, predicted drawdown from independent pumping tests captured observed behavior at later time while early time predicted drawdown deviated.
TCE Dissolution Modeling in Fractured Media	Expensive and time-consuming to model TCE field dissolution using discrete fracture approach as it requires detailed deterministic and statistical information of the geometry of fractured zone and the spatial distribution of fracture apertures. This information is not typically available between boreholes. On the other hand, stochastic continuum approach could be comparatively less expensive and time consuming, as it does not require these detail information about the spatial distribution of fractures.
TCE Attenuation Using Compound Specific Isotopic Analysis	Along with redox and chemical data, the isotopic data from the site support the fact that biodegradation of TCE is occurring at the Smithville site. In addition, numerical simulation studies of McLaren et al. (2012) suggest that the stability of the plume is due to first-order degradation. The dominant process is most likely reductive dechlorination of TCE.

	The further conversion of DCE to more degraded compounds is also supported by chemical and isotopic data.
DNAPL Simulations in Fractured Media	CompFlow simulations suggest that DNAPL penetration from the fracture into the matrix can take place in the carbonate units at the Smithville site. Imbibition is controlled by the capillary-saturation curves of the units. The penetration of DNAPL from the fracture into the matrix is different from the phenomenon of aqueous-phase contaminants diffusing from the DNAPL in the fracture into the matrix. Substantial agreement with observed mass removal data and TCE plumes was achieved by modifying the composition of the DNAPL source and also by reducing the hydraulic conductivity in the source region of the Eramosa member. Model results support earlier estimates that indicated that the pump-and-treat system has only recovered a small volume of TCE. It also suggests that the pump-and-treat system has been ineffective in controlling the plume and the stability of the plume is due to first-order degradation. Application of multiphase compositional models (CompFlow) to realistic field-scale problems may be time-consuming and not currently feasible.

2. Project Background

Chlorinated solvents are the most prevalent contaminants at Department of Defense (DoD) sites (SERDP, 2006) and occupy 12 out of the top 20 places of the most hazardous organic compounds encountered in groundwater. These are released as Dense Non-aqueous Phase Liquids (DNAPLs) and there is considerable uncertainty in their fate due to potential variable release histories and geologic heterogeneity. Accidental spills and long-term leaks that occur during production, storage or transportation activities, along with their chemical stability, made them one of the most ubiquitous and recalcitrant pollutants of groundwater and soil (Alvarez and Illman, 2006). DNAPL source zones can contribute to long-term groundwater contamination over decades or centuries; thus, their remediation and management is of high importance. Over the past decade, considerable effort has been expended towards understanding the fundamental processes affecting the fate of DNAPLs spilled or released in heterogeneous unconsolidated geologic materials. This includes the role played by geological heterogeneity on DNAPL source-zone architectures consisting of ganglia and pools, DNAPL dissolution mechanisms, and aqueous-phase plume migration. In spite of these efforts, it is widely recognized that few, if any, sites contaminated by DNAPLs have been remediated with respect to either the dissolved contaminants contained in the aqueous phase or the removal of the DNAPL source. While progress has been made with respect to process understanding in the context of DNAPL fate and migration in heterogeneous unconsolidated deposits, there remains a paucity of knowledge on the behaviour of DNAPLs spilled in fractured geologic media. Further, it is acknowledged that there is a critical need to improve the ability to predict the response of the aqueous phase plume to the architecture and depletion of DNAPLs in the source zone. As a consequence, there is a need to develop effective technologies: 1) to assess the role and impact of sorption and diffusion of DNAPLS into low-permeability matrices; 2) to assess the impact of DNAPLs located in low-permeability matrices on contaminant concentrations in more permeable media; 3) to improve our understanding of how the depletion of DNAPLs in flow-limited and/or flow accessible zones affects plume response in terms of plume size, strength, and longevity; 4) to develop and/or improve predictive models of impacts of the DNAPL source zone on plume response in terms of plume size, strength, and longevity that will assist in cleanup decision making; and 5) to develop cost-effective approaches for evaluating DNAPL source function.

3. Objectives

The main objectives of this research are: 1) to develop computational tools for predicting aqueous-phase plume response to DNAPL source zone architecture and depletion for both porous and fractured geologic media; 2) to conduct a suite of numerical experiments to investigate the relationship between DNAPL source-zone characteristics and dissolve-phase plume migration in porous and fractured media; 3) to develop a stochastic information fusion (SIF) technology to define the DNAPL source and its characteristics by exploiting available hydraulic head and concentration data as well as signatures of stable isotope data of chlorinated solvents; 4) to conduct laboratory experiments to validate the proposed computational approaches; and 5) to apply the technique at a well-characterized fractured rock site.

To achieve these objectives, the project was broken up into eight different tasks:

1. Modification of *CompFlow* to include capabilities for discrete fractures and stable isotope fractionation. An existing model *CompFlow*, developed by Unger et al. (1995, 1996, 1998), will be modified to account for discrete fractures and stable isotope fractionation. As part of this task, the code will also be parallelized to take advantage of networked supercomputers and Linux clusters, as the new modifications are computationally demanding.

2. Modification of *CompFlow* to include capabilities for inverse modeling. A stochastic information fusion (SIF) technology will be developed to integrate and maximize various pieces of information to provide the best unbiased estimate of contaminant distributions, as well as their loading histories and locations. SIF will also quantify the uncertainty associated with these estimates, which is vital to remediation strategies. Previously ignored data, including observed well hydrographs, concentration history, isotopic signatures of the contaminants, geologic information, and point measurements of the hydraulic properties will be incorporated.

3. Numerical experiments using *CompFlow*. A suite of numerical experiments will be conducted to investigate the relationship between DNAPL source architectures, source-zone mass depletion, and dissolved-phase contaminant and isotope plume evolution in both porous and fractured geologic media. These investigations will include 1) the relative benefits of partial source zone remediation on mass flux and concentration reduction in fractured porous media; 2) the effect of DNAPL dissolution processes and matrix diffusion on transport in fractured porous media; 3) the maximum vertical and lateral extent of multi-component aqueous-phase plumes and DNAPL source-zone distributions; and 4) the effects of isotope fractionation in heterogeneous porous media containing flow-limited zones and in fractured rocks. We anticipate clear trends will emerge as to which types of media will be problematic vs. manageable for both monitoring and remedial actions in a decision making framework, and how much uncertainty is to be expected for a given level of site characterization.

4. Refinement of analytical techniques to analyze compound-specific hydrogen of chlorinated solvents. The current techniques for compound-specific hydrogen isotope determinations of chlorinated solvents are not sensitive enough for use in analyzing field samples. Thus, new methodologies with lower quantification limits (ppb level) will be developed. This will allow compound specific stable isotope determinations to be made for hydrogen, carbon, and chlorine in field studies, which will improve the ability to delineate different plumes, investigate the fate of plumes, monitor degradation rates, study degradation mechanisms (pathways), and assess the usefulness of isotopic _fingerprinting‘ in matrix diffusion of DNAPLs.

5. Batch and column experiments. Batch studies will be designed to test the behaviour of chlorinated solvents during various processes such as diffusion, sorption, dissolution, and

degradation (abiogenic and biogenic), and consequently determine the fractionation factors of each isotope (H, C, Cl) during each process. We will use different porous media and fractured blocks for these tests.

Column studies will be conducted to determine whether stable isotopic data can be utilized to constrain the source function. For example, the source function will be varied by injecting TCE from different manufacturers into a well-defined source zone at a uniform or varying rate.

Experimentally determined fractionation factors of the different compounds will be integrated into the *CompFlow* model to forecast the isotopic behaviour of different compounds in the subsurface during various different processes.

6. Laboratory sandbox and fractured rock block studies. The data analysis environment developed under tasks 1 and 2 will be validated with laboratory sandbox studies involving homogeneous and heterogeneous porous media, and a fractured limestone block.

7. Field studies. The methods developed in this proposal will be applied to the Smithville, ON, Canada site managed by the Ontario Ministry of the Environment (MOE), as there are abundant site data and it has close proximity to the University of Waterloo. We will incorporate available data from the Smithville site to study the flow and transport of immiscible and dissolved phase contaminants (e.g. PCBs, TCE, and TCB) at the site through numerical simulations using the modified version of *CompFlow* developed under tasks 1 and 2. We also intend to collect additional samples and data from the site for analysis and experimentation to further our understanding of contaminant distribution and source zone characterization, and validate the computational approaches developed in this proposal at the field scale.

8. Numerical modeling of lab and field data. Laboratory and field data collected will be analyzed using the forward and SIF computational tools developed.

4. Methods, Results, and Discussion

Although the tasks in this project are related and dependent upon each other, they are also diverse and unique. Therefore, the methods, results, and discussion of data for each task will be discussed separately.

TASK 1 – MODIFICATION OF COMPFLOW: STABLE ISOTOPE FRACTIONATION AND DISCRETE FRACTURES

4.1 A multiphase flow and multispecies reactive transport model for DNAPL-involved Compound Specific Isotope Analysis: Introduction

Stable isotope analysis has been recognized as a valuable technique to quantify the physicochemical processes that influence isotope signatures. This approach is based on the theory that molecules with light isotopes of an element can react more rapidly than those with heavy isotopes and thus the ratio of heavy to (typically more abundant) light isotopes increases for the reactants as the reaction proceeds (isotope enrichment). Isotope fractionation is commonly interpreted by means of the Rayleigh equation which describes the relation between the fraction of mass remaining (or the change in concentration) and the change in the isotope ratio of an element in terms of a fractionation or enrichment factor. These techniques have been used to quantify the rates of the reactions when isotope fractionation occurs and to differentiate between the fractionation effects caused by various physical and chemical transport processes for inorganic and organic contaminants [Mariotti et al., 1988; Aravena and Robertson, 1998; Poulson and Drever, 1999; Hunkeler and Aravena, 2000; Hunkeler et al., 2001]. For example, the contribution of intrinsic biodegradation to contaminant remediation or natural attenuation can be uniquely quantified by measuring the rate of isotope enrichment, provided the isotope ratio is not influenced by other transport processes such as sorption and dissolution [Slater et al., 2000; Hunkeler et al., 2004]. By analyzing multiple isotopes simultaneously, it is also feasible to differentiate the reaction pathways in which different elements are involved during the transformations [Hunkeler et al., 2009]. If multiple sources of contaminants have different isotope signatures, a fingerprinting approach can be used to identify the contaminant sources together with the effect of degradation on the isotopic composition of the contaminants released from the source [Beneteau et al., 1999].

Isotope approaches based on Compound Specific Isotope Analysis (CSIA) have gained widespread attention as a tool for quantifying biotransformation processes [Beneteau et al., 1999; Schmidt et al., 2004; Hirschorn et al., 2007; Abe et al., 2008]. Van Breukelen et al. (2005) suggested that CSIA for carbon in Chlorinated Aliphatic Hydrocarbons (CAH) could provide additional insight into CAH degradation in the field. Using CSIA, Hunkeler et al. (2004) investigated carbon isotope fractionation for PCE and TCE during dissolution and concluded that the $\delta^{13}C$ of TCE in the aqueous phase could be similar to that in the DNAPL phase. Provided the isotope signatures in the aqueous phase are the same as those of DNAPL phase, it may be possible to use aqueous phase isotope signatures to identify which DNAPL pools or blobs are acting as source zones.

The contributions of dilution and biodegradation to natural attenuation were quantified using an analytical model which could extend the applicability of the Rayleigh equation from closed to open systems [Van Breukelen, 2007]. Numerical models have also been used to simulate advective-dispersive transport of multiple CAH species with carbon and chlorine isotope fractionation [Béranger et al., 2005; Van Breukelen et al., 2005; Van Breukelen, 2007;

Elsner and Hunkeler, 2008; Hunkeler et al., 2009]. Specifically, Beranger et al. (2005) utilized an optimization algorithm to estimate the degradation rates of light and heavy isotopes and enrichment factors from measured concentration and $\delta^{13}C$ values for CAHs. Van Breukelen et al. (2005) simulated carbon isotope fractionation during sequential degradation of CAHs using PHREEQC-2, a 1-D reactive transport simulator, and quantified the reductive dechlorination of CAHs by CSIA. Atteia et al. (2008) presented a semi-analytical model with first-order reaction (MIKSS), and compared the results from MIKSS and RT3D for the carbon isotope. For chlorine isotope modeling, Elsner and Hunkeler (2008) and Hunkeler et al. (2009) applied multi-chain reactions to reflect multistep chlorine isotope (isotopologue) fractionation patterns. Van Breukelen et al. (2005) and van Breukelen and Prommer (2008) evaluated the effect of sorption on carbon isotope signatures using a contaminant transport model with first-order reactions or monod-type degradation. Morrill et al. (2009) presented the effect of DNAPL dissolution and degradation rate constants on carbon isotope values using an analytical solution for a single component nonequilibrium dissolution model with the assumption that a DNAPL pool is in a static state. Despite these efforts to simultaneously characterize reactive transport and isotope fractionation, it is worth noting that most previous studies were limited to aqueous-phase transport in a simplistic one-dimensional or two-dimensional domain.

It is well recognized that a DNAPL source zone is difficult to characterize due to the re-distribution of the source by natural and anthropogenic perturbations and/or density-driven flow [Mackay and Cherry, 1989; Mercer and Cohen, 1990; Huyakorn et al., 1994]. In addition, it is not straightforward to characterize the groundwater flow system at a contaminated site, which is critical for aqueous-phase contaminant transport, due to many sources of uncertainty including heterogeneity, ill-defined flow and transport parameters, unknown site history, etc. For an improved interpretation of the DNAPL and aqueous phase contaminant isotope signatures, an understanding of both the evolution of the contaminant source and the groundwater flow system is a prerequisite.

In this study, a comprehensive three-dimensional multiphase flow and multispecies reactive transport model is presented that can simulate the gas, water, and NAPL flow and the transport of any number of chemical species together with the isotope fractionation of transforming components. Its applicability to a complex hydrogeologic system will be demonstrated along with a series of verification simulations of DNAPL dissolution and multi-component transport with isotope fractionation. For illustrative purposes, we investigate the effect of different DNAPL spill and degradation rates on the temporal and spatial distribution of the isotope signatures of CAHs, which can provide insight into the field application of DNAPL-involved CSIA.

4.1.1 Model description

4.1.1.1. Multiphase flow multispecies reactive transport model

The *CompFlow-Bio* simulator is a three-dimensional multiphase multispecies compositional model [Unger et al., 1995]. The model can simulate the flow of gas (g), aqueous (q), and NAPL (n) phase fluids and the transport of multiple compounds in each phase including water and air, and any number of contaminants. Mass conservation of each species (p) in phase l (=$g, q,$ or n) is described by the following equation:

$$\frac{\partial}{\partial t}\left(\phi S_l M_l X_{p,l}\right) = -\nabla\cdot\left(M_l X_{p,l}\mathbf{v}_l\right) + \nabla\cdot\left(\phi S_l M_l \mathbf{D}_l\right)\cdot\nabla X_{p,l} \pm Q_{p,l} \pm Re_{p,l} \qquad (4.1.1)$$

where the Darcy flux ($\mathbf{v}_l$) of each phase is given by

$$\mathbf{v}_l = -\frac{k_{rl}}{\mu_l}\mathbf{K}\cdot\nabla\left(P_l + \rho_l g z\right) \tag{4.1.2}$$

and the hydrodynamic dispersion tensor ($\mathbf{D}_l$) is defined as:

$$\phi S_l \mathbf{D}_{l_{ij}} = \alpha_T^l \left|\mathbf{v}_l\right| \delta_{ij} + \left(\alpha_L^l - \alpha_T^l\right)\frac{\mathbf{v}_{l_i}\mathbf{v}_{l_j}}{\left|\mathbf{v}_l\right|} + \phi S_l \tau d_l \delta_{ij} \tag{4.1.3}$$

Symbols used in these equations are defined in Appendix A.

In this study, the partitioning of components between phases is assumed to be at equilibrium. The partitioning of component p between the NAPL and gas phases, and between aqueous and gas phases are determined by the following relations as:

$$X_{p,g} = Z_{p,gn} X_{p,n} \tag{4.1.4a}$$

$$X_{p,g} = Z_{p,gq} X_{p,q} \tag{4.1.4b}$$

where $Z_{p,gn}$ and $Z_{p,gq}$ are the equilibrium partitioning coefficients, derived from Raoult's and Henry's laws, respectively. The NAPL phase dissolution for equilibrium partitioning can be derived from (4.1.4) as

$$X_{p,q} = \left(Z_{p,gn}/Z_{p,gq}\right) X_{p,n} \tag{4.1.5}$$

where $Z_{p,gn}/Z_{p,gq}$ is the NAPL dissolution ratio under an equilibrium condition. The details of the *CompFlow-Bio* simulator are presented in Unger et al. (1996). All the physical properties for components used in this study are taken from Yaws (2003), and the calculations of natural abundances for the isotope compounds are based on Melander (1960). Table 4.1.1 summarizes the simulation parameters in this study used for multiphase equilibrium partitioning.

Table 4.1.1: Simulation parameters for multiphase equilibrium partitioning.

Porous medium property	Value
Porosity [-]	0.10
Permeability [m^2]	$1.0\text{x}10^{-12}$
Water viscosity [kPa·S]	$9.81\text{x}10^{-6}$
Dispersivity [m]	0.0
Diffusion coefficient [m^2/day]	
Stagnant case	$1.7\text{x}10^{-4}$
Dynamic case	$1.7\text{x}10^{-5}$
Equilibrium partitioning coefficient:	
$Z_{p,gq}$ [-]	$1.05\text{x}10^{0}$ a)
$Z_{p,gn}$ [-]	$1.71\text{x}10^{-5}$ a)

a) assumed at P_g = 120 kPa

4.1.1.2. Dechlorination of CAHs and isotope fractionation

Molecules that contain elements with different numbers of heavy (H) and light (L) isotopes are denoted as isotopologues [Hunkeler et al., 2009]. For chlorinated hydrocarbons, if a

compound has two or more chlorine constituents, three or more possible isotopologues can occur. Figures 4.1.1a and 4.1.1b present the possible chlorine isotopologue fractionations for a molecule of PCE. According to Hunkeler et al. (2009), the isotopologue approach (where different isotopologues are treated as independent species) has the advantage of easily reflecting both chemical and physical isotope effects. Figures 4.1.1c and 4.1.1d present a sequential chlorinated hydrocarbon degradation reaction, a series known as a carbon isotope sequential reaction. Based on isotopologue theory suggested by Hunkeler et al. (2009), PCE, TCE, DCE, and VC have five, four, three, and two isotopologues with a possible combination of ^{35}Cl and ^{37}Cl, respectively. The dotted arrows in Figure 4.1.1b denote a light chlorine isotope split-off by the degradation reaction, while the solid arrows denote a heavy chlorine isotope split-off. Based on carbon isotopes (^{12}C and ^{13}C), PCE can be expressed as light PCE (PCE_L), which has only light carbons and heavy PCE (PCE_H) which has one light and one heavy carbon. When simulating the carbon isotopes in chlorinated carbons with chain degradation, the heavy and light carbon isotopes are independent of the sequential dechlorination process (Figure 4.1.1d). A total of 20 and 10 hydrocarbon isotopologues need to be considered to simulate chlorine and carbon isotope fractionations, respectively. Aqueous and gas phase components also need to be included in addition to the CAH components.

A multi-chain degradation reaction model can be used to describe isotopologue and isotope fractionations of CAHs [Hunkeler et al., 2009]. The reaction term $Re_{p,q}$ in Eq. (4.1.1) can be expressed as:

$$Re_{p,q} = \phi S_q M_q \left(\sum_{p_{Pr}=1}^{c_n^{Pr}} \omega_{p_{Pr}} \lambda_{p_{Pr}}^{Pr} X_{p_{Pr},q} - \sum_{p_{Dg}=1}^{c_n^{Dg}} \omega_{p_{Dg}} \lambda_{p_{Dg}}^{Dg} X_{p,q} \right) \tag{4.1.6}$$

where the superscripts and subscripts Pr and Dg represent parent and daughter components, respectively. Note that the dechlorination is limited to the aqueous phase CAHs and thus $Re_{p,n}$ or $Re_{p,g} = 0$. The positive term in Eq. (4.1.6) indicates component p is produced from its parent components, while the negative term indicates the degradation of component p to its daughter component.

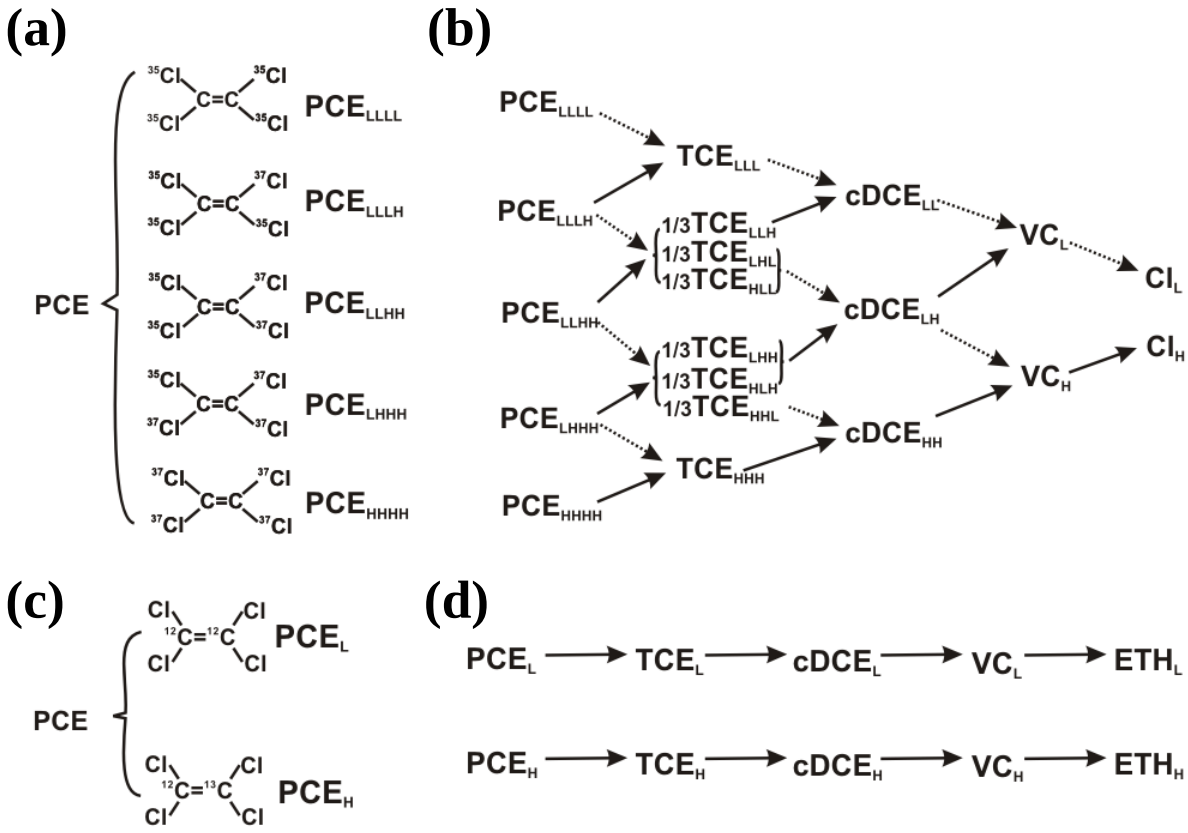

Figure 4.1.1: (a) Chlorine isotopologues of PCE (L and H represent ^{35}Cl and ^{37}Cl, respectively) and (b) sequential multichain degradation reaction of CAH chlorine isotopologues. (c) Carbon isotopologues of PCE (L and H for ^{12}C and ^{13}C, respectively) and (d) single chain degradation reaction (after Hunkeler et al., 2009).

4.1.1.3 Degradation rate constants for isotopologues

The rate constants of the heavy and light chlorine isotope split-offs are calculated from the bulk rate constants by a model suggested by Hunkeler et al. (2009). Because the rate constants are combined with the Rayleigh equation, kinetic isotope effects (KIE) are required to calculate the heavy and light rate constants ($^{H}\lambda_p$ and $^{L}\lambda_p$) for each isotopologue.

$$^{H}\lambda_p = \frac{\lambda_p}{^{H}P_p / KIE_p + (1 - {}^{H}P_p)} \tag{4.1.7a}$$

$$^{L}\lambda_p = \frac{\lambda_p}{^{H}P_p + (1 - {}^{H}P_p) \times KIE_p} \tag{4.1.7b}$$

where λ_p is the bulk degradation rate constant for species p, and $^{H}P_p$ is the probability that a heavy isotope is in a reactive position. The rate constants of the heavy and light chlorine and carbon isotope split-offs for CAHs are listed in Table 4.1.2, calculated based on the bulk rate constants and KIEs in Hunkeler et al. (2009).

Analyzing stable isotope fractionation requires an isotopic signature of a compound. The isotopic signatures of chlorine and carbon compounds can be expressed as delta values of carbon, δ^{13}C, and chlorine, δ^{37}Cl, respectively, and they are defined as

$$\delta^{13}C = 1000 \times \left(R_C / R_C^0 - 1 \right) \tag{4.1.8a}$$

$$\delta^{37}Cl = 1000 \times \left(R_{Cl} / R_{Cl}^0 - 1 \right) \tag{4.1.8b}$$

where R_C and R_{Cl} are the ratios of the amount of heavy and light carbon and chlorine in a sample, respectively, and R_C^0 and R_{Cl}^0 are the reference isotope ratios for carbon and chlorine compounds, respectively. For PCE chlorine isotopologues, for example, R_{Cl} is calculated from the mole fractions of five isotopologues as follows:

$$R_{Cl} \equiv \frac{[^{37}Cl]}{[^{35}Cl]} = \frac{4X_{PCE_{H_4}} + 3X_{PCE_{L_1H_3}} + 2X_{PCE_{L_2H_2}} + X_{PCE_{L_3H_1}}}{4X_{PCE_{L_4}} + 3X_{PCE_{L_3H_1}} + 2X_{PCE_{L_2H_2}} + X_{PCE_{L_1H_3}}} \tag{4.1.9}$$

where $X_{PCE_{L_iH_{(4-i)}}}$ is the mole fraction of an isotopologue having i numbers of light (L) and (4- i) heavy (H) chlorine isotopes among a total of 4 chlorine in PCE. For PCE carbon isotopes, R_C is straightforward to compute as

$$R_C = [^{13}C]/[^{12}C] = X_{PCE_H} / X_{PCE_L} \tag{4.1.10}$$

Table 4.1.2: Degradation rate constants (1/day) and source injection rate (m^3/day) for a Chlorine isotopologues and Carbon isotopes

Chlorine isotopologue				Carbon isotope		
	$^{L}\lambda_p$	$^{H}\lambda_p$	Q		$^{L}\lambda_p$ or $^{H}\lambda_p$	Q
PCE_{LLLL}	6.85×10^{-4}	NA	1.63×10^{-8}	PCE_L	6.85×10^{-4}	7.89×10^{-7}
PCE_{LLLH}	5.14×10^{-4}	1.71×10^{-4}	2.10×10^{-8}	PCE_H	6.82×10^{-4}	8.92×10^{-9}
PCE_{LLHH}	3.43×10^{-4}	3.42×10^{-4}	1.01×10^{-8}			
PCE_{LHHH}	1.71×10^{-4}	5.13×10^{-4}	2.17×10^{-9}			
PCE_{HHHH}	NA	6.84×10^{-4}	1.77×10^{-10}			
TCE_{LLL}	1.37×10^{-3}	NA		TCE_L	1.37×10^{-3}	
$TCE_{LL\mathbf{H}}$	NA	1.36×10^{-3}		TCE_H	1.35×10^{-3}	
$TCE_{LH\mathbf{L}}$	1.37×10^{-3}	NA				
$TCE_{HL\mathbf{L}}$	1.37×10^{-3}	NA				
$TCE_{LH\mathbf{H}}$	NA	1.36E-03				
$TCE_{HL\mathbf{H}}$	NA	1.36E-03				
$TCE_{HH\mathbf{L}}$	1.37×10^{-3}	NA				
TCE_{HHH}	NA	1.37×10^{-4}				
DCE_{LL}	2.74×10^{-3}	NA		DCE_L	2.74×10^{-3}	
DCE_{LH}	1.37×10^{-3}	1.37×10^{-3}		DCE_H	2.69×10^{-3}	
DCE_{HH}	NA	2.74×10^{-3}				
VC_L	5.48×10^{-3}	NA		VC_L	5.48×10^{-3}	
VC_H	NA	5.47×10^{-3}		VC_H	5.34×10^{-3}	

4.1.3. Verification examples

The multiphase compositional model with isotope fractionation is verified for (1) DNAPL-aqueous phase partitioning (dissolution), (2) aqueous phase multi-chain and multi-component reactive transport, and (3) aqueous phase multi-component transport with isotope fractionation. For the verification of DNAPL-aqueous phase partitioning, simulation results in a simplistic system are compared to analytical solutions. Reactive multi-chain and multi-component transport is verified by comparing the simulation results with the semi-analytical solution of the Chain-decay Multispecies Model (CMM) [*Sudicky et al., 2013*]. The results for multi-component transport with isotope fractionation are compared to the numerical solutions presented by Hunkeler et al. (2009).

4.1.3.1. Multiphase equilibrium partitioning

The DNAPL-aqueous phase equilibrium partitioning is verified by simulating the dissolution of PCE in a hypothetical one-dimensional column consisting of two nodes centered at cells of dimension 1 m × 1 m × 1 m. Initially, a DNAPL saturation (S_n) of 0.001 is assigned at one (source) cell with the other (receptor) cell being saturated with pure water ($S_w = 1.0$). All the parameters used for the simulations are listed in Table 4.1.1. When the aqueous phase pressure is specified to be equal at both nodes (i.e. a stagnant flow condition), PCE NAPL in the source cell dissolves at its solubility and diffuses into the receptor cell. Figure 4.1.2a shows the temporal evolution of PCE saturation in the source cell and the PCE mole fraction in the receptor cell. The dissolution rate from PCE DNAPL at the source cell needs to be instantaneously equilibrated with the accumulation in the other cell, and this can be expressed in mole/day as follows:

$$M_n \left.\frac{\partial\left(\phi S_n\right)}{\partial t}\right|_{source} = M_q \left.\frac{\partial\left(\phi S_q X_{PCE,q}\right)}{\partial t}\right|_{receptor} \tag{4.1.11}$$

Figure 4.1.2b shows that the left and right terms in (4.1.11) are the same during the simulation period. Note that the aqueous mole fraction of PCE at the source cell remained the same as the PCE solubility, which can be derived from ($Z_{p,gn}/Z_{p,gq} \cong 1.62 \times 10^{-5}$).

Equilibrium partitioning is simulated when water flows from the source to receptor cells. Constant pressure boundary conditions of 120 kPa and 119.9 kPa are specified at the source and receptor cells, respectively. When the advective flux dominates the dispersive flux from the source to receptor, the rate of PCE dissolution needs to be equilibrated with the advective PCE flux such that

$$M_n \left.\frac{\partial\left(\phi S_n\right)}{\partial t}\right|_{source} \approx M_q \left|\mathbf{v}_q\right| X_{PCE,q}\Big|_{source \rightarrow receptor} \tag{4.1.12}$$

Figure 4.1.2c shows that the amount of PCE dissolving from the NAPL phase at the source cell is the same as the amount of PCE moving from the source to receptor cells until most of NAPL phase PCE enters into the aqueous phase PCE.

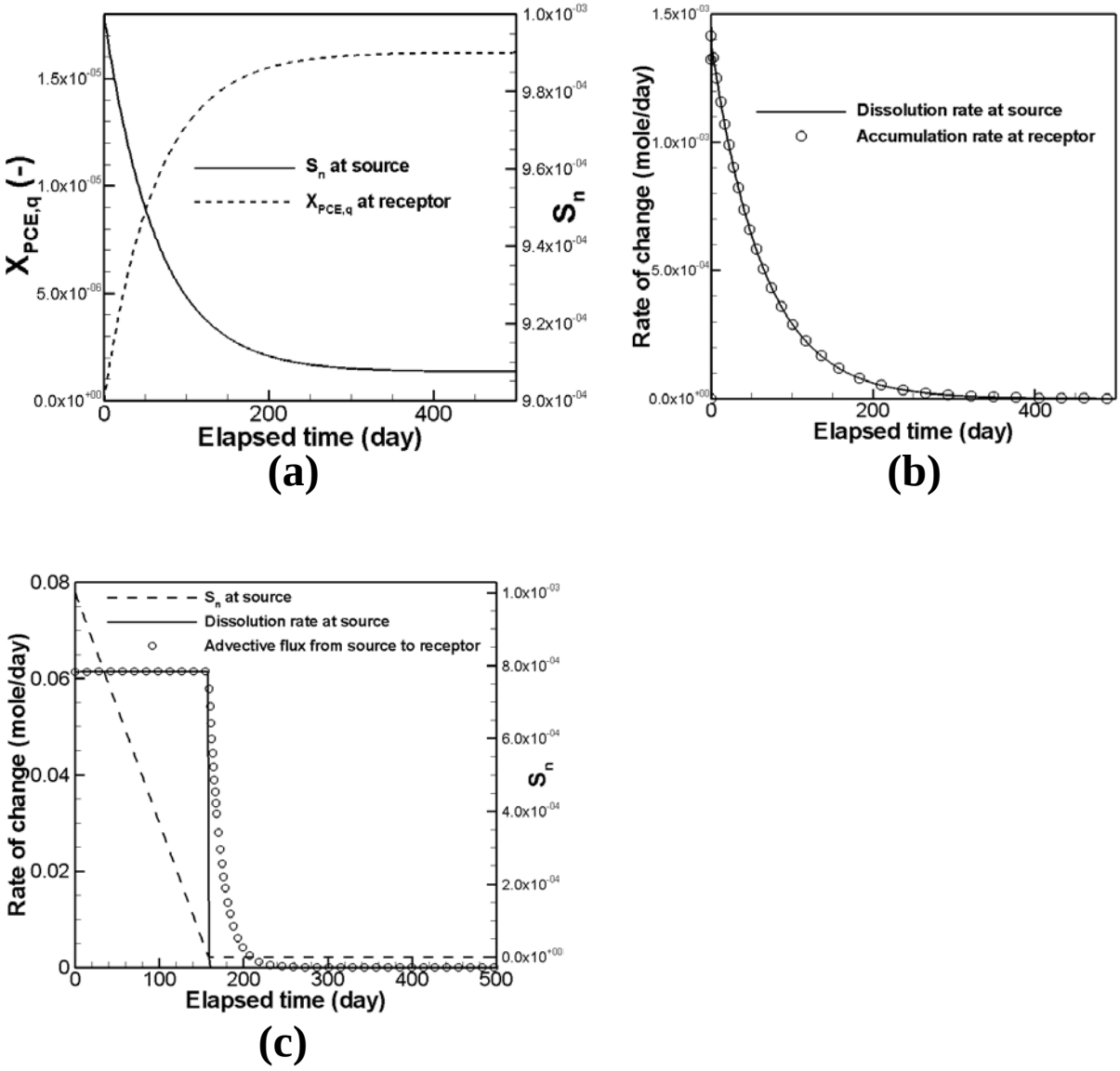

Figure 4.1.2: (a) Temporal evolution of PCE saturation at source (solid line) and the aqueous PCE mole fraction at receptor. (b) shows that the rate of PCE dissolution at source is the same as the rate of accumulation at receptor. In (c), it is illustrated that the rate of PCE dissolution at source is the same as the advective mass flux from the source to receptor cells for advection-dominated case.

4.1.3.2. Multi-chain reactive transport with isotope fractionation

Transport of chlorinated hydrocarbons with sequential dechlorination reactions and isotope fractionation are simulated in a one-dimensional homogeneous column consisting of 800 cells of length 1 m with a cross-sectional area of 1 m^2. The flow and transport conditions are the same as those of Hunkeler et al. (2009) where the average linear groundwater velocity is 0.1 m/day with a porosity of 0.1, and the dispersivity and diffusion coefficients are 1.0 m and 2.6×10^{-5} m^2/day, respectively. All the cells in the domain are initially saturated exclusively with water. A steady-state groundwater flow field is established by applying constant pressure boundary conditions on both sides of the domain, to establish a hydraulic gradient of 0.001 throughout the domain. The PCE source mixed with water ($Q_{PCE+water}$= 1.0×10^{-2} m^3/day) is continuously injected at the origin (x=0) with the natural abundance of each PCE isotopologue for chlorine and each isotope for carbon being specified according to the reference ratios, R_{Cl}^0 and R_C^0 (Table 4.1.2). The injection rate for PCE (Q_{PCE}= 5×10^{-7} m^3/day) is about five orders of magnitude less than the water injection rate (Q_{water}= 9.9995×10^{-3} m^3/day) so as not to form a DNAPL phase. Bulk degradation rates (λ_p) for PCE, TCE, cDCE, VC, and ETH are listed in Table 4.1.2.

The spatial distribution of the mole fractions of the CAHs (normalized by the maximum mole fraction of PCE at the origin) is simulated using the compositional model and the results after 20 years of injection are compared results obtained from the Hunkeler et al. (2009) and the semi-analytical solutions. In Figure 4.1.3a, the PCE mole fraction decreases monotonically as the distance increases from the source due to the degradation reaction while the mole fractions of its daughter species such as TCE, DCE, and VC increase until they reach a maximum value and then decrease with distance. The final product of the sequential reactions (i.e., ETH and Cl^-) increases monotonically before they are controlled by the boundary condition at the downstream exit. Simulation results for transport with multispecies chain degradation show an excellent match with those in Hunkeler et al. (2009) and the analytical solutions. Figures 4.1.3b and 4.1.3c show that the isotope ratios for chlorine and carbon, respectively, increase with distance. At the injection point, $\delta^{37}Cl$ values for all the species start from the reference value (~ 0 ‰) and increase up to about 14 ‰ for TCE (Figure 4.1.3b). Due to higher rates of isotope enrichment for carbon isotopes, the isotope ratios ($\delta^{13}C$) for daughter species at the origin can differ from each other as shown in Figure 4.1.3c: 0 ‰ for PCE, -3.3 ‰ for TCE, -8.6 ‰ for DCE and -59 ‰ for VC. The comparison of the results to Hunkeler et al. (2009) shows that the difference is less than 10^{-3} ‰.

4.1.4. Multiphase flow and isotope fractionation

Illustrative examples are presented for the simultaneous simulation of the multiphase flow, dissolution, and multispecies reactive transport with isotope fractionation. According to Mackay and Cherry (1989), DNAPL can slowly migrate downwards for decades until it reaches impermeable bedrock where the NAPL contaminant source can produce various contaminant plumes consisting of the daughter products of the source. Using the multiphase compositional isotope fractionation model, the effects of the formation and flow of the DNAPL phase of CAHs on chlorine and carbon isotope fractionation are examined. Simplified 1-D simulations are performed to identify the effect of DNAPL spill rates and degradation rates on isotope fractionation, followed by an example in a heterogeneous 3-D domain. One-dimensional

simulations compare the results obtained for cases low and high rates of degradation and isotope enrichment for different rates of PCE injection. For case 1, the simulation parameters are the same as those in the verification example with an increased injection rate. For cases 2 and 3, the degradation rate constants and enrichment factors are increased by one order of magnitude, respectively. Finally, for case 4, both are increased by an order. Table 4.1.3 summarizes details of the simulation conditions.

Table 4.1.3: Simulation conditions for evaluating the effect of PCE source spill rates (m^3/day), degradation rate constants (1/day), and enrichment factors (‰) on multi-phase contaminant transport and isotope fractionations

Case		PCE source spill rate		Degradation rate constant		Enrichment factor	
		Low[a)]	High[b)]	Low[c)]	High[d)]	Low[e)]	High[f)]
case 1	A	X		X		X	
	B		X	X		X	
case 2	A	X			X	X	
	B		X		X	X	
case 3			X	X			X
case 4			X		X		X

[a)] $Q_{PCE} = 5.0 \times 10^{-7}$; $Q_{Water+PCE} = 1.0 \times 10^{-2}$ (m^3/day)
[b)] $Q_{PCE} = 2.5 \times 10^{-4}$; $Q_{Water+PCE} = 1.0 \times 10^{-2}$ (m^3/day)
[c)] $\lambda_{PCE} = 6.8 \times 10^{-4}$; $\lambda_{TCE} = 1.4 \times 10^{-3}$; $\lambda_{cDCE} = 2.7 \times 10^{-3}$; $\lambda_{VC} = 5.5 \times 10^{-3}$ (1/day)
[d)] $\lambda_{PCE} = 6.8 \times 10^{-3}$; $\lambda_{TCE} = 1.4 \times 10^{-2}$; $\lambda_{cDCE} = 2.7 \times 10^{-2}$; $\lambda_{VC} = 5.5 \times 10^{-2}$ (1/day)
[e)] $\varepsilon_{PCE}^{Cl} = -2$; $\varepsilon_{TCE}^{Cl} = -3$; $\varepsilon_{cDCE}^{Cl} = -2$; $\varepsilon_{VC}^{Cl} = -2$ (‰)
[f)] $\varepsilon_{PCE}^{Cl} = -20$; $\varepsilon_{TCE}^{Cl} = -30$; $\varepsilon_{cDCE}^{Cl} = -20$; $\varepsilon_{VC}^{Cl} = -20$ (‰)

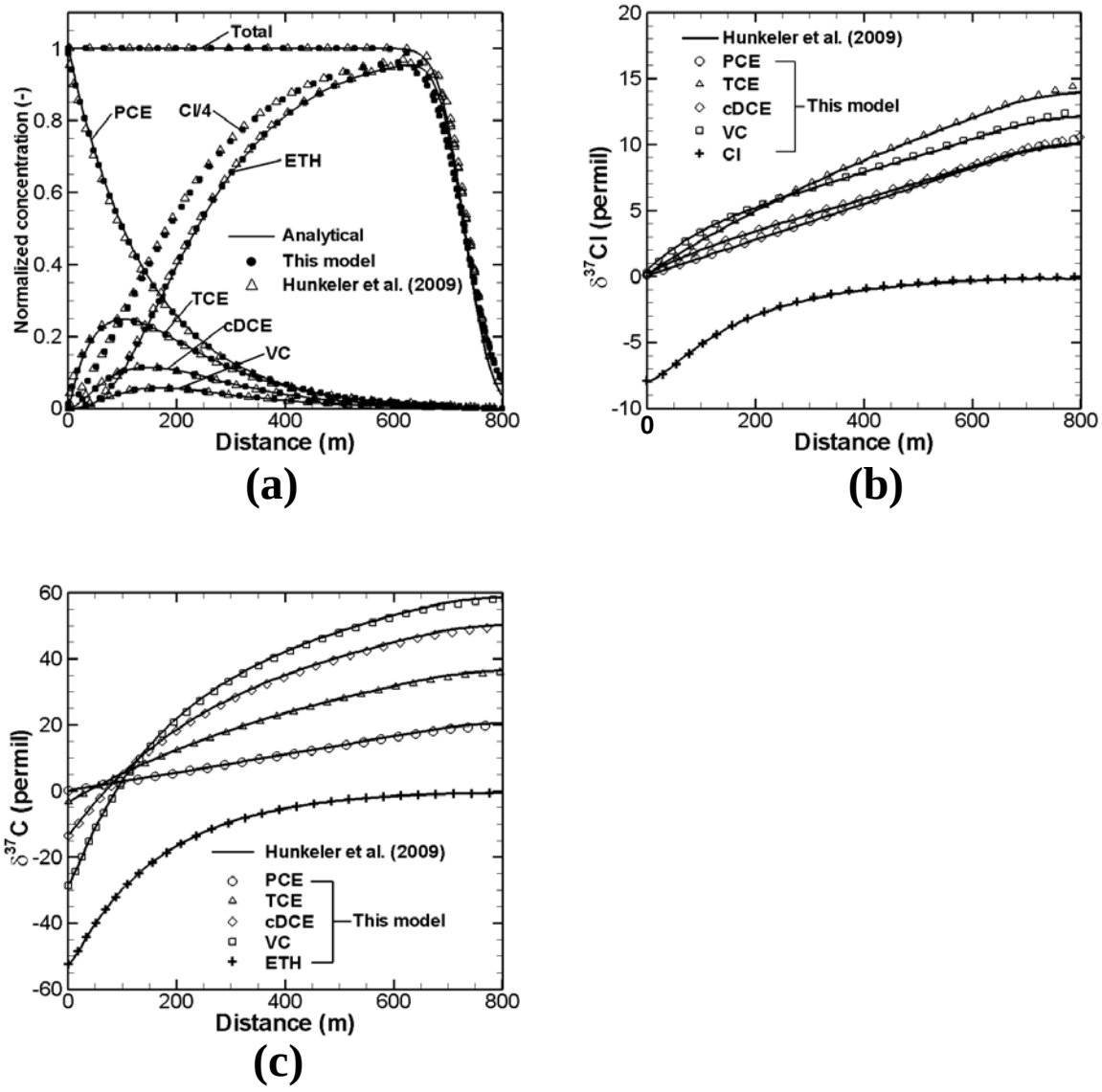

Figure 4.1.3: (a) Numerical and analytical solutions for the spatial distribution of aqueous CAHs mole fractions after 20 years of injection of PCE at origin. Simulated chlorine (b) and carbon (c) isotope signatures for CAHs are compared to the results in Hunkeler et al. (2009).

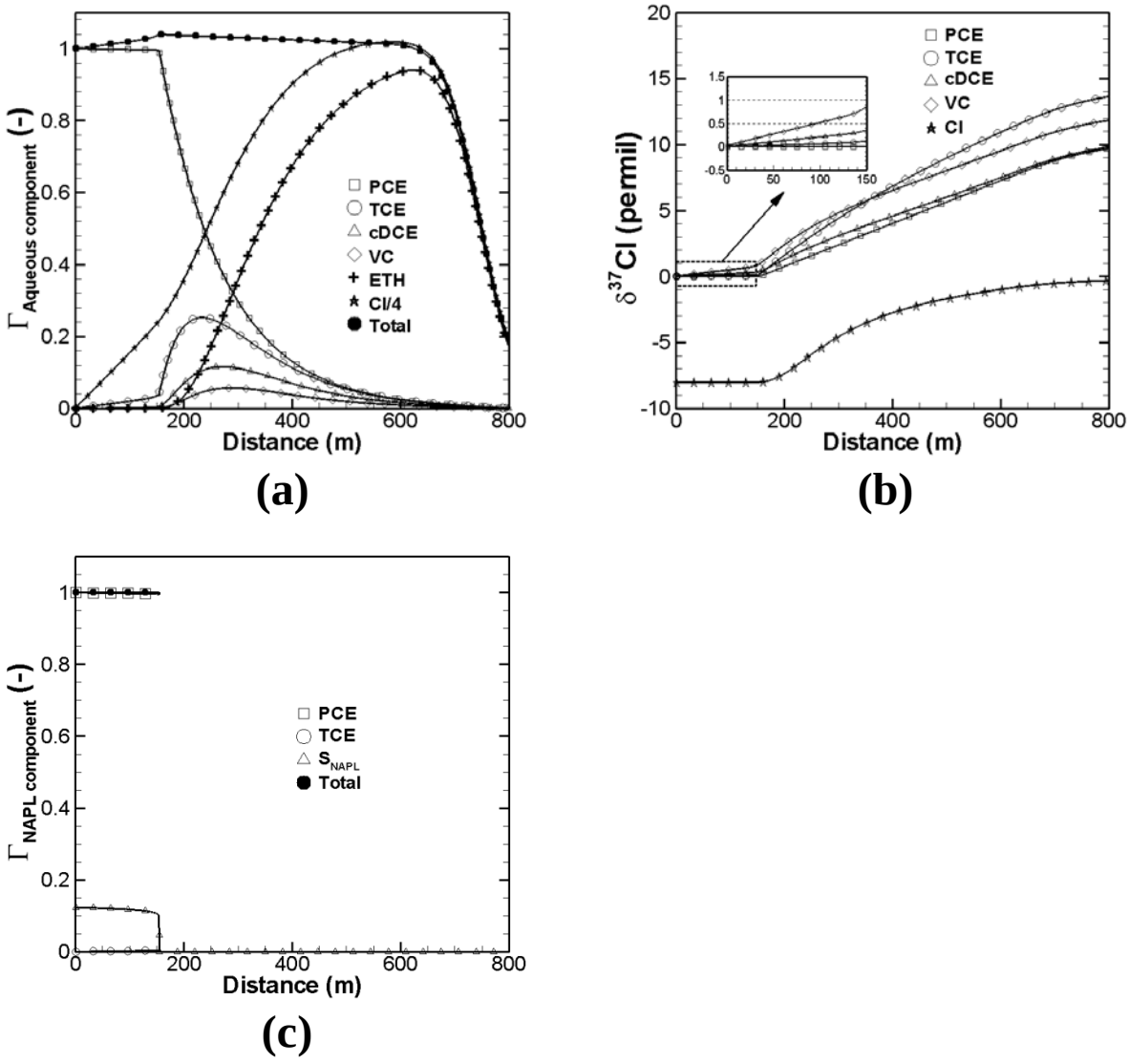

Figure 4.1.4: The spatial distribution of (a) aqueous CAHs mole fractions and (b) chlorine isotope signatures for CAHs after 20 years of injection of PCE at origin. (c) PCE injection rate was increased to generate the NAPL phase of PCE.

4.1.4.1. One-dimensional simulations with lower rates of degradation and enrichment

Multiphase flow and reactive transport with isotope fractionation was simulated for the case when the domain and simulation parameters remained the same as those applied to the aqueous phase reactive transport simulation in the verification example (see case 1a and Figure 4.1.3). However, the spill rate of the PCE isotopologues was increased ($Q_{PCE} = 2.5 \times 10^{-4}$ m^3/day), as the DNAPL phase (S_n > 0) is often observed under real-world contamination conditions. The simulation results shown in Figures 4.1.4a and 4.1.4b for case 1b are comparable to those from the verification example (Figures 4.1.3a and 4.1.3b). It is noted that in Figure 4.1.4a, the mole fractions are normalized by the maximum PCE aqueous mole fraction

($[X_{PCE,q}]_{max} \cong 1.62 \times 10^{-5}$). The concentration profiles in Figure 4.1.4a are different from those of the aqueous injection case in Figure 4.1.3a. In Figure 4.1.3a the relative mole fraction of aqueous PCE ($\Gamma_{PCE,q}$) is maintained close to unity but the relative mole fractions for the degradation products increase from the injection point (x = 0) to $x \approx$ 154 m. The increase of the degradation products results in the total dissolved CAHs being larger than $[X_{PCE,q}]_{max}$, where the PCE NAPL phase exists (Figure 4.1.4c). When the PCE NAPL phase flows along with the groundwater and dissolves into the aqueous phase for transport and reaction, the dissolution condition can be different in the upstream and downstream zones. Because aqueous CAHs in the downstream zone have experienced degradation while flowing from the upstream zone, the dissolution of the source PCE NAPL can be limited by existing dissolved degradation products of higher solubility (with smaller molecular weight). Thus, the total CAHs mole fraction can be higher than the solubility of the (PCE) source (Figure 4.1.4a). This result implies that dissolution can compete with the degradation reaction in the source zone, thus influencing the aqueous CAH composition.

Figure 4.1.4b shows the spatial distributions of $\delta^{37}Cl$ in CAHs and indicates that the evolution of $\delta^{37}Cl$ values are similar to those shown in Figure 4.1.3b from the NAPL migration front to the downstream end of the domain, but that PCE degradation products become slightly enriched with ^{37}Cl within the source zone as the distance increases from the injection point. These results are consistent with the isotopic trends observed in laboratory studies [*Morrill et al., 2009*]. The isotope signature for aqueous PCE in Figure 4.1.4b (close to that of the PCE NAPL source) shows that the aqueous PCE originated predominantly from the NAPL phase through dissolution. The results in Figure 4.1.4 imply that the aqueous contaminant composition and isotope signatures in the source zone can be different from those in the NAPL phase with higher rates of degradation and isotope enrichment if dissolution competes with the degradation reaction in the source zone.

4.1.4.2. One-dimensional simulations with higher rates of degradation and enrichment

The effects of the changes in the rates of degradation and enrichment on the transport of CAHs and compound specific isotope ratios are next examined. For simulation case 2, all the parameters are the same as those in case 1, but the bulk degradation rates for all CAHs (λ_p) are increased by one order of magnitude (Table 4.1.3). The results in Figures 4.1.5a and 4.1.5b show that the degradation of the PCE, injected as the aqueous phase (case 2a), as well as isotope enrichment for all the CAHs, are much more rapid than the results provided in Figures 4.1.3a and 4.1.3b (case 1a). It is interesting to note that the DNAPL phase with the higher PCE spill rate (case 2b) influences not only the aqueous phase concentration and isotopic signatures (Figures 4.1.5c and 4.1.5d), but also the composition of the DNAPL phase with the equilibrium partitioning between the aqueous and NAPL phases (Figure 4.1.5e). This implies that there can be an apparent degradation of PCE NAPL even when degradation of the PCE NAPL phase is not allowed in the model.

For simulation case 3, Figures 4.1.6a and 4.1.6b show the results for chlorine isotope enrichment when the enrichment factors (ε_p^{Cl}) are increased by one order of magnitude, but the degradation constants are kept the same as the reference cases. The results indicate that the heavy chlorine isotopes are quickly enriched with increased ε_p^{Cl} values except in the aqueous PCE within the source zone, where dissolution may dominate degradation. When both degradation rates and enrichment factors are increased by one order of magnitude (case 4), the influence

becomes synergistic and the enrichment of heavy chlorine for aqueous PCE becomes noticeable even in the source zone (Figures 4.1.6c and 4.1.6d).

The simulation results clearly illustrate that the formation and flow of a NAPL phase can significantly influence the transport of aqueous CAHs and isotope enrichment in the source zone when the rates of degradation and enrichment become higher. It was also illustrated from the results that higher degradation rates can change the composition of the NAPL phase (apparent degradation) even when the degradation of NAPL phase CAHs are not allowed in the model.

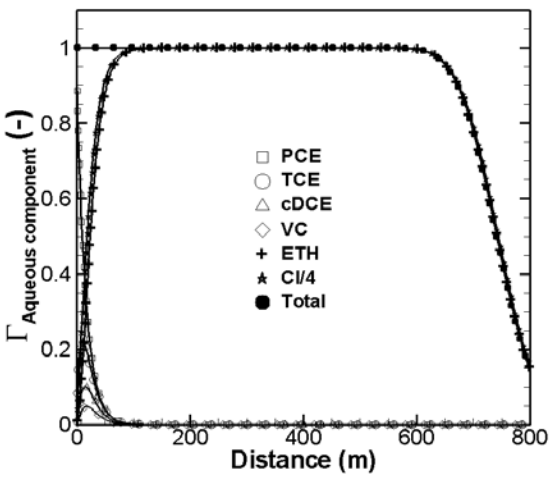

(a)

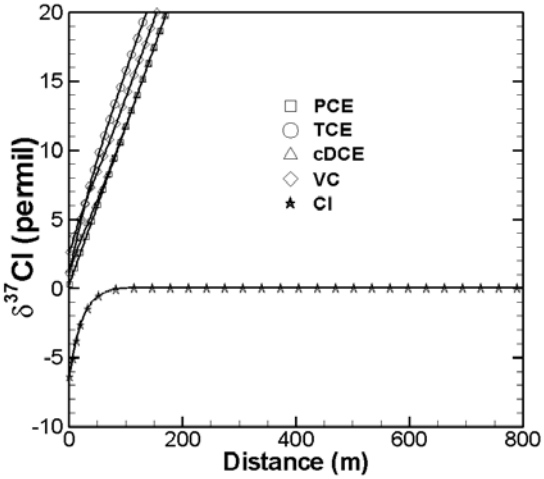

(b)

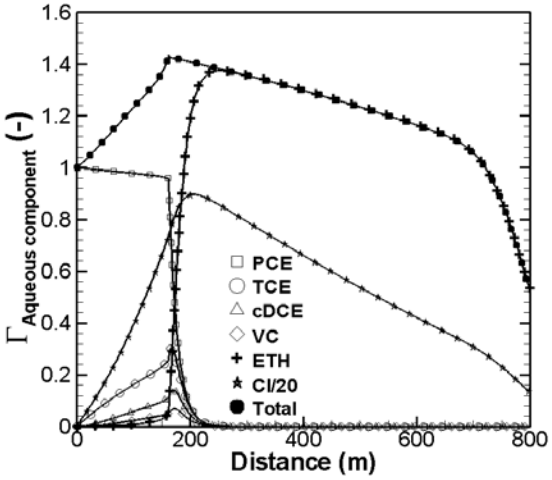

(c)

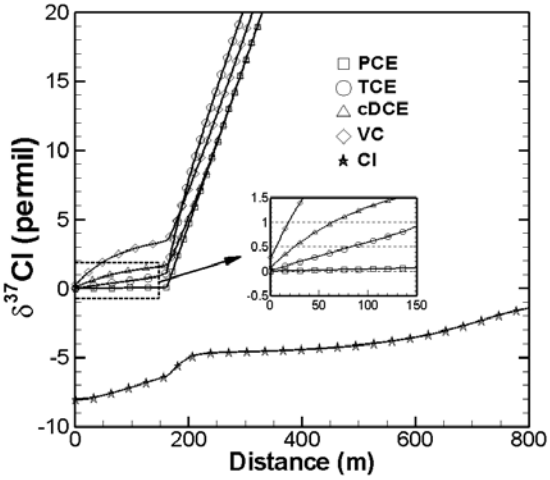

(d)

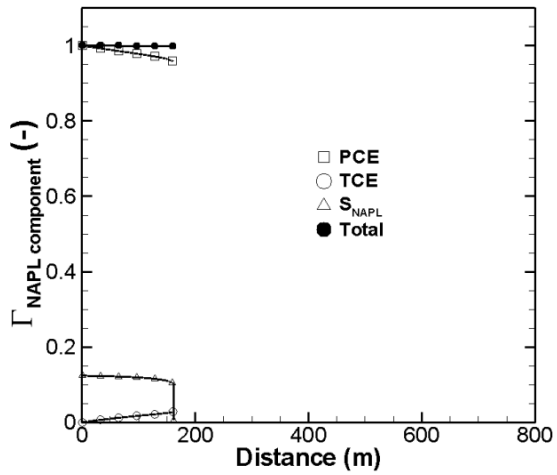

(e)

Figure 4.1.5: The spatial distribution of (a and c) aqueous CAHs mole fractions and (b and d) chlorine isotope signatures for CAHs after 20 years of injection of PCE at origin when the bulk degradation rates for CAHs were increased by an order from the reference simulation cases 1a and 1b. (a and b) shows the results from a lower injection rate case while (c, d, and e) are from higher rate of injection. (e) indicates that NAPL phase composition can be different from that of the source (pure PCE).

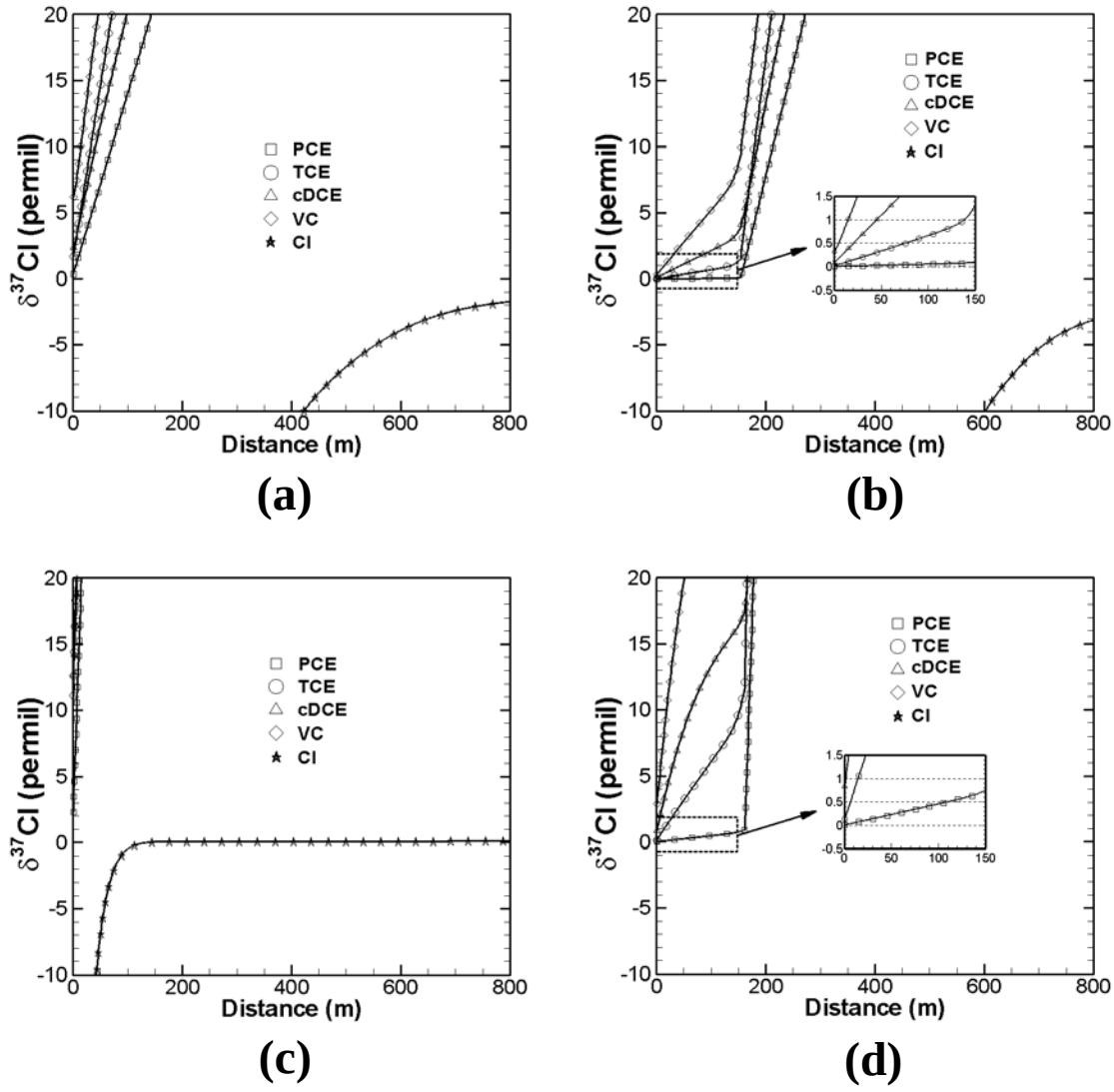

Figure 4.1.6: The spatial distribution of (a and c) aqueous CAHs mole fractions and (b and d) chlorine isotope signatures for CAHs after 20 years of injection of PCE at origin. (a and b) show the results when only the chlorine isotope enrichment factors for CAHs were increased by an order and (c and d) show the results when both rates of degradation and enrichment were increased by an order from the reference simulation case 1b (for a higher rate of PCE injection).

4.1.4.3. Three-dimensional simulations

DNAPL migration with isotope fractionation was simulated in a three-dimensional heterogeneous domain of 40 m × 20 m × 6 m dimension (Figure 4.1.7a). The domain was discretized using base cells of 1 m × 1 m × 1 m which were refined near the injection point to 0.5 m × 0.5 m × 0.5 m cells to reduce numerical dispersion in the vicinity of the zone where the PCE DNAPL is injected. The permeability follows a lognormal distribution (geometric mean and variance of log permeability given as -24.97 m^2 and 0.59) with a horizontal correlation length equal to 10.0 m and a vertical value equal to 1.1 m (Figure 4.1.7b). The relation among the

relative permeability, saturation, and pressure for aqueous and DNAPL phase flow was determined by the Brooks-Corey equation as given in Unger et al. (1998) and Miles et al. (2008).

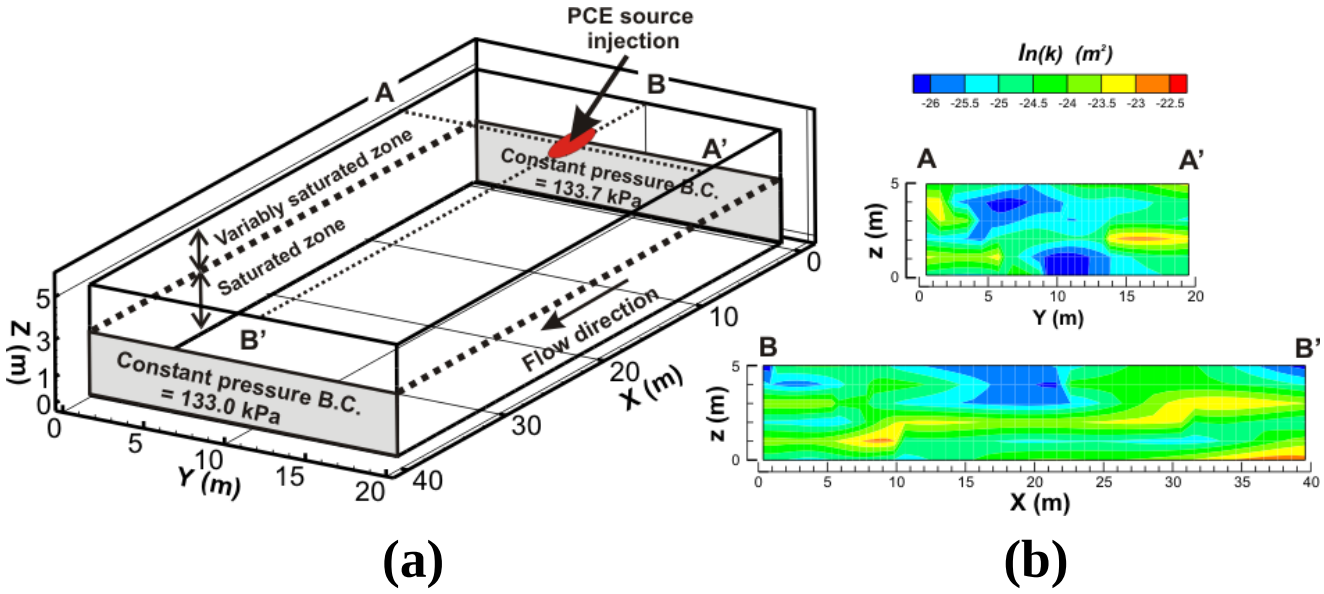

Figure 4.1.7: (a) A three-dimensional domain for the simulation of DNAPL and groundwater flow, dissolution, and reactive transport with isotope fractionation with boundary conditions. (b) shows a log-permeability field that was generated based on the statistical characteristics of CFB Borden site (Sudicky, 1986).

The parameters used to simulate the DNAPL PCE isotope composition, degradation, and isotope enrichment are adopted from several references to field and laboratory studies (Table 4.1.4). First-order decay rates (λ_p) for each contaminant were from Suarez and Rifai (1999) and the bulk enrichment factors for carbon (ε_p^C) were obtained by averaging the values estimated by Atteia et al. (2008) and Sherwood Lollar et al. (2000). The bulk enrichment factors for chlorine (ε_p^{Cl}) were determined based on the values of Abe et al. (2008) and Numata et al. (2002). The carbon and chlorine isotope composition of the injected PCE are averages of the estimates given in the studies by Beneteau et al. (1999) and van Warmerdam et al. (1995). For the given parameters, two simulations are performed with different PCE injection rates. Table 4.1.5 lists the carbon isotopes and chlorine isotopologues for PCE injection rates with respect to scenarios 1 and 2, while Table 4.1.6 lists the corresponding degradation rate constants. Scenario 1 is designed to inhibit DNAPL movement after it reaches the bottom of the simulation domain by ensuring that the total dissolution rate of PCE DNAPL equilibrates with the PCE spill rate at that location. Scenario 2 is designed to induce the flow of the DNAPL phase at the bottom of the domain by increasing the PCE spill rates (see Table 4.1.6).

Steady-state groundwater flow was established before injecting PCE (mixed with water) at the surface. The water table was assumed to be located about 2 m below ground surface. Constant pressure boundary conditions were assigned on both sides of the domain to set the

groundwater hydraulic gradient of 1.8×10^{-3}. The mean groundwater Darcy flux along the *x*-axis is 8.73×10^{-3} m/day, which can be converted to an average linear groundwater velocity of 2.57×10^{-2} m/day given that the effective porosity used is 0.34.

Table 4.1.4: Parameters applied to 3-D Borden site isotope fractionation simulation

Isotope	PCE	TCE	cDCE	VC	Reference
1. First-order reaction rates (yr^{-1})					
	3.65	1.10	0.73	1.10	Suarez and Rifai (1999) [a)]
2. Bulk enrichment factor (‰)					
C	-5.5	-14.8	-20.4	-22.4	Sherwood et al. (2000)
Cl	-10.7[b]	-5.6[b]	-1.5[c]	-1.8[c]	Numata et al. (2002)[b)] Abe et al. (2008)[c)]
3. Isotope value in pure phase (‰)					
C (VPDB)	-34.8[d)]				van Warmerdam et al. (1995) Beneteau et al. (1999)
Cl (SMOC)	-2.5[d)]				van Warmerdam et al. (1995) Beneteau et al. (1999)

[a)] mean of reductive dechlorination of field/in situ studies.;
[b)] mean and converted from fractionation factor;
[c)] converted from AKIE;
[d)] mean values for PPG manufacturer, which are estimated by van Warmerdam et al. (1995) and Beneteau et al. (1999).

Table 4.1.5: Continuous PCE source spill rates (*Q*, m^3/day) for 3-D Borden site simulations

Chlorine isotopologue			Carbon isotope		
	Scenario 1	Scenario 2		Scenario 1	Scenario 2
PCE_{LLLL}	6.52×10^{-5}	3.28×10^{-4}	PCE_L	1.95×10^{-4}	9.89×10^{-4}
PCE_{LLLH}	8.38×10^{-5}	4.22×10^{-4}	PCE_H	2.17×10^{-6}	1.10×10^{-5}
PCE_{LLHH}	4.04×10^{-5}	2.03×10^{-4}	Water	8.02×10^{-4}	0.0
PCE_{LHHH}	8.64×10^{-6}	4.35×10^{-5}			
PCE_{HHHH}	6.93×10^{-7}	3.49×10^{-6}			
Water	8.01×10^{-4}	0.0			

Saturation distributions after 20 years of DNAPL spill for both the lower and higher PCE spill rates are shown in Figure 4.1.8. In either case, the injected DNAPL flows downward through the unsaturated and saturated zones until it reaches the bottom of the domain. With the higher spill rate, DNAPL moves primarily along the groundwater flow direction at the bottom of

the domain, while spreading laterally to the sides of the domain (Figure 4.1.8b). Both cases show a significant difference in NAPL saturation above and below water table: saturation above the water table ranges from 0.2 to 0.3, indicating that the DNAPL introduced into the system dissolves into the aqueous phase more easily when the pore space is saturated. In Figure 4.1.8b, the DNAPL saturation front migrates less than 10 m from the injection point and the mean velocity of the DNAPL phase at the domain bottom is less than 1.37×10^{-3} m/day, which is more than one order of magnitude smaller than the groundwater flow velocity. Figure 4.1.9 compares the mole fractions of CAHs and isotope signatures in the CAHs for the lower and higher injection cases, along the observation lines shown in Figure 4.1.8. The results in Figure 4.1.9 illustrate that the effect of dispersion (dilution) strongly affects the concentration of CAHs for the case of a low PCE release rate (scenario 1), while the influence becomes less significant for isotopic signatures. With the formation and flow of a NAPL phase as shown in Figures 4.1.8b, 4.1.9b, and 4.1.9d, it is clear that dissolution plays a key role in determining the CAH concentrations and isotopic signatures in the source zone.

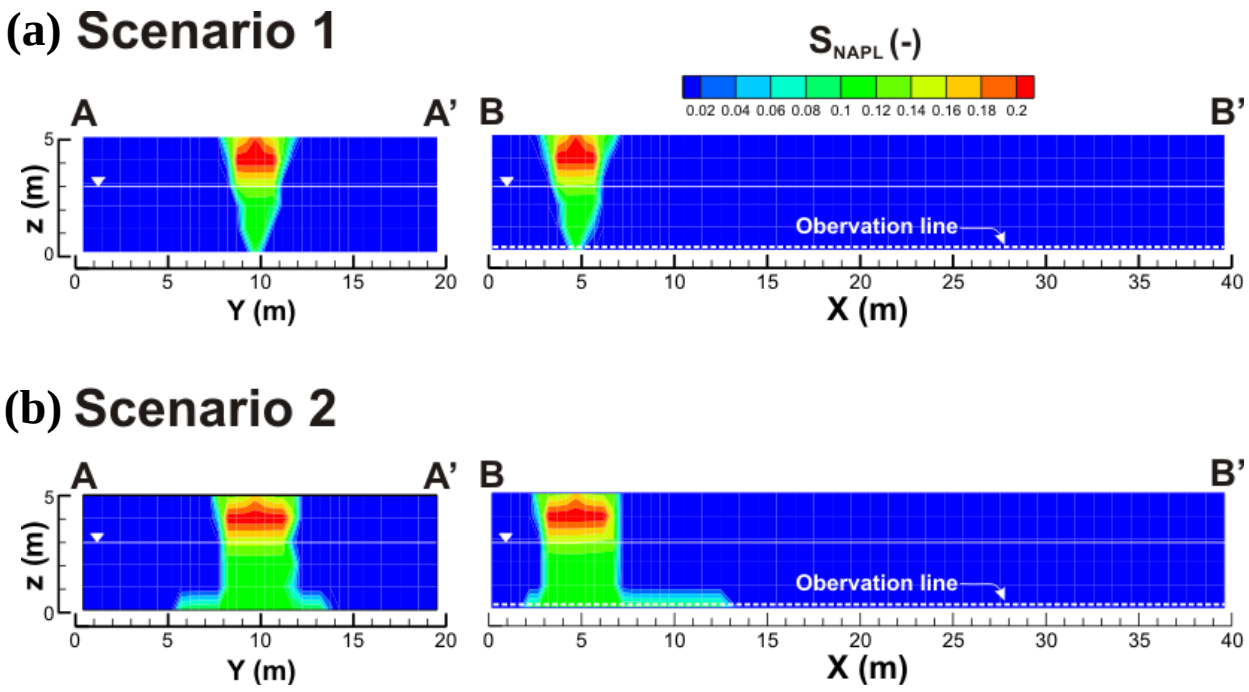

Figure 4.1.8: DNAPL saturation distributions in the three-dimensional heterogeneous domain after 20 years of injection of PCE DNAPL. (a) DNAPL injection rate for scenario 1 was adjusted to restrict the source zone below the injection point and (b) the rate was increased to allow the DNAPL to flow along with groundwater at the bottom of the domain for scenario 2.

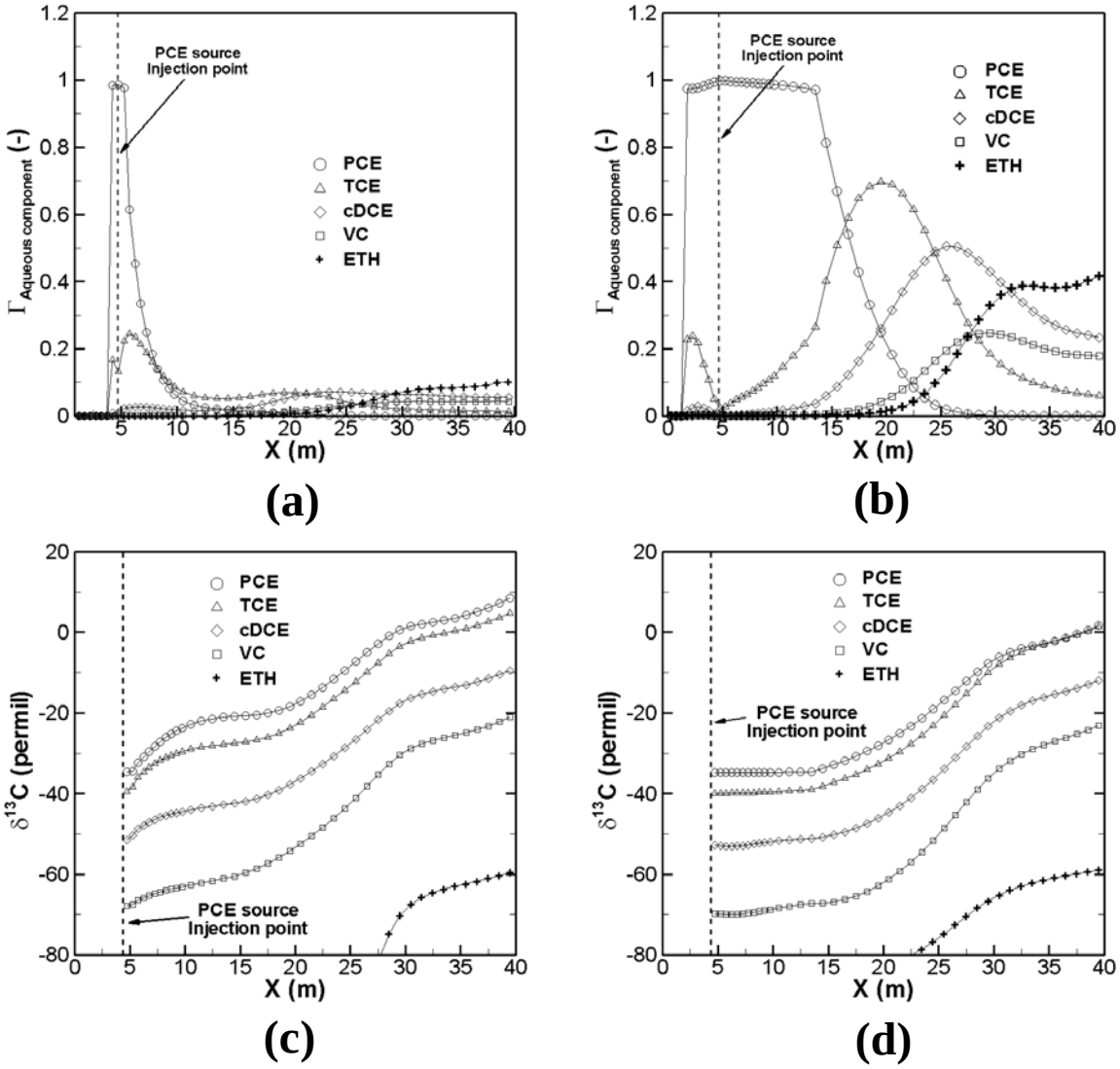

Figure 4.1.9: (a and b) aqueous CAHs mole fractions and (c and d) carbon isotope signatures for CAHs along the observation lines shown in Figure 8, after 20 years of injection of PCE, with (a and c) lower and (b and d) higher rates of PCE injection.

The results of the three-dimensional heterogeneous sandy aquifer simulations illustrate the necessity and importance of characterizing the source zone and groundwater flow field for the application of CSIA. The results also illustrate the complexities that must be considered when determining and interpreting the isotopic signatures associated with the DNAPL contaminants. The three-dimensional compositional isotope fractionation model presented in this study can be used to simultaneously characterize the source zone, groundwater flow system, and multi-chain reactive transport with the isotope fractionation process.

Table 4.1.6: Degradation rate constants (1/day) for chlorine isotopologue and carbon isotopes (scenarios 1 and 2)

Chlorine isotopologue			Carbon isotope	
	$^{L}\lambda_{p}$	$^{H}\lambda_{p}$		$^{L}\lambda_{p}$ or $^{H}\lambda_{p}$
PCE_{LLLL}	1.01×10^{-2}	NA	PCE_{L}	1.00×10^{-2}
PCE_{LLLH}	7.58×10^{-3}	2.42×10^{-3}	PCE_{H}	9.95×10^{-3}
PCE_{LLHH}	5.05×10^{-3}	4.84×10^{-3}		
PCE_{LHHH}	2.53×10^{-3}	7.25×10^{-3}		
PCE_{HHHH}	NA	9.67×10^{-3}		
TCE_{LLL}	3.03×10^{-3}	NA	TCE_{L}	3.01×10^{-3}
$TCE_{LL\mathbf{H}}$	NA	2.98×10^{-3}	TCE_{H}	2.97×10^{-3}
$TCE_{LH\mathbf{L}}$	3.03E-03	NA		
$TCE_{HL\mathbf{L}}$	3.03E-03	NA		
$TCE_{LH\mathbf{H}}$	NA	2.98×10^{-3}		
$TCE_{HL\mathbf{H}}$	NA	2.98×10^{-3}		
$TCE_{HH\mathbf{L}}$	3.03×10^{-3}	NA		
TCE_{HHH}	NA	2.98×10^{-3}		
DCE_{LL}	2.00×10^{-3}	NA	DCE_{L}	2.00×10^{-3}
DCE_{LH}	1.00×10^{-3}	9.98×10^{-3}	DCE_{H}	1.96×10^{-3}
DCE_{HH}	NA	2.00×10^{-3}		
VC_{L}	3.02×10^{-3}	NA	VC_{L}	3.01×10^{-3}
VC_{H}	NA	3.01×10^{-3}	VC_{H}	2.95×10^{-3}

4.2.1 Three-phase flow in discretely fractured rock: Introduction

Understanding of two and three phase fluid flow and solute transport is applicable to many fields: Petroleum engineering is tasked with optimizing production of oil from a reservoir by forced injection of water, given the presence of resident gas trapped in the formation; sequestration of carbon in geologic repositories involves injection of supercritical carbon dioxide deep below the water table; underground nuclear waste storage at Yucca Mountain is concerned with migration of radionuclides away from the vadose zone repository over the long term; and contaminant hydrogeology is often faced with spills of non-aqueous phase liquid (NAPL) contaminants that migrate through the vadose and saturated zones. These problems frequently arise in the geologic context of heterogeneous and fractured rock. Given the complex subsurface environment and the intricacies of multiphase flow, practitioners often employ numerical models to assist in their problem solving. One example in the field of contaminant hydrogeology where numerical modeling is being applied is at the former polychlorinated biphenyl waste transfer facility near Smithville, Ontario, Canada (Slough et al., 1999). To assist in quantifying the extent of the source zone and dissolved plume, and to evaluate possible remediation strategies at the Smithville site, numerical models are presently being employed (McLaren et al., 2012).

In a general sense, this study outlines one approach to numerical modeling of three mutually interactive phases (i.e. the aqueous, non-aqueous, and gas phases) in discretely fractured rock. We look at issues of representing fractures and the rock matrix in the domain spatially (geometric connectivity) and how to couple the fractures with matrix and fractures with intersecting fractures to quantify flow and transport processes (flux connectivity). From a contaminant hydrogeology perspective, because of the Smithville site and many other industrial sites like it, we want to model source zone evolution of a contaminant in the subsurface based on the following conceptual pathway: Beginning with contaminant/NAPL release at the ground surface, the invading liquid migrates downward in the vadose zone under the influence of gravity. It displaces the air and/or water initially present in the PM/rock matrix pores or fracture void space. Each phase may flow from fracture-to-fracture, matrix-to-matrix, fracture-to-matrix (imbibition), matrix-to-fracture, or matrix-to-matrix flow across a fracture plane. The mode of flow depends on the three phase saturation conditions, phase total potentials, and capillary pressure (noting that capillarity causes the aqueous phase to be the most wetting and gas to be the least wetting). In the vadose zone, fractures act as barriers to aqueous and NAPL flow because capillarity causes them to be preferentially filled by the gas phase. Flow of the invading phase continues through the vadose zone, capillary fringe, and eventually to the water table. At the water table, the NAPL may form a lens if it is less dense than water, or may continue to infiltrate deeper if it is more dense than water. Below the water table, fractures act as conduits for flow due to their relatively high permeability. Assuming a finite release of NAPL, the advance of the liquid will eventually halt and a terminal source zone architecture will be manifest. Concurrent with the evolution of the source zone, physical processes such as dissolution, volatilization, sorption, diffusion and dispersion, and biodegradation may occur. These processes may lead to a plume of dissolved contaminant being transmitted away from the source zone over long periods of time via advective and diffusive fluxes of the solvent phase. Additional influences to the source zone and plume include precipitation at the ground surface, temporal variation in the height of the water table, and/or changes in the ambient barometric pressure.

Many of the concepts listed above, such as matrix and fracture flow, imbibition, equilibrium phase partitioning, etc., are well established in the literature. The concept of *fracture*

cross flow is not as well researched. (We recognize that this term has been used elsewhere, particularly in the dual-continuum modeling literature, for flow over fracture-matrix interfaces, but herein we use it for direct matrix-to-matrix flow across a fracture plane.) This type of flow is depicted conceptually in Figure 4.2.1 (extended from Wang and Narasimhan (1993), Figure 7.2.1.)

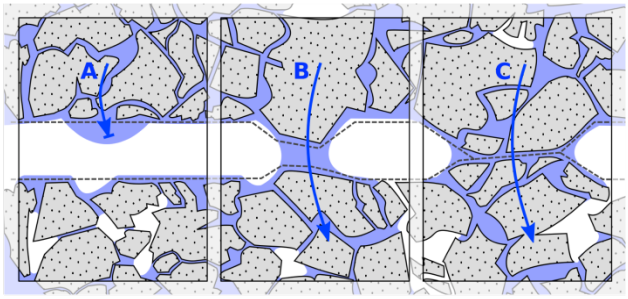

Figure 4.2.1: Schematic representation of two phases, wetting and non-wetting, e.g. aqueous and gas, in a fractured porous medium with wetting phase a) at a capillary barrier, or exhibiting fracture cross flow via b) a liquid bridge or c) an asperity contact bridge.

Because capillary barriers, depicted in Figure 4.2.1a, are influential to wetting-phase flow in the vadose zone, fracture cross flow becomes an important mechanism to circumvent such barriers. Some theoretical and laboratory work has been done to gain insight into fracture cross flow. Makurat (2000) measured single-phase fracture cross flow under different fracture stress-strain conditions. Considering two phases, Dejam and Hassanzadeh (2011) have recently put forth some theoretical work for *liquid bridging* or *capillary cross flow* depicted in Figure 4.2.1b, an idea put forth by Saidi (1987). Firoozabadi and Markeset (1995) showed that flowing petroleum exhibits these liquid bridging effects in laboratory experiments using milled sandstone blocks in various configurations across 1000 μm, smooth-walled fractures. We hypothesize that a second mechanism for fracture cross flow is flow through matrix material in areas where opposing walls of a fracture make direct contact, as in Figure 4.2.1c. Herein, this shall be termed *asperity contact bridging*. Some researchers have numerically modeled dynamic closure of rough walled fractures based on hydromechanical stress and strain (e.g. Unger and Mase (1993), McDermott and Kolditz (2006), and Walsh et al. (2008). Those and their supporting works, describe measurable properties of the rock and the hydromechanical system that form a basis for quantitatively estimating the amount of fracture surface area where opposite walls are in direct contact. It is through this surface area where we believe that Darcian flow occurs. And under this supposition, we allow for this flow mechanism in our numerical model.

Models for flow through fractured porous media can be subdivided into three categories, as reviewed by Narasimhan (1982): equivalent porous media (EPM), dual continuum (which may be further divided into dual-permeability (DK) Barenblatt et al (1960) or dual-porosity (DP) (Warren and Root, 1963; Kazemi, 1969; Reiss, 1980) with the distinction being whether fluid is immobile or mobile in the porous medium), and discrete fracture network (DFN) approach (Grisak and Pickens, 1980; Nooishad et al., 1982). EPM models have been successfully applied to contaminant transport problems in highly fractured, high porosity systems (Cokuner and Hyde, 1998), but may be unsuitable for many other transport applications (Lee et al, 1992; Balfour, 1991) including more sparse fracture patterns (McKay et al., 1993; Jorgensen et al., 1998), or in cases where fracture flow is of explicit interest. Kazemi and Gilman (1993) provide a brief overview of DP and DK models. DK models have been applied to nuclear waste

repository modeling (e.g. Liu et al., 1998) and continue to be developed for the petroleum industry (e.g. Sarma and Aziz, 2006). The drawback to this class of models is the use of a *shape factor* scaling the mass transfer between the matrix and fracture continua that may not be uniquely defined for a given geological setting (Unger et al., 2004). This class handles fracture cross flow implicitly because fractures do not cross-cut the matrix, but in a two-phase context the transfer function is fundamentally ill-defined (Hoteit and Firoozabadi, 2008). As computer power has increased, so has the use of DFN models, which generally bear an extra computational burden of small volume nodes and sharp spatial contrasts in permeability. DFN models using three mobile phases have been used in petroleum reservoir problems. Geiger et al. (2009) developed a model using a hybrid finite-element finite-volume model for stochastically generated fracture networks with complex geometry based on the numerical *IMPES* technique. Hoteit and Firoozabadi (2008) have proposed a succession of single-phase DFN, and oil and water two-phase DFN flow and transport models with capillarity using combined discontinuous Galerkin and mixed hybrid finite-element methods (Hoteit and Firoozabadi, 2005, 2006, 2008a,b). In references (Hoteit and Firoozabadi, 2008a,b) in particular, contrasts in capillary pressure may restrict non-wetting phase flux in heterogeneous PM or at a fracture plane. More recently, Moortgat et al. (2011) expanded this platform to include compressible three phase flow, but it is presented in the context of carbon dioxide sequestration in a homogeneous, unfractured, porous medium. Lesinigo et al. (2011) present another DFN model that uses Darcian flow in the porous media with Stokes-Brinkman flow in fractures to better capture kinetic fluid flow in single phase flow problems.

In this study, we expand on the work of Slough et al. (1999) by augmenting the numerical model *CompFlow Bio*. This model is a three-phase, multi-component flow and transport simulator that uses equilibrium phase partitioning of component species in three spatial dimensions. A control volume, first order finite difference approach is used to discretize the governing three-phase flow equations. Phase pressures, saturations, and component mole fractions are solved for using a fully-implicit scheme. We use a newly-implemented non-uniform mesh generator to incorporate *(n-1)-dimensional* discrete fractures with in a fashion that reduces the number of control volumes when compared with traditional approaches. Macro-scale relative permeability and capillary pressure versus saturation (k_r-S-P_c) relationships create capillary barrier effects (Figure 4.2.1a) and indirectly handle liquid bridged flow (Figure 4.2.1b) .We make use of the measureable geometric and hydromechanical properties to include asperity contact in our formulation that allow for asperity contact bridged flow (Figure 4.2.1c). Furthermore, we continue directly from Slough et al. (1999) to derive how small volume nodes that arise at the intersection of fractures in three dimensions can be algebraically eliminated from the numerical system.

In this section, we present the governing equations and the control volume, finite difference formulation of the numerical model. We provide results from a large-scale, three-dimensional, two phase simulation extended from the source zone modeling described by McLaren et al. (2012) as a demonstration of our domain discretization process. This problem involves two-phase flow (aqueous and NAPL) in a 200 × 50 × 43 m domain with fractures spaced on the order of one per meter.

4.2.2 Theory

4.2.2.1 Governing equations

CompFlow Bio is a numerical model that includes: three mobile phases (aqueous, non-aqueous and gas); multiple components (water, one or more oil species, air/nitrogen, and zero or more gas species); and flow and transport of thermal energy. It uses equilibrium partitioning to transfer components between phases. Equations are discretized by control-volume finite-element/finite-difference approaches. In this study, the control-volume finite-difference scheme is used for flow and transport of three components $p\epsilon\{w,a,c\}$, water, air/nitrogen, and TCE, in three phases $l\epsilon\{q,n,g\}$, aqueous, non-aqueous (NAPL) and gas phases, respectively. Temperature is held constant.

The governing equations have been reported in the literature before in references (Forsyth, 1993; Yu et al., 2009), but the following summarizes those applicable to this investigation. In its most general form, the equation for conservation of moles of component species *p* is:

$$\frac{\partial}{\partial t}\left[\phi\sum_l S_l M_l X_{pl} + \rho_b K_d M_q X_{cq}\right] = -\sum_l \nabla\cdot\left(M_l X_{pl}\vec{v}_l\right) + \sum_l \nabla\cdot\left(\phi S_l \mathbb{D}_l M_l \nabla X_{pl}\right) + Q_p \tag{4.2.1}$$

The Darcy velocity is given by:

$$\vec{v}_l = -\mathbb{K}\frac{k_{rl}}{\mu_l}(\nabla P_l - \rho_l g\nabla d) \tag{4.2.2}$$

and, the dispersion tensor from Bear (1972) has the form:

$$\phi S_l \mathbb{D}_l = \alpha_L^l|\vec{v}_l|\delta_{IJ} + \left(\alpha_L^l - \alpha_T^l\right)\frac{\vec{v}_l\vec{v}_l^T}{|\vec{v}_l|} + \phi S_l \tau D_l^*\delta_{IJ} \tag{4.2.3}$$

A summary of the notation is given by:

t is time [d]

ϕ is porosity [-]

S_l is saturation of phase l [-]

X_{pl} is mole fraction of species p in phase l [-]

M_l is molar density of phase l [mol/m^3]

Q_p is a source/sink term for species p [mol·m^{-3}·d^{-1}]

$\mathbb{K}$ is the intrinsic permeability tensor [m^2]

k_{rl} is relative permeability of phase l [-]

μ_l is coefficient of dynamic viscosity of phase l [kg·m^{-1}·d^{-1}]

P_l is fluid pressure of phase l [kg/m^3]

ρ_l is mass density of phase l [kg/m^3]

ρ_b is bulk density of the porous medium [kg/m^3]

K_d is sorption coefficient [m^3/kg]

g is the gravitational acceleration constant [m/d^2]

d is depth [m]

δ_{IJ} is the Dirac delta function at matrix indices *I* and *J*

Note that the intrinsic permeability tensor is assumed to be aligned with the principle spatial axes and thus for PM, has the form:

$$\mathbb{K} = \begin{bmatrix} k_{x_1x_1} & 0 & 0 \\ 0 & k_{x_2x_2} & 0 \\ 0 & 0 & k_{x_3x_3} \end{bmatrix} \tag{4.2.4}$$

while for fractures with effective hydraulic aperture *2b*, planar directions the *I* and *J* and normal direction *K*, the intrinsic permeability components are given by:

$$k_{II} = k_{JJ} = \frac{(2b)^2}{12} \tag{4.2.5}$$

The above formulation leaves fifteen unknown variables per control volume: three saturations S_l, nine mole fraction values X_{pl}, and three pressures P_l. Various constraints and assumptions exist among the unknowns that eventually reduce the number of unknowns to three *primary variables* per control volume. The following description makes such a reduction in the system under the assumption that all three phases are present in a control volume (CV). If a phase is not present, the numerical model undergoes *primary variable switching* for the affected CVs. This, as well as a description of system closure in all primary variable configurations, is given in Forsyth and Shao (1991). The constraints and assumptions, beginning with unity saturation, are:

$$S_q + S_g + S_n = 1 \tag{4.2.6}$$

The sum of mole fractions of all components in a phase must equal unity. The system is reduced by three primary variables with the following:

$$\sum_p X_{pl} = 1 \tag{4.2.7}$$

Equilibrium partitioning is employed to transfer components between phases. Air is considered non-condensable, thus it is not allowed in any phase but gas. Water is assumed to be insoluble in NAPL. Partitioning relationships reduce the number of unknowns by six. The general form of the partitioning relationship and no-partition assumptions, are:

$$X_{pl_2} = Z_{pl_2 l_1} X_{pl_1};\ \ X_{aq} = X_{an} = \ X_{wn} = 0 \tag{4.2.8}$$

where $Z_{pl_2 l_1}$ is some constant partitioning coefficient or a function of temperature, pressure, etc., between phases l_1 and l_2 [-].

Finally, constraints exist among the phase pressures due to capillarity. With experimentally determined data to parameterize the two-phase capillary pressure relationships, $P_{c,gn}$, $P_{c,gq}$ and $P_{c,nq}$, the constraint equations are:

$$\begin{gathered} P_q = P_n - \hat{\alpha} P_{c,nq}(S_q) - (1-\hat{\alpha}) P_{c,nq}(S_q = 1) \\ P_g = P_n + \hat{\alpha} P_{c,gn}(S_g) + (1-\hat{\alpha})\left[P_{c,gq}(S_g) - P_{c,nq}(S_q = 1)\right] \\ \hat{\alpha} = \min\langle 1, S_n / S_n^* \rangle \end{gathered} \tag{4.2.9}$$

where $P_{c,gn}$, $P_{c,gq}$, $P_{c,nq}$ are two-phase capillary pressure curves as functions of saturation [kPa] and S_n^* is a blending parameter [-].

The blending function $\hat{\alpha}$ and parameter S_n^* provide a linear transition from the gas-aqueous $P_{c,gq}$ to the gas-NAPL-aqueous $P_{c,gn}$ and $P_{c,nq}$ capillary pressure system. This yields the correct the capillary pressure in the absence of NAPL and when NAPL is present in sufficient quantity $S_n \geq S_n^*$. The linear transition was introduced in Forsyth (1991) to remove the discontinuity in the relationships proposed in (Kaluarachchi and Parker, 1989) and (Abriola and Pinder, 1985) that transition abruptly at a critical NAPL saturation.

In addition to the relative permeability k_{rl}, capillary pressure $P_{c,l_1 l_2}$, and equilibrium partitioning relationships $Z_{pl_1 l_2}$, and viscosity μ_l, there are additional variables that are functions of pressure and saturation. These add to the non-linearity of the problem:

$$M_{l\epsilon\{q,n\}} = \frac{1 + \hat{C}_l (P_l - P_{ref})}{\sum_p \left(\max\langle 0, X_{pl}\rangle / M_p^*\right)};\ \ M_g = \frac{P_g}{RT} \tag{4.2.10}$$

$$\rho_l = M_l \sum\nolimits_p X_{pl} \omega_p \tag{4.2.11}$$

where ω_p is the molecular mass of component p [kg/mol].

4.2.3 Discrete fracture conceptualization

The goal of the numerical model is to represent the void space of rough-walled fractures explicitly and capture the interactions between the rock matrix, and the fracture network using physically based, quantitative relationships. To represent these geologic features computationally, the domain is discretized into three-dimensional (3D) rectangular boxes representing matrix CVs and two-dimensional (2D) rectangular planes representing fractures. A CV is entirely fracture or porous medium. All faces of CVs are parallel to one of the *xy*-, *yz*-, or *xz*-principal coordinate planes. Thus, all fracture intersections occur at 90° angles. Fractures intersections are captured by one-dimensional line and zero-dimensional point CVs where two and three orthogonal fractures meet.

Figure 4.2.2 depicts a rough-walled fracture and surrounding matrix. This is represented by three CVs: one for the fracture and two for the matrix above and below. The matrix CVs have physical dimensions of length, width and height, whereas fracture CVs have length and width only. Aperture is a property of the fracture. Asperity contact is accounted for by dispensing a portion of the 2D fracture's surface area (defined as a dimensionless factor, α, varying from 0 to 100%) to allow direct contact between the adjacent matrix blocks. This reduces the fracture CVs volume by that same factor. In Figure 4.2.2 the asperity contact area is depicted as a cylinder, but the model does not incorporate any specific geometry for its internal representation and thus there are no explicit effects on flow or transport.

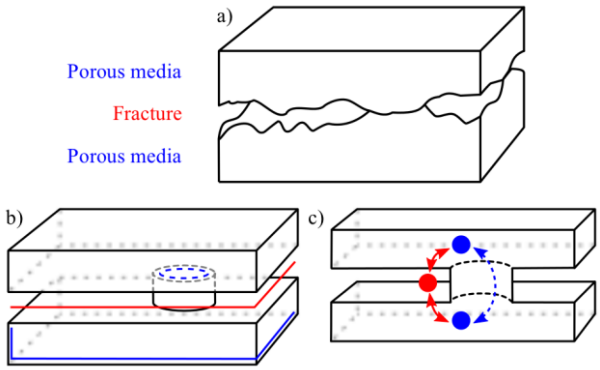

Figure 4.2.2: Discrete fracture conceptualization showing a) a schematic of a rough-walled fracture, b) the two dimensions of a planar fracture CV (red lines), three dimensions of a matrix CV (blue lines) and some asperity contact area (blue dashed line), and c) connection between adjacent PM blocks via asperity contact area (blue dashed arrow) and the contact of PM with the fracture CV (red arrow).

Conceptually, a fracture is formed by two parallel plates separated by some distance or aperture *2b*. The cubic law is employed to determine the intrinsic permeability. No distinction is made between the hydraulic aperture and the mechanical aperture of a fracture, similar to the approach of Reynolds and Kueper (2000). Also as determined in (Reynolds and Kueper, 2000), the effect of fracture roughness is captured by macro-scale relative permeability and capillary pressure relationships.

4.2.4 Geometric discretization of fracture and matrix nodes

The numerical model aims to allow flexibility in the location of fracture planes while maintaining a low number of CVs in the domain. Conventional "row, column and file" grid-based spatial discretization schemes, as depicted in Figure 4.2.3, require fracture CVs to lie on and terminate at the boundaries of PM volumes. (Note that the figure can be easily reinterpreted as a hexahedral finite-element mesh.) The boundaries of PM volumes form grid lines that are continuous across the whole domain. Greater flexibility in the location of fractures, while not inducing more fully domain-cutting grid lines, is achieved by breaking down the structured grid in areas local to fractures. This transforms the initially regular grid of consisting of only porous media nodes to a non-uniform mesh of porous media and fracture CVs.

The process of domain discretization follows four main steps: matrix block discretization; fracture insertion with matrix block bisection and subdivision of the fracture into fracture CVs; fracture intersection refinement and elimination; and addition of asperity contact connections. First, the domain is subdivided into a regular "row, column and file" lattice of rectangular blocks with sizes given as model inputs. Second, fractures are inserted iteratively. Each insertion may cause one or more previously added matrix and/or fracture CVs to be bisected on the plane of the new fracture. The large, conceptual fracture is divided into sub-unit CVs based on the boundaries of preexisting CVs. As an optional third step, fracture CVs may be refined outwards from fracture intersections. A graphic example of this is in Slough et al. (1999, Figure 7c). The refined node size intervals are specified as model parameters. Fracture intersection nodes may also be eliminated during this phase. The fourth and final step is to add connections between matrix CVs across fracture planes to allow for asperity contact bridged flow.

An example of the second step above, insertion of a non-fully crosscutting fracture, is shown in Figure 4.2.4: CVs A and B exist before insertion of the fracture. A is then split into A' and A" and new connections to B are formed based on the new interfacial areas. The fracture is contained entirely within the original A, so it does not need to be subdivided further; the fracture becomes node C. Connections C to A' and C to A'' are made. The connection A' to A" is first constructed as the interface area not obstructed by C, but later in the fourth step, it becomes the sum of the unobstructed area plus the asperity contact area through C.

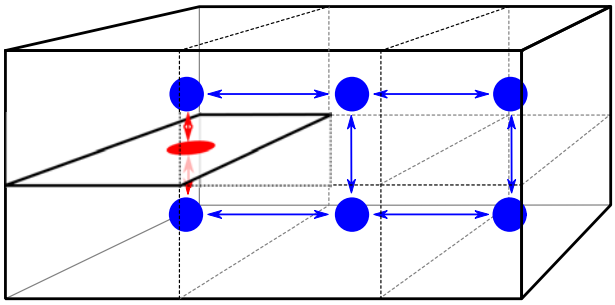

Figure 4.2.3: Schematic diagram of a conventional discrete fracture network control volume discretization with six porous media control volumes and one fracture control volume.

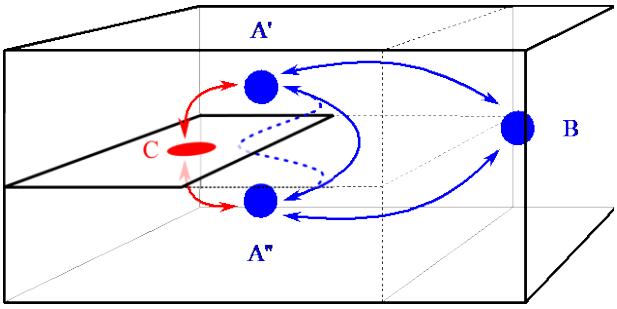

Figure 4.2.4: Schematic diagram of three matrix control volumes, A', A'', and B, one fracture control volume, C, and all associated connections. The connection between A' and A'' is the sum of direct contact area (solid blue arrow), plus the asperity contact area through C (dashed blue arrow).

Other more complicated fracture insertion scenarios exist because of different configurations of preexisting PM and fracture CVs. CVs may have many neighbours on each face (e.g. in Figure 4.2.1, Figure 4.2.4 A' has neighbours A" and C on its bottom face) and hence the mesh we form is unstructured. There are many cases that must be considered when inserting/subdividing fractures and building the mesh that we will not discuss. However, the final neighbour relationships are determined by the existence of some shared interfacial area between CVs. Interfacial area is a crucial piece of information for use in influence coefficients and we quantify this area in equation (4.2.13). This equation itself has several calculation options that we illustrate with examples. Final points to raise regarding mesh construction are that fractures are subdivided based on the most refined CVs surrounding them at the time of insertion and that the resultant mesh is highly dependent on the order in which fractures are inserted.

To begin describing how interface areas are calculated, we begin by first considering the volume of PM and fracture CVs. In general, CVs have spatial dimensions Δx_1, Δx_2 and Δx_3 [m] aligned with the primary Cartesian axes, x_1, x_2 and x_3. Thus, the volume of a CV is given by:

$$V_i = \begin{cases} \Delta x_{1,i}\Delta x_{2,i}\Delta x_{3,i} & \text{for porous media} \\ 2b_i\Delta x_{I,i}\Delta x_{J,i}(1-\alpha) & \text{for fractures} \end{cases} \tag{4.2.12}$$

where V_i is the volume of CV with index i [m^3]; I and J are Cartesian directions, $I,J\epsilon\{1,2,3\}$ with $I \neq J$; α is the asperity contact area [-]; and $2b$ is fracture aperture [m]. We reduce a fracture CV's volume in proportion to the asperity contact area referring to the schematic in Figure 4.2.2b.

Interfacial areas between matrix CVs are calculated using the same Δx_1, Δx_2 and Δx_3 dimensions, but care is taken to handle cases where faces of two CVs are not congruent, such as A' to B above, and where fractures partially obstruct the interface of two matrix CVs, such as A' to A" above:

$$A_{ij} = \begin{cases} \Delta x_I \Delta x_J & \text{for congruent faces} \\ \left(\Delta x_{I,i} \cap \Delta x_{I,j}\right)\left(\Delta x_{J,i} \cap \Delta x_{J,j}\right) & \text{for incongruent faces} \\ \min\langle 2b_i, 2b_j\rangle \left(\Delta x_{I,i} \cap \Delta x_{I,j}\right) & \text{for incongruent abutting fractures} \\ (1-\alpha)A_{ij} & \text{for fracture-matrix interfaces} \\ A_{ij} - (1-\alpha)\sum_{\forall f}\left[\bigcap_{k=\{i,j,f\}} \Delta x_{I,k} \bigcap_{k=\{i,j,f\}} \Delta x_{J,k}\right] & \text{otherwise} \end{cases} \tag{4.2.13}$$

where A_{ij} is the interface area between CVs with indices *i* and *j* [m^2]; f is one of possibly several fracture CVs that partially obstructing the interface of matrix CVs *i* and *j*; and ∩ is an operator for the overlap [m] of like dimensions of two CVs.

To illustrate each of these cases, we refer to Figure 4.2.5. The trivial case of two congruent CV faces is in Figure 4.2.5a where ⓪ $= \Delta x_{2,i} = \Delta x_{2,j}$ and ① $= \Delta x_{3,i} = \Delta x_{3,j}$ and $A_{ij} =$ ⓪ × ①. Figure 4.2.5b shows a case where faces are incongruent in the x_2-direction only and we have ② $= \left(\Delta x_{2,k} \cap \Delta x_{2,l}\right) = \Delta x_{2,l}$ and ③ is the same as ①. In Figure 4.2.5c, we have the case of two incongruent abutting fractures. Here, ④ $= \Delta x_{2,f1} \cap \Delta x_{2,f2}$ for which overlapping distance is found by subtracting the ending x_2-coordinate of f_2 from the starting x_2-coordinate of f_1, and the two respective fracture apertures are used in calculating ⑤ $= \min\langle 2b_{f1}, 2b_{f2}\rangle$. Figure 4.2.5d shows the interface area between an incongruent fracture and a matrix CV with $A_{mf} = (1-\alpha)$⑥ × ⑦, where ⑥ and ⑦ are calculated as a simpler case of distance ④ and we multiply by a ratio complementary to the asperity contact area as per Figure 4.2.5c. Note that $A_{mf} \neq A_{nf}$. A final example showing two incongruent matrix CVs with one partially obstructing fracture is also in Figure 4.2.5d. Here, we wish the interfacial area between *m* and *n* to be the sum of the area of direct contact area plus the asperity contact area through *f*. This can be expressed equivalently by taking the entire matrix-matrix interface area and subtracting the area of the obstructing fracture: $A_{mn} =$ ⑧ × ⑨ $- (1-\alpha)$⑥ × ⑦ with ⑥ $= \Delta x_{2,m} \cap \Delta x_{2,f} \cap \Delta x_{2,n} = \Delta x_{2,n}$, ⑦ $= \Delta x_{3,m} \cap \Delta x_{3,f} \cap \Delta x_{3,n} = \Delta x_{3,f}$, and ⑧ and ⑨ are analogous to ④. The advantage of using a subtraction of obstructing fracture interface areas becomes evident as more fractures obstruct a matrix-matrix interface and the pattern of the direct contact area becomes irregular, as may be the case if f_1 and f_2 were to obstruct *m* and *n*.

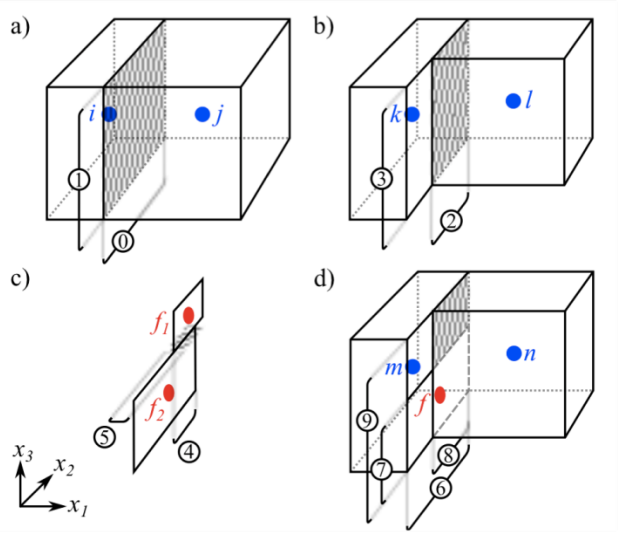

Figure 4.2.5: Four cases of interface area calculations with a) congruent control volumes, b) incongruent control volumes, c) abutting fracture CVs with different apertures, and d) incongruent matrix CVs with their interface partially obstructed by a fracture.

In the third case of equation (4.2.13), taking the minimum of the apertures $2b_i$ and $2b_j$ is arbitrary. The arithmetic or harmonic mean could be used instead. The current choice reflects the area available to flow assuming a step-like narrowing rectangular opening from one to the other with the remainder of the end face area in the larger aperture fracture representing a no-flow fracture-matrix interface.

4.2.5 Numerical formulation

When discretized using first order accurate time and spatial derivatives to capture the molar flux of component *p* from control volume *i* to neighbour node *j*, equation (4.2.1) becomes:

$$\begin{aligned}&\frac{V_i B_i}{\Delta t^{N+1}}\left\{\left[\sum_l \phi S_{l,i} M_{l,i} X_{pl,i}\right]^{N+1} - \left[\sum_l \phi S_{l,i} M_{l,i} X_{pl,i}\right]^{N} + \rho_b K_{d,i} M_{q,i}^{N+1} X_{pq,i}^{N+1}\right\} \\ &= \sum_{j\epsilon\eta_i}\sum_l \left[\gamma_{ij}\lambda_{l,\mathrm{ups}\langle i,j\rangle}\Gamma_{l,ij}^{N+1} X_{pl,\mathrm{ups}\langle i,j\rangle}^{N+1} + \gamma_{ij}^{*} S_{l,ij}^{N+1} M_{l,\mathrm{ups}\langle i,j\rangle}^{N+1}\left(X_{pl,j}^{N+1} - X_{pl,i}^{N+1}\right)\right] \\ &+ Q_{p,i}^{N+1}\end{aligned} \tag{4.2.14}$$

The potential difference [kPa] between nodes *i* and *j* is given by:

$$\Gamma_{l,ij}^{N+1} = \Gamma_{l,j}^{N+1} - \Gamma_{l,i}^{N+1} = \left(P_{l,j}^{N+1} - \rho_{l,j}^{N+1} d_j g\right) - \left(P_{l,i}^{N+1} - \rho_{l,i}^{N+1} d_i g\right) \tag{4.2.15}$$

The *influence coefficient* for the advective flux, a term that bundles together several temporally-static physical and geometric properties for use in repetitive calculations, for the node pair *i* and *j* is:

$$\gamma_{ij} = A_{ij} \frac{k_{II,i} k_{II,j} \left(\Delta x_{I,i} + \Delta x_{I,j} \right)}{k_{II,j} \Delta x_{I,i} + k_{II,i} \Delta x_{I,j}} \left(\frac{\Delta x_{I,i} + \Delta x_{I,j}}{2} \right)^{-1} \tag{4.2.16}$$

where I is the vector component normal to the ij interface. The *influence coefficient* of the diffusive flux, lagged in time, is:

$$\gamma_{ij}^{*} = \alpha_{L,ij}^{l} \left(\vec{n}_{ij} \cdot \vec{v}_{l,ij}^{N} \right) + \alpha_{TH,ij}^{l} \left| \vec{n}_{ij} \cdot \vec{v}_{l,TH,ij}^{N} \right| + \alpha_{TV,ij}^{l} \left| \vec{n}_{ij} \cdot \vec{v}_{l,TV,ij}^{N} \right| + \phi D_{l}^{*} \tau \tag{4.2.17}$$

with $\vec{v}_{l,ij}^{N} \coloneqq \left[v_x, v_y, v_z \right]^T$ the velocity of phase l at the interface of i and j defined component-wise in equation (4.2.30) below [m/d]; the transverse-horizontal velocity $\vec{v}_{l,TH,ij}^{N} = \left\| \vec{v}_{l,ij}^{N} \right\| / \sqrt{v_x^2 + v_y^2} \left[-v_y, v_x, 0 \right]^T$, a vector perpendicular to flow direction which lies in the xy-plane, or $\vec{v}_{l,TH,ij}^{N} = \left\| \vec{v}_{l,ij}^{N} \right\| \left[\sqrt{2}, \sqrt{2}, 0 \right]^T$ if velocity is vertical; the transverse vertical velocity $\vec{v}_{l,TV,ij}^{N} = \left\| \vec{v}_{l,ij}^{N} \right\| \left[v_x v_z, v_y v_z, -v_x^2 - v_y^2 \right]^T$, a vector perpendicular to the other two, or the zero vector in the case of pure vertical flow; and, with normal vectors in the set $\vec{n}_{ij} \epsilon \{ [\pm 1,0,0]^T, [0, \pm 1,0]^T, [0,0, \pm 1]^T \}$.

Source/sink terms are one of two currently implemented ways to create *boundary conditions* (BCs) in the numerical model. (Herein, a *boundary condition* is some hydrogeologically significant constraint we impose on a CV, rather than the term's more strict mathematical definition.) Values for the term $Q_{p,i}^{N+1}$ in [mol/d] for component p can calculated in depending on which boundary type the modeler wishes to express. Calculations for a *constant rate component injector*, *hydrostatic boundary*, *gas boundary*, and a *recharge boundary* are explained here.

Constant rate component injector source terms, which inject a component at a prescribed rate up to a maximum pressure threshold in their containing CVs, are defined as:

$$Q_{p,i}^{N+1} = \begin{cases} \hat{Q}_{p,BC} & \text{if } \hat{Q}_{l,BC} < \gamma_{i,BC} \lambda_{l,BC} \left(P_{\max,BC} - P_{l,i}^{N+1} \right) \\ \gamma_{i,BC} \lambda_{l,BC} \left(P_{\max,BC} - P_{l,i}^{N+1} \right) \hat{X}_{p,BC} & \text{otherwise} \end{cases} \tag{4.2.18}$$

where $\hat{Q}_{p,BC}$ is the user-defined molar injection rate of component p [mol/d]; $\hat{Q}_{l,BC}$ is injection rate of phase l [mol/d], calculated as the sum of $\hat{Q}_{p,BC}$ for which p is in l; $\hat{X}_{p,BC} = \hat{Q}_{p,BC} / \hat{Q}_{l,BC}$ is the mole fraction of p being injected in l; and $P_{\max,BC}$ is the maximum injection pressure [kPa].

Hydrostatic boundary source/sink terms, which inject or remove multiple components to keep the CV at a predefined pressure below the water table, are given by:

$$Q_{p,i}^{N+1} = \sum_{l} \begin{cases} \gamma_{i,BC}\lambda_{l,BC}\left(P_{l,BC}^{N+1} - P_{l,i}^{N+1}\right)X_{pl,BC} & \text{if } l = q \text{ and } P_{l,i}^{N+1} < P_{l,BC}^{N+1} \\ \gamma_{i,BC}\lambda_{l,i}^{N+1}\left(P_{l,BC}^{N+1} - P_{l,i}^{N+1}\right)X_{pl,i}^{N+1} & \text{if } P_{l,i}^{N+1} > P_{l,BC}^{N+1} \\ 0 & \text{otherwise} \end{cases} \quad (4.2.19)$$

where $\gamma_{i,BC} = 2\pi b_{BC}\Delta x_{i,I}\sqrt{k_{i,JJ}k_{i,KK}}/\log(0.37\sqrt{V_i/(\pi\Delta x_{i,I})}/r_w)$ [m^3] is an influence coefficient combining the radius r_w [m] of a fictitious well bore in direction *I* with node *i*'s spatial dimensions and permeability, and with source/sink efficiency b_{BC} [-]. We note that in the case of under-pressurization, the first criterion causes injection of all components within the BC-defined aqueous phase. This is the only phase for which positive $Q_{p,i}^{N+1}$ terms exist. The second criterion removes all components from the aqueous, NAPL, or gas phase(s). Gas boundaries, which are above the water table, are implemented in a similar manner, except the gas phase $l = g$ is used in the first pressure criterion.

Recharge boundaries are implemented by reuse of the constant rate component injection boundary, except that multiple source terms are added based on model parameters for a compositionally-defined aqueous phase (e.g. $\hat{X}_{cq,BC}$, $\hat{X}_{wq,BC} = 1 - \hat{X}_{cq,BC}$ and the rate of aqueous phase recharge in [mm/d] are inputs, and $Q_{c,i}^{N+1}$ and $Q_{w,i}^{N+1}$ are calculated internally), and where the influence coefficient is $\gamma_{i,BC} = 2b_{BC}\Delta x_{i,J}\Delta x_{i,K}k_{i,II}/\Delta x_{i,I}$.

A final use of the $Q_{p,i}^{N+1}$ term is the *air penalty source term*. This is a source that helps the numerical system to converge by injecting small amounts of the air component. This only occurs when the saturation of gas in a node is low, and thereby avoids negative gas phase saturation and/or negative air component mole fraction. This source term is given by:

$$Q_{a,i}^{N+1} = \begin{cases} V_i B_i \phi M_g\left(S_g^* - S_g^{N+1}\right)/\Delta t^{N+1} & \text{if } S_g^{N+1} < S_g^* \\ 0 & \text{otherwise} \end{cases} \quad (4.2.20)$$

The second of the two BC types is the *invariant property boundary*. It is implemented by setting B_i = 10^6, or some other suitably large number, to maintain constant pressure and composition in the CVs that the user chooses. This large value in equation (4.2.14) effectively over represents the node's volume causing any flux in or out (terms on the right hand side of the equation) to be insignificant.

A summary of the notation is given by:

N is a time step number;
i, j with $i \neq j$, are indices of the *i*th *and j*th CV;
η_i is the set of control volumes that are neighbours of node *i*;
$\text{ups}\langle i,j\rangle = \begin{cases} i & \Gamma_{l,ij} \geq 0 \\ j & \Gamma_{l,ij} < 0 \end{cases}$ is the upstream node based on total potential of phase *l*;
BC the subscript denotes a variable or constraint in a source/sink term;
B_i is a volume multiplier used to cause invariant properties in node *i* [-];
Δt^{N+1} is the time step [d];

$S_{l,ij}^{N+1} = \frac{S_{l,i}^{N+1} S_{l,j}^{N+1} (V_i + V_j)}{S_{l,j}^{N+1} V_i + S_{l,i}^{N+1} V_j}$ is the harmonic mean of saturations weighted by node volume [-];

$\lambda_{l,i} = k_{rl,i} M_{l,i} / \mu_{l,i}$ is the phase mobility term [mol·d·m^{-2}·kg^{-1}];

$\lambda_{l,BC} = M_{l,BC} / \mu_{l,BC}$ is a mobility term for phase *l* at the boundary [mol·d·m^{-2}·kg^{-1}]; and

$\tau = \left(\phi_{\eta_i} S_{l,\eta_i}^{N}\right)^{7/3}$ is the tortuosity factor [-].

Relative permeability and capillary pressure functions are tabular inputs to the model. Residual saturation of a phase is determined by the first non-zero relative permeability entry in the table and values intermediate to data points are calculated by linear interpolation. Great care is taken to ensure continuity and smoothness of the k_{rl} curve as a phase moves from its immobile range $k_{rl}(S_l) = 0,\ S_l \epsilon [0, S_{lr})$, to its mobile range $k_{rl}(S_l) > 0,\ S_l \epsilon [S_{lr}, 1]$, or else the numerical solver may fail with symptoms of "flip-flopping" about a nearly converged solution. In the current implementation, this is accomplished by splicing the following *ad hoc* transformed cosine curve $k_{rl} = k_{rl}(S_{lr})\left[1 - \cos\left(\pi\left(S_l - \hat{S}_{\text{smooth}}\right)/\left(S_{lr} - \hat{S}_{\text{smooth}}\right)\right)\right]/2$, on the interval $S_l \epsilon \left[\hat{S}_{\text{smooth}}, S_{lr}\right]$. $\hat{S}_{\text{smooth}}$ [-] is an arbitrary parameter chosen to be greater than the shift value used for computing numerical derivatives in saturation but less than the residual saturation of the phase.

4.2.6 Algebraic development of fracture node elimination

In order to adequately represent domains and fracture spacing at our scale of interest (~100 m in size with multiple fractures per meter) and maintain tractability in the simulation, it is necessary to remove the small volume nodes at the intersection of fracture planes. Slough et al. (1999) demonstrated that small volume nodes negatively impact simulation time steps. To resolve this issue, Slough et al. (1999) proposed that under the assumption that such small volume nodes are at steady state (i.e. inflow is equal to outflow), they can be algebraically eliminated from the numerical system. We now proceed by developing flow equations in a manner analogous to that presented in (Slough et al., 1999), but with a clear extension to 3D fracture intersections in order to support the objectives of this work. For 3D fracture intersections, the process occurs in two steps: elimination of point (0D) intersections; followed by elimination of line (1D) intersections. Ultimately, this process creates new neighbours and new influence coefficients for each fracture CV adjacent to an intersection. As before, influence coefficients for advective fluxes bundle together a number of temporally-static physical and geometric properties for reuse.

For simplicity, consider the case of advective flow between a fracture node pair *ij* in the direction *I* with all matrix CVs removed from the system. Flow from can be characterized by:

$$F_{l,ij} = \gamma_{ij} \lambda_{l,ups\langle i,j \rangle} (\Gamma_{l,j} - \Gamma_{l,i}) \tag{4.2.21}$$

where $F_{l,ij}$ is the volumetric flow rate from *i* to *j* [m^3/d]. Relying on the assumption of steady-state advective flow in node *i* (i.e. inflow is equal to outflow), we have:

$$\sum_{j\epsilon\eta_i} F_{l,ij} = 0 \tag{4.2.22}$$

with $\eta_i = \{j_1, j_2, \dots, k, \dots, j_n\}$, the set of neighbours of i. k merely denotes some neighbour to which specific reference is made.

Figure 4.2.6 depicts the arrangement of three orthogonal fractures intersecting to form one point intersection and three line intersections. This example is completely general and can be extended to cases involving through-going fractures. Node *a* must be eliminated first, followed by *b*, *c*, and *d*. The final result gives flow relationships between nodes *E*, *F*, and *G* with the physical and geometric properties of *a*-*d* embedded in the new influence coefficients.

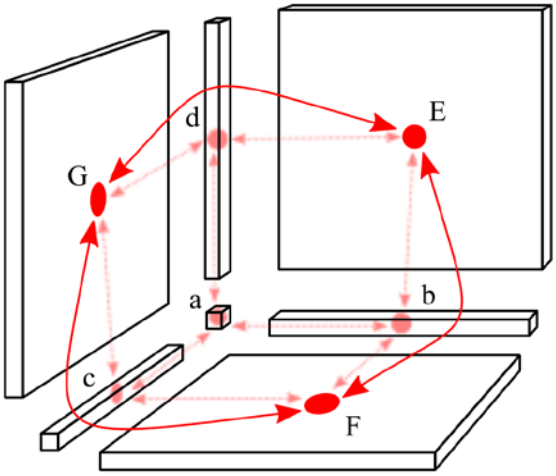

Figure 4.2.6: Control volumes at the intersection of three fractures: point node a; line nodes b, c and d; and 2D fracture planes E, F and G. Control volumes are separated spatially for clarity.

From equation (4.2.21), we can substitute node *a* as *i*, η_a = {*b*, *c*, *d*} and rearrange to obtain:

$$\Gamma_{l,a} = \frac{\sum_{j\epsilon\eta_a} \gamma_{aj}\lambda_{l,ups\langle a,j\rangle}\Gamma_{l,j}}{\sum_{j\epsilon\eta_a} \gamma_{aj}\,\lambda_{l,ups\langle a,j\rangle}} \tag{4.2.23}$$

Thus, flow from *a* to a specific neighbour *k* can be rewritten as:

$$F_{l,ak} = \gamma_{ak}\lambda_{l,ups\langle a,k\rangle}\left(\Gamma_{l,k} - \frac{\sum_{j\epsilon\eta_a} \gamma_{aj}\lambda_{l,ups\langle a,j\rangle}\Gamma_{l,j}}{\sum_{j\epsilon\eta_a} \gamma_{aj}\lambda_{l,ups\langle a,j\rangle}}\right) \tag{4.2.24}$$

$$F_{l,ak} = \frac{\gamma_{ak}\lambda_{l,ups\langle a,k\rangle}}{\mu_l \sum_{j\epsilon\eta_a}\gamma_{aj}\lambda_{l,ups\langle a,j\rangle}}\left(\Gamma_{l,k}\sum_{j\epsilon\eta_a}\gamma_{aj}\lambda_{l,ups\langle a,j\rangle} - \sum_{j\epsilon\eta_a}\gamma_{aj}\lambda_{l,ups\langle a,j\rangle}\Gamma_{l,j}\right) \tag{4.2.25}$$

For clarity, expanding the bracketed term in equation (4.2.25) yields:

$$- \frac{\begin{matrix}\gamma_{aj_1}\lambda_{l,ups\langle a,j_1\rangle}\Gamma_{l,k} + \cdots + \gamma_{ak}\lambda_{l,ups\langle a,k\rangle}\Gamma_{l,k} + \cdots + \gamma_{aj_n}\lambda_{l,ups\langle a,j_n\rangle}\Gamma_{l,k} \\ \gamma_{aj_1}\lambda_{l,ups\langle a,j_1\rangle}\Gamma_{l,j_1} + \cdots + \gamma_{ak}\lambda_{l,ups\langle a,k\rangle}\Gamma_{l,k} + \cdots + \gamma_{aj_n}\lambda_{l,ups\langle a,j_n\rangle}\Gamma_{l,j_n}\end{matrix}}{\gamma_{aj_1}\lambda_{l,ups\langle a,j_1\rangle}(\Gamma_{l,k}-\Gamma_{l,j_1}) + \cdots + \gamma_{ak}\lambda_{l,ups\langle a,k\rangle}(\Gamma_{l,k}-\Gamma_{l,k}) + \cdots + \gamma_{aj_n}\lambda_{l,ups\langle a,j_n\rangle}(\Gamma_{l,k}-I}$$

$$F_{l,ak} = \frac{\gamma_{ak}\lambda_{l,ups\langle a,k\rangle}}{\sum_{j\epsilon\eta_a}\gamma_{aj}\lambda_{l,ups\langle a,j\rangle}}\sum_{j\epsilon\eta_a}\gamma_{aj}\lambda_{l,ups\langle a,j\rangle}\left(\Gamma_{l,k}-\Gamma_{l,j}\right)$$

$$F_{l,ak} = \sum_{j\epsilon\eta_a}\left[\frac{\gamma_{aj}\lambda_{l,ups\langle a,j\rangle}\gamma_{ak}\lambda_{l,ups\langle a,k\rangle}}{\sum_{j^*\epsilon\eta_a}\gamma_{aj^*}\lambda_{l,ups\langle a,j^*\rangle}}\right]\left(\Gamma_{l,k}-\Gamma_{l,j}\right) \tag{4.2.26}$$

where j is the index of the outer summation and j^* is the index of the inner summation.

At this point, another assumption must be made to simplify this expression for practical application in the numerical model: that the phase mobility terms are all equal given that they are already constant by the assumption of steady state flow. This is not desirable, but a second approximation can reintroduce upstream weighting:

$$F_{l,ak} \cong \sum_{j\epsilon\eta_a}\underbrace{\left[\frac{\gamma_{aj}\gamma_{ak}}{\sum_{j^*\epsilon\eta_a}\gamma_{aj^*}}\right]}_{:=\gamma'_{jk}}\lambda\left(\Gamma_k-\Gamma_j\right) \cong \sum_{j\epsilon\eta_a}\gamma'_{jk}\lambda_{l,ups\langle j,k\rangle}\left(\Gamma_k-\Gamma_j\right) = \sum_{j\epsilon\eta_a}F_{l,jk} \tag{4.2.27}$$

Equation (4.2.27) finally shows that the flow across an eliminated node can be calculated directly with the new *influence coefficient*:

$$\gamma'_{jk} := \frac{\gamma_{aj}\gamma_{ak}}{\sum_{j\epsilon\eta_a}\gamma_{aj}} \tag{4.2.28}$$

which is appropriate for any two neighbours of the eliminated node, a. With a algebraically eliminated, the neighbour set of b expands from $\eta_b = \{a, E, F\}$to $\eta_b = \{c, d, E, F\}$ with:

$$\gamma'_{bc} := \frac{\gamma_{ab}\gamma_{ac}}{\gamma_{ab}+\gamma_{ac}+\gamma_{ad}}, \gamma'_{bd} := \frac{\gamma_{ab}\gamma_{ad}}{\gamma_{ab}+\gamma_{ac}+\gamma_{ad}}, \text{and } \gamma'_{cd} := \frac{\gamma_{ac}\gamma_{ad}}{\gamma_{ab}+\gamma_{ac}+\gamma_{ad}}$$

Under the same pretenses, the algebraic manipulation is then repeated on node *b*. Delehjktion of *b* produces a new influence coefficient between *E* and *F*. Making direct use of the result in (4.2.28), we have:

$$\begin{aligned} \gamma''_{EF} &:= \frac{\gamma_{bE}\gamma_{bF}}{\sum_{j\epsilon\eta_b}\gamma_{bj}} \\ &= \frac{\gamma_{bE}\gamma_{bF}}{\gamma_{bE}+\gamma_{bF}+\gamma'_{bc}+\gamma'_{bd}} \\ &= \frac{\gamma_{bE}\gamma_{bF}}{\gamma_{bE}+\gamma_{bF}+\frac{\gamma_{ab}\gamma_{ac}}{\gamma_{ab}+\gamma_{ac}+\gamma_{ad}}+\frac{\gamma_{ab}\gamma_{ad}}{\gamma_{ab}+\gamma_{ac}+\gamma_{ad}}} \end{aligned} \tag{4.2.29}$$

Due to the general derivation, expression (4.2.29) can be applied to any of the node pairs *EF*, *FG* or *EG*. Thus, all the small volume intersection nodes may be removed from the system, leaving only the 2D fracture planes in Figure 4.2.6 and their associated connections.

The velocity term for use in the diffusive flux, a velocity at the interface, is given by taking the volume-weighted average of the two respective node-centred velocities. We use a node-centred velocity because it works for all node pairs by avoiding spatially ill-defined interfacial areas of neighbours joined across an eliminated node and maintaining symmetry in the matrix-vector numerical system. The velocity vector can be constructed component-wise for node i, phase l in direction component *I* by:

$$\vec{v}_{l,i,I} = \left(-\sum\nolimits_{j\epsilon\eta_i} F_{l,ij}\vec{n}_{ij,I}\right)/\left(\phi_i A^*_{i,I}\right) \tag{4.2.30}$$

where $\vec{n}_{ij,I}$ is a unit-length vector that is normal to the face of i over which flow occurs to *j* (e.g. from the example in Figure 4.2.6**:**, velocity from *E* to *F* is calculated with the *E*-*b* interface normal), and $A^*_{i,I}$ is the *I*-component of the surface area of node *i* used expressly for this calculation. The volume-weighted average velocity at the supposed interface between *i* and *j* is given by $\vec{v}_{l,ij} = \left(\vec{v}_{l,i}V_i + \vec{v}_{l,j}V_j\right)/\left(V_i + V_j\right)$.

4.2.7 Application

4.2.7.1 Large-scale simulation

To demonstrate the capability of our new mesh generator and flow and transport formulation we apply it to a “real world” problem: two mobile phases (aqueous and NAPL), a 3-d fractured rock domain with an intermediate fracture density (spacing on the order of 1 m), and at a spatial scale relevant to a NAPL source zone investigation (on the order of 100 m). Conceptually, we base the example on the DNAPL spill site at Smithville, Ontario; we extend the numerical modeling effort of McLaren et al. (2012). The domain is 200 × 50 × 43 m in length, width and height respective to the ambient groundwater flow direction, and contains six horizontally-layered hydrostratigraphic units of varying thickness. Each geological unit has distinct porosity, intrinsic permeability, relative permeability, capillary pressure relationships, and fracture network characteristics (Slough et al., 1999; McLaren et al., 2012). After the

numerical model reaches a pseudo-steady state/equilibrium with respect to the ambient groundwater flow, non-aqueous phase TCE is released at the top of the domain, just below the water table, over a 50 × 10 m area in the upgradient portion of the domain for a period of one year. This DNAPL release zone size is reduced from the 50 × 50 m area estimated by Golder Associates Ltd. (1999) judiciously so, for the purposes of this demonstration, the width of the source area does not span the width of the domain.

Figure 4.2.7 shows fracture apertures and fracture CVs in the downgradient 150 m portion of the fracture network. The random fracture generator produced approximately 1800 conceptual fractures that are discretized into 170,000 final fracture CVs. This count excludes 12,000 point intersection and 80,000 line intersection CVs removed in the algebraic node elimination step. The original 40 × 10 × 43 CV regular grid of PM nodes became an unstructured mesh of 120,000 PM nodes. The total number of CVs is approximately 290,000, which yields about 780,000 unknowns in the numerical system of equations. The results in the following figures, inclusive of domain discretization, aqueous phase flow equilibrium, and TCE injection, took approximately seven days of computation time on a 3.3 GHz Intel i7 CPU.

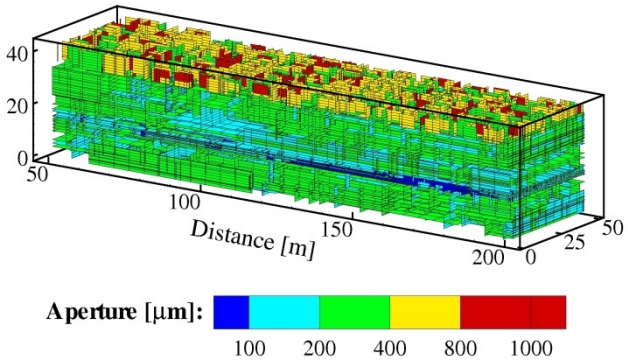

Figure 4.2.7: Fracture network in the 200×50×43 m domain totaling ~170,000 CVs. Fracture CVs are coloured according to aperture.

Results of the simulation are shown in Figure 4.2.8 and 4.2.9 after one year of TCE injection. Figure 4.2.8 shows NAPL saturation. We see that most of the free-phase contaminant in the fracture network; some NAPL has imbibed into the rock matrix in limited areas. This result is stylistically similar the simulation results depicted in McLaren et al. (2012), Figures 9a-d. The dissolved plume of contaminant in the fracture network, Figure 4.2.9a, and in the rock matrix, Figure 4.2.9b, show extensive dispersion of the plume.

To exemplify the effectiveness of the localized node bisection technique (see Figure 4.2.4) in reducing the total number of control volumes in the domain, we contrast the mesh in the realization above with hypothetical meshes employing the traditional technique (see Figure 4.2.3). In the extreme end member where we do not compromise in the 1 mm resolution of the random fracture size and location, a regular grid to accommodate this realization would have about 1200, 360 and 140 grid lines in the x-, y- and z-directions, respectively. This would yield over 60,000,000 matrix CVs before fractures are added. In a more moderate case, supposing that fracture resolution was relaxed to 1 m, the number of matrix CVs would total 430,000. Recall that this realization using our node bisection technique yielded 120,000 PM nodes. These

examples represent different choices in the computational time versus numerical accuracy tradeoff decision spectrum.

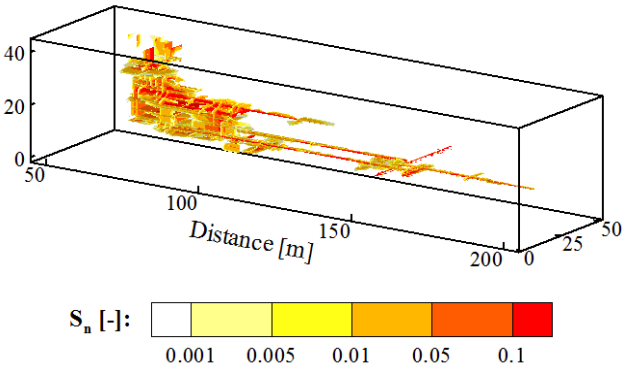

Figure 4.2.8: NAPL saturation in the fractures and matrix at one year. NAPL is predominantly in the fracture network.

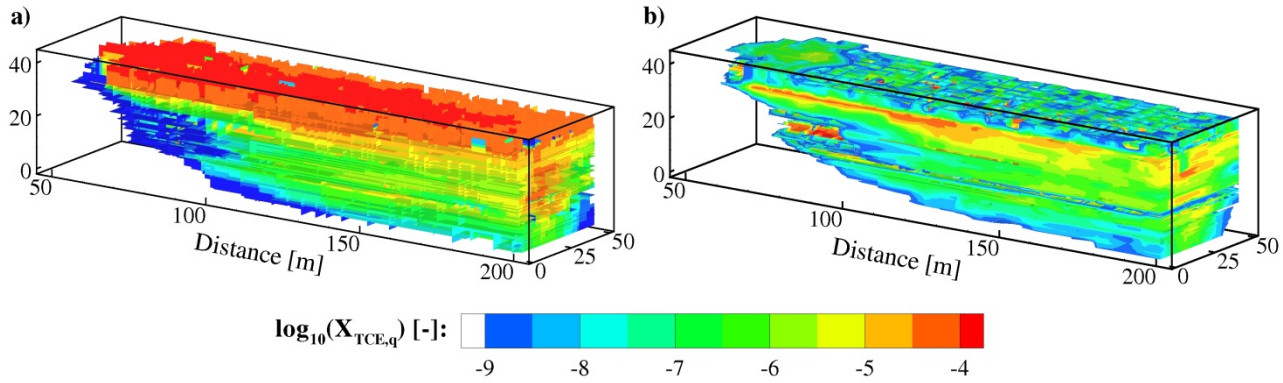

Figure 4.2.9: Mole fraction of TCE in the aqueous phase in the fracture network at one year.

We note that the demonstration above is the largest simulation (in terms of number of CVs) attempted with this version of CompFlow to date. It also approaches the limit of what we can model in a practical way (in terms of computational time) given our current computational resources and use thereof. This limit may be increased with a faster computer or if we were to employ parallel computing. The tractability of a given simulation is not only governed by the number of CVs, but also by the complexity of the physical system. If a mobile gas phase introduced yielding the three mutually-interactive phase capability that we have described, the limit on permissible number of CVs is drastically reduced due to the increased computational burden in finding solutions to the non-linear system of equations.

4.3 A semi-analytical solution for simulating contaminant transport subject to chain-decay reactions

4.3.1 Introduction

Contaminants released in the subsurface are transported by various physical processes such as diffusion, advection, and dispersion. The contaminants may also react and cause them to transform into other species. In such a case, the traditional treatment of contaminant transport does not apply because of sorption and mass loss processes that are not accounted. However, many contaminants are reactive with other contaminants within fluids or with the porous medium, which necessitates that one explicitly accounts for these processes. In particular, reactive contaminant transport is a topic of great interest to account for processes involving denitrification, degradation of pesticides and their products, radioactive decay, and bioremediation of organic compounds. Comprehensive numerical models (e.g., Simunek et al., 1994; Clement, 1997; Zheng and Wang, 1999; Widdowson et al., 2002; Therrien et al., 2005; Yu et al., 2009) have been developed to account for these complexities, but analytical solutions are still necessary to verify these numerical models and to perform scoping calculations. In addition, accurate solutions from analytical or semi-analytical models (e.g., Khandelwal and Rabideau, 1999; Neville et al., 2000; Clement, 2001; Samper-Calvete and Yang, 2007; Lu and Sun, 2008) can be computed more efficiently than numerical models. The solutions may also be used for predicting contaminant concentrations and for analyzing laboratory or field data to determine solute transport parameters. One other important reason may be that because of their relative simplicity, analytical solutions still have an important role in screening studies (Alvarez and Illman, 2006) and to assess the performance of natural attenuation and bioremediation (Illman and Alvarez, 2009). More recently, such solutions have been used in the analysis of permeable reactive barriers (e.g., Rabideau et al., 2005; Park and Zhan, 2009; Mieles and Zhan, 2012). An additional benefit is that analytical solutions can be readily used for Monte Carlo probabilistic simulations of contaminant transport to account for uncertainties in groundwater velocity, transport parameters, and contaminant source boundary conditions, among other factors (e.g., Eykholt et al., 1999).

Various analytical solutions have been developed to accommodate chain-decay reactive transport problems. In particular, Cho (1971) utilized Laplace transforms to derive a one-dimensional solution for advective-dispersive transport of ammonium with nitrification and denitrification in soil assuming a first-order reaction rates. Meanwhile, van Genuchten (1985) developed a one-dimensional analytical solution that considers the transport of four species involved in a consecutive (or serial) first-order decay chain using Laplace transforms and implemented the solution in a computer program called CHAIN. Lunn et al. (1996) then utilized the Fourier sine transform (as opposed to the Laplace transform) to obtain the one-dimensional solution of Cho (1971) in a simpler way. One of the key advantages of using the Fourier sine transform approach was in the flexibility to introduce new initial and boundary conditions which allows for developing new solutions for different conditions.

Sun et al. (1999a,b) and Sun and Clement (1999) developed a general method to derive analytical solutions of any number of species with first-order sequential degradation in multiple dimensions. In particular, they presented a substitution method to transform the multiple species transport equations into a decoupled set of transport equations for single species. This implies that any previously derived analytical solutions for single-species transport with first-order reactions rate can be directly used for multiple species transport problems. Sun et al. (1999a) demonstrated the approach by obtaining an analytical solution for a five species serial-parallel

reactive transport system. Results from the analytical solution compared very favourably with a previously developed numerical code. Sun et al. (1999b) then used the solution for a single radioactive tracer decay solution from Bear (1979) to obtain a solution for three-species transport with first-order reactions. More recently, Clement (2001) presented a generalized approach to derive analytical solutions to multispecies transport following the approach of Sun et al. (1999a). Clement's (2001) approach relies on a similarity transformation method that can handle wider ranging problems involving serial, parallel, converging, diverging and/or reversible first-order reaction systems. It is important to note that the methods developed to this point are only applicable to all species having identical retardation factors.

New analytical solutions that consider different retardation factors for each species have been developed more recently. For example, Bauer et al. (2001) obtained analytical solutions for one-, two, and three-dimensional contaminant transport of decay chains for a homogeneous medium. Their solution was unique in a sense that variable retardation coefficients can be included and that their analysis extended to multiple porosity media. Quezada et al. (2004) extended the approach developed by Clement (2001) and presented a generalized method for solving coupled, multi-dimensional, multi-species reactive transport equations. As in Bauer et al. (2001), the solutions can handle distinct retardation factors, but the solution was limited to a three-species system. To extend the number of species that the solution can handle, Srinivasan and Clement (2008a,b) then developed closed-form analytical solutions for the chain decay problem with an arbitrary number of species with spatially varying initial conditions and an exponentially decaying Bateman-type source condition. One limitation of this approach was that it was limited to a one-dimensional system. More recently, Guerrero et al. (2009) developed a one-dimensional analytical solution for multi-species transport in a finite domain with constant boundary conditions. Similar to other recent solutions, the Guerrero et al. (2009) solution allows for various contaminant species to have different retardation factors, however, it is one-dimensional and can handle only sequential chain decay problems. Guerrero et al. (2010) then extended Guerrero et al. (2009)'s work to handle time-varying boundary conditions. Most recently, Mieles and Zhan (2012) published a one-dimensional, steady-state, analytical solution for serial and parallel degradation pathways with unique first-order reaction rates as well as retardation factors.

Our review suggests that there is currently a lack of a multidimensional analytical solution to the chain-decay reactive transport problem that can handle varying retardation factors for individual species and various reaction pathways in multiple dimensions. Therefore, the main objective of this paper is to present a set of new, semi-analytical solutions to simulate three-dimensional contaminant transport subject to first-order chain-decay reactions. The three dimensional domain considered is semi-infinite in areal extent and the aquifer is taken to be of finite thickness. The solutions can treat the transformation of contaminants into daughter products, leading to decay chains consisting of multiple contaminant species and various reaction pathways that can be either straight or branching. The model in its current form is capable of accounting for up to seven species and four decay levels. The complex pathways are represented by means of first-order decay and first-order production terms, while branching ratios account for decay stoichiometry. Besides advection, dispersion, bio-chemical decay and daughter product formation, the model also accounts for sorption of contaminants onto the aquifer solid phase with each species having a different retardation factor. The solutions are obtained by exponential Fourier, Fourier cosine and Laplace transforms. Similar limiting forms of the solutions can be obtained analytically, but we obtain almost all solutions by numerically inverting the analytical

solutions obtained in Laplace and exponential Fourier space. Various test cases are presented and the solutions are verified against a previously-derived analytical model and a more sophisticated numerical model. Finally, we discuss the potential utilities of this solution.

4.3.2. Statement of problem

4.3.2.1 Modeling scenarios

A schematic view of a waste disposal facility and contaminant migration pathways under consideration is shown in Figure 4.3.1. Contaminants leaching from the disposal facility are considered to migrate vertically downward through the unsaturated zone until they reach the saturated zone. Groundwater flow in the saturated zone is assumed to be essentially one-dimensional in the horizontal plane with a constant groundwater velocity, *v*. After they enter the saturated zone at the water table, contaminants migrate by one-dimensional advection with flowing groundwater and by three-dimensional dispersion. Due to mixing processes, the contaminant plume as it reaches the edge of the waste facility, will have reached a thickness *H* below the water table and will show an approximately Gaussian distribution in the lateral (*y*-) direction. Alternately, we also consider the case where the width of the souce in the *y*-direction is a step function rather than Gaussian in shape.

The new analytical solution can model the transformation of contaminants into daughter products, leading to decay chains consisting of multiple contaminant species. Example of decay chains that can be handled are shown in Figure 4.3.2. Besides advection, dispersion, bio-chemical decay and daughter product formation, this new model also accounts for sorption of contaminants on the the aquifer solid phase with retardation factors that can be different for each species.

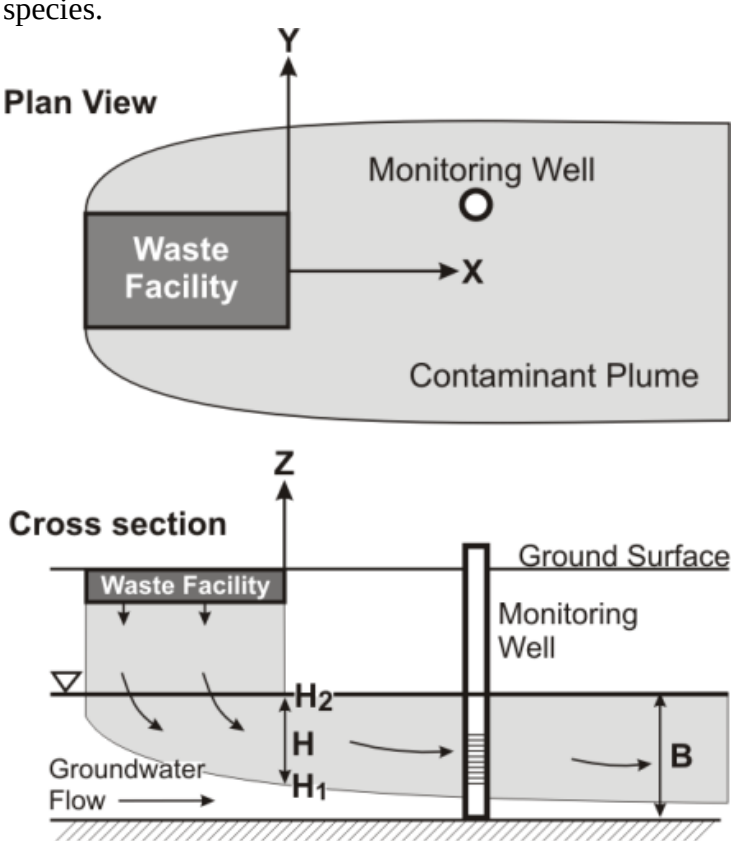

Figure 4.3.1: Schematic view of a waste disposal facility and subsurface contaminant migration.

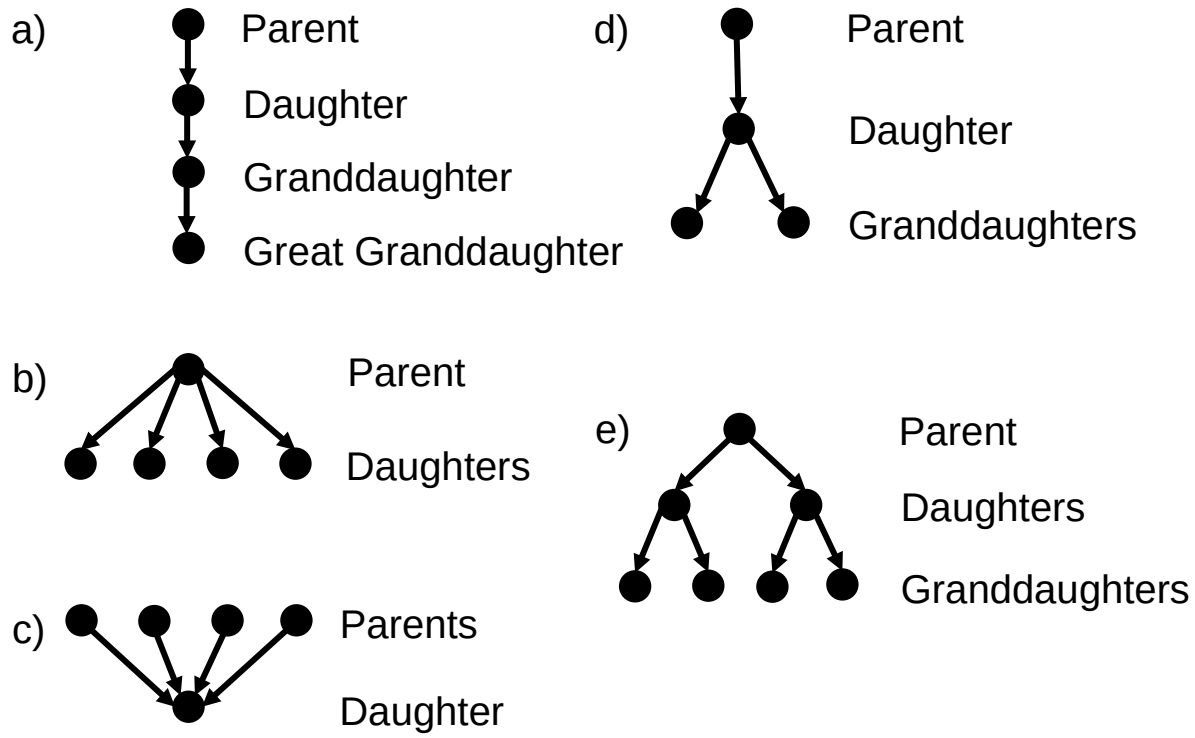

Figure 4.3.2: Example decay chains representing contaminant transformation and daughter product formation: a) straight decay chain; b) diverging decay chain; c) converging decay chain; d) four-member branched decay chain; and e) seven-member branched decay chain.

4.3.3 Governing equations

The governing equation for the *i*-th member of a decay chain can be written as:

$$D_x \frac{\partial^2 c_i}{\partial x^2} + D_y \frac{\partial^2 c_i}{\partial y^2} + D_z \frac{\partial^2 c_i}{\partial z^2} - v \frac{\partial c_i}{\partial x} + \lambda_i R_i c_i - \sum_{j=1}^{m_i} \eta_{ij} \lambda_j R_j c_j = R_i \frac{\partial c_i}{\partial t} \qquad (4.3.1)$$

where c_i = dissolved concentration in the *i*-th contaminant species, x, y, z = Cartesian coordinates, t = time, D_x, D_y, D_z = dispersion coefficients, v = average linear groundwater velocity, λ_i = first-order decay coefficient of *i*-th species, R_i = retardation coefficient of *i*-th species, λ_j = first-order decay coefficient of parent species *j*, η_{ij}, = fraction of parent *j* that transforms into species *i*, and m_i = number of immediate parents of species *i*. The dispersion coefficients are related to the groundwater velocity, v, through the dispersivities, α_x, α_y, α_z, as

$$\begin{aligned} D_x &= \alpha_x |v| + D^* \\ D_y &= \alpha_y |v| + D^* \\ D_z &= \alpha_z |v| + D^* \end{aligned} \qquad (4.3.2)$$

where D^* is the effective molecular diffusion coefficient. Implicit in the way (4.3.1) and (4.3.2) are written is the assumption that all members of the decay chain are consider to have the same mechanical dispersion and molecular diffusion characteristics. This assumption could be relaxed but is a reasonable assumption since diffusion coefficients for many contaminants do not vary markedly. The summation term in (4.3.1) represents the contribution of all immediate parents j to the production of species i. For straight decay chains, the number of parent species, m_i, and the decay fraction η_{ij}, are both equal to unity. For branched decay chains on the other hand, m_i, may be greater than one, but the contribution of each parent, η_{ij}, is typically less than one.

Initial and boundary conditions associated with (4.3.1) are

$$c_i\left(x,y,z,0\right)=0 \tag{4.3.3}$$

$$\frac{\partial c_i}{\partial t}\left(0,y,z,t\right)+\gamma_i c_i\left(0,y,z,t\right)-\sum_{j=1}^{m_i}\eta_{ij}\gamma_j c_j=0 \tag{4.3.4a}$$

$$c_i\left(0,y,z,0\right)=c_{pi}\left\{\exp\left(-\frac{y^2}{2S_i^2}\right)\right\}\cdot\left[H\left(z-H_1\right)-H\left(z-H_2\right)\right] \tag{4.3.4b}$$

$$c_i\left(\infty,y,z,t\right)=0 \tag{4.3.4c}$$

$$c_i\left(x,\pm\infty,z,t\right)=0 \tag{4.3.5d}$$

$$\frac{\partial c_i}{\partial z}\left(x,y,0,t\right)=0 \tag{4.3.6e}$$

$$\frac{\partial c_i}{\partial z}\left(x,y,B,t\right)=0 \tag{4.3.7f}$$

where γ_i is the source decay constant. Initial condition (4.3.3) specifies an initially contaminant free aquifer. Boundary conditions (4.3.4a) and (4.3.4b) describe the decay and production of contaminant at the source (x = 0 m) and the spatial distribution of concentration along the source plane, respectively. A value of the coefficient $\gamma_i = 0$ corresponds to the case of a constant source concentration. Boundary condition (4.3.4b) describes a source concentration that is vertically uniform between elevations H_1 and H_2 and equal to zero elsewhere in the vertical plane where $H(z-H_i)$ is the Heaviside step function. The source concentration profile in the y-direction is described by a Gaussian distribution with standard deviation S_i and c_{pi} is the peak concentration value at the center of the Gaussian distribution. If a rectangular patch source-zone is desired in the y-z plane, then the right-hand side of (4.3.4b) would be replaced by $c_{pi}\left[H(y+y_0)-H(y-y_0)\right]\cdot\left[H(z-H_1)-H(z-H_2)\right]$. Equations (4.3.4c) – (4.3.4f) complete the description of boundary conditions for the aquifer system which is semi-infinite in the x-direction, infinite in the y-direction and finite in the z-direction.

The solution to (4.3.1) – (4.3.4) for each species is given in Appendix B. The solution is obtained through application of Fourier transforms to treat the *y*- and *z*-coordinates and use of the Laplace transform to remove the time dependence of the transport equation. The final solution is obtained by numerical inversion of the Laplace-transformed solutions, using the algorithm developed by de Hoog et al. (1982), and by integrating the exponential Fourier transform by Gauss quadrature.

The general three-dimensional transport equation (4.3.1) can be readily simplified to describe the cases of one- or two-dimensional transport, as well as the steady-state solutions for cases involving a constant source by applying the final-value theorem to the Laplace-transformed solutions as shown in Appendix B.

4.3.4. Verification tests

In this section, the results for a number of verification problems are presented. The tests were designed to test the accuracy of the multi-species transport solution and the correctness of the computer code Chain-decay Multispecies Model (CMM) used to compute the various solutions presented here. The developed code was also tested against various published computer codes for a range of problems which test different aspects of the transport solution.

4.3.4.1 One-dimensional transport of three-member radionuclide decay chain

The first problem analyzed is that of the three-member radionuclide decay chain:

$$U^{234} \rightarrow Th^{230} \rightarrow Ra^{226}$$

This problem involves one-dimensional transport with a constant source. Model parameters for this problem are listed in Table 4.3.1. Our solution is verified with HydroGeoSphere (Therrien et al., 2005), a fully-integrated surface-subsurface flow and transport simulator. The results for this verification problem are presented in Figure 4.3.3. Depicted are the concentration profiles of the three radionuclides at time t = 10,000 yrs. The CMM results are represented by the solid lines, while the symbols represent the solution obtained with HydroGeoSphere. The agreement between the two solutions is excellent for all three species. Figure 4.3.3 shows that at distances greater than about 220 m from the source, the concentrations of both U^{234} and Th^{230} become very small. At large distances, the dominant species is Ra^{226}. The different behaviour of Ra^{226} compared to U^{234} and Th^{230} reflects the fact that Ra^{226} is weakly sorbed compared to U^{234} and Th^{230} because of its lower retardation factor. This example illustrates the importance of a model being able to account for different retardation factors for different contaminant species.

Table 4.3.1: Transport parameters for one-dimensional radionuclide transport problem.

Parameter	Units	Value
Groundwater velocity, v	m/yr	100
Dispersion coefficient, D_x	m^2/yr	1,000
Dispersion coefficient, D_y	m^2/yr	0.0
Dispersion coefficient, D_z	m^2/yr	0
Retardation factor, R		
U^{234}		1.43×10^4
Th^{230}		5.0×10^4
Ra^{226}		5.0×10^2
Decay coefficient, λ		
U^{234}	yr^{-1}	2.83×10^{-6}
Th^{230}	yr^{-1}	9.00×10^{-6}
Ra^{226}	yr^{-1}	4.33×10^{-6}
Source decay coefficient, γ		
U^{234}	yr^{-1}	0.0
Th^{230}	yr^{-1}	0.0
Ra^{226}	yr^{-1}	0.0
Initial source concentration, c_p		
U^{234}		1.0
Th^{230}		0.0
Ra^{226}		0.0

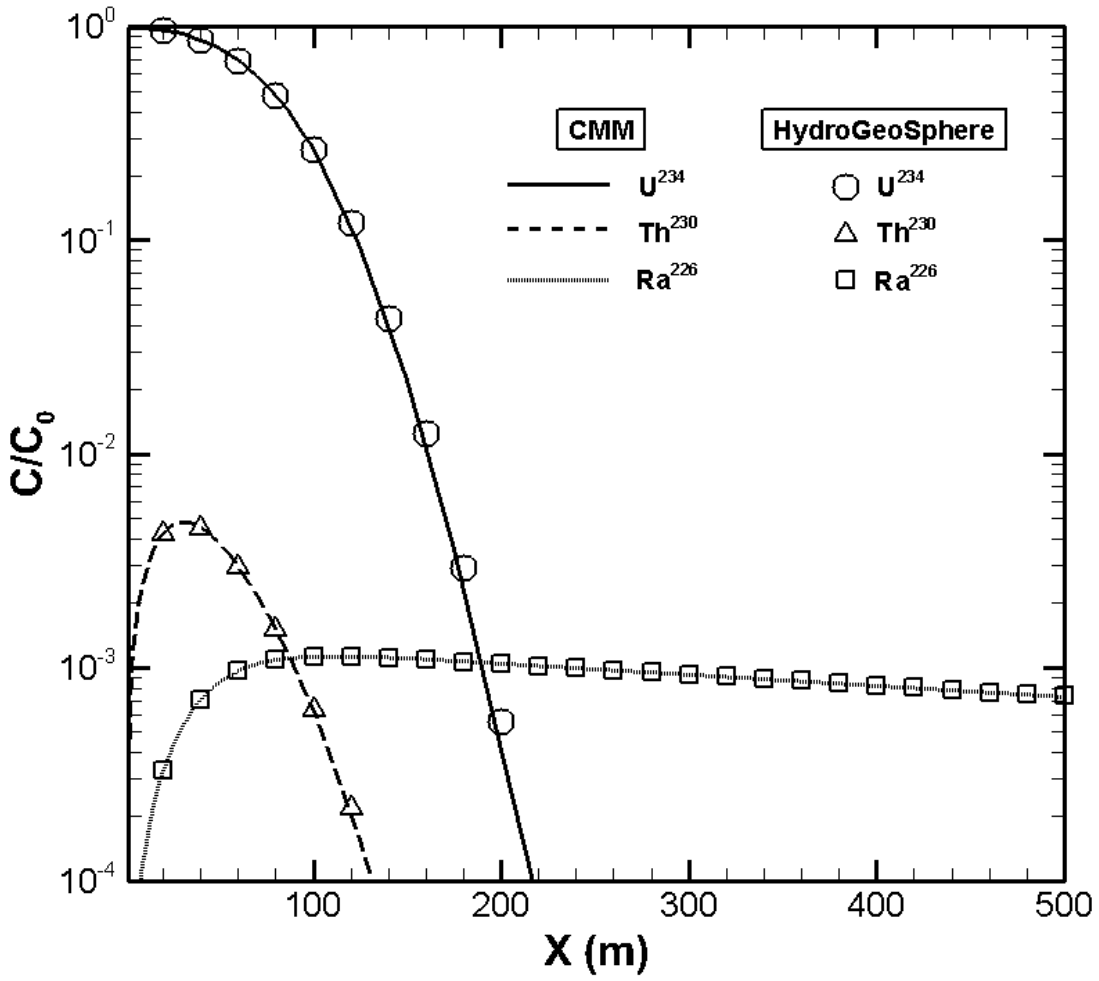

Figure 4.3.3: Comparison between CMM (curves) and HydroGeoSphere (symbols) for one-dimensional transport of radionuclide decay chain.

4.3.4.2 One-dimensional transport of a 4-member, branched decay chain

The second test problem was designed to verify the ability of our solution to correctly handle the case of a branching decay chain. This problem involves the one-dimensional transport of the following hypothetical branched decay chain (Figure 4.3.2d):

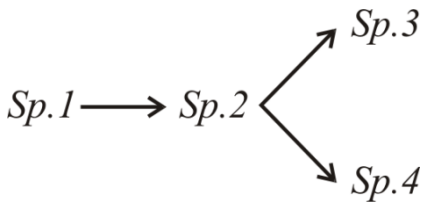

In other words, the parent component Species 1 transforms completely into daughter component Species 2; Species 2, in turn, transforms into two granddaughter components, Species 3 and Species 4, with equal decay fractions $\eta_{32} = \eta_{42} = 0.5$. The model parameters for this problem are listed in Table 4.3.2. In contrast to the first problem, the second test problem includes a decaying source boundary condition. Our solution for this test problem was again compared against HydroGeoSphere. For the numerical simulations using HydroGeoSphere, a one-dimensional homogeneous domain of size 120 m is used and the domain is discretized using a 1 m nodal spacing. For the flow problem, boundary conditions and medium properties were assigned values to obtain a uniform linear groundwater velocity equal to 0.3 m/yr. For transport, a specified concentration ($C_{sp.1} = 1.0$) was assigned at $x = 0$ m. The comparison is presented in Figure 4.3.4 which shows concentration profiles for the 4 members of the decay chain at a time of $t = 600$ years. The solid and dashed lines again represent the CMM solution, while the HydroGeoSphere solution is represented by the symbols. Agreement between the two solutions is very good, except that the concentration values obtained with HydroGeoSphere for Species 1, 2, 3 and 4 are very slightly lower than the CMM results at the end of the simulation domain. The maximum difference between two models is 2.3×10^{-2}. The results that are displayed in Figure 4.3.4 again illustrate the potential significance of incorporating hazardous daughter production formation in contaminant fate and transport analyses. While the concentration of the original product, Species 1, decreases exponentially, its daughter, Species 2, and granddaughters, Species 3 and 4, products increase with distance from the source zone ($x = 0$ m) until they reach a maximum concentration. The granddaughter products are produced at the same rate and also have similar decay and sorption coefficients, with the decay rate coefficient of Species 3 being slightly higher. Both the CMM and HydroGeoSphere codes produce the expected results that the concentration profiles of Species 3 and 4 are similar with Species 4 having somewhat higher concentrations.

Table 4.3.2: Transport parameters for one-dimensional, branched decay chain problem.

Parameter	Units	Value
Groundwater velocity, v	m/yr	0.3
Dispersion coefficient, D_x	m^2/yr	3.0
Dispersion coefficient, D_y	m^2/yr	0.0
Dispersion coefficient, D_z	m^2/yr	0.0
Retardation factor, R		
Species 1		1.50
Species 2		2.0
Species 3		1.0
Species 4		1.0
Decay coefficient, λ		
Species 1	yr^{-1}	6.93×10^{-3}
Species 2	yr^{-1}	3.47×10^{-3}
Species 3	yr^{-1}	1.16×10^{-3}
Species 4	yr^{-1}	1.00×10^{-3}
Source decay coefficient, γ		
Species 1	yr^{-1}	0.0
Species 2	yr^{-1}	0.0
Species 3	yr^{-1}	0.0
Species 4	yr^{-1}	0.0
Initial source concentration, c_p		
Species 1		1.0
Species 2		0.0
Species 3		0.0
Species 4		0.0

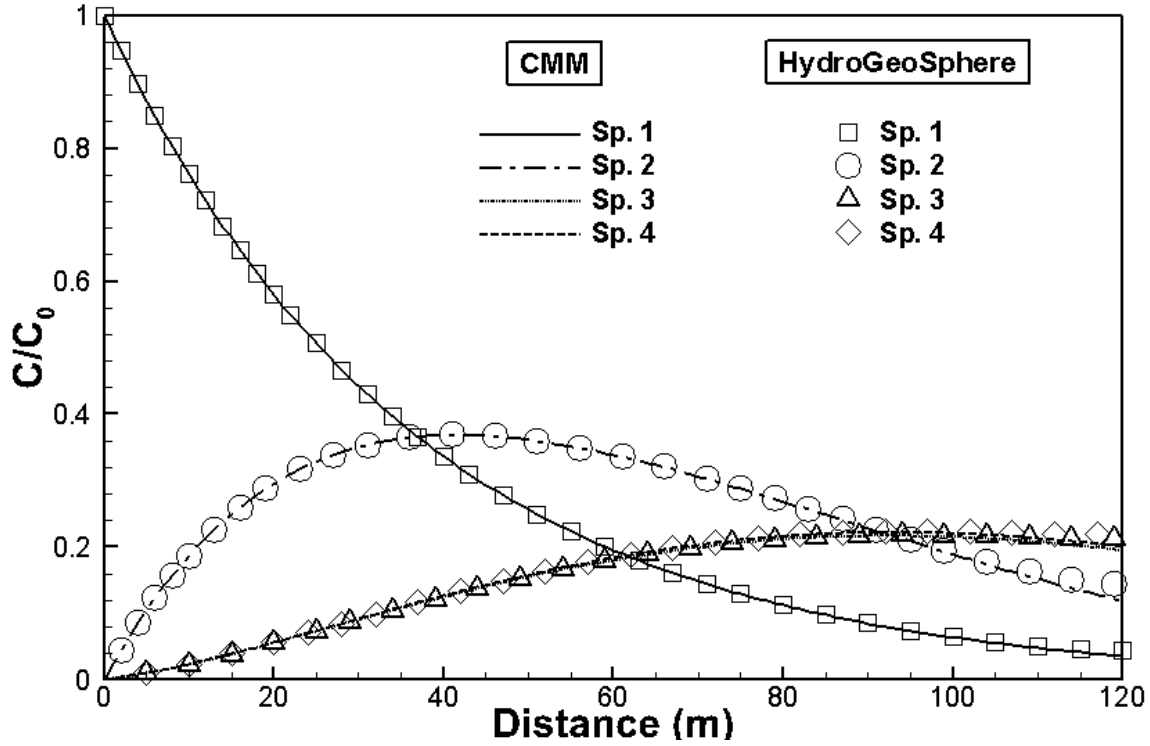

Figure 4.3.4: Comparison between CMM (curves) and HydroGeoSphere (symbols) for 1D transport of a 4-member branched decay chain.

4.3.4.3 Three dimensional transport of a 7-member decay chain

The third verification problem was designed to test a number of remaining features of our solution, including three-dimensional transport of a complex decay chain. The results from our solution are again compared to HydroGeoSphere. This problem involves a 7-member branched decay chain (Figure 4.3.2e).

The parent component Species 1 transforms equally into two daughter products, Species 2 and 3, each of which subsequently transform into two granddaughter products, Species, 4, 5 and Species 6, 7, respectively, with

$$\eta_{42} = \eta_{52} = \eta_{63} = \eta_{73} = 0.5$$

A schematic view of the modeling scenario is shown in Figure 4.3.5. The problem involves a 1 m thick source at the top of the aquifer a total saturated zone thickness of B = 10 m. The width of the patch source is 20 m and it is centered at y = 0 m. The transport parameters for this problem are listed in Table 3. In the HydroGeoSphere model, the problem is simulated in a domain of size 200 m × 40 m × 10 m and the domain is discretized using 1 m × 1 m × 0.5 m hexahedral elements. A specified concentration boundary condition ($C_{sp.1}$ = 1.0) is assigned to the nodes located in the rectangular patch source at x = 0 m. The simulation results obtained using the CMM model are compared to those of HydroGeoSphere. A three-dimensional view of the simulation results obtained using CMM and HydroGeoSphere is shown in Figure 4.3.6. The concentration distributions for the simulations are symmetric with respect to y = 0 m because the flow field of the simulation is steady state and uniform. The CMM results (solid curves) each of the seven species at t = 5 years match well with those obtained with HydroGeoSphere (dashed curves), although there is a small difference for species 1 and 2 on the y-z plane at x = 0 m. This

slight discrepancy is mainly due to difficulties in the Fourier transform inversions in the vicinity of the patch source.

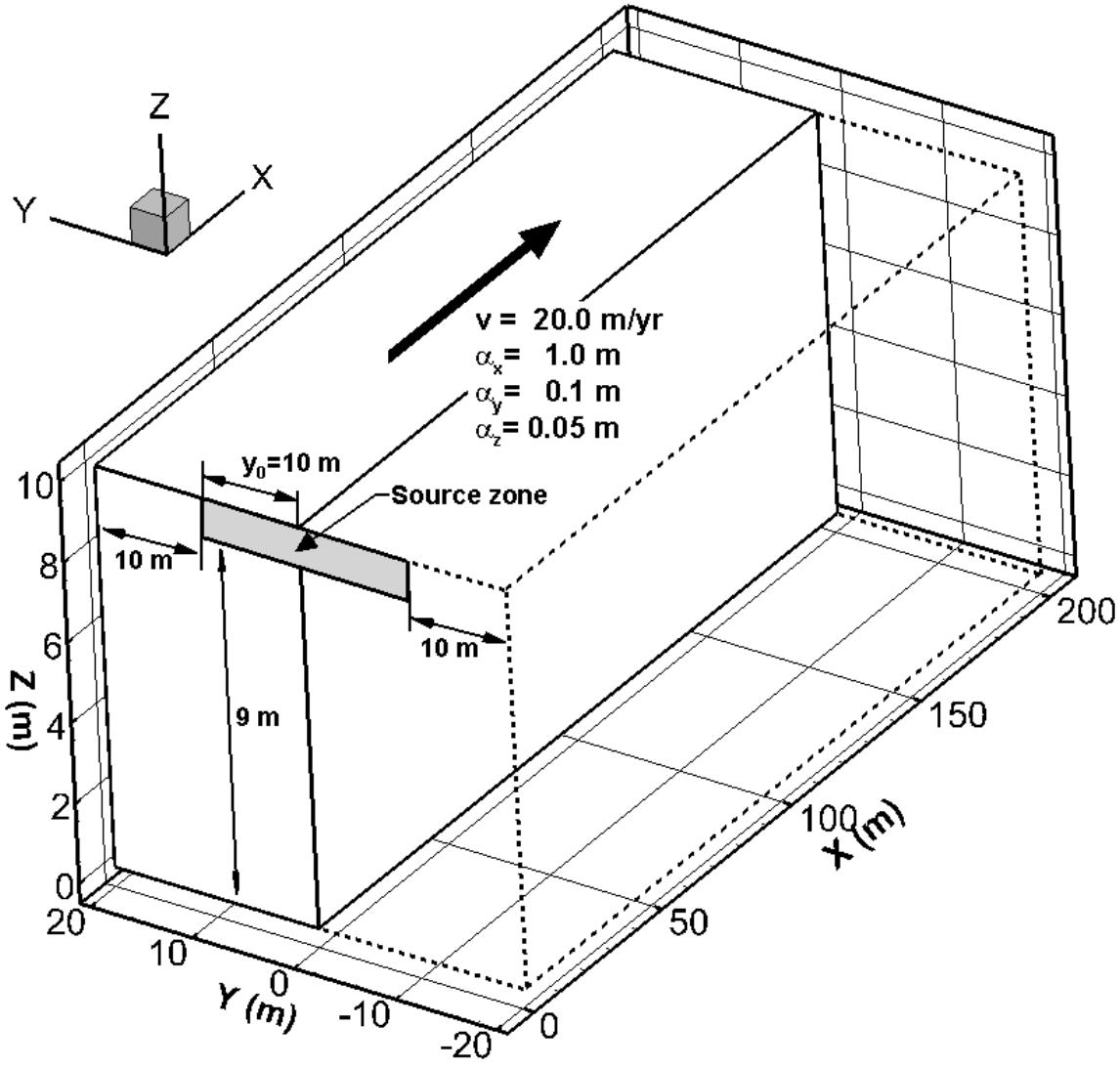

Figure 4.3.5: Schematic of simulation domain: contaminant source is assigned to the gray rectangular patch zone with a dimension of -10 m ≤ y ≤ 10 m and 9 m ≤ z ≤ 10 m at x = 0 m.

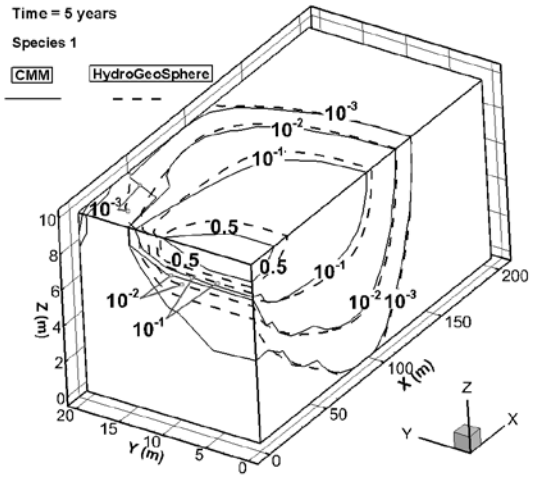
Time = 5 years
Species 1
CMM
HydroGeoSphere
10-3
10-2
10-1
10-3
0.5
0.5
0.5
10-1
10-2
10-3
10-2
10-1
Z (m)
Y (m)
X (m)

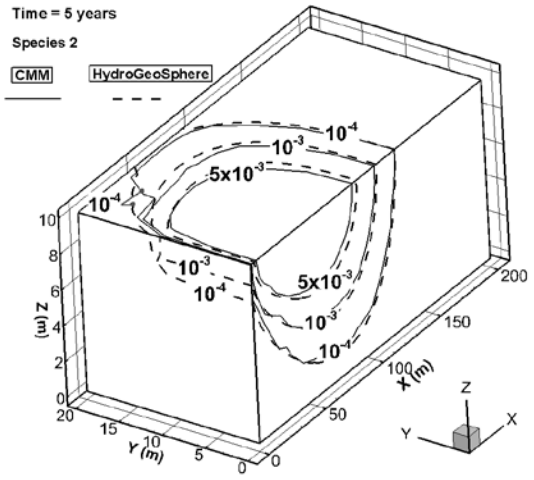
Time = 5 years
Species 2
CMM
HydroGeoSphere
10-4
10-3
5x10-3
10-4
10-3
5x10-3
10-4
10-3
10-4
Z (m)
Y (m)
X (m)

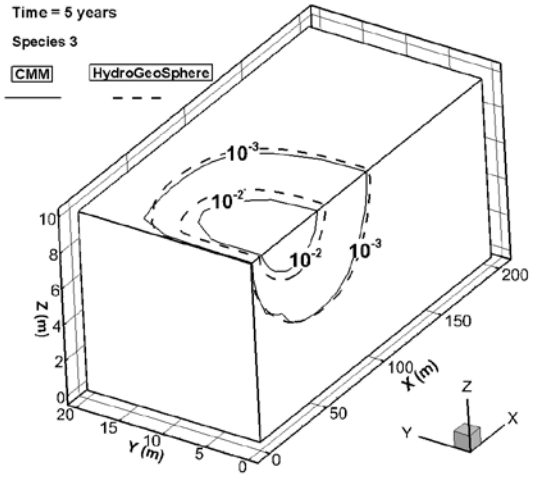
Time = 5 years
Species 3
CMM
HydroGeoSphere
10-3
10-2
10-2
10-3
Z (m)
Y (m)
X (m)

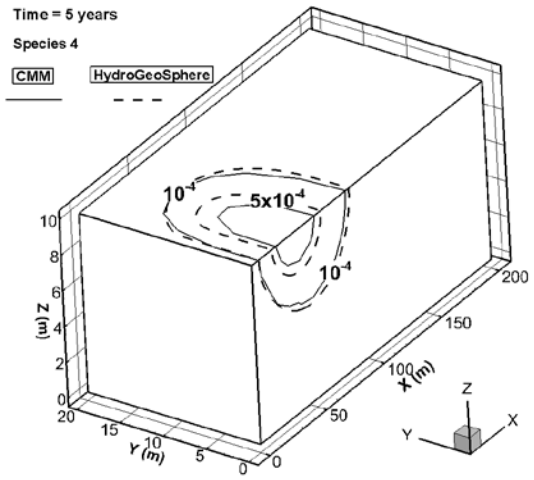
Time = 5 years
Species 4
CMM
HydroGeoSphere
10-4
5x10-4
10-4
Z (m)
Y (m)
X (m)

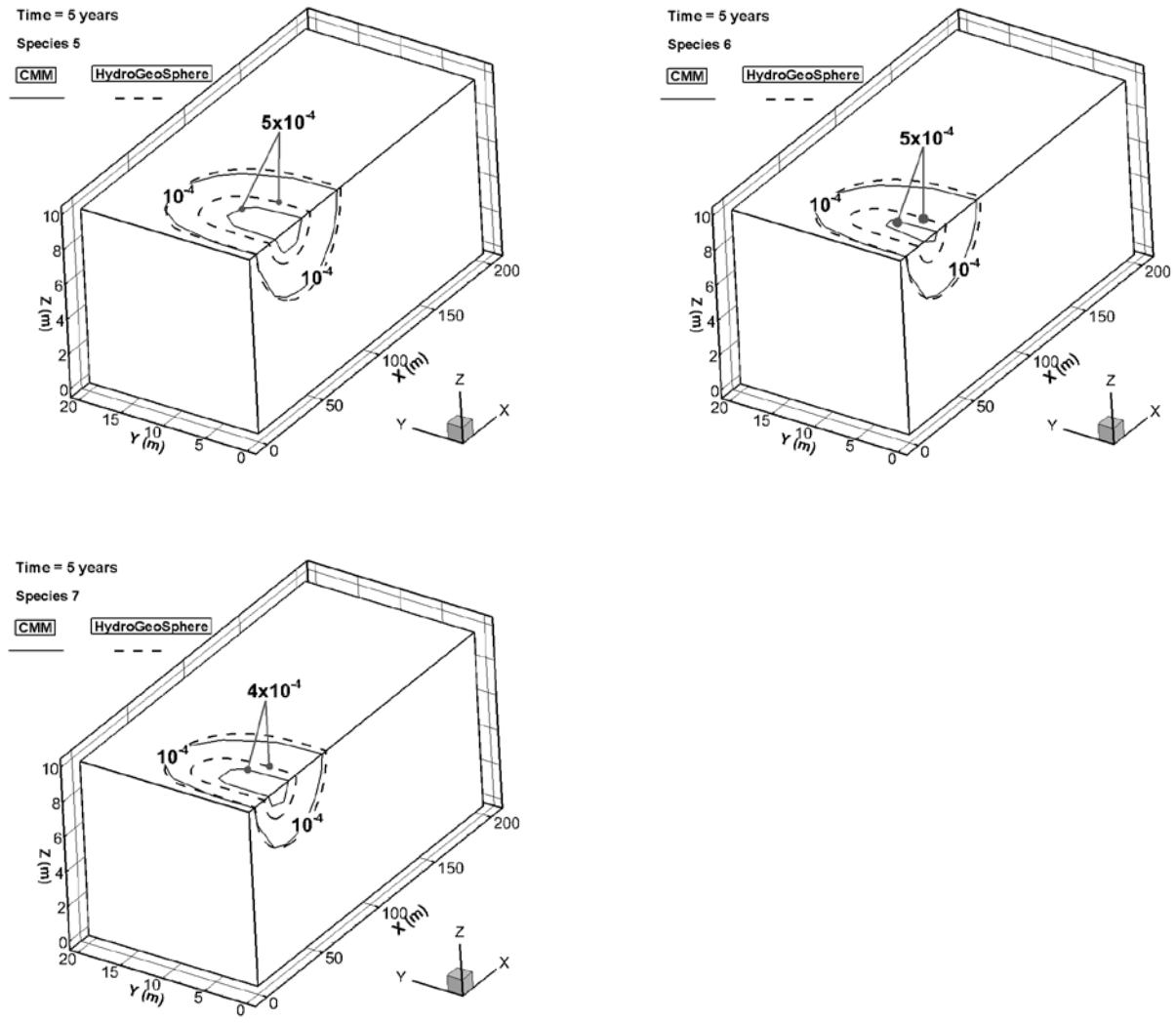

Figure 4.3.6: Comparison between CMM (solid curves) and HydroGeoSphere (dashed curves) solutions for a seven-member decay chain problem at 5 yrs (continued).

TASK 2: MODIFICATION OF COMPFLOW: INVERSE MODELING

4.4: Modification of Compflow: inverse modeling

Currently, bioremediation techniques have gained more attention as a potentially more efficient and cost effective contaminant remediation strategies. As an example bioremediation (hereafter referred to as BR) is particularly efficient for the degradation of chlorinated compounds like PCE, TCE, DEC and VC. However, in order to gain a regulatory acceptance for the use of BR at a field site, one must demonstrate that BR is efficiently occurring. The use of compound-specific stable carbon isotope ratios is a way to assess the effectiveness of degradation of chlorinated ethenes in the subsurface. In practice, during biodegradation of chlorinated ethenes has been observed a trend of increasing of isotopic enrichment in ^{13}C in the products with respect to ^{12}C. This happens because the bonds ^{12}C – ^{12}C are weaker than ^{12}C – ^{13}C, as a consequence, the dechlorination rate is faster for molecules containing only ^{12}C, leading to an enrichment of molecules with ^{12}C – ^{13}C bonds.

To define whether a compound R_{sample}, is enriched in ^{13}C compared to the standard material $R_{standard}$, the isotopic signature is common used:

$$\delta^{13}C = 1000\left(\frac{R_{sample}}{R_{standard}} - 1\right) \tag{4.4.1}$$

where R is the ratio between ^{13}C–^{12}C. The relative changes in the isotopic signatures are expressed using the fractionation factor,

$$\alpha = \frac{1000 + \delta^{13}C_{product}}{1000 + \delta^{13}C_{reactant}} \tag{4.4.2}$$

or by the enrichment factor

$$\varepsilon = 1000(\alpha - 1) \tag{4.4.3}$$

In practice, ε or α are used to understand the effectiveness of the biodegradation.

The total carbon C of each of the species is used to know the concentrations of ^{12}C and ^{13}C by

$$
\begin{aligned}
{}^{12}C &= \frac{C}{1+\left(\frac{\delta^{13}C}{1000}+1\right)R_{standard}} \\
{}^{13}C &= \frac{\left(\frac{\delta^{13}C}{1000}+1\right)R_{standard}}{1+\left(\frac{\delta^{13}C}{1000}+1\right)R_{standard}}C
\end{aligned}
\tag{4.4.4}
$$

By the Equations (4.4.3) and (4.4.4) one can calculate the enrichment factors and the concentrations of the lighter and heavier isotope by using the sampled C and the isotopic signature. In particular when the transport involves the following reactions *PCE - TCE - DCE - VC - ETH* we measure the total carbon C_{PCE}, C_{TCE}, C_{DCE}, C_{VC}, C_{ETH} and the isotopic signatures $\delta^{13}C_{PCE}$, $\delta^{13}C_{TCE}$, $\delta^{13}C_{DCE}$, $\delta^{13}C_{VC}$, $\delta^{13}C_{ETH}$ obtaining ${}^{12}C_{PCE}$, ${}^{12}C_{TCE}$, ${}^{12}C_{DCE}$, ${}^{12}C_{VC}$, ${}^{12}C_{ETH}$ and ${}^{13}C_{PCE}$, ${}^{13}C_{TCE}$, ${}^{13}C_{DCE}$, ${}^{13}C_{VC}$, ${}^{13}C_{ETH}$ by means of Equation (4.4.4).

When the degradation rate is primarily a function of the contaminant concentration, and when the microbial mass is not increasing or decreasing over time within the region of interest, Mariotti et al. (1981), using the Raylegh equation, demonstrated that the ratio of the rate constants for first order reactions is related to the fractionation factor by:

$$
\alpha = \frac{{}^{12}k}{{}^{13}k} \tag{4.4.5}
$$

where ${}^{12}k$ and ${}^{13}k$ are the rate constants of the reactions involving lighter and heavier isotopes, respectively.

Predictive modeling of natural attenuation of chlorinated ethenes at field sites requires knowledge of several parameters, including first order decay coefficients and retardation factors. Although first order decay coefficients and isotopic enrichment factors can be measured in laboratory, these laboratory-measured parameters may not be representative of field conditions. Therefore, it is desirable to have the ability to estimate these parameters from field measurements of contaminant concentrations through inverse modeling.

The research work aimed to expand previously developed inverse modeling technology to estimate decay coefficients and fractionation factors for PCE, TCE, DEC and VC in multi-dimensional flow field and heterogeneous geologic media and to analyze the necessary and sufficient conditions to obtain them.

Numerical experiments are being conducted to simulate the isotopic enrichment in ${}^{13}C$ during the degradation of chlorinated ethenes. Previous results obtained by Clement et al. [2011] concerned the estimation of the first order decay coefficients and the enrichment factors by an analytical, one dimensional, multi species, reactive transport model for simulating the concentrations and isotopic signatures of PCE and its daughter products. The transport equation under these hypotheses simplifies in

$$R_i \frac{\partial c_i}{\partial t} + v \frac{\partial c_i}{\partial x} - D_x \frac{\partial^2 c_i}{\partial x^2} = y_i k_{i-1} c_{i-1} - k_i c_i \tag{4.4.6}$$

where c_i denotes the concentration of the i^{th} species, R_i is its retardation factor, v the velocity, D_x, the hydrodynamic dispersion coefficient, k_i is the first order contaminant destruction rate constant and $y_{i/j}$ is the effective yield factor which describes the mass of species i produced from the species j. In matrix form

$$\begin{bmatrix} R_1 & 0 & 0 & 0 \\ 0 & R_2 & 0 & 0 \\ 0 & 0 & R_3 & 0 \\ 0 & 0 & 0 & R_4 \end{bmatrix} \begin{bmatrix} \frac{\partial c_1}{\partial t} \\ \frac{\partial c_2}{\partial t} \\ \frac{\partial c_3}{\partial t} \\ \frac{\partial c_4}{\partial t} \end{bmatrix} + v \begin{bmatrix} \frac{\partial c_1}{\partial x} \\ \frac{\partial c_2}{\partial x} \\ \frac{\partial c_3}{\partial x} \\ \frac{\partial c_4}{\partial x} \end{bmatrix} - D_x \begin{bmatrix} \frac{\partial^2 c_1}{\partial x^2} \\ \frac{\partial^2 c_1}{\partial x^2} \\ \frac{\partial^2 c_1}{\partial x^2} \\ \frac{\partial^2 c_1}{\partial x^2} \end{bmatrix} = \begin{bmatrix} -k_1 & 0 & 0 & 0 \\ y_2 k_1 & -k_2 & 0 & 0 \\ 0 & y_3 k_2 & -k_3 & 0 \\ 0 & 0 & y_4 k_3 & -k_4 \end{bmatrix} \begin{bmatrix} c_1 \\ c_2 \\ c_3 \\ c_4 \end{bmatrix} \tag{4.4.7}$$

and using the vector notation

$$\mathbf{R}\mathbf{c}' + v_x \mathbf{c}_x - D_x \mathbf{c}_{xx} = \mathbf{K}\mathbf{c} \tag{4.4.8}$$

Since the coefficient matrix **K** on the right hand side of Equation (4.4.7) has cross coupling terms the set of partial differential equations must be solved simultaneously. Clement observed that **K** matrix is lower diagonal and he proposed to transform the problem in a domain ***B***, using a linear algebra transformation. Once the diagonalization of the matrix **K** has carried out and under the assumption that the retardation factors are identical for all the chemicals, $\mathbf{R} = \delta_{ij} R$, Equation (4.4.8) becomes

$$\mathbf{R} \frac{\partial \mathbf{b}}{\partial t} + v_x \frac{\partial \mathbf{b}}{\partial x} - D_x \frac{\partial^2 \mathbf{b}}{\partial x^2} = \tilde{\mathbf{K}}\, \mathbf{b} \tag{4.4.9}$$

where **b** is the vector of the transformed concentrations and $\tilde{\mathbf{K}}$ is the transformed matrix equal to

$$\begin{bmatrix} -k_1 & 0 & 0 & 0 \\ 0 & -k_2 & 0 & 0 \\ 0 & 0 & -k_3 & 0 \\ 0 & 0 & 0 & -k_4 \end{bmatrix} \tag{4.4.10}$$

By the transformation, Equation (4.4.9) becomes a set of independent partial differential equations that can easily solved.

In the research work the numerical model combined with the transformation method proposed by Clement et al. (2001) has been used for the numerical simulation. The method developed by for the 1D-homogeneous case has mathematically extended and numerically applied to the 3D-heterogeneous.

Under the following hypotheses

- 3D heterogeneous medium;
- multispecies transport;
- no injected/pumped fluid volume per unit of volume of the aquifer

the classical convection-dispersion equation of reactive solute in porous media takes the following form:

$$R_i \frac{\partial c_i}{\partial t} + v_l \frac{\partial c_i}{\partial x_l} - \frac{\partial}{\partial x_l}\left(D_{lm} \frac{\partial c_i}{\partial x_m} \right) = \sum_{j=1}^{i-1} y_{i/j} k_j c_j - k_i c_i + \sum_{j=i+1}^{n} y_{i/j} k_j c_j \quad i = 1,\ldots,n \tag{4.4.11}$$

where D_{lm} is the hydrodynamic dispersion tensor computed on the basis of Darcy velocity and n is the number of species. For PCE-TCE-DCE-VC we have

$$R_i \frac{\partial c_i}{\partial t} + v_l \frac{\partial c_i}{\partial x_l} - \frac{\partial}{\partial x_l}\left(D_{lm} \frac{\partial c_i}{\partial x_m} \right) = y_i k_{i-1} c_{i-1} - k_i c_i \quad i = 1,\ldots,n \tag{4.4.12}$$

In matrix notation:

$$\begin{aligned} &\mathbf{R}\mathbf{c}_t + v_x \mathbf{c}_x + v_y \mathbf{c}_y + v_z \mathbf{c}_z - \frac{\partial}{\partial x}(D_{xx}\mathbf{c}_x + D_{xy}\mathbf{c}_y + D_{xz}\mathbf{c}_z) - \\ &\frac{\partial}{\partial y}(D_{yx}\mathbf{c}_x + D_{yy}\mathbf{c}_y + D_{yz}\mathbf{c}_z) - \frac{\partial}{\partial z}(D_{zx}\mathbf{c}_x + D_{zy}\mathbf{c}_y + D_{zz}\mathbf{c}_z) = \mathbf{K}\mathbf{c} \end{aligned} \tag{4.4.13}$$

where the subscripts *t*, *x*, *y* and *z* of **c** denote the first partial derivative with respect to the time and *x*, *y* and *z* axis, respectively.

Also in this case the reaction coefficient matrix **K** has cross coupling terms, as a result, the set of coupled partial differential equations must be solved simultaneously. At this stage the linear algebra transformation, **S,** is introduced:

$$\begin{aligned}
&\mathbf{c} = \mathbf{Sb} \\
&\mathbf{c_x} = \frac{\partial}{\partial x}(\mathbf{Sb}) = \mathbf{Sb_x} \\
&\mathbf{c_{xx}} = \mathbf{Sb_{xx}} \\
&\mathbf{c}_t = \mathbf{Sb}_t
\end{aligned} \tag{4.4.14}$$

and

$$\mathbf{b} = \mathbf{S}^{-1}\mathbf{c} \tag{4.4.15}$$

Since **S** does not depend on *t*, *x*, *y* and *z*, by substituting Equations (4.4.14) in (4.4.13) and rearranging we have

$$\begin{aligned}
&\mathbf{S^{-1}RSb}_t + v_x\mathbf{b}_x + v_y\mathbf{b}_y + v_z\mathbf{b}_z - \frac{\partial}{\partial x}(D_{xx}\mathbf{b}_x + D_{xy}\mathbf{b}_y + D_{xz}\mathbf{b}_z) - \\
&\frac{\partial}{\partial y}(D_{yx}\mathbf{b}_x + D_{yy}\mathbf{b}_y + D_{yz}\mathbf{b}_z) - \frac{\partial}{\partial z}(D_{zx}\mathbf{b}_x + D_{zy}\mathbf{b}_y + D_{zz}\mathbf{b}_z) = \mathbf{S^{-1}KSb}
\end{aligned} \tag{4.4.16}$$

If R_i is the same for all the considered species, the first term on the left side of Equation (4.4.16) yields

$$\mathbf{S^{-1}RS} = \mathbf{RS^{-1}Sb} = \mathbf{Rb} \tag{4.4.17}$$

Eventually Equation (4.4.16) takes the following form

$$\begin{aligned}
&\mathbf{Rb}_t + v_x\mathbf{b}_x + v_y\mathbf{b}_y + v_z\mathbf{b}_z - \frac{\partial}{\partial x}(D_{xx}\mathbf{b}_x + D_{xy}\mathbf{b}_y + D_{xz}\mathbf{b}_z) - \\
&\frac{\partial}{\partial y}(D_{yx}\mathbf{b}_x + D_{yy}\mathbf{b}_y + D_{yz}\mathbf{b}_z) - \frac{\partial}{\partial z}(D_{zx}\mathbf{b}_x + D_{zy}\mathbf{b}_y + D_{zz}\mathbf{b}_z) = \tilde{\mathbf{K}}\,\mathbf{b}
\end{aligned} \tag{4.4.18}$$

where

$$\tilde{\mathbf{K}} = \mathbf{S^{-1}KS} \tag{4.4.19}$$

The following properties are used to evaluate the transformation matrix **S:** *if **P** is a square matrix whose column vectors are the eigenvectors of a matrix **A**, then **P**$^{-1}$**AP**=**L**, where **L** will be a diagonal matrix; also the diagonal entries of **L** are the eigenvalues of **A**. The matrices **A** and **D** are known to be similar matrices.* The advantage is that the matrix **S** has to be computed just once by means of solving the similarity transformation problem (4.4.19).

In practice the solution, extended to a 3D-heterogeous case, has been implemented by the following steps:

1. assembling the reaction matrix **K** and performing the similarity transformation (4.4.19).

2. Transforming IC & BCs (initial conditions and boundary conditions) of the concentration domain to b-domain by means of S^{-1}.
3. Solving the problem of uncoupled differential equations by means of FEM or FDM in the b-domain for each of the species by means of appropriate numerical solutions.
4. Transforming back $b(x,y,z,t)$ into the concentrations $c=c(x,y,z,t)$.

The estimation of the decay coefficients and fractionation factors for PCE, TCE, DEC and VC has been implemented by the method of spatial moments.

In 2D case (the extension to a 3D case is immediate) the zero[th] moment is defined as:

$$m^{o}{}_{i} = \lim_{\Omega_n \to \infty} \iint_{D_n} nc_i(x_1, x_2)dx_1dx_2 = \int_{-\infty}^{+\infty}\int_{-\infty}^{+\infty} nc_i(x_1, x_2)dx_1dx_2 \qquad (4.4.20)$$

with (x_1, x_2) in $\Omega_n \subseteq R^2$ and $\partial\Omega_n$ border of $\Omega_n / \Omega_n = [a_n, b_n] \times [f_n, d_n]$ large enough but finite such that $c(x_1, x_2) \to 0$ and $\frac{\partial c_i}{\partial x_i}(x_1, x_2) \to 0 \ \forall (x_1, x_2) \in \partial\Omega_n$. Using the spatial moments means finding the improper integral of the advection-dispersion equations i.e. integrating over Ω_n and doing the limit for Ω_n to infinity. That is

$$\lim_{\Omega_n \to \infty} \int_{\Omega_n} \left(R_1 n \frac{\partial c_1}{\partial t} + u_l \frac{\partial c_1}{\partial x_l} - \frac{\partial}{\partial x_l}\left(D_{lm} \frac{\partial c_1}{\partial x_m} \right) + k_1 n c_1 - \frac{M_1}{\rho H}\delta(x_1 - x_{lo1})\delta(x_2 - x_{lo2})\delta(t - t_o) \right) dx_1 dx \quad (4.4.21)$$

for the first species of the chain reaction. In Equation (4.4.21), δ is the Dirac delta function, ρ is the water density, M_1 is the total mass of the species 1 present at location (x_{lo1}, x_{lo2}) at time t_o. and H, is the thickness of the aquifer. By using the following properties

1. $$\iint_{\Omega_n} R_1 n \frac{\partial c_1}{\partial t} dx_1 dx_2 = R_1 \frac{\partial}{\partial t} \iint_{\Omega_n} n c_1 dx_1 dx_2 \Rightarrow R_1 \frac{\partial}{\partial t}\left(\lim_{\Omega_n \to \infty} \iint_{\Omega_n} n c_1 dx_1 dx_2 \right) = R_1 \frac{\partial m_1^{\,o}}{\partial t}$$

2. $$\iint_{\Omega_n} u_l \frac{\partial c_1}{\partial x_l} dx_1 dx_2 = \int_{\partial\Omega_n} u_i c_1 n_i dl - \iint_{\Omega_n} c_1 \frac{\partial u_l}{\partial x_l} dx_1 dx_2 = 0 \text{ since } c_1 = 0 \text{ in } \partial\Omega_n \text{ and } \frac{\partial u_l}{\partial x_l} = 0$$

3. $$-\iint_{\Omega_n} \frac{\partial}{\partial x_l}\left(D_{lm} \frac{\partial c_1}{\partial x_m} \right) dx_1 dx_2 = -\int_{an}^{bn}\int_{cn}^{dn} \frac{\partial}{\partial x_l}\left(D_{lm} \frac{\partial c_1}{\partial x_m} \right) dx_1 dx_2 =$$

$$-\left(\int_{an}^{bn}\int_{cn}^{dn} \frac{\partial}{\partial x_1}\left(D_1 \frac{\partial c_1}{\partial x_1} \right) dx_1 dx_2 + \int_{an}^{bn}\int_{cn}^{dn} \frac{\partial}{\partial x_2}\left(D_2 \frac{\partial c_1}{\partial x_2} \right) dx_1 dx_2 \right) =$$

$$= -\left(\int_{an}^{bn} dx_2 \int_{cn}^{dn} \frac{\partial}{\partial x_1}\left(D_1 \frac{\partial c_1}{\partial x_1} \right) dx_1 + \int_{an}^{bn} dx_1 \int_{cn}^{dn} \frac{\partial}{\partial x_2}\left(D_2 \frac{\partial c_1}{\partial x_2} \right) dx_2 \right) =$$

$$-\left(\int_{an}^{bn} \left[D_1 \frac{\partial c_1}{\partial x_1} \right]_{cn}^{dn} dx_2 + \int_{cn}^{dn} \left[D_2 \frac{\partial c_1}{\partial x_2} \right]_{an}^{bn} dx_1 \right) = 0 \text{ since } \frac{\partial c_1}{\partial x_l} = 0 \text{ in } \partial\Omega_n$$

$$4.\ \iint_{\Omega_n} k_1 n c_1 dx_1 dx_2 = k_1 \iint_{\Omega_n} n c_1 dx_1 dx_2 \Rightarrow k_1 \lim_{\Omega_n \to \infty} \iint_{\Omega_n} n c_1 dx_1 dx_2 = k_1 m_1^o$$

$$5.-\iint_{\Omega_n} \frac{M_1}{\rho H} \delta(x_1 - x_{lo}) \delta(x_2 - x_{lo}) \delta(t - t_o) dx_1 dx_2 \Rightarrow$$

$$-\frac{M_1}{\rho H} \delta(t - t_o) \lim_{\Omega_n \to \infty} \iint_{\Omega_n} \delta(x_1 - x_{lo}) \delta(x_2 - x_{lo}) dx_1 dx_2 = -\frac{M_1}{\rho H} \delta(t - t_o)$$

we have

$$R_1 \frac{\partial m_1^o}{\partial t} + k_1 m_1^o - \frac{M_1}{\rho H} \delta(t - t_0) = 0 \tag{4.4.22}$$

The zero[th] moment for the other species can be computed in the same manner by

$$\lim_{\Omega_n \to \infty} \int_{\Omega_n} \left(R_i n \frac{\partial c_i}{\partial t} + u_l \frac{\partial c_i}{\partial x_l} - \frac{\partial}{\partial x_l} \left(D_{lm} \frac{\partial c_i}{\partial x_m} \right) = n y_i k_{i-1} c_{i-1} - n k_i c_i \right) dx_1 dx_2 \quad i = 2, \ldots, N \tag{4.4.23}$$

leading to the following system of equations

$$\begin{aligned}
R_1 \frac{\partial m_1^o}{\partial t} + k_1 m_1^o - \frac{M_1}{\rho H} \delta(t - t_0) &= 0 \\
R_2 \frac{\partial m_2^o}{\partial t} + k_2 m_2^o - k_1 y_2 m_1^o &= 0 \\
R_3 \frac{\partial m_3^o}{\partial t} + k_3 m_3^o - k_2 y_3 m_2^o &= 0 \\
R_4 \frac{\partial m_4^o}{\partial t} + k_4 m_4^o - k_3 y_3 m_4^o &= 0
\end{aligned} \tag{4.4.24}$$

By adding the initial conditions we obtain

$$
\begin{aligned}
&\frac{\partial m_1^o}{\partial t} = -\frac{k_1}{R_1} m_1^o \\
&\frac{\partial m_2^o}{\partial t} = -\frac{k_2}{R_2} m_2^o + \frac{k_1}{R_2} y_2 m_1^o \\
&\frac{\partial m_3^o}{\partial t} = -\frac{k_3}{R_3} m_3^o + \frac{k_2}{R_3} y_3 m_2^o \\
&\frac{\partial m_4^o}{\partial t} = -\frac{k_4}{R_4} m_4^o + \frac{k_3}{R_4} y_3 m_4^o \\
&m_1^o(0) = \frac{M_1}{\rho H},\ m_2^o(0) = 0,\ m_3^o(0) = 0,\ m_4^o(0) = 0
\end{aligned}
\tag{4.4.25}
$$

or in matrix form

$$
\begin{aligned}
&\mathbf{m_o}'(t) = \mathbf{A}\mathbf{m_o}(t) \\
&\mathbf{m_o}(0) = \mathbf{m_0}
\end{aligned}
\tag{4.4.26}
$$

where

$$
\mathbf{m_o} = \begin{bmatrix} m_1^o & m_2^o & m_3^o & m_4^o \end{bmatrix}^T
$$

$$
\mathbf{m'_o} = \begin{bmatrix} \frac{\partial m_1^o}{\partial t} & \frac{\partial m_2^o}{\partial t} & \frac{\partial m_3^o}{\partial t} & \frac{\partial m_4^o}{\partial t} \end{bmatrix}^T
$$

$$
\mathbf{m_o}(0) = \begin{bmatrix} M_1/(\rho H) & 0 & 0 & 0 \end{bmatrix}^T
$$

and

$$
\mathbf{A} = \begin{bmatrix}
-\frac{k_1}{R_1} & 0 & 0 & 0 \\
\frac{k_1}{R_2} y_2 & -\frac{k_2}{R_2} & 0 & 0 \\
0 & \frac{k_2}{R_3} y_3 & -\frac{k_3}{R_3} & 0 \\
0 & 0 & \frac{k_3}{R_4} y_4 & -\frac{k_4}{R_4}
\end{bmatrix}
$$

An analytical solution of the system of differential equations (4.4.26) is found by the eigenvalues methods. The solution (not shown) non-linearly depends on k_i and R_i.

By assuming R as a constant and known and the initial mass of the contaminant M_1, in terms of ^{12}C and ^{13}C a set of equations in terms of the relevant parameters is obtained

$$\text{for } i = 1,2,3,4$$
$$^{12}m_i^o = {}^{12}m_i^o(^{12}k_1, ^{12}k_2, ^{12}k_3, ^{12}k_4, R, t, M_1) \qquad (4.4.27)$$
$$^{13}m_i^o = {}^{13}m_i^o(^{13}k_1, ^{13}k_2, ^{13}k_3, ^{13}k_4, R, t, M_1)$$

In order to estimate the decay coefficients parameters by means the zeroth method for each of the isotope many spatially measurements of concentrations of the different species are used at one time. Such measurements, are necessary and sufficient conditions to obtain unique solution for the problem (4.4.27) (i.e. 8 equations in 8 unknowns if one knows the initial mass M1).

In practice in order to estimate the fractionation factors and the decay coefficients the following steps are required

1. measuring the total concentration of C and of the isotopic signatures $\delta^{13}C$ for each species in different points at different times;
2. computing quantity of carbon ^{13}C and ^{12}C for each species by the known relationships
3. Computing the zeroth moments from the sampled concentrations.
4. Using optimization technique to estimate parameters k_i using the Equation (4.4.27) obtained from the system of differential equations (4.4.26).
5. Calculating the fractionation factors for each species using $\alpha_i = {}^{13}k_i / {}^{12}k_i$

The effects of noise in measurements on the estimation are also investigated in the research. While noise in concentration measurements will affect the quality of estimated parameters, its influence decreased when the number of measurements was increased.

The method can be usefully coupled with the Hydraulic Tomography during a remediation techniques injecting and pumping water from the subsurface and measuring drawdowns and concentrations of the contaminants at each wells, eventually obtaining the heterogeneous structures and the transport parameters.

The inverse code is expanded to support variable time step. This can make the simulation process faster and more flexible than previous version. Because of the use of the Adjoint method in the sensitivity calculation, all the variable time steps, i.e. both forward and inverse part, are required to be arranged together before any calculation. Forward results for the calculation of adjoint equation are recorded. Comparison with constant time step shows this scheme can provide the same results with less time. Simulations of chain reaction decay are being conducted with a heterogeneous hydraulic conductivity field. Results will be compared to those a homogeneous field. The difference between these two will be investigated to examine the effect of heterogeneity on isotope chain decay.

TASK 3: NUMERICAL EXPERIMENTS USING COMPFLOW

4.5 Impact of Source Mass Depletion at the Compliance Boundary in Fractured- Porous Media

4.5.1 Conceptual model of the Smithville site

Numerical experiments of TCE DNAPL migration are based on the conceptual model of the Smithville, Ontario, site described by Slough et al. (1999b). The hydrostratigraphy of the site consists of an approximately 6 m thick clay till overburden with a thin layer of sandy till at its base, which is underlain by about 40 m of carbonate bedrock weathered to varying degrees. The base of the system (shale) was treated as an impermeable unit (Figure 4.5.1a). Note that regional hydrogeology and geochemistry indicate that groundwater flow in the Clinton group (that includes the base Rochester shale unit) is significantly lower compared to that in the upper carbonate formations and thus it is reasonable to assume that the base of carbonate formations is a no-flow boundary as it is assumed throughout this study. It is also noted that aqueous phase contaminant diffusion and sorption/desorption as well as nonaqueous phase fluid movement into and out of relatively low-permeability units within the carbonate formations (such as a tight dolostone layer that represents the lower Vinemont formation), can significantly influence the pattern and duration for natural attenuation of contaminant concentration and the efficiency of remediation.

A fracture network, generated by Slough et al. (1999b) based on the observed statistical characteristics for fracture geometry, was used for TCE migration simulations in this study (Figure 4.5.1b).

Table 4.5.1: Flow and transport parameters for each stratigraphic unit.

	Permeability $[m^2]$	*Porosity [-]*	*Dispersivity (X,Z directions) [m]*	*Diffusion Coefficient* $[m^2/day]$
Clay	1.76×10^{-15}	0.5	0.1; 0.001	8.7×10^{-5}
Sandy Till	1.0×10^{-11}	0.3	3.0; 0.01	
Permeable Dolostone	1.43×10^{-13}	0.0624	3.0; 0.01	
Weathered Dolostone	5.69×10^{-14}	0.03	3.0; 0.01	
Tight Dolostone	1.0×10^{-15}	0.03	0.1; 0.001	

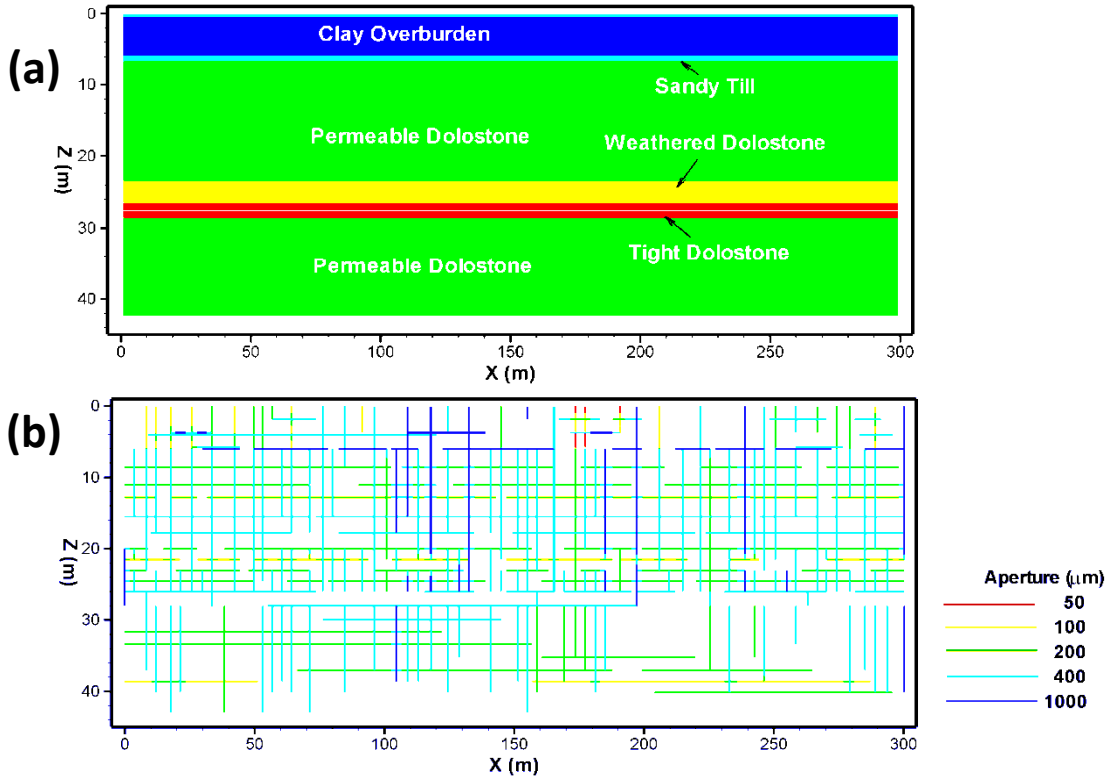

Figure 4.5.1: (a) Hydrostratigraphy and (b) fracture network geometry based on the Smithville site

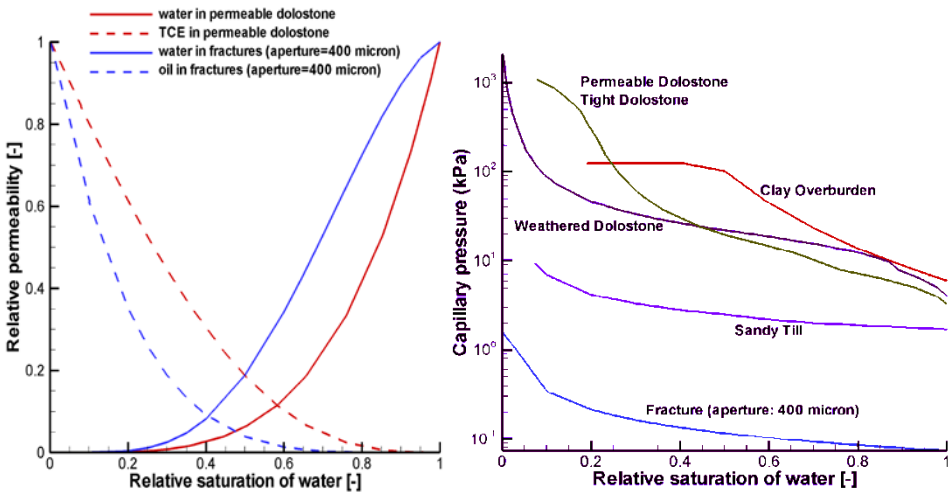

Figure 4.5.2: Typical relations among saturation, relative permeability, and capillary pressure in fractures and matrix blocks.

Flow and transport properties of the hydrostratigraphic units shown in Figure 4.5.1 are summarized in Table 4.5.1 and Figure 4.5.2. It is noted that the entry pressure for different

materials ranges from 1.7 (Sandy Till) to 6.0 kPa (Clay Overburden) and it can significantly influence the DNAPL migration pattern in fractured porous media (Slough et al., 1999b).

Physicochemical properties of the fluids, water and DNAPL, are summarized in Table 4.5.2. The TCE contaminant is assumed to have a maximum dissolved aqueous phase concentration of 1384 mg L^{-1} at equilibrium.

Table 4.5.2: Physicochemical parameters for water and TCE DNAPL fluids.

	Molecular weight [g/mole]	*Density [mole/L]*	*Compressibility [1/kpa]*	*Viscosity [kpa-sec]*
Water	18.02	55.3	3.0×10^{-6}	1.23×10^{-6}
TCE	131.5	11.1	4.3×10^{-7}	1.19×10^{-6}

4.5.2 TCE migration simulations: Preliminary results

A steady-state groundwater (aqueous phase) flow was simulated before injecting TCE DNAPL by specifying the water pressure on the left (1.5 m) and right (0 m) boundaries and by applying recharge at the top at the rate of 50 mm yr^{-1} (Figure 4.5.3). 3000 L of TCE was injected over two years at the injection zone shown in Figure 4.5.3 and then it was allowed to migrate to the downstream compliance boundary located at x = 300 m for 1000 years. For illustrative purposes we consider the DNAPL to be comprised only of TCE and degradation processes are ignored.

Figure 4.5.4 shows the distributions of TCE saturation and aqueous phase concentration at t = 1 year and at the end of the injection period (t = 2 years). These results illustrate typical source zone architecture for DNAPL spilled in fractured porous media: spilled nonaqueous DNAPL migrates downwards through fractures by gravity with a portion of DNAPL imbibing into the matrix, it is then dissolved into the aqueous phase liquid (groundwater) and carried in the downgradient direction. Figure 4.5.4 shows that the TCE contaminant can either diffuse as a dissolved aqueous phase or flow as a nonaqueous phase into the matrix blocks depending on the DNAPL entry pressure for the matrix.

Figure 4.5.5 shows the TCE migration patterns after the injection ceased. It is clear in Figure 4.5.5 that significantly high TCE concentration are maintained at the downgradient compliance boundary for hundreds of years due to the slow depletion of nonaqueous phase TCE in the source-zone matrix blocks. As implied by the lower rock entry pressure and lower permeability in the tight dolostone zone, TCE imbibition into the matrix occurred in this zone, which then acted as an aqueous phase contaminant source.

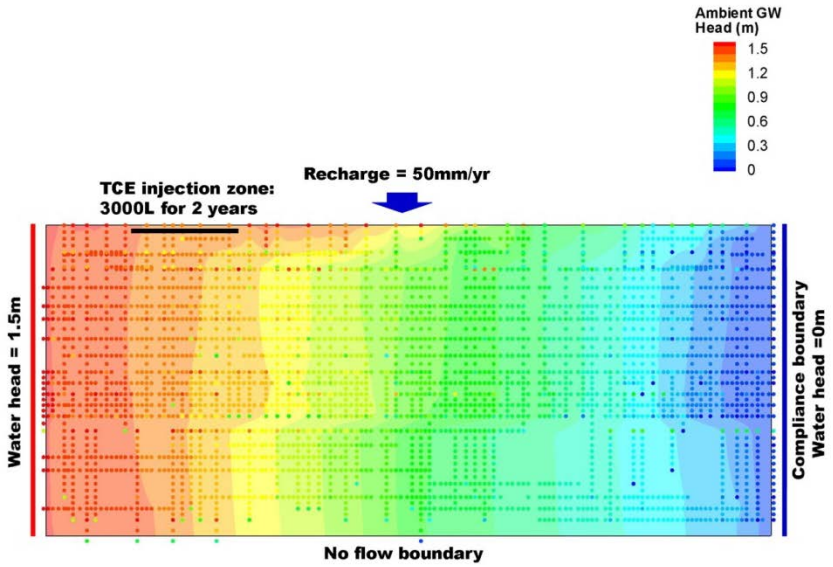

Figure 4.5.3: Initial and boundary conditions for TCE migration simulations.

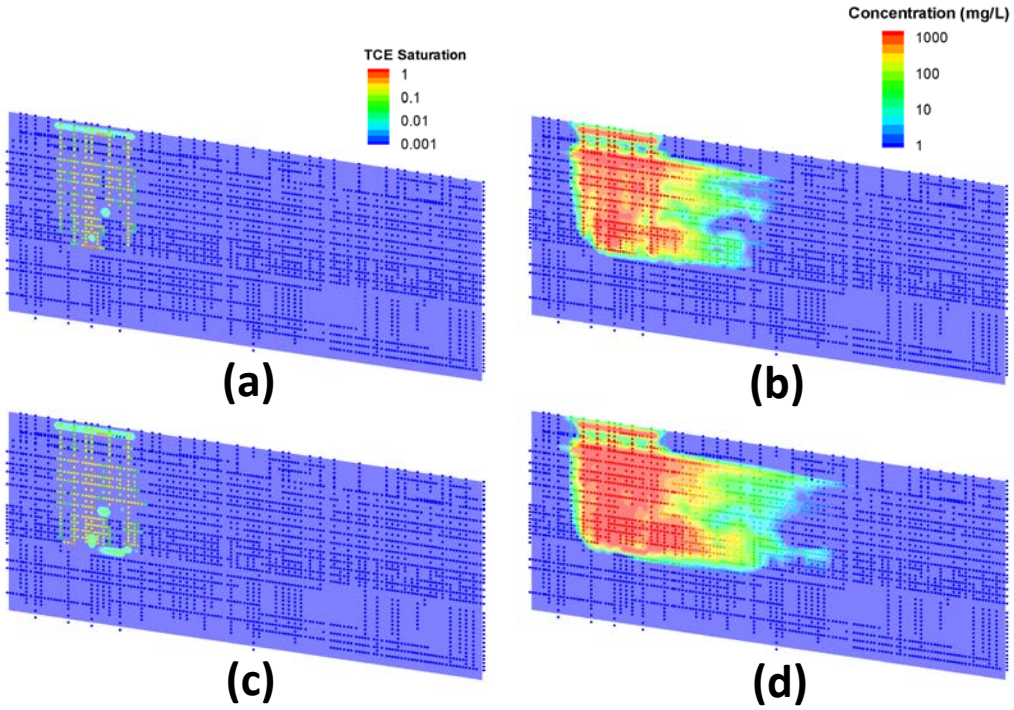

Figure 4.5.4: TCE saturation (a, c) and aqueous phase TCE concentration (b, d) distributions at t=1 yr (a, b) and t=2 yr (c, d).

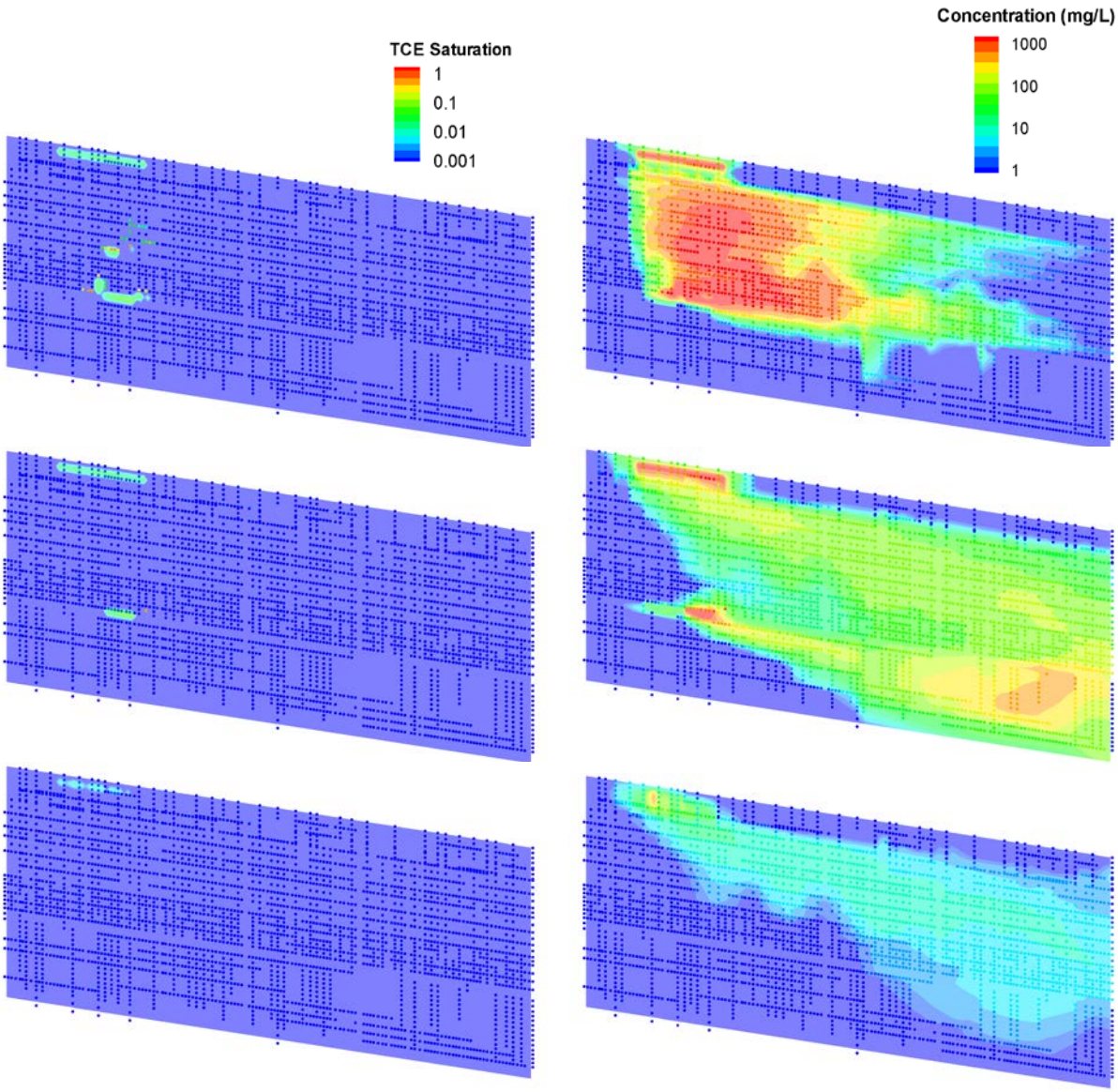

Figure 4.5.5: TCE saturation (left) and mole fraction (right) distributions at t = 5 yr (upper), t = 50 yr (middle), and t = 500 yr (lower).

Figure 4.5.6 shows the evolution of the TCE mass over time in terms of equivalent volume. The results in Figure 4.5.6 confirm that the nonaqueous phase TCE introduced into the system was slowly dissolved and migrated downgradient over hundreds of years. It is noted that most of the TCE injected (96.6 %) remained in the matrix blocks at the end of the injection period (t=2 yr) either in aqueous or nonaqueous phases. Note also the double peak in maximum TCE concentrations in the matrix at the compliance boundary in Figure 4.5.7 around year 50. This reflects the penetration of greater concentrations of TCE into the matrix of the less permeable layer of tight dolostone at depth, as seen in Figure 4.5.5 (middle right diagram).

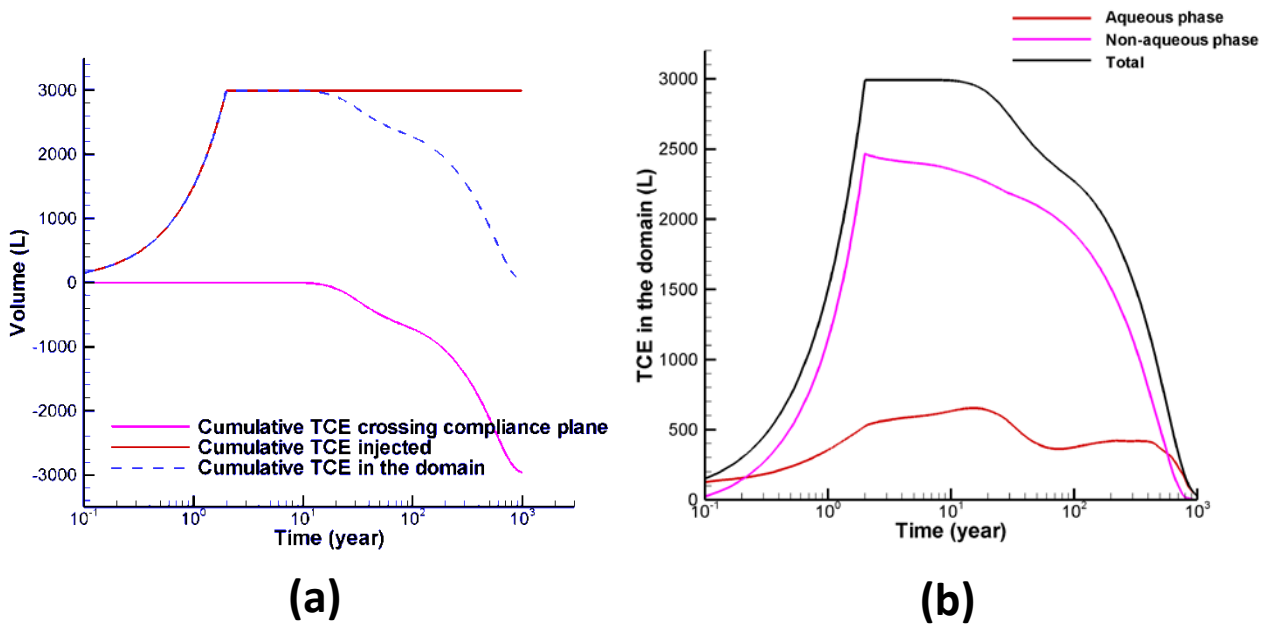

Figure 4.5.6: (a) Cumulative TCE volume injected, crossing the compliance boundary, and quantity remaining in the domain over time, and (b) TCE volume in the domain in aqueous and nonaqueous phases.

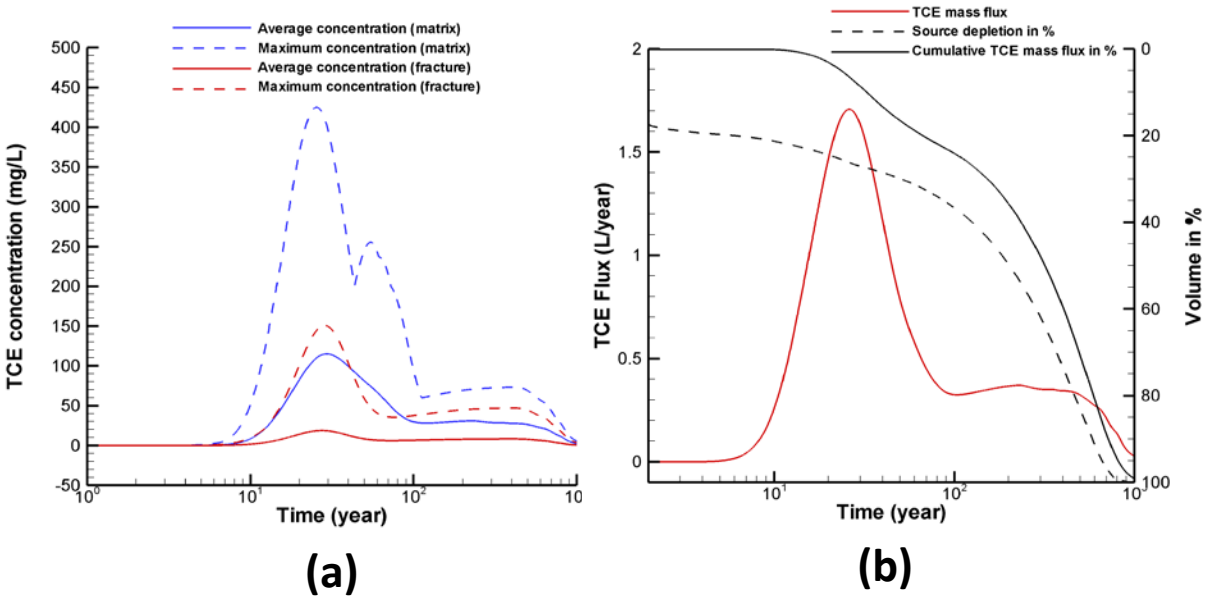

Figure 4.5.7: (a) Average and peak TCE concentrations at the downstream compliance boundary and (b) the TCE source depletion and mass flux in the compliance boundary.

4.5.3 TCE concentration and mass flux at the compliance boundary

Figure 4.5.7 shows the average and maximum TCE concentrations at the compliance boundary and also the TCE mass crossing the boundary over time. Although the concentrations and the flux peaked at t~30 yr, it is observed that significantly high concentration and mass flux are maintained for hundreds of years since the source depletion (dissolution) was slow.

Maji and Sudicky (2008) evaluated the efficiency of partial source-zone remediation by examining the relation between fractional mass reduction and fractional flux reduction. Similarly, in this study we examined the relationship between the percent source depletion and the mass flux relative to the maximum after the time of peak mass flux at the compliance boundary (Figure 4.5.8). The result shown in Figure 4.5.8 clearly illustrates that TCE flux can be significantly lowered (by about 80 %) with the depletion of about 10 % of source zone DNAPL.

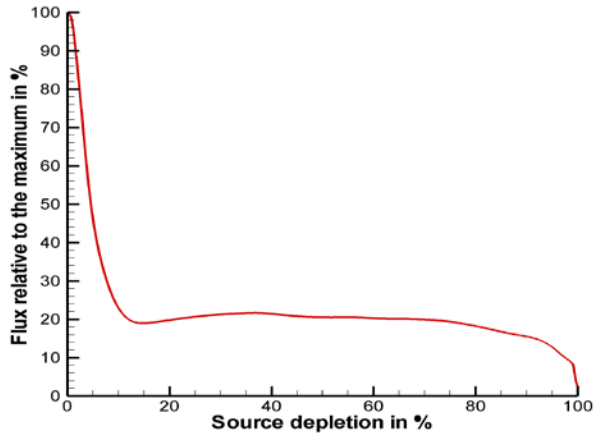

Figure 4.5.8: Percent source depletion versus relative mass flux at the compliance boundary.

TASK 4: ANALYSIS OF COMPOUND-SPECIFIC STABLE HYDROGEN ISOTOPES

4.6 Refinement of analytical techniques to analyze compound-specific hydrogen of chlorinated Solvents: Introduction

Analytical techniques to evaluate stable carbon and chlorine isotopic signatures in a variety of organic compounds are well established (e.g. Hunkeler and Aravena, 2000; Shouakar-Stash et al., 2006). The ability to combine more than one isotopic tool (e.g. carbon and chlorine compound-specific isotopic analysis) has created a new two dimensional powerful tool (Shouakar-Stash et al., 2006). Together, these techniques can be used to discriminate between sources, degradation pathways and the extent and differences between abiogenic and biogenic processes.

Shouakar-Stash et al. (2003) carried a column experiment to dechlorinate tetrachloroethylene (PCE) to TCE using iron. The results showed that the dechlorination products (TCE) have completely different hydrogen isotope ratios than the manufactured TCEs. Compared to the positive values of δ2H in manufactured TCEs (larger than +470 ‰), the dechlorinated products had very depleted δ^2H (less than -300 ‰). This finding has strong implications for distinguishing dechlorination products (PCE to TCE) from manufactured TCE. In addition, the results of this study show the potential of combining $^2H/^1H$ analyses with $^{13}C/^{12}C$ and $^{37}Cl/^{35}Cl$ for isotopic fingerprinting applications in organic contaminant hydrogeology. Although the application of hydrogen stable isotopes is proved to be very useful, analytical limitations prevented the findings from the laboratory experiment to be tested in the field and subsequently delayed its application to real life field studies.

The current techniques for hydrogen isotopes are not sensitive enough to be used in analyzing field samples. In particular, the old detection limit was around 2000ppb for TCE and it was an offline methodology (i.e. not an Online Compound-Specific Isotope Analysis Technique). Therefore, it is critical to develop a new methodology based on an online methodology with lower quantification limits (ppb level) to analyze compound-specific hydrogen of chlorinated solvents. This will allow for the application of compound-specific hydrogen, carbon and chlorine isotopes in field studies, including delineating different plumes, investigating the fate of plumes, monitoring degradation rates and also studying degradation mechanisms (pathways) and assessing the usefulness of isotopic 'fingerprinting' in matrix diffusion of DNAPL's.

The objective of this study is to develop a new compound-specific hydrogen isotope analysis methodology. The new methodology will be validated by conducting a comparison analyses on several standards by the means of the conventional methodology described in Shouakar-Stash et al. (2000) and Shouakar-Stash et al. (2003) proposed analytical technique will be based on purge-and-trap system.

4.6.1 Methodology

The following chemical compounds were used in this task: tetrachloroethene (PCE) (C_2Cl_4), trichloroethene (TCE) (C_2HCl_3), cis-dichloroethene (cis-DCE) ($C_2H_2Cl_2$). Several standards of these compounds that come from different suppliers were used to insure considerable isotopic ranges of $\delta^{37}Cl$ and δ^2H.

The following items were used during the analysis procedure: 60 mL clear vials, 27 x 135 mm (Chromatographic Specialties Inc., cat # C85B75960); tegrabond disc (septa), 125/10 MIL

silicone/teflon, 22 mm (Chromatographic Specialties, cat # C8812122M); PTEF stir bars, diameter 4 mm, length 12 mm (Fisher Scientific [Fisherbrand], cat # 14-511-60A); open top cap, 24-400 thread, polypropylene (Chromatographic Specialties, cat # C85169624G); Chromium (Cr) powder (200 micron, 99.0+%) (Goodfellow, cat# CR006020/2); Thick wall quartz tube (1/4" OD, 1/16" ID); A DB-5 gas chromatographic column (30 m x 0.250 mm, 0.25 microm film thickness from J & W Scientific Inc., cat # 1225032) for the separation of organic compounds; SPME fiber (75um Carboxen-PDMS for Merlin Microseal™, 23 gauge needle Manual holder from Supelco, cat # 57344-U) for the extraction of organic compounds from aqueous solution; SPME injection sleeve (0.75 mm ID, Supelco, cat # 2-6375,05) is used as an inlet liner. Therm-O-Ring™ Seals 1/4'' (Supelco, cat # 21004-U); and 11 mm Thermolite® septa are used for the GC inlet (RESTEK, cat # 20365).

4.6.1.1 Instrumentation

A continuous flow-isotope ratio mass spectrometer (CF-IRMS) coupled with a gas chromatograph (GC) and a reduction system (R) was utilized to perform this analysis. An Agilent 6890 GC equipped with split/splitless injection inlet and DB-5 capillary column was used to separate the various organic compounds present in aqueous solutions. Once separated, all compounds were converted to hydrogen gas by the means of the reduction system and then various hydrogen gas pulses were introduced to the CF-IRMS. A Delta plus XL (from ThermoFinnigan, Bremen, Germany) CF-IRMS was used to perform the isotopic measurements of hydrogen stable isotopes (δ^2H) by Faraday cups that are dedicated for m/z 2 and 3.

4.6.1.2 Metal Reduction Selection

The new methodology for the hydrogen stable isotope ratio determination of chlorinated compounds utilizes chromium as a reducing agent to produce hydrogen gas that can be analyzed by CF-IRMS. During the development of this analytical methodology, several metals (platinum, chromium, magnesium, metal alloys) were tested before considering chromium as the best reduction agent. The "200 micron Goodfellow" Cr powder was selected, based on its reduction yield and precision. The other metals/alloys did not produced low yields and/or poor reproducibility.

4.6.1.3 Sample Analysis

The δ^2H values of chlorinated organic compounds were measured using the Faraday cups on the positive ions m/z = 2 and 3. The positive masses result from the hydrogen molecules losing an electron in the source and then the ions get separated according to their mass to charge ratios (m/z). Finally, they are collected in the corresponding Faraday cups 2 and 3.

The hydrogen isotopic compositions are reported in permil (‰) deviation from isotopic standard reference material using the conventional δ notation.

The δ^2H values were calibrated and reported relative to the reference material, Vienna Standard Mean Ocean Water (VSMOW). Whereby $\delta^2H_{VSOMW} = 0‰$ (Coplen, 1996).

The sample analysis consists of the following steps: 1) Sample preparation and this involve diluting the samples to a concentration of 500 µg/L for the desired compound(s). Samples are prepared in 60 mL VOC type vials with a 5 mL headspace; 2) Extracting organic compounds from the aqueous solution by the means of SPME fiber. The extraction process lasts for 20 minute. 3) Injection of the organic compounds on the capillary column in order to separate the various compounds present in the sample. The injection takes place by a thermal desorption of

the organic compounds of the SPME in the split/splitless injection inlet at 270°C. The mode of the injection inlet was set at a splitless mode in most of the analyses that were performed in this study. However, this can be adjusted based on concentrations of the samples that are measured; 3) Directing the separated compounds into the reduction system in order for the various compounds to produce hydrogen gas before they are introduced into the IRMS. The outflow from the GC is controlled throughout the run where it is vented before and after the retention time of the desired organic compounds to the waste vent in order to avoid the introduction of undesired compounds into both the reduction system and the IRMS; 4) Finally, the measurement of the isotopic ratios of the hydrogen gas pulses introduced one after the other from the reduction system by the means of CF-IRMS.

4.6.1.4 Standards

A set of standards is prepared daily and added to every batch. At least two standards with two distinct isotopic ratios are added to every run. The two standards are prepared at different concentrations in order to correct for the linearity effect associated with the method. For example for the TCE analyses, IT2-1001 and IT2-1003 TCE standards are utilized in every batch. The isotopic compositions of these two standards are 467 and 682 ‰, respectively. The range of over 200 ‰ of these two standards provides a reasonable isotopic bracket when analyzing TCE samples.

4.6.2 Results and Discussion

4.6.2.1 Blank

To determine the contribution of masses 2 and 3 from the background and the materials used during the standard/sample preparation, different blanks were examined. Injections from evacuated vials and from vials filled with air were test and both masses 2 and 3 were below detection limits. On the other hand, the results obtained from the aqueous blanks where only ultrapure water (milli-Q water, resistivity $\leq$18 MΩcm) was used followed by an extraction by direct-SPME and headspace-SPME methods showed a detectable peak for water. This means that a measurable amount of water is being adsorbed on the SPME fiber during the extraction of organic compounds. The amount of co-desorbed water is much higher in the direct-SPME compared with the headspace-SPME extraction. This phenomenon did not have an effect on the accuracy of the isotopic composition of chlorinated solvents as water was separated from other organic compounds by the GC column. However, they did have an effect on the quantification limits of the methodology.

To avoid contamination due to carry over between consecutive samples, SPME fiber is baked between samples.

4.6.2.2 Method Calibration and Accuracy

The accuracy of the new methodology was confirmed and calibrated by analyzing several chlorinated solvent standards by the conventional off-line technique described in Shouakar-Stash et al., (2000) and the modifications added in Shouakar-Stash et al. (2003). The outcome results from the conventional method were then compared with those obtained from the current new methodology.

Briefly, the conventional method involves the following steps: 1) injection of a 10 µL of pure phase standard (TCE IT2-1001) into a 25cm long quartz tube filled with approximately 2

grams of manganese metals. The injection is performed on a vacuum line and by the means of liquid nitrogen to freeze organics down during the break sealing of the quartz tubes; 2) baking the quartz reaction tubes in a furnace for 5 hours at 900^{o}C to produce hydrogen gas; 3) analyzing of hydrogen gases by the means of IRMS coupled with an Elemental Analyzer (EA-IRMS). Manganese is used as a reducing agent and reduces the compounds to produce hydrogen gas.

Table 4.6.1 demonstrates a comparison of the results obtained from analyzing two TCE standards (IT2-1001 and IT2-1003) and two cis-DCE standards (IT2-1010 and IT2-1011) by the conventional and the new methodology.

Table 4.6.1: Comparison between the hydrogen isotopic results obtained from the two methods: a) the conventional (off-line) and b) the current compound-specific isotope analysis (CSIA) (on-line) measurement results.

	Conventional Off-line			Current CSIA Online		
Compound	δ^2H_{VSMOW} (‰)			δ^2H_{VSMOW} (‰)		
	n	Average	Standard Deviation	n	Average	Standard Deviation
IT2-1001 (TCE)	5	467	10	6	464	5
IT2-1003 (TCE)	5	682	12	6	682	6
IT2-1010 (cis-DCE)	5	434	13	6	430	6
IT2-1011 (cis-DCE)	4	646	10	6	645	7

The comparison of the isotopic results obtained for the two methods (Table 4.6.1) indicate that the new methodology provides an excellent accuracy over a range of 250‰ for δ^2H. The external precision of the CF-IRMS CSIA methodology is better than ±7 ‰ (Table 4.6.1) and it is slightly better than the precision achieved from the off-line EA-IRMS method.

4.6.2.3 Linearity

A linearity (peak intensity dependency) test of the technique was performed and the results showed a dependency between the peak intensity and the delta value of the standard. This relationship is best expressed in a polynomial (second order) regression line.

The dependency between the two parameters increases with the decrease of the peak areas. This dependency is generally small and within the analytical uncertainty when samples and standards are analyzed within 1 volts of peak intensity. However, when the peak intensity varies dramatically (larger than 1 V) a linearity correction is necessary to achieve accurate results.

Therefore, standards at various concentrations are included in every run to utilize them for the linearity correction.

4.6.2.4 Quantification limits

Although the method has a low detection limit (lower than 50 ppb). However, the quantification limit, where results are obtained with an acceptable accuracy and precision, is 400 ppb. Standards and samples with concentrations below 400 ppb produce isotopic values with poor precision.

TASK 5: BATCH AND COLUMN EXPERIMENTS

4.7 Introduction

In the last 10 years, compound-specific carbon stable isotopes have been increasingly used as an indicator of chemical and biological degradations of chlorinated solvents in groundwater (e.g. Hunkeler et al., 1999; Sherwood Lollar et al., 1999; Elsner et al., 2007). More recently, compound-specific chlorine stable isotopes are being used to investigate the behavior of these compounds (Shouakar-Stash et al., 2006; Abe et al., 2009). In order to accurately interpret isotopic data obtained for chlorinated solvents in groundwater systems, the isotopic effects of subsurface processes must be well understood. The majority of the previous studies that used compound-specific stable isotopes (mainly carbon isotopes) to distinguish different plumes (i.e., fingerprinting) and trace them back to the release source point (e.g. Hunkeler et al., 2004; Chartrand et al., 2005) assumed that isotopic fractionations associated with physical processes such as sorption and diffusion are negligible. These assumptions were based on studies conducted on carbon stable isotopes (e.g., Slater et al., 2000). In this study batch and column experiments are conducted to determine fractionation factors for carbon, chlorine and hydrogen isotopes as TCE undergoes processes of sorption, desorption, and degradation (both abiotic and biotic).

4.7.1 Batch Experiments

Several batch experiments have been conducted to investigate the effects of TCE sorption to different media on its carbon and chlorine isotopic composition. Carbonate, shale, activated carbon, and four different sands (Ottawa Sand, 4030 Sand, F75 Sand, and Borden Sand) have been used as sorption media and these results were presented in part in last year‘s interim report. Additional batch experiments have been conducted in preparation for the sandbox laboratory experiment (Task 6) to observe the isotopic effects of abiotic degradation on TCE and its daughter products. For the sandbox experiment, the use of anaerobic bacteria to study isotopic trends during the biotic degradation of TCE is unlikely because it will be difficult to maintain the appropriate conditions in such a large tank. Therefore, batch experiments were designed to examine the use of zero-valent iron as a surrogate to cause TCE degradation (abiotic) and isotope fractionation.

4.7.1.1 Methodology

Two sets of batch experiments were done using two different iron types, Peerless and Connelly. The initial TCE concentration was 300 ± 20 ppm. Water samples were collected after 0.5 hr, 1 hr, 6 hr, 1 d, 2 d, 3d, 5d, 7d, and 14 d and analyzed for TCE concentration and 37Cl isotopes.

4.7.1.2 Results and Discussion

Changes in TCE concentration during degradation on Peerless and Connelly zero-valent iron are illustrated in Figures 4.7.1 and 4.7.2, respectively. There was a general decrease in TCE concentration over time for both types of iron, but more TCE was degraded on the Peerless than the Connelly iron. The two week period was not long enough to observe complete degradation of all the TCE in either batch. Changes in the isotopic signature δ37Cl are presented in Figures 4.7.3 and 4.7.4. For both experiments the solution became enriched in heavier chlorine isotopes over the duration of the experiment. The isotopic shift observed was ~ 0.3 ‰ for the Peerless

iron and ~0.7 ‰ for the Connelly iron. Despite more degradation appearing to occur on the Peerless iron, a greater isotopic shift was observed on the Connelly iron.

The problem with using zero-valent iron is that the experiment imitates a remediation technique rather than the natural attenuation and biodegradation of TCE. Another option for the sandbox could be the addition of Fe-bearing minerals such as goethite or pyrite, which naturally exist in some sandy aquifers and can cause isotope fractionation. More research needs to be done on this issue and, if necessary, a batch or column experiment should be conducted prior to the main experiment.

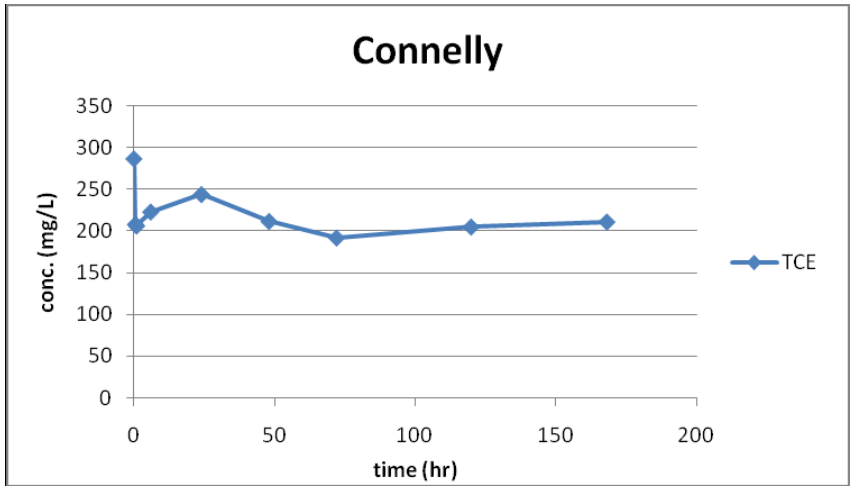

Figure 4.7.1.1: TCE concentration results for Connelly iron.

Figure 4.7.1.2: TCE concentration results for Peerless iron.

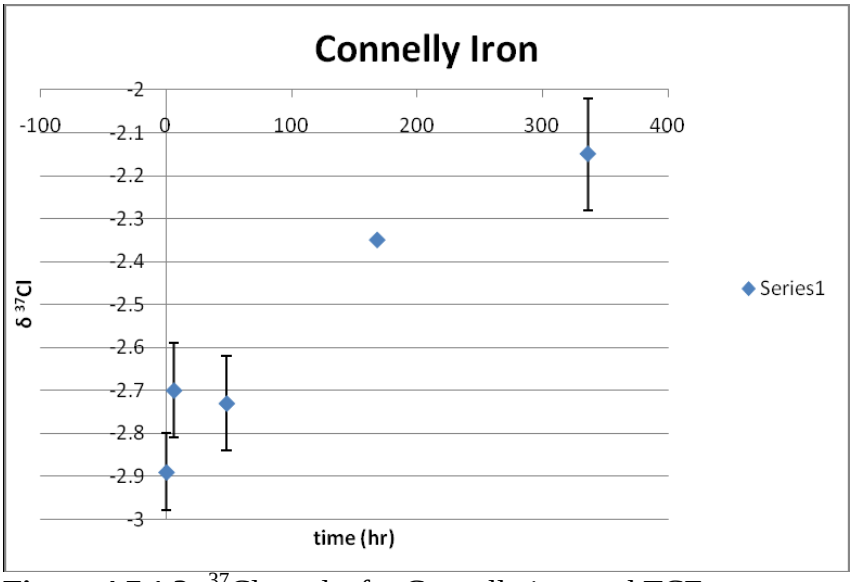

Figure 4.7.1.3: ^{37}Cl results for Connelly iron and TCE.

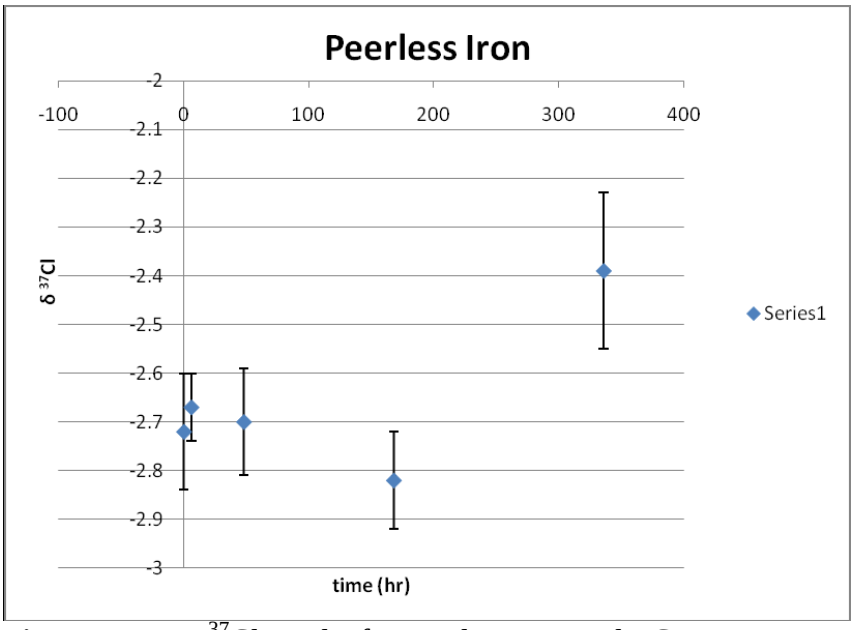

Figure 4.7.1.4: ^{37}Cl results for Peerless iron and TCE.

4.7.2 Laboratory Column Experiment: The Effect of Sorption on ^{37}Cl and ^{13}C Isotope Fractionation

During the last decade, compound-specific isotope analysis (CSIA) has emerged as one of the most useful techniques in the determination of organic contaminants sources as well as understanding the transformation mechanisms of these contaminants in the subsurface (van Warmerdam et al., 1995; Hunkeler et al., 2004; Chartrand et al., 2005; Morrill et al. 2005).

There are a number of subsurface processes such as degradation, dissolution, sorption, diffusion, and volatilization that might cause isotopic fractionations. However, there is a general acceptance that physical processes are usually associated with the least isotopic fractionations and in some cases these isotopic fractionations can be negligible when compared with the analytical uncertainties of some of the current analytical methodologies (e.g. Schüth et al. 2003, Hunkeler et al., 2004). This conclusion is based on carbon isotopes fractionation of TCE and to our knowledge, the effect of physical processes on chlorine isotope fractionation has not been investigated yet. The current study focuses on determining the effect of sorption and desorption of TCE on chlorine stable isotopes.

4.7.2.1 Methods and materials

Since sorption of TCE depends on the organic carbon content (f_{oc}) of the soil (Karickhoff et al. 1979, Shwarzenbach and Westall, 1981), three different media containing various amounts of organic carbon were chosen for this study. The first column (C2) contained Ottawa silica sand with no organic carbon content. The Ottawa silica sand is a coarse grain sand with no organic carbon content (as the sand is made of nearly pure quartz sandstone, it has been assumed that the organic carbon content is zero).The second column (C3) consisted of Borden sand with small organic carbon content. Borden sand is fine-to medium-grain sand with an average organic carbon content of 0.02% (MacKay et al. 1986). The last column (C6) contained a mixture of Borden sand and 1% (by volume) granular activated carbon (GAC). The organic carbon content for column C6 was calculated to be 0.28%.

C2 and C3 columns were constructed of Plexiglas, while C6 was constructed of stainless steel. The Plexiglas columns have a diameter of 5 cm and a length of 50 cm. The stainless steel column has a diameter of 10.3 cm and a length of 15.4 cm. The sampling ports are placed vertically along the column with 2.5 cm and 2.4 cm for Plexiglas and stainless steel columns, respectively (Figure 4.7.2.1). In order to sample the column at the center, 16 gauge airtight needles were placed into the column halfway through Nylon Swagelok installed on the columns wall. The needles were filled with silica fibre which acts as a filter to prevent sand grains blocking the needle.

The physical properties of the columns were calculated by measuring the mass of the empty columns; and then measuring the mass of the columns again when they were filled with dry soil; and measuring the mass of the column once again when they were saturated (Table 4.7.2.1). Two stainless steel screens (1 mm and 0.2 mm mesh sizes) were placed at either end of each column to contain the porous medium. Once all columns were packed with sand, they were flushed with CO_2 gas for ~90 minutes to remove air bubbles trapped in the pores and then slowly wetted from the bottom with ultra-pure water using a peristaltic pump. Once a steady outflow rate was obtained (~400 mL/day), columns were flushed with sodium azide solution (2 g/L) for a few days to maintain abiotic conditions in the columns. Eh, pH, and dissolved oxygen (DO) of outflow water were monitored to ensure that stable and oxic conditions were maintained. Experiments were conducted at room temperature (~22˚C).

a)

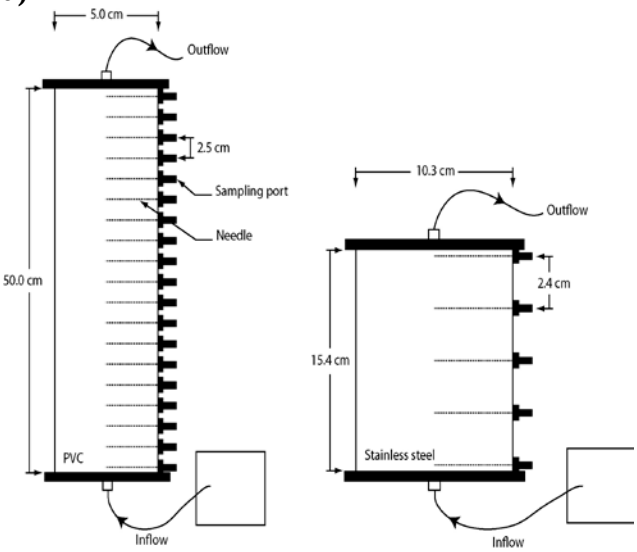

b)

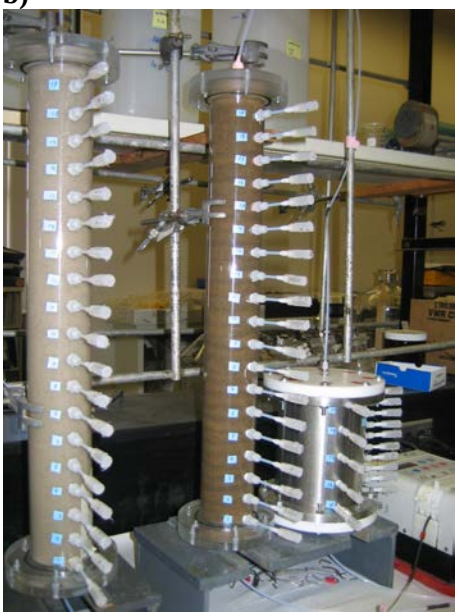

Figure 4.7.2.1: a) Columns design; the Plexiglas column (left) and the stainless steel column (right); b) from left to right: C2 (Ottawa sand column), C3 (Borden sand column), C6 (Borden sand + activated carbon.

Table 4.7.2.1: Physical properties of the columns

Column ID	Type of Medium	Porosity	Dry Bulk Density (g/cm^3)	Volume of pores (ml)
C2	Ottawa sand	0.385	1.77	378
C3	Borden Sand	0.395	1.76	388
C6	Borden Sand + GAC	0.336	1.77	431.6

TCE solution was prepared at a concentration of ~5 ppm for C2 and C3, and at near-saturation (~1 000 ppm) for C6 since GAC is a strong sorbent. Stainless steel was used for the GAC column as it is more resistant to higher concentrations of TCE. The injection solution included was contained in a collapsible Teflon bag to minimize headspace. The TCE solution was injected into the column at a rate of ~400 mL/day and samples were obtained from the bag, selected sampling ports, and the column effluent using glass syringes and analysed for TCE concentration and isotopes (^{13}C and ^{37}Cl). The volume collected depended in part on the anticipated TCE concentration, but was generally 1 or 2 mL for concentration, and 1 mL and 2 mL for ^{37}Cl and ^{13}C isotopic analyses, respectively. In order to monitor the effect of desorption on isotope fractionation, once the outflow concentration reached the inflow solution concentration, the injecting solution was switched to ultra-pure water and liquid samples were collected for TCE concentration and carbon and chlorine isotopes analyses.

4.7.2.2 Analytical procedures

For TCE analysis, the aqueous samples were extracted using a pentane internal standard containing 500 µg/L of 1,2-dibromoethane at sample-pentane ratio of 1:1. The samples were placed in 5 ml glass screw-cap vials which contained pentane and then the vials were placed on a rotary shaker for 15 minutes at 300 rpm. Afterward, ~ 1 mL of the pentane was transferred to 2 mL glass crimp-top vials. Using Hewlett Packard 7673 liquid auto-sampler, a 1 µL sample was injected onto a DB-624 capillary column in a Hewlett Packard 5890 Series II gas chromatograph which was equipped with a ^{63}Ni electron capture detector (ECD). The detector temperature was 300 °C and the injection temperature was 200 °C. The column temperature was raised from 50 to 150 °C at a rate of 15 °C/min and then held for 1 minute. The carrier gas was pre-purified helium and the make-up gas was 5% methane and 95% argon.

Chlorine isotope ratios were analysed using a continuous flow-isotope ratio mass spectrometer (CF-IRMS) developed by Shouakar-Stash et al. (2006). The chlorine stable isotope results were reported as $\delta^{37}Cl$ which is defined as the difference between the measured ratios of the sample and reference over the measured ratio of the reference. The reference for chlorine isotopes is Standard Mean Ocean Chloride (SMOC).

Compound-specific carbon isotope ratios were determined in the Environmental Isotope Laboratory of the University of Waterloo using a gas chromatography-combustion-isotope ratio mass spectrometry (GC-C-IRMS) system (More details are provided by Hunkeler and Aravena, 2000). The carbon stable isotope results were reported as $\delta^{13}C$.The reference for carbon isotopes is the international standard Vienna Peedee Belemnite (VPDB).

4.7.2.3 Results and discussion

The concentration results are shown in Figures 4.7.2.2 to 4.7.2.4. Samples are taken from sampling ports 1, 11, and 20, from which port 1 is located at the bottom of the column and is closest to the TCE source solution. Port 20 is the column effluent which is the furthermost from the TCE source solution. The results for C2 and C3 show that a concentration plateau (that was close to the input TCE concentration) was reached for the C2 and C3 after injecting the columns with approximately 2 pore volumes of TCE solution. Since the residence time for the columns was about one pore volume per day, it can be concluded that the solute was not retarded due to sorption. However, the maximum TCE concentration at the outflow of C6 was achieved after injecting about 12 pore volume of TCE solution, while the residence time for C6 is approximately 1.5 pore volume a day. This is an indication of a significant sorption of TCE within C6.

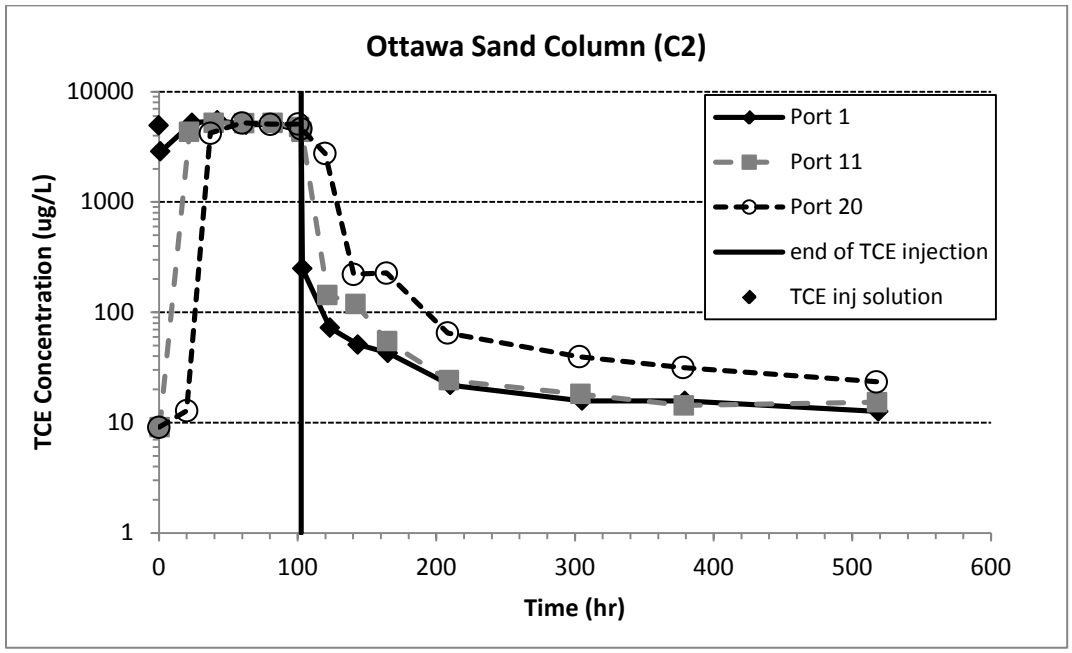

Figure 4.7.2.2: TCE concentration results for the Ottawa sand column.

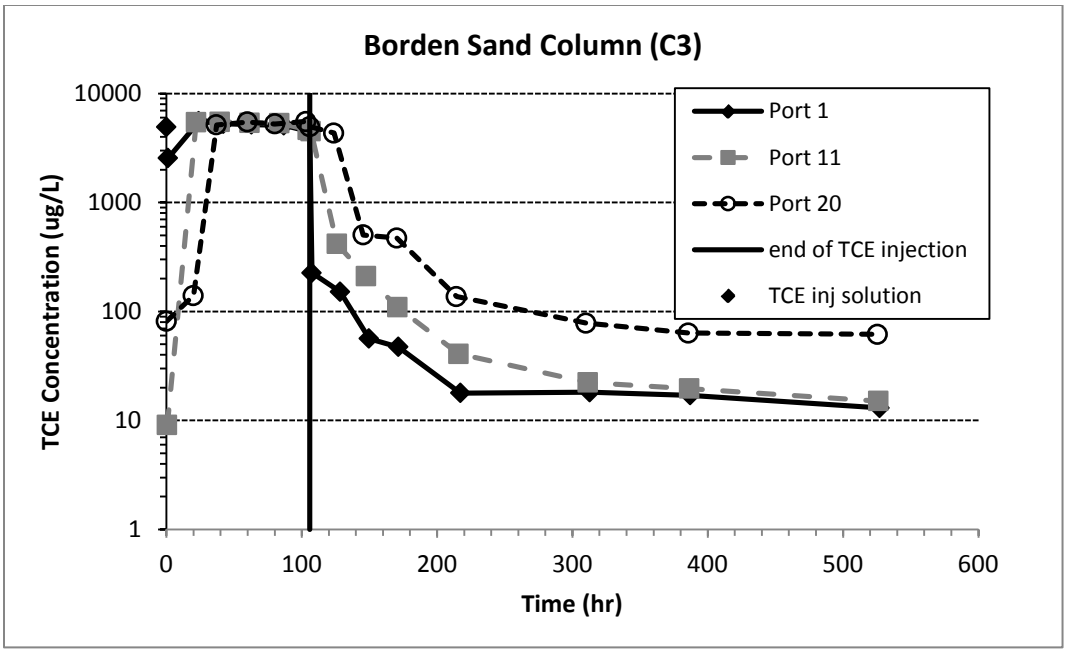

Figure 4.7.2.3: TCE concentration results for the Borden sand column.

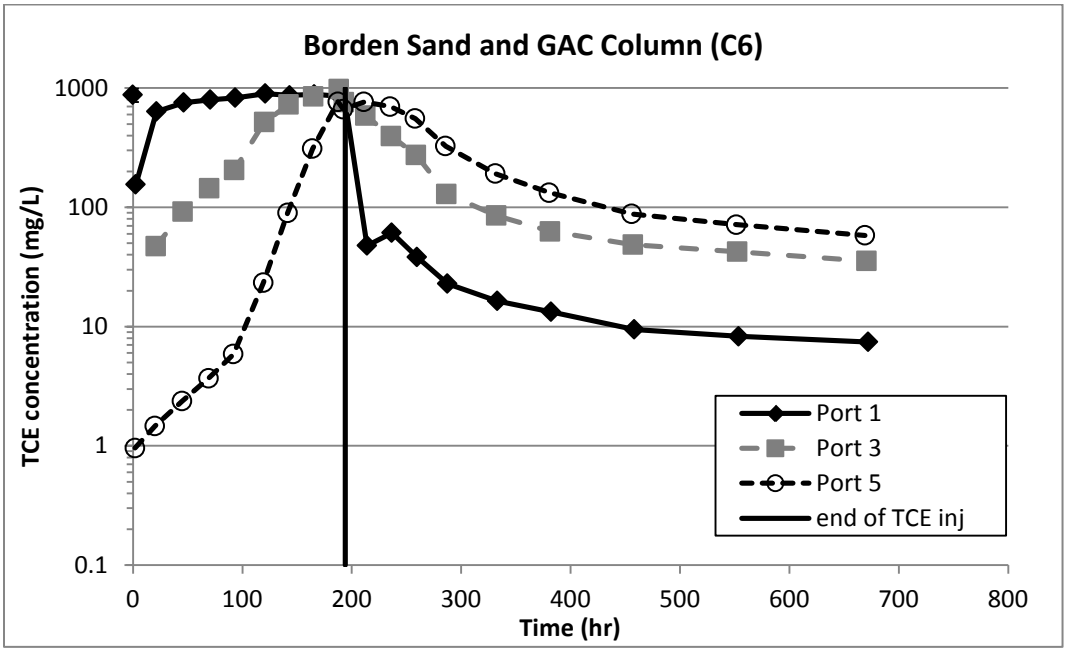

Figure 4.7.2.4: TCE concentration results for the Borden sand mixed with granular activated carbon column.

The results for ^{37}Cl and ^{13}C isotope are shown in Figures 4.7.2.5 to 4.7.2.10. The $\delta^{37}Cl$ and $\delta^{13}C$ values of the effluent samples are normalized to the $\delta^{37}Cl$ and $\delta^{13}C$ values of the source solution samples. We will consider port 20 in our discussions since samples taken from this point passed through the sand and had a chance to sorb to the material inside the columns. As can be seen in Figures 4.7.2.5, 4.7.2.7, and 4.7.2.9, the ^{37}Cl isotopes show enrichment in the early times which means that lighter isotopes are being sorbed and the remaining solution is enriched in

heavier isotopes. Once the column was flushed with clean water and desorption was happening, we see depletion of ^{37}Cl isotopes followed by a slight enrichment to the end of the experiment which indicates that there is a preference in isotopes being desorbed as well, such that lightest sorbed isotopes started to desorb and re-enter into the solution first and then slightly heavier sorbed isotopes are being desorbed. This trend becomes stronger from C2 to C3 to C6. The ^{13}C isotopes show enrichment during both sorption and desorption parts of the experiment (Figures 4.7.2.6, 4.7.2.8, and 4.7.2.10), but the values are very small considering the typical range of uncertainty for ^{13}C CSIA which is ±0.5‰.

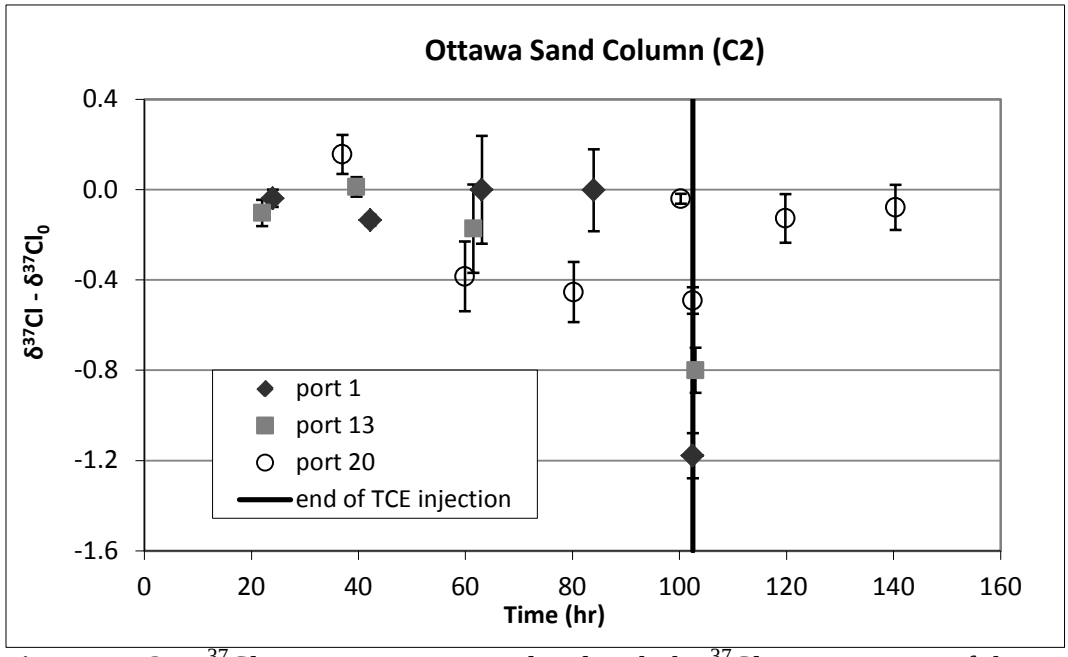

Figure 4.7.2.5: ^{37}Cl isotope ratios normalized with the ^{37}Cl isotope ratios of the source solution.

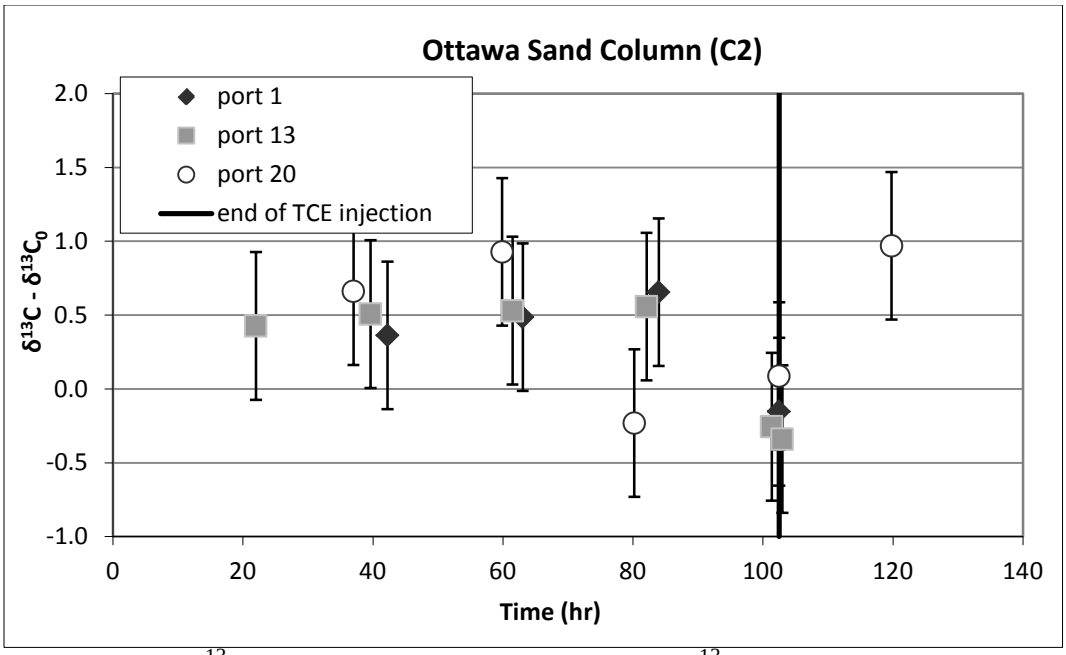

Figure 4.7.2.6: ^{13}C isotope ratios normalized with the ^{13}C isotope ratios of the source solution.

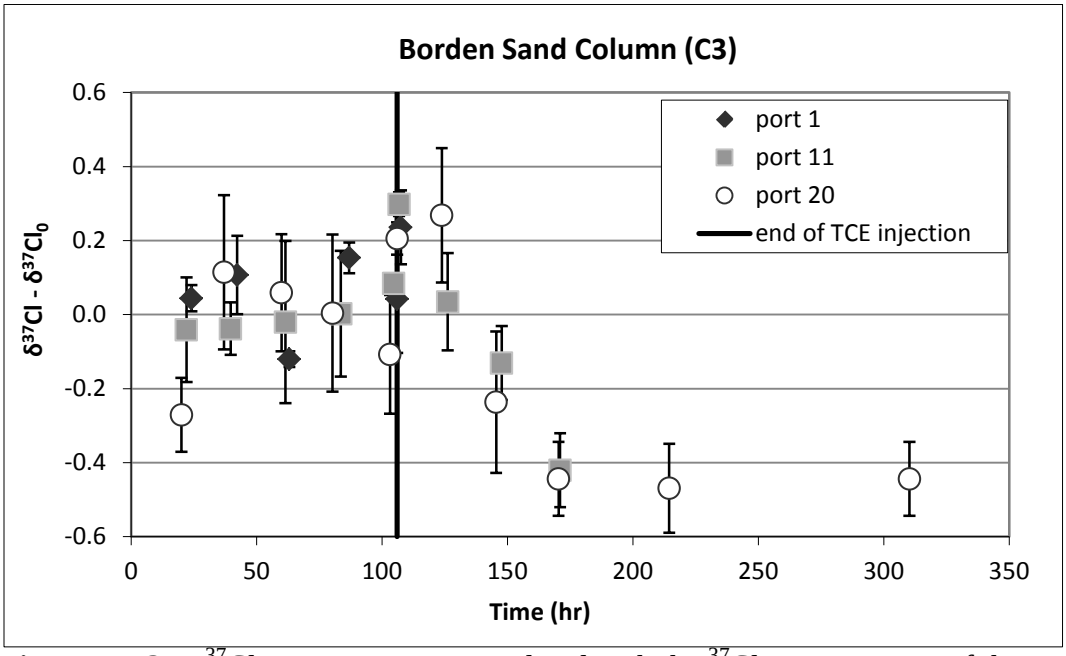

Figure 4.7.2.7: ^{37}Cl isotope ratios normalized with the ^{37}Cl isotope ratios of the source solution.

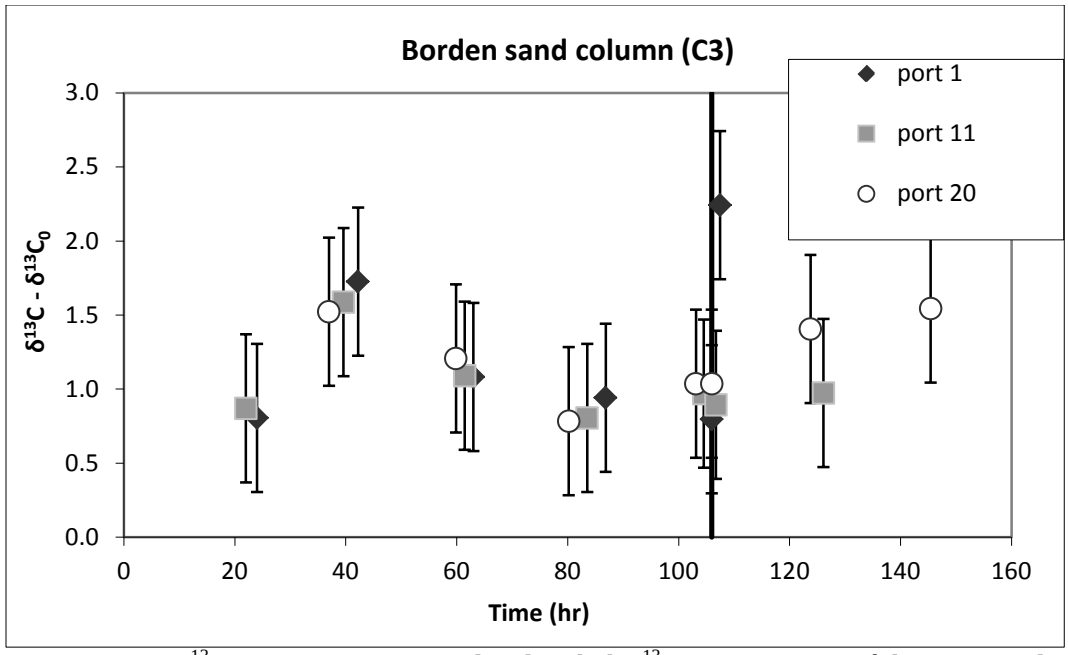

Figure 4.7.2.8: ^{13}C isotope ratios normalized with the ^{13}C isotope ratios of the source solution.

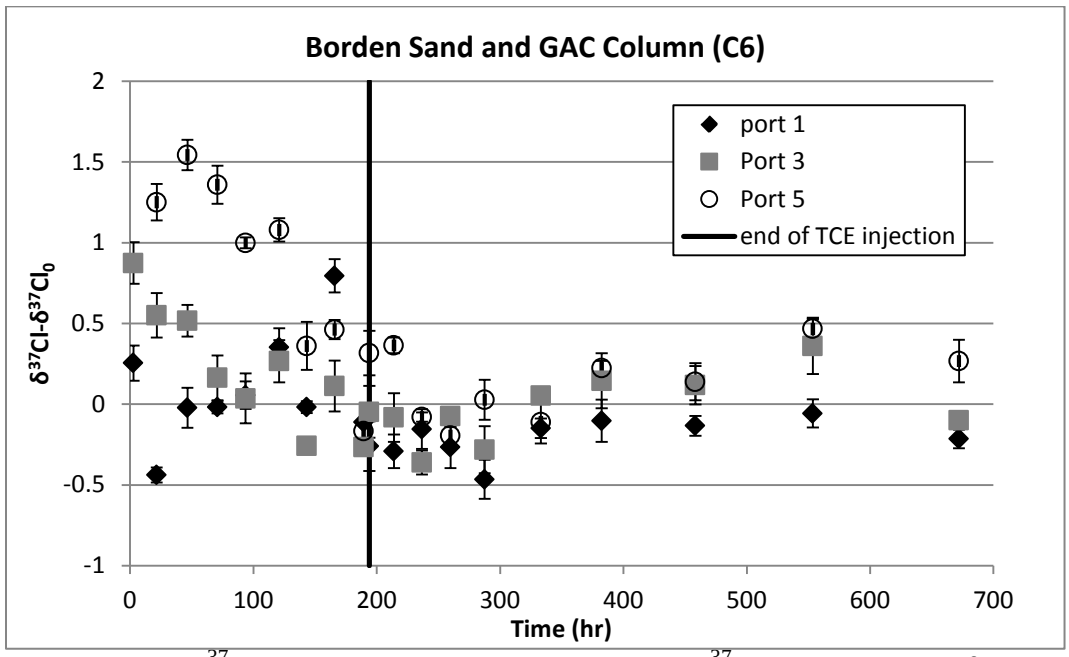

Figure 4.7.2.9: ^{37}Cl isotope ratios normalized with the ^{37}Cl isotope ratios of the source solution.

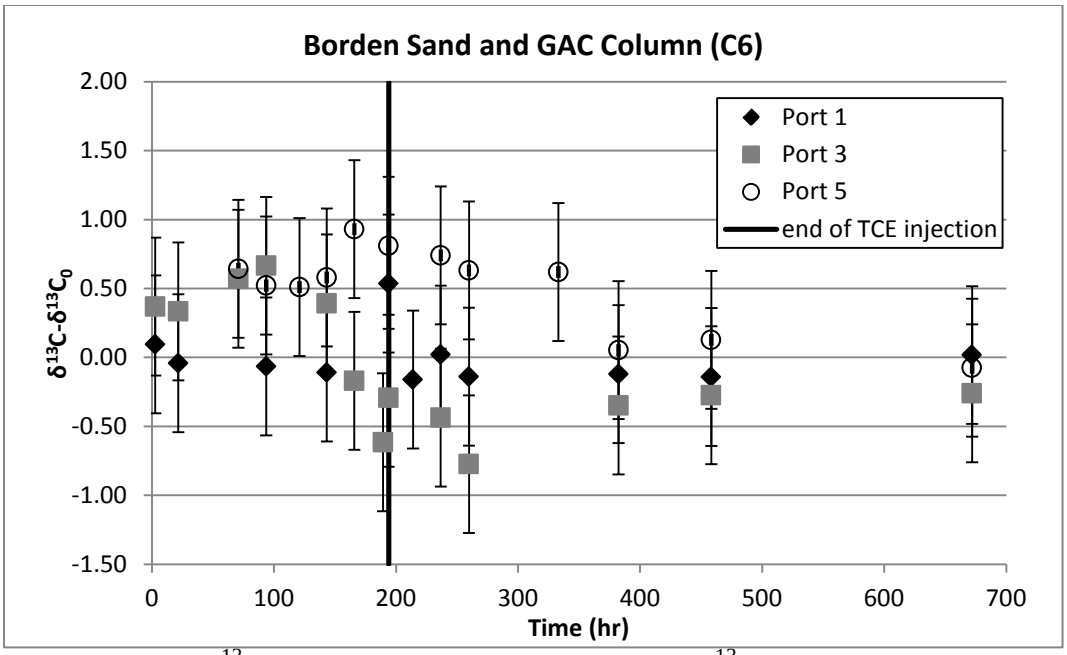

Figure 4.7.2.10: ^{13}C isotope ratios normalized with the ^{13}C isotope ratios of the source solution.

A summary of minimum and maximum isotopes ratios are provided in Table 4.7.2.2. As can be seen, ^{37}Cl isotopes fractionation is increasing as the fraction of carbon and therefore the rate of sorption is increasing (C6>C3>C2). However, ^{13}C isotope results do not show a specific trend and the fractionation is very small considering the analytical uncertainty for ^{13}C CSIA (±0.5‰).

Table 4.7.2.2: Maximum and minimum normalized values for $\delta^{37}Cl$.

Column ID	Min – Max $\delta^{37}Cl$ normalized values (‰)	Difference (‰)	Min – Max $\delta^{13}C$ normalized values (‰)	Difference (‰)
C2 (Ottawa sand)	-0.49 – 0.16	0.65	-0.23 – 0.97	1.2
C3 (Borden sand)	-0.47 – 0.27	0.74	0.78 – 1.54	0.76
C6 (Borden sand + GAC)	-0.19 – 1.54	1.84	-0.07 – 0.93	1.0

4.7.3 Laboratory Column Experiment: The Effect of Biodegradation on ^{37}Cl and ^{13}C Isotope Fractionation: Introduction

Several researchers have used Compound-Specific Isotope Analysis (CSIA) to verify biodegradation of chlorinated compounds (Hunkeler et al., 1999; Sherwood Lollar et al., 1999; Bloom et al., 2000; Sherwood Lollar et al., 2001; Slater et al., 2001; Chartrand et al., 2005; Morrill et al., 2005). Most of the studies to date have used carbon isotopes results. However, there is limited data available on chlorine and hydrogen isotopes (Sturchio et al., 1998; Shouakar-stash et al., 2003). The main objective of this column experiment is to examine the bacteria activity in different concentrations of TCE and also to investigate the effect of biodegradation on Cl, C, and H isotopes fractionation. The isotope results will be modeled using CompFlow model developed by Unger et al. (1995, 1996, 1998) and modified by Dr. Sudicky's research group to account for isotope fractionation. Hence, samples were taken from the column for TCE and by-products concentration analysis, ion chromatography, and stable isotope analysis. However, since the budget was limited, we were not able to analyze the samples for isotopes yet. We will provide our findings about the effect of different TCE concentration on bacteria activity.

4.7.3.1 Methods and materials

For this experiment, two identical Plexiglas columns (50 cm length, 5 cm diameter) were filled with US Ottawa sand (F-85). Then the columns were flushed with CO_2 for 90 minutes (to remove air from the pores inside the column) and were saturated with natural groundwater from North Campus Research Site (University of Waterloo, Waterloo, ON, Canada). Both columns were run at the similar conditions except for that one of the columns was inoculated with bacteria (C10) and the other one used as a control (C8). The bacteria used for this experiment is called KB-1 culture which was provided by SiREM Lab, Guelph, ON, Canada. KB-1 contains a type of Dehalococcoides (Dhc) capable of complete dechlorination of chlorinated ethenes to harmless ethene.

Since reductive dechlorination occurs in an anaerobic environment, de-oxygenated groundwater was used to make TCE solution for the experiment. In order to remove oxygen from North Campus groundwater, it was put in 5L glass bottles and sparged with nitrogen gas for eight hours prior to making TCE solution. Then, the water was spiked with certain amount of TCE to achieve desired TCE concentration. The TCE solution was transferred to collapsible Teflon bag (to minimize the head space) and was connected to the column from the bottom of the column. The Teflon bag was placed in a glove bag which was filled with nitrogen to minimize oxygen intrusion into the TCE solution through the Teflon bag (Figure 4.7.3.1).

Figure 4.7.3.1: TCE source solution in The Teflon collapsible bags which are placed in glove bags.

Resazurin which is an oxidation-reduction indicator was added to water which is blue when the water is saturated with oxygen (7ppm) and turns to pink when oxygen content of water is about 1ppm and turns colourless once there is no oxygen in water. The source TCE solution used for our experiment was pink always since the solution was exposed to air for a very short time while spiking with TCE and also during transferring the solution into the Teflon bag. Sodium lactate (60% syrup) was added to the TCE source solution as the electron donor. The amount of lactate needed was calculated based on the following stoichiometry equations:

TCE – lactate

$$C_3H_5O_3^- + 2C_2HCl_2 + 3H_2O \rightarrow 2C_2H_4 + 3CO_2 + 5H^+ + 6Cl^-$$

Sulfate – lactate

$$C_3H_5O_3^- + 3SO_4^- + 8H^+ \rightarrow 3H_2S + 6CO_2 + 6H_2O$$

Nitrate – lactate

$$C_3H_5O_3^- + 12NO_3^- + 17H^+ \rightarrow 6N_2 + 15CO_2 + 21H_2O$$

The lactate was added twice the amount calculated. In order to determine the hydraulic properties of the column, sodium bromide was added to the source TCE solution.

Prior to injecting TCE solution into the column, 13 mL of KB-1 was injected into C10 through sampling ports 4, 7, 11, and 14 in order to spread the bacteria and also reduce the medium since KB-1 contains nitrate and sulfate reducing bacteria that consume oxygen. The oxidation-reduction potential (ORP) of the column effluent was monitored three days after injecting bacteria which was reduced to from 171 mV prior bacteria injection to -83 mV. Once the reduced condition was maintained, 8 mL of KB-1 was injected into the column through the same ports as before followed by TCE solution injection from the bottom of the column using a peristaltic pump. Effluent and source solution samples were collected from both columns for anions concentration analysis including Br, nitrate, and sulfate; and chlorinated solvents

concentration analysis including TCE, DCE isomers, and VC, and H, Cl, and C isotopes analysis. In order to prevent bacteria moving to the TCE source solution, a media break was installed in the line between the source solution and the column (Figure 4.7.3.2).

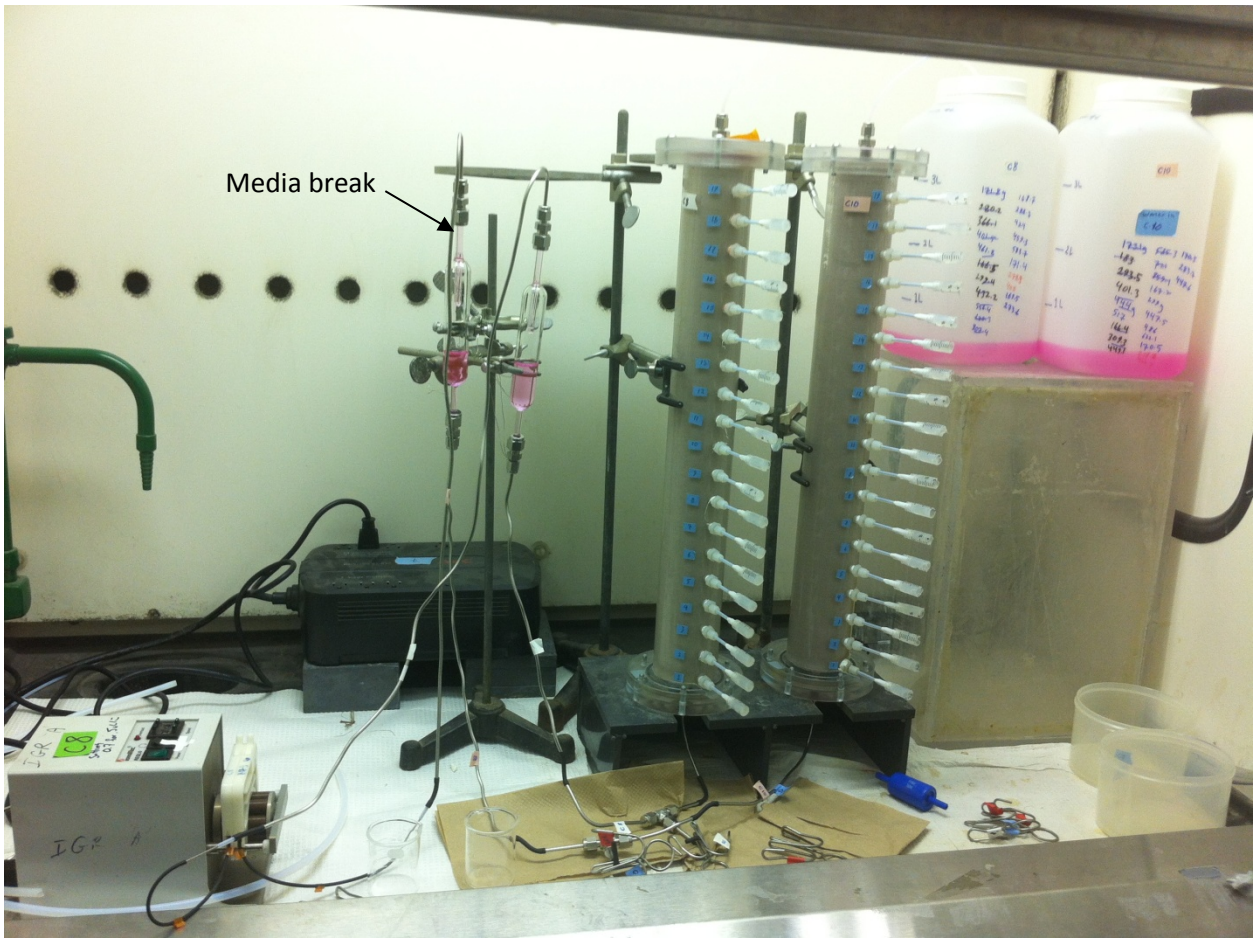

Figure 4.7.3.2: C8 (left) and C10 (right). A media break was installed in the line between the TCE source solution and the column to prevent movement of the bacteria from the column into the source solution.

4.7.3.2 Analytical procedures

For TCE analysis, the aqueous samples were extracted using a pentane internal standard containing 500 µg/L of 1,2-dibromoethane at sample-pentane ratio of 1:1. The samples were placed in 5 ml glass screw-cap vials which contained pentane and then the vials were placed on a rotary shaker for 15 minutes at 300 rpm. Afterward, about 1 mL of the pentane was transferred to 2 mL glass crimp-top vials. For analysis, the sample is placed on Hewlett Packard 7673 liquid auto-sampler. A 1 µL sample is injected onto a DB-624 capillary column in a Hewlett Packard 5890 Series II gas chromatograph which is equipped with a ^{63}Ni electron capture detector (ECD). The detector temperature is 300 °C and the injection temperature is 200 °C. The column temperature is raised from 50 to 150 °C at a rate of 15 °C/min and then is held for 1 minute. The carrier gas is pre-purified helium and the make-up gas is 5% methane and 95% argon.

For VC and DCE isomers, a headspace is created in the aqueous samples with a ratio of 16:4 mL headspace to aqueous sample. The samples are placed on a rotary shaker for 15 minutes to allow equilibration between the liquid and gas phases. Then the sample is placed on a CombiPal autosampler for analysis. A 1 mL samples is then injected onto an Agilent 5975C triple axis Mass Spectrometer operating in EI mode. The column is an RTX-1ms capillary column (30cm × 0.25cm ID × 1µm). The GC has an initial temperature of 50ºC, with a temperature program of 15ºC/min reaching a final temperature of 150ºC and then is held at 150ºC for one minute. The MS ion source is 230ºC while the MS quad is set for 150ºC and the injector temperature is 200ºC. The carrier gas is ultra-pure helium with a flow rate of 32 mL/min. The split ratio is 20:1 for the injector.

For anion analysis, 2 mL of sample was put in a 5 mL plastic Dionex IC autosampler vial. The sample is then placed on a Dionex AS-40 autosampler. A 25 uL sample was then injected onto a Dionex TCS-2000 Ion Chromatograph equipped with an Ion-Eluent Generator and conductivity detector. A Dionex IonPac AS18 column (4 x 250 mm) was used. The mobile phase, 30 mM KOH at a flow rate of 1.0 mL/min was used.

4.7.3.3 Results and Discussions

4.7.3.3.1 C10

The concentration of source TCE solution was about 500 mg/L. Sodium bromide was added to the solution as a conservative tracer. The ORP of the column effluent was -95 mV at the time TCE source solution was connected to the column. Effluent samples were taken frequently for chlorinated solvents and anions (Br, NO_3^-, SO_4^{2-}) analysis for the first 3 days to capture the break-through curve. The tracer test result for C10 is shown in Figures 4.7.3.3. The code ONED_1 (Christopher J. Neville, 2001) was used to find the best-fit to the experimental data. The best-fit parameters are listed in Table 4.7.3.1.

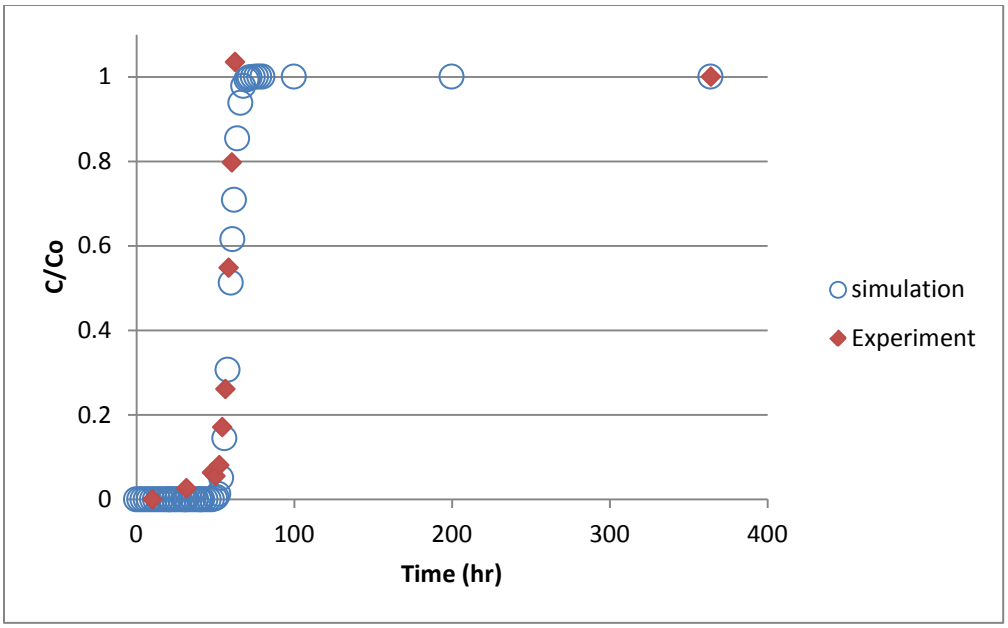

Figure 4.7.3.3: C10 conservative tracer test and simulation results using ONED_1 program

Table 4.7.3.1: Hydraulic parameters of C10.

Column ID	Darcy Velocity, q (cm/hr)	porosity	Longitudinal Dispersivity (cm)
C10	0.2	0.24	0.1

TCE and by-products concentration analysis of C10 shows highest concentration of cis-DCE (1 mg/L) and VC (0.012 mg/L) produced after 56 hours of TCE solution injection while the concentration of TCE was about 50 mg/L. After this time, cis-DCE and VC production started to decrease. VC production was stopped once the concentration of TCE reached about 200 mg/L and cis-DCE was produced in very low concentrations (below 50 µg/L). The concentration of nitrate in the TCE source solution was about 12 mg/L and was zero at the effluent samples up to 68 hours after source solution injection and started to rise up and reached the inflow concentration once the effluent TCE concentration was about 250 mg/L. At the same time ORP of the column effluent increased to -2 mV and kept rising to positive numbers (high oxygen level) afterwards. It means that the nitrate reducing bacteria were active for the first 68 hours and the TCE concentration of 250 mg/L was inhibitory to the nitrate reducing bacteria and therefore, ORP went up and dechlorinating bacteria became inactive in positive ORP. The concentration of sulfate remained unchanged in the effluent samples compared to the inflow sulfate concentration (Figure 4.7.3.4).

The concentration of TCE inside the Teflon bag (source) decreased from 500 mg/L to about 200 mg/L in 50 days. TCE mass loss might have been occurred due to diffusion of TCE through the bag into the air and also sorption of TCE to the bag surface. Once the concentration of the source solution became around 200 mg/L, ORP of the column became negative again and

nitrate concentration of the effluent samples became zero (Figure 4.7.3.5) which indicates that nitrate reducing bacteria are active again. However, cis-DCE production was still low and no VC was detected. Fresh TCE solution with a TCE concentration of about 120 mg/L was prepared and connected to the column on day 51. The cis-DCE production started to increase around day 67 (2 mg/L) and reached its highest level of 55 mg/L around day 90. The inflow TCE concentration was about 88 mg/L at that time. However, VC is not observed in the effluent samples yet. The concentration of TCE in the bag dropped from 120 mg/L to about 67 mg/L after 47 days of connecting it to the column. The source solution was exchanged with a fresh TCE solution with a concentration of 35 mg/L. The TCE and by-products concentration results are shown in Figure 4.7.3.6. The lactate concentration at the effluent samples was always lower than the source samples.

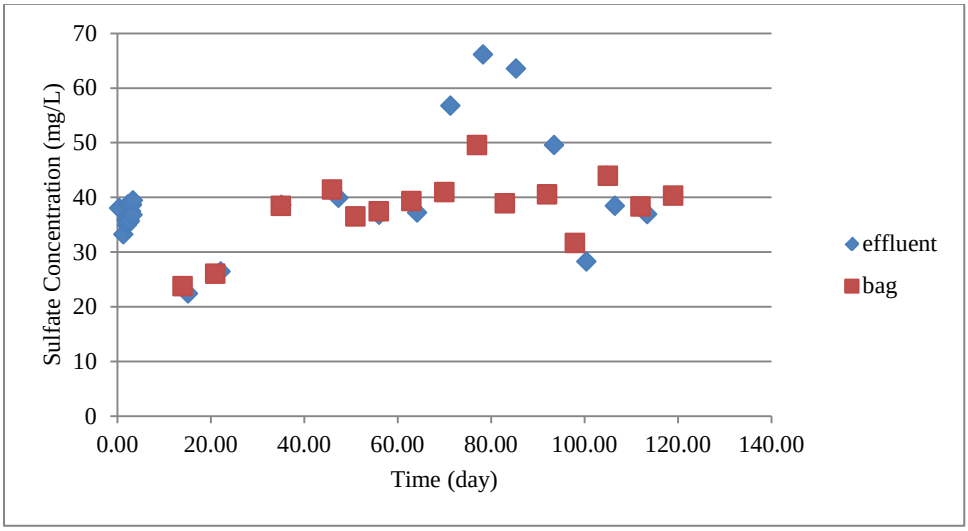

Figure 4.7.3.4: Inflow and outflow sulfate concentrations for C10.

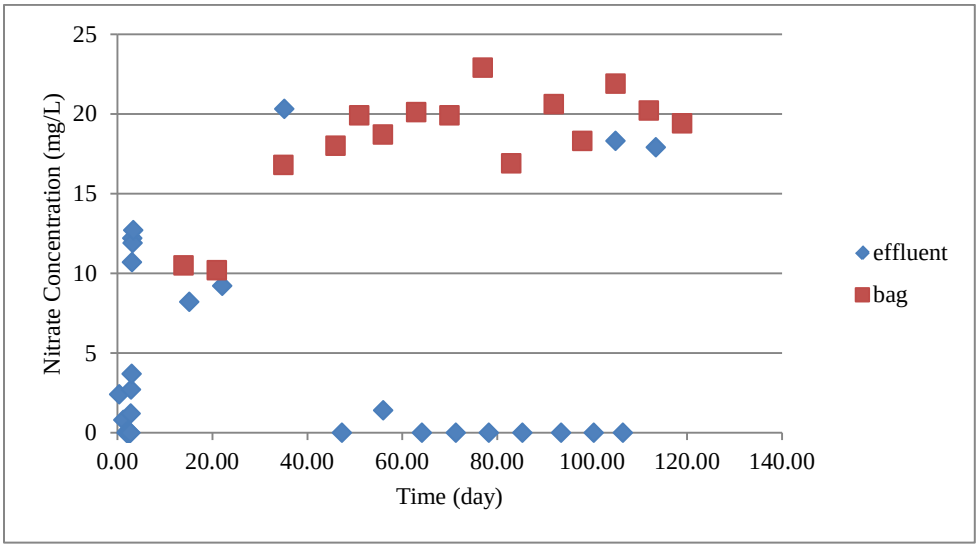

Figure 4.7.3.5: Inflow and outflow nitrate concentrations for C10.

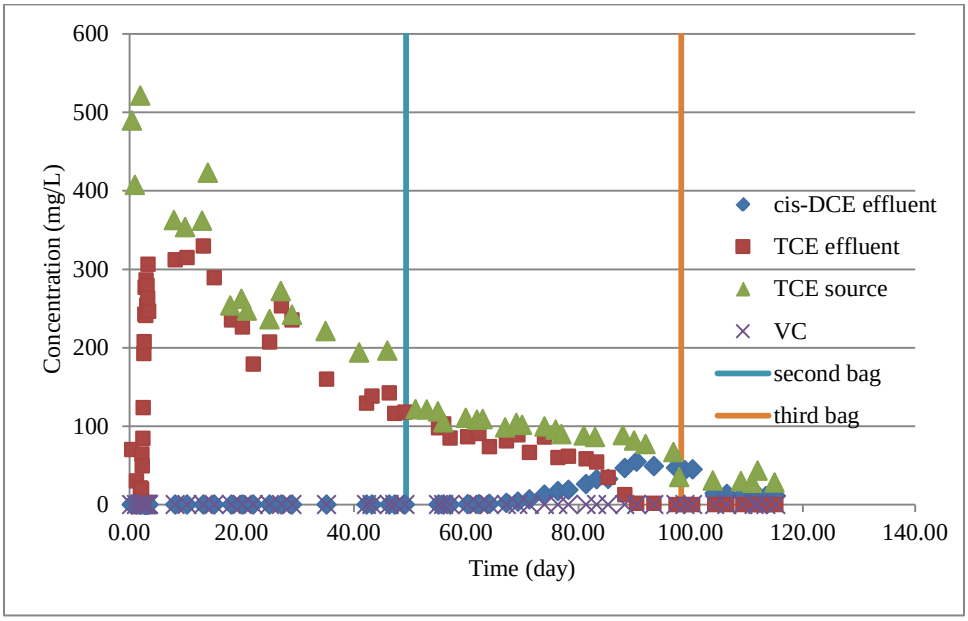

Figure 4.7.3.6: TCE and its by-products concentrations of the source solution and effluent samples of C10.

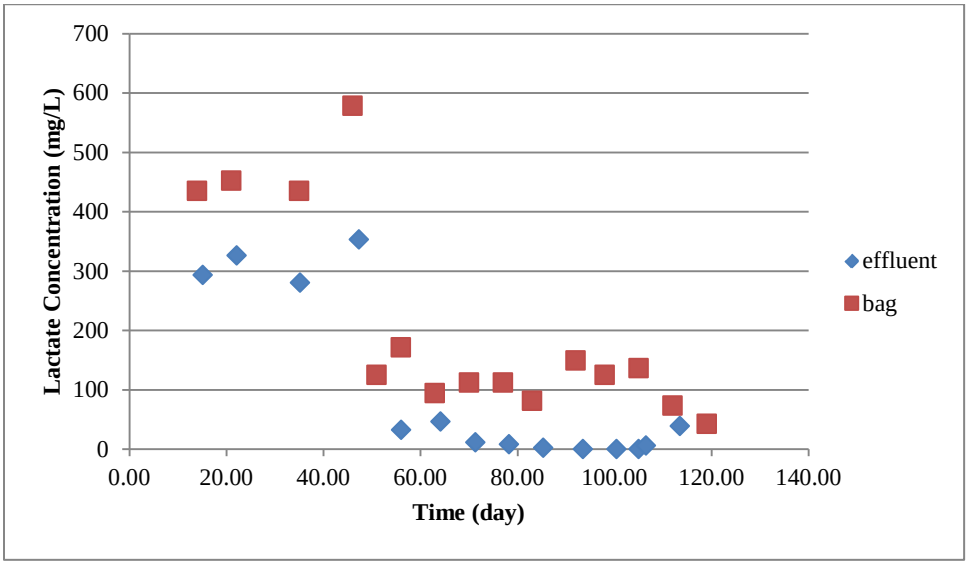

Figure 4.7.3.7: Inflow and outflow lactate concentrations for C10.

4.7.3.3.2 C8

The tracer test result for C8 is shown in Figure 4.7.3.8 and a summary of physical prosperities found using ONED_1 code is provided in Table 4.7.3.2. The reason for conducting C8 column experiment was to examine if there are any bacteria capable of dechlorinating TCE and also to examine if there are some bacteria which consume lactate in the source solution. However, any of TCE by-products was observed in C8 effluent samples (Figure 4.7.3.9) and the lactate concentration remained almost the same in the source solution and effluent samples (Figure 4.7.3.10).

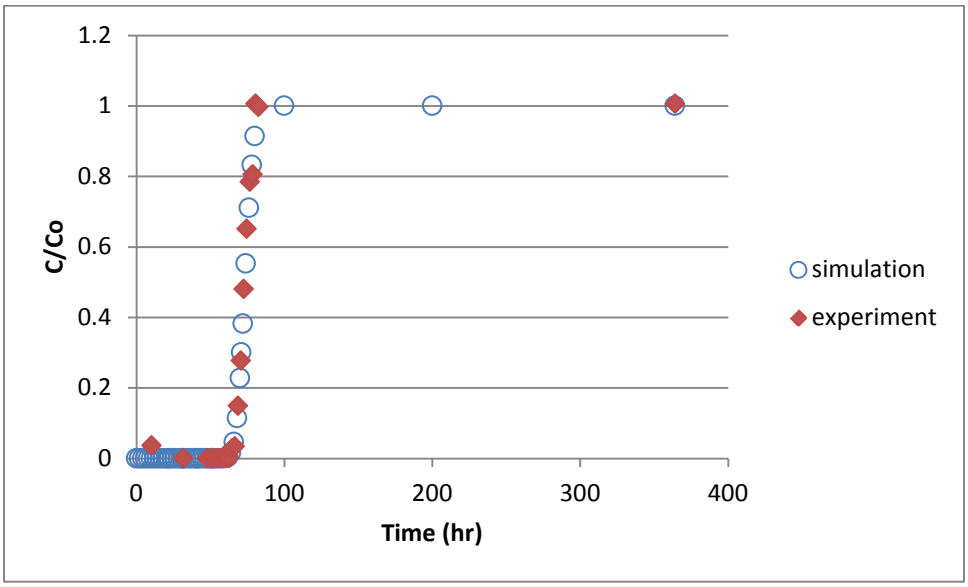

Figure 4.7.3.8: C8 conservative tracer test and simulation results using ONED_1 program.

Table 4.7.3.2: Hydraulic parameters of C8.

Column ID	Darcy Velocity, q (cm/hr)	porosity	Longitudinal Dispersivity (cm)
C8	0.17	0.25	0.1

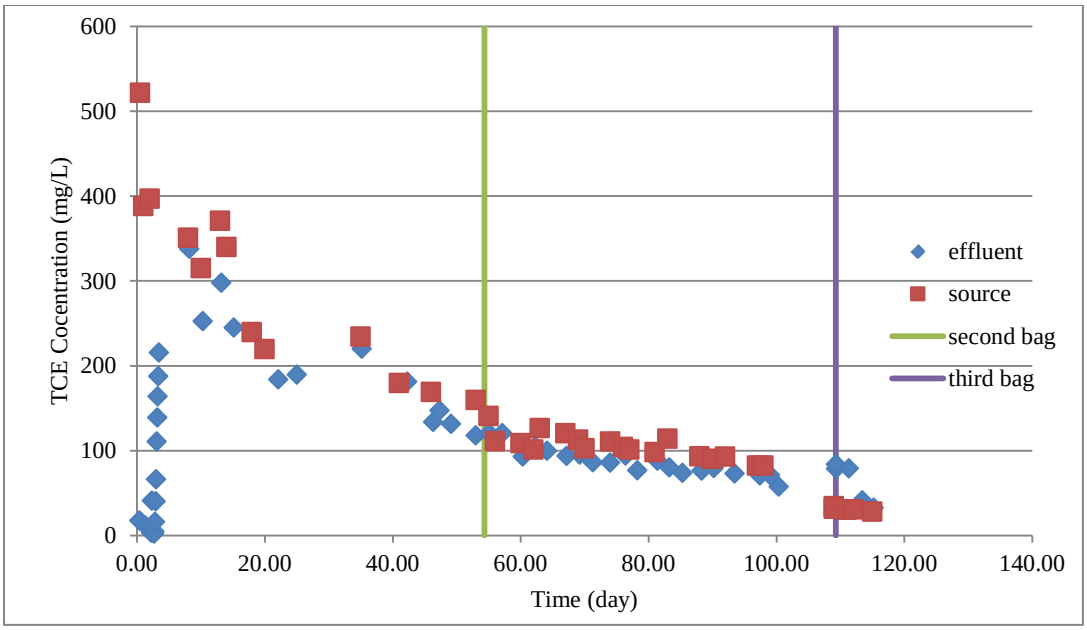

Figure 4.7.3.9: TCE concentrations of the source solution and effluent samples of C8.

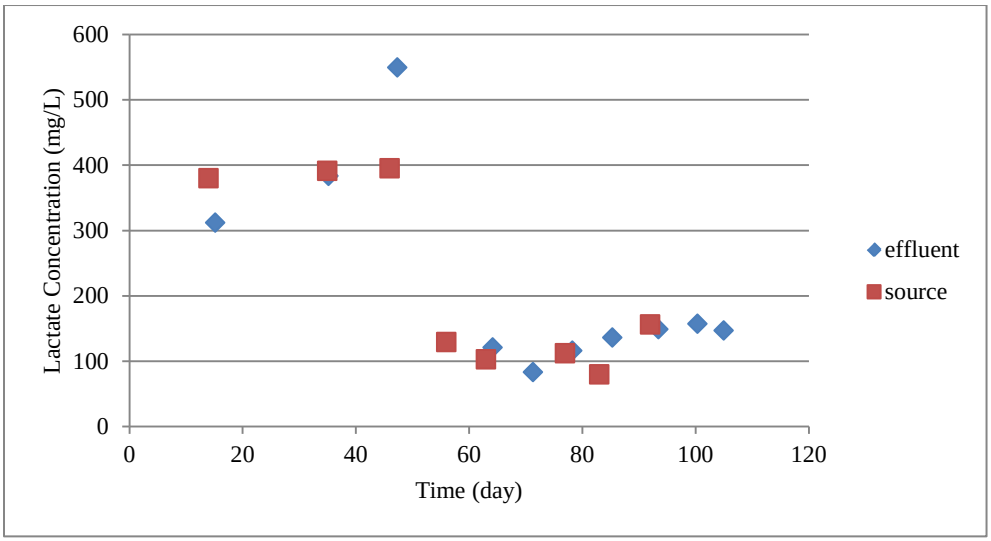

Figure 4.7.3.10: Inflow and outflow lactate concentrations for C8.

TASK 6: SANDBOX AND FRACTURED ROCK BLOCK STUDIES

4.8.1: Sandbox studies

In order to examine the effect of physical processes (such as sorpion and diffusion) and biodegradation on Cl, C, and H isotopes fractionation all in one place and in a bigger scale, a tank with dimensions of 2.4m × 1.20 m × 0.14 m was constructed by the Engineering machine shop at the University of Waterloo. However, the budget was not enough to conduct the experiment. A summary of tank design, packing, and the preliminary tests have done so far will be discussed.

The tank is made of stainless steel and glass which are safe in contact with chlorinated solvents. A total number of 135 sampling ports and 45 pumping wells were installed on the stainless steel panel of the tank (Figure 4.8.1.1).

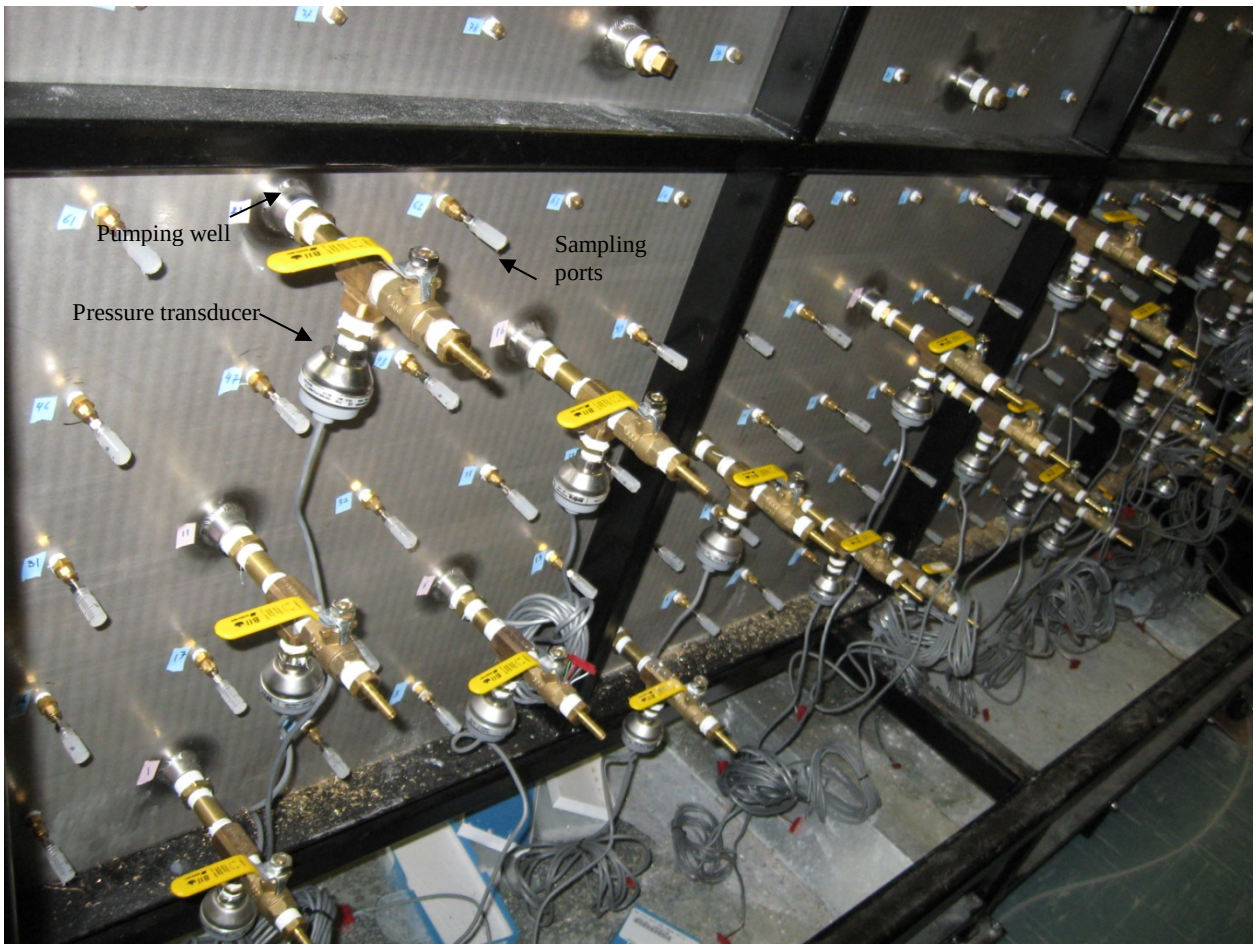

Figure 4.8.1.1: The sampling ports and pumping wells installed on the stainless steel panel of the sandbox. Pressure transducers are attached to the pumping wells.

There is a water reservoir at each side of the tank which is separated from the sand body using a perforated stainless steel sheet covered with a very fine stainless steel mesh. Prior putting the sand in the tank, the sketch of different layers was drawn on the glass side. Then a layer of

bentonite was put at the bottom of the tank. The tank was packed with different sand and silt types up to the height of 1.05 cm (Figure 4.8.1.2). The sands and silts were purchased from the US Silica, Ottawa, IL. The sandbox was packed wet to prevent the settlement which might have occurred in case of packing the sandbox dry and saturate it afterwards. De-ionized water was used to pack the sandbox to minimize the bacteria and algae growth.

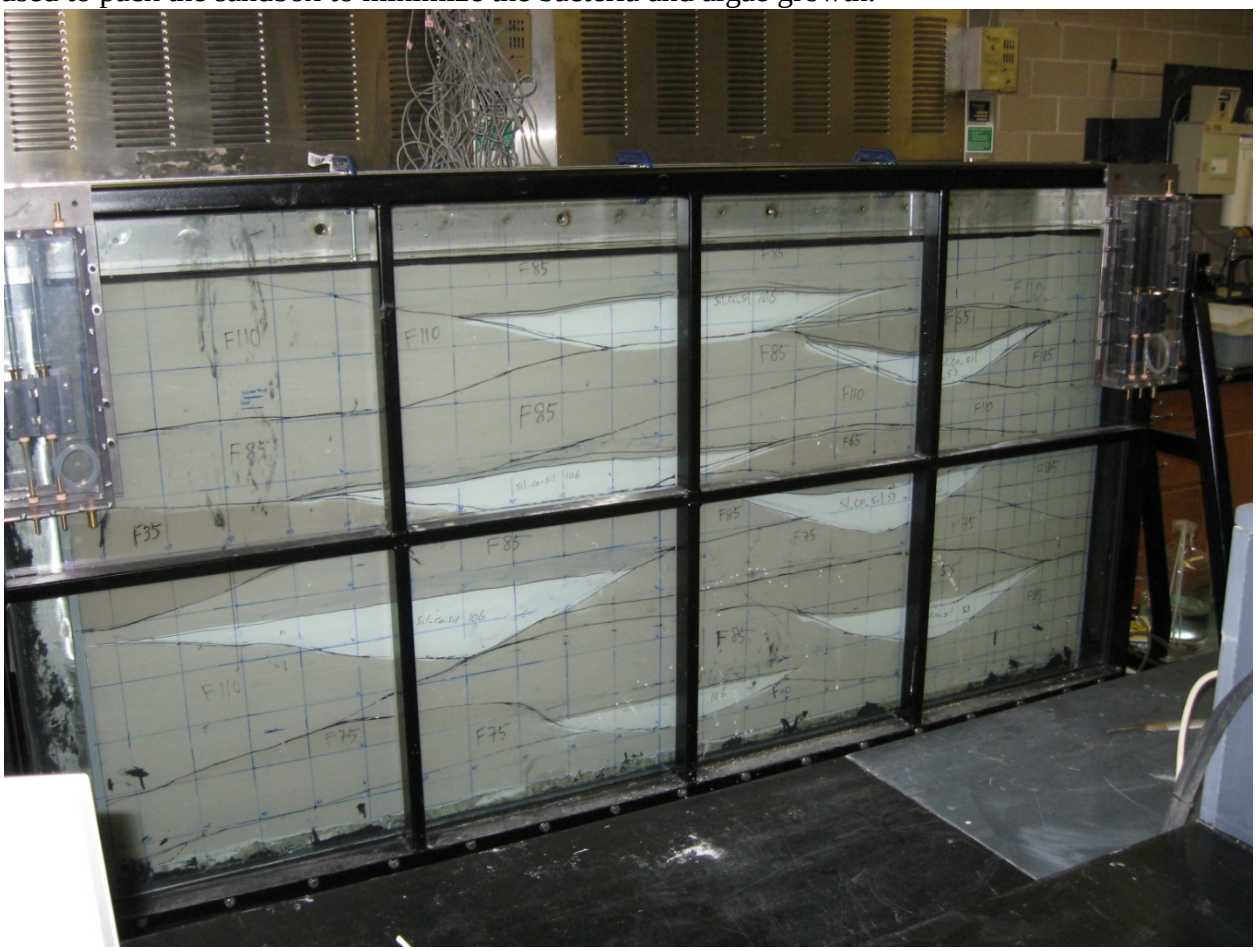

Figure 4.8.1.2: Different layers of sand and silt in the sandbox.

Once the sandbox was filled, a Lexan sheet was placed on top of the sand and the edges were sealed with silicone.

Understanding the hydraulic conductivity (K) distribution in the subsurface is essential for the study of the solute transport. Traditional method of collecting point data to measure hydraulic conductivity (K) in large scales can be time consuming and expensive. Also this method is constructive and might not result in accurate measurement of K. However, pumping tests can be done for measuring hydraulic conductivity and specific storage (S_s) with spending less time and money. Interpretation of these tests usually is done using methods such as Theis (1935) or Hantush (1960) methods. These methods assume that the aquifer is homogeneous and provide effective K and S_s of the soil. A newly developed method called Hydraulic Tomography is capable of obtaining information on K and Ss of soil through the analysis of multiple pumping tests. This method first was suggested by Neuman (1987). There are several laboratory and field

experiments which utilized HT to model subsurface heterogeneity (e.g. Liu et al., 2002; Illman et al., 2007, 2008, 2010; Liu et al., 2007; Illman et al., 2009; Cardiff et al., 2009).

A total of 34 pumping tests were performed at different pumping wells throughout the sandbox. A peristaltic pump was used to pump water from the wells. Pressure transducers were calibrated prior to the pumping for three different reservoir head. The head was set to the middle value for the pumping test. The static head was recorded by all pressure transducers for 30 s prior to the pumping. Then the pumping was done for 90 s to 120 s. To maintain the constant head for the duration of the experiment, the extracted water was pumped back to both end reservoirs. A sample of the drawdown curve during pumping test at port 3 is shown in Figure 4.8.1.3.

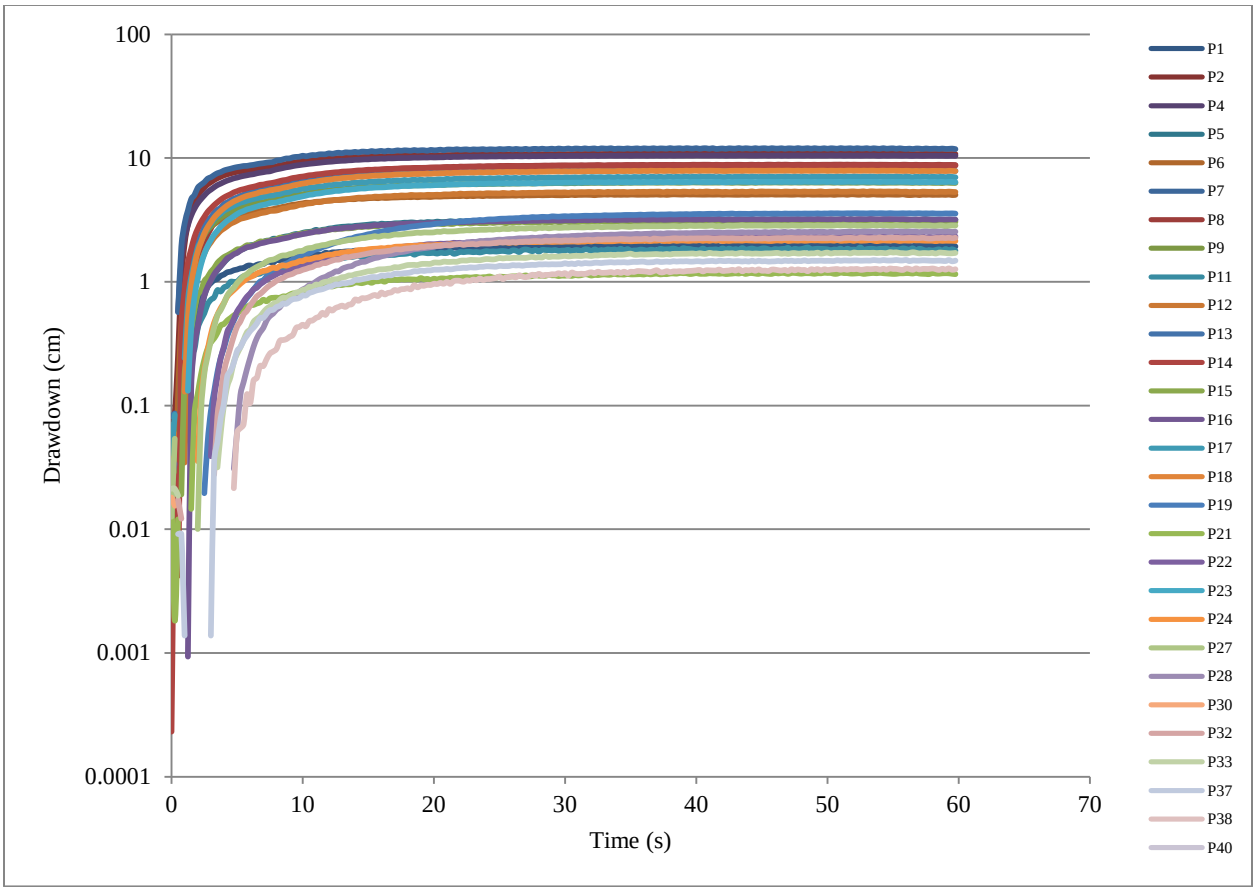

Figure 4.8.1.3: Drawdown curves during pumping test at port 3.

The drawdown curves will be processed by Steady-State Hydraulic Tomography (Yeh and Liu, 2000) and Transient Hydraulic Tomography (Zhu and Yeh, 2005) to obtain K and S_s values. SSHT uses only one point on the steady state part of the drawdown to estimate K and THT uses several points on the drawdown curve to estimate S_s.

4.8.2 Transient hydraulic tomography in a fractured dolostone rock block: Introduction

Subsurface flow and transport are controlled by the hydraulic properties of the medium (hydraulic conductivity (K), specific storage (S_s)) and their spatial variability, which are critical for the assessment of contaminant transport and other problems. In a fractured geologic medium, the high contrast of these hydraulic properties between the fractures and the matrix along with their spatial variability makes it challenging to characterize the medium accurately. In a fractured medium, fractures usually have higher K and lower S_s values than the rock matrix, while the opposite is true for the matrix. Thus, while pumping tests are conducted, pressure propagates rapidly through connected fractures unlike the rock matrix. This large contrast in the hydraulic properties between the fractures and matrix has led to various conceptual models (e.g., Neuman, 1987; National Research Council, 1996; Neuman, 2005; Illman et al., 2009) to describe flow and transport in fractured geologic media.

For example, our inability to characterize the fracture and matrix in detail has led to the creation of the equivalent porous continuum concept (e.g., Bear, 1972; Peters and Klavetter, 1988; Pruess et al., 1990). The large contrast in fracture and matrix porosities and the slow mixing process between them then prompted the use of dual porosity/mass transfer model (e.g., Bibby, 1981; Moench, 1984; Zimmerman et al., 1993; McKenna et al., 2001; Reimus et al., 2003). In the dual porosity model, the fracture continuum acts to conduct and store fluids, while the matrix only stores fluids. A dual permeability model (Duguid and Lee, 1977; Wu et al., 2002; McLaren et al., 2000; Illman and Hughson, 2005) is used when both the fracture and matrix continua conduct and store fluids. These models are, however, only suitable for describing or predicting the flow and transport behavior averaged over a large volume of fractured media, which often fail to meet our high-resolution requirements with respect to contaminant transport investigations. The desire for high-resolution predictions, thus promoted the development of discrete fracture network models (e.g., Long et al., 1982; Schwartz et al., 1983; Smith and Schwartz, 1984; Andersson and Dverstorp, 1987; Dershowitz and Einstein, 1988; Dverstorp and Andersson, 1989; Cacas et al., 1990; Dverstrop et al., 1992; Slough et al., 1999; Park et al., 2001a, 2001b, 2003; Darcel et al., 2003; Benke and Painter, 2003; Cvetkovic et al., 2004; Frampton and Cvetkovic, 2010; McLaren et al., 2012).

The discrete fracture approach, however, requires detailed specification of fracture geometries and spatial distributions which are difficult to obtain in the field (Neuman, 1987, 2005). Uncertainty in characterizing fractures due to our limited characterization technologies then becomes the logic behind the stochastic continuum concept (Neuman, 1987; Tsang et al., 1996; Vesselinov et al., 2001; Ando et al., 2003; Park et al., 2004; Illman and Hughson, 2005; Illman et al., 2009).

Over the past few decades, different hydraulic and pneumatic characterization techniques have been developed to characterize saturated and unsaturated fractured geologic media. For example, Hsieh et al. (1985) conducted cross-hole pumping tests at the Oracle site in Arizona, USA, consisting of fractured granite and obtained the anisotropy of K as well as a value of S_s by treating the fractured rock as a uniform, anisotropic medium. Likewise, numerous single-hole pneumatic injection tests (Guzman et al., 1996) in unsaturated fractured tuffs at the Apache Leap Research Site (ALRS) in central Arizona were interpreted by Illman and Neuman (2000) and Illman (2005) using type curve methods to obtain local scale estimates of air permeability (k) and air-filled porosity (ϕ). Bulk estimates of k and ϕ of the tuff at the ALRS were inferred through numerous cross-hole pneumatic injection tests conducted by Illman et al. (1998; see also, Illman, 1999). In particular, Illman and Neuman (2001) interpreted one of 44 cross-hole

pneumatic injection tests at the same site using type curves to obtain k and ϕ estimates. Due to the highly heterogeneous nature of the fractured tuff at the ALRS, many early time pressure records from various cross-hole pneumatic injection tests deviated significantly from the type curves developed by Illman and Neuman (2001) hence allowing them to analyze only one test among 44. To circumvent the lack of match of transient data to type curves that treat the medium to be homogeneous, Illman and Neuman (2003) analyzed the steady state portion of the pressure records from the other available tests. Because the steady state approach only yields k estimates, an asymptotic approach (Illman and Tartakovsky, 2005a, b) which is analogous to the straight-line method of Cooper and Jacob (1946) but developed for three-dimensional flow, was utilized to interpret the rest of the tests to obtain k and ϕ estimates. Estimates of hydraulic or pneumatic parameters obtained via type-curve, steady-state, and asymptotic analyses all are obtained on the premise that the medium is treated to be uniform. These equivalent parameters are frequently used in various research and practical applications, but Wu et al. (2005) and others have questioned the meaning of these parameters.

Another important issue in site characterization is the quantification of connectivity of high K pathways that may contribute to fast movement of water and contaminants as well as low K zones that can store contaminants. There are a number of hydraulic, solute transport, and geophysical approaches that have contributed to the understanding of connectivity (Knudby and Carrera, 2005, 2006; Day-Lewis et al., 2003), although the characterization approaches are still under considerable debate. Le Borgne et al. (2006) and Williams and Paillet (2002) used cross-borehole flow meter pulse tests to characterize subsurface connections between discrete fractures. In this method, hydraulic stress is applied to a borehole through pumping and the propagation of the pressure pulse through the flow system is monitored using a flow meter. Typically, type curves are utilized to analyze the test data. While flowmeters are useful in detecting connections between boreholes, type-curve analysis of flowmeter data cannot yield a map of fractures or their hydraulic parameters that reveals their connectivity. Despite the controversy, Illman (2006) suggested that one possible alternative to imaging the connectivity of hydraulic parameters is hydraulic tomography.

There are a number of inverse algorithms for hydraulic and pneumatic tomography (e.g., Gottlieb and Dietrich, 1995; Vasco et al., 2000; Yeh and Liu, 2000; Vesselinov et al., 2001; Bohling et al., 2002; Brauchler et al., 2003; McDermott et al., 2003; Zhu and Yeh, 2005; 2006; Li et al., 2005; 2008; Ni and Yeh, 2008; Fienen et al., 2008; Castagna and Bellin, 2009; Xiang et al., 2009; Liu and Kitanidis, 2011; Cardiff and Barrash, 2011; Schöniger et al., 2012). During a hydraulic tomography survey, water is sequentially extracted from or injected into different areas of an aquifer and the corresponding pressure responses are monitored at other intervals to obtain drawdown or buildup data sets. Pneumatic tomography is analogous, but the pumped or injected fluid is air and the investigation takes place in the unsaturated zone. In particular, Yeh and Liu (2000) developed the sequential successive linear estimator (SSLE) to analyze steady-state head records from a hydraulic tomography survey. SSLE is an iterative geostatistical inverse method that analyzes available head data from sequential pumping tests to estimate the distribution of hydraulic parameters. In the laboratory, Liu et al. (2002) and Illman et al. (2007, 2008, 2010, 2011) demonstrated the effectiveness of steady state hydraulic tomography (SSHT) using SSLE to estimate the K heterogeneity and its uncertainty. Zhu and Yeh (2005) then extended SSLE for transient hydraulic tomography (THT) to analyze transient drawdown data to estimate both K and S_s heterogeneity simultaneously. Liu et al. (2007) demonstrated encouraging results from the laboratory sandbox experiment for THT. They not only identified the K and S_s distribution in the

laboratory sandbox using THT, but also successfully reproduced the observed drawdown as a function of time of an independent aquifer test using estimated K and S_s field. More recently, Berg and Illman (2011a) used laboratory sandbox data to show that THT yields the best predictions of independent pumping tests among several heterogeneity characterization and modeling approaches.

In the field, a number of studies have been published (e.g., Bohling et al., 2007; Straface et al., 2007; Cardiff et al., 2009; Li et al., 2008; Illman et al., 2009; Brauchler et al., 2011; Castagna et al., 2011; Berg and Illman, 2011b; Huang et al., 2011; Cardiff et al., 2012). In particular, Berg and Illman (2011b) showed that performing the inversion with multiple pumping tests (i.e., hydraulic tomography) yields improved results when compared to the analysis of individual pumping tests at a highly heterogeneous field site consisting of glaciofluvial deposits. While synthetic, laboratory, and field studies on hydraulic tomography in unconsolidated deposits are encouraging, research on the application of hydraulic or pneumatic tomography to fractured rock is limited.

The first study on the pneumatic tomography of fractured rocks was published by Vesselinov et al. (2001). These authors developed a geostatistical inverse algorithm based on the pilot point method to interpret multiple cross-hole pneumatic injection tests (Illman and Neuman, 2001; 2003) in unsaturated fractured tuffs at the ALRS. The simultaneous inversion of pressure buildup records from three cross-hole pneumatic injection tests amounted to the pneumatic tomography to image the k and ϕ heterogeneity. The results of the pneumatic tomography were compared to kriged k fields based on single-hole pneumatic injection tests (Chen et al., 2000) and were found to share a similar internal structure. In addition, k estimates obtained through pneumatic tomography were compared to single-hole k estimates along several boreholes yielding a general correspondence between the two estimates.

Brauchler et al. (2003) then developed a hydraulic and pneumatic tomography approach based on the inversion of travel times of the pressure pulse. The algorithm was based on the relation between the peak time of a recorded transient pressure curve and the diffusivity of the investigated system. It was tested in a large diameter cylindrical sample of unsaturated fractured sandstone in the laboratory. The three-dimensional reconstructions of the high diffusivity areas coincided with the location of a vertical fracture.

More recently, Hao et al. (2008) applied the SSLE algorithm to a synthetically generated fractured medium to investigate the feasibility of hydraulic tomography to detect fracture zones and their connectivity. The hypothetical fractured rock aquifer was a 2D vertical square domain consisting of five orthogonal vertical and two horizontal fracture zones embedded in a rock matrix. They satisfactorily imaged the high K zones from the observation data collected from multiple pumping tests, which reflected the fracture pattern and its connectivity in the synthetic fractured aquifers although estimated values of K and S_s fields were smoother than the true fields. They found that the fracture pattern and connectivity became more vivid and the estimated hydraulic properties approached true values as the number of wells and monitoring ports increased.

Ni and Yeh (2008) extended the SSLE algorithm to pneumatic tomography to delineate fracture permeability, porosity, and connectivity in unsaturated fractured rocks. Their pneumatic tomography algorithm considers compressibility of air and SSLE fully utilizes the cross-correlation between head and pneumatic properties everywhere in a geologic medium. This cross-correlation is ignored by the pilot point approach, as explained by Huang et al. (2011).

Most recently, Illman et al. (2009) interpreted two cross-hole pumping tests at the Mizunami Underground Research Laboratory (MIU) construction site in central Japan and analyzed them using the THT code of Zhu and Yeh (2005) to map the three-dimensional distribution of K and S_s, their connectivity, as well as their uncertainty. They were able to identify two fast flow pathways or conductive fault zones at the site as well as low K zones, despite the availability of only two cross-hole pumping tests. They assessed the soundness of the estimated fracture K and S_s tomograms using three different approaches: 1) by comparing the calibrated and observed drawdown records as well as predicted the drawdown responses at the monitoring intervals that were not used in the construction of the K and S_s tomograms; 2) by comparing the estimated K and S_s tomograms to previously known fault locations, and 3) by utilizing coseismic groundwater pressure changes recorded during several large earthquakes as a means to evaluate the K and S_s tomograms. While the results were encouraging, there were only two pumping tests available for inverse modeling which precluded Illman et al. (2009) from investigating whether THT could be utilized to map finer details of hydraulic heterogeneity in fractured rocks. The work of Illman et al. (2009) motivates us to conduct a laboratory fractured rock block experiment in which a large number of pumping tests can be conducted and THT can be tested in a controlled setting. Conducting a larger number of pumping test in a controlled environment can help determine whether finer details of K and S_s heterogeneity can be imaged. In addition, pumping tests that are not used for the THT analysis can be utilized to validate the K and S_s tomograms (e.g., Illman et al., 2007; Liu et al., 2007).

Therefore, the main objectives of this study are to investigate the ability of THT to image the K and S_s tomograms of a fractured rock block without the a priori knowledge of fracture locations as well as fracture geometry data and to compare the tomograms to the known fracture locations. We conduct the study using a dolostone rock sample with known fracture locations that is encased in a flow cell. The fractured rock block is initially subjected to flow through tests in order to obtain an estimate of effective hydraulic conductivity (K_{eff}). We then conduct synthetic simulations of pumping tests to design the actual tests for the hydraulic tomography survey of the fractured rock block. With an improved understanding of how the drawdowns propagate through the fractured rock block, we conduct multiple cross-hole pumping tests using multiple observation ports to obtain drawdown data. These drawdown data are then interpreted using the SSLE code developed by Zhu and Yeh (2005) to conduct transient hydraulic tomography, which yields K and S_s tomograms as well as their uncertainty estimates. The obtained K and S_s tomograms are then assessed through a number of methods to test their validity.

4.8.2.1 Experimental design

4.8.2.1.1 Rock block preparation and flow cell design

A dolostone rock sample from the Guelph Formation for the laboratory experiments was obtained from a quarry in Wiarton, Ontario, Canada. The Guelph Formation is a carbonate ramp sequence and mainly composed of tan to dark brown, microcrystalline to fine crystalline, pervasive and massive dolomites (Coniglio et al., 2003, 2004). The dimensions of the dolostone rock sample are 91.5 cm in length, 60.5 cm in height and 5.0 cm in depth.

Tension fractures were induced by placing a triangular bar underneath the rock sample and forcing it to fracture along it. In order to seal the edges of the fractures, we utilized titanium putty (Devcon, Danvers, MA, USA) as a sealant. The sealant was applied on the rock surface leaving

the fractures open. After the putty dried, we poured resin (Environmental Technology, Inc., CA, USA) to cover the front, back, top and bottom surface of the rock in order to prevent any evaporation or leakage, and to make the surfaces smooth. This allowed for water flow to take place only from the left and right surfaces that connect to the constant head reservoirs (Figure 1). After the resin dried and hardened, water was injected at several ports to ensure that the horizontal and vertical fractures did not become sealed.

The sealed fractured block was then placed in a flow cell (122 cm in length, 65 cm in height and 6.5 cm thick) constructed of stainless steel with plexiglass used as a front plate (Figure 4.8.2.1). We applied silicon to seal any gaps present between the flow cell and the rock block. The flow cell consisted of constant head reservoirs at the left and right boundaries where it is in contact with the fractured rock block. This allowed for the horizontal fracture to be in contact with the constant head reservoirs allowing for water flow along the length of the rock block. All other boundaries are considered to be "no-flow" boundaries.

4.8.2.1.2 Fractured rock block instrumentation

We installed 31 ports on the fractured rock block to monitor water pressure using a pressure transducer (Figure 4.8.2.1). Each port was connected to a 0 - 1 pounds per square inch gauge (psig) pressure transducer (model 209, Alpha Controls & Instrumentation, Markham, ON, Canada) to record pressure measurements at different locations of the fractured domain during the hydraulic tests. Seventeen pressure transducers were placed on fractures, fourteen were installed on the matrix and two were utilized to record pressure in the constant head reservoirs. Ports placed on fractures were also utilized for water extraction during the pumping tests.

The data acquisition system used for recording pressure measurements consisted of a 64-channel data acquisition board from National Instruments. A hub that separates excitation and output currents for the transducers was assembled. A dedicated PC with National Instruments LabVIEW software also was part of the automated data acquisition system.

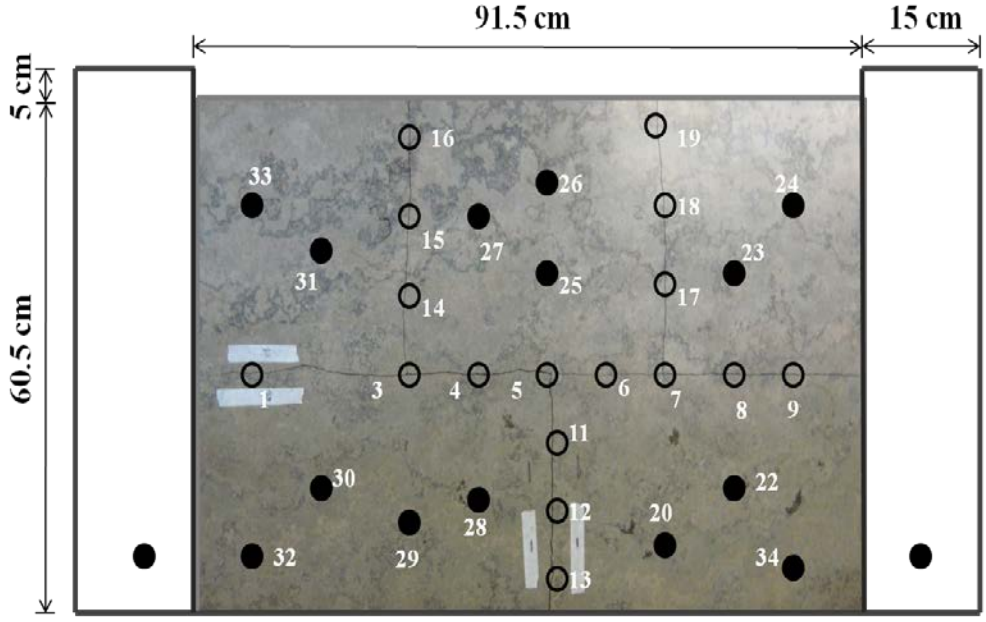

Figure 4.8.2.1: Experimental setup of the hydraulic tests on the fractured rock block. Open black circles indicate port locations on the fractures. Black solid circles indicate port locations within the matrix and the constant head reservoirs.

4.8.2.2 Description and interpretation of flow-through tests on the fractured rock block

4.8.2.2.1 Description of flow-through tests

After the fractured block was enclosed in a flow cell, we filled the rock block with water from the bottom and in the constant head reservoirs to allow for the fractured rock block to saturate over several weeks. To minimize air entrapment, we allowed air to escape from the top before we sealed the top of the block. We then conducted four flow-through tests following the work of Illman et al. (2007, 2010) to estimate the bulk or effective hydraulic conductivity (K_{eff}) and the hydraulic aperture of the fractured block. Flow-through tests were conducted by fixing the hydraulic gradient across the rock sample and measuring the water outflow rate at the effluent dripping point using a graduated cylinder. The flow rate was measured in both directions (left to right and right to left) by fixing the hydraulic gradient across the fractured block, and for two different hydraulic gradients in each direction under confined conditions. The hydraulic gradient across the rock block was fixed by setting drip points at the end reservoirs at different heights. A peristaltic pump (MasterFlex, Model 7550-30, Cole-Parmer, Montreal, QC, Canada) was used to supply water continuously into the influent reservoir and the drip point maintained constant head.

4.8.2.2.2 Interpretation of flow-through tests

The flow through tests can be interpreted to obtain the hydraulic aperture of the horizontal fracture through the cubic law (Romm, 1966):

$$b = \left(\frac{12\mu QL}{\rho g W \Delta H} \right)^{\frac{1}{3}} \tag{4.8.2.1}$$

where, b is hydraulic aperture (L), μ ($ML^{-1}T^{-1}$) is the dynamic viscosity at room temperature (20°C), Q (L^3T^{-1}) is the discharge or flow rate through fracture, L (L) is the fracture length in the direction of flow, ρ (ML^{-3}) is the fluid density at room temperature, g (LT^{-2}) is the acceleration due to gravity, W (L) is the fracture width perpendicular to the direction of flow, and ΔH (L) is the hydraulic head loss across the fracture plane.

The estimated values of hydraulic aperture of the fracture system from four different flow-through tests varied between 0.047 cm and 0.050 cm and are summarized in Table 4.8.2.1. The hydraulic aperture values are bulk estimates that consider not only the horizontal, but the vertical fractures present in the rock block (Figure 4.8.2.1).

From the flow-through tests, the K_{eff} of the fractured block was estimated using Darcy's Law:

$$Q = -K_{eff} A \frac{dh}{dl} \tag{4.8.2.2}$$

where A (L^2) is bulk cross-sectional area and (dh/dl) is the hydraulic gradient across the system. The estimated K_{eff} from four different flow-through tests are also summarized in Table 4.8.2.1, which varied between 1.30×10^{-2} cm/s to 1.70×10^{-2} cm/s.

Table 4.8.2.1: Summary of the flow-through tests and the estimated hydraulic parameters

Test	Flow direction	Constant head at left reservoir (cm)	Constant head at right reservoir (cm)	Hydraulic Gradient	Flow Rate (mL/s)	Hydraulic aperture (cm)	K_{eff} (cm/s)
Test 1	Left to Right	60.0	55.0	0.05	0.28	0.050	1.70×10^{-2}
Test 2	Left to Right	60.1	48.5	0.13	0.50	0.047	1.30×10^{-2}
Test 3	Right to Left	54.6	60.0	0.06	0.27	0.048	1.50×10^{-2}
Test 4	Right to Left	48.4	60.6	0.13	0.51	0.047	1.30×10^{-2}

4.8.2.3 Synthetic simulations for the design of pumping tests used for hydraulic tomography

4.8.2.3.1 Description of synthetic pumping tests

We next utilized the groundwater flow and solute transport code, HydroGeoSphere (HGS) to simulate the pumping tests on the computer to design the actual pumping tests that will be utilized for the hydraulic tomography survey of the fractured rock block. The domain used for the forward simulation was 91.5 cm in length by 60.5 cm in height and 5 cm thick (one element thick) and was composed of variably-sized rectangular elements. The element size varied from 0.05 cm by 0.01 cm to 1.375 cm by 1.375 cm. The finer elements were located along the fracture and the coarser elements were located away from the fractures. Figure E1a in Appendix E shows the domain used for simulating the pumping tests and Figure E1b shows the fracture faces. The darker areas in Figure E1a indicate the highly refined areas of the model domain. We assigned constant head boundary conditions (h = 63.5 cm) for left and right boundaries and no flow for the remaining outer boundaries to simulate actual experimental conditions.

The hydraulic aperture obtained from the flow-through tests is assigned to the elements for the horizontal and vertical fractures. HGS then calculates the fracture hydraulic conductivity (K_f) from the hydraulic aperture (Therrien et al., 2009):

$$K_f = \frac{\rho g b^2}{12\mu} \tag{4.8.2.3}$$

Based on the average hydraulic aperture (0.049 cm) from the flow-through tests, HGS calculated a K_f of 17.46 cm/s.

Initial estimates of the matrix hydraulic conductivity (K_m = 1.00×10^{-7} cm/s to 1.00×10^{-4} cm/s) and specific storage (S_s) values for both fractures (S_{sf} = 1.00×10^{-9} cm^{-1} to 1.00×10^{-6} cm^{-1}) and matrix (S_{sm} = 1.00×10^{-9} cm^{-1} to 1.00×10^{-6} cm^{-1}) were obtained from the literature (i.e, Schwartz and Zhang, 2003; Singhal and Gupta, 2010). A range of values were selected to conduct a suite of forward simulations to examine the drawdown behavior in the fractured rock block.

A synthetic simulation of a pumping test was then conducted with pumping taking place at port 5 at a pumping rate of 4 cm^3/s in an attempt to gain insight into the drawdown behavior that will propagate through the fractured rock block. Results from the simulation revealed drawdown responses at observation ports located on fractures, while no response was observed at the ports located within the matrix during the duration of the synthetic pumping test.

Following the synthetic simulation of a pumping test, an identical, real pumping test was then carried out at port 5 of the actual fractured rock block and pressure responses at all the monitoring ports were recorded.

4.8.2.3.2 Traditional interpretation of a single pumping test

The hydraulic parameters of the fractured rock block from the previous section were then adjusted by matching the simulated (dashed) and observed drawdown curves during the real pumping test at port 5 of the fractured rock sample (Figure 4.8.2.2). Examination of Figure 4.8.2.2 reveals that, a good match between the observed and simulated drawdown can be obtained for the bulk of the drawdown responses except for very early time.

The manual calibration resulted in higher specific storage values [for both the fractures (S_{sf} = 8.00×10^{-4} cm^{-1}) and the matrix (S_{sm} = 3.00×10^{-3} cm^{-1})] than the literature values. One reason for this may be due to wellbore storage in the ports which is not accounted for explicitly in the numerical model. While these specific storage values are certainly higher, the literature values are representative of pumping tests conducted at a significantly larger scale in the field at greater depths (e.g., Illman et al., 2009; Castagna et al., 2011), and the storage estimates from the fractured rock block nevertheless, yields the best calibrated results.

In order to further verify the high S_s values than what we expect for values obtained in the field, we conducted a Jacob's semilogarithmic analysis [Cooper and Jacob, 1946] of several observation port data from several pumping tests to obtain bulk estimates. Those results yielded a mean K of 2.80×10^{-2} cm/s and mean S_s of 1.8×10^{-3} cm^{-1} which suggests that a higher S_s value can be obtained from this fractured rock block. These parameters (fractures: K_f = 17.46 cm/s; S_{sf} = 8.00×10^{-4} cm^{-1} and the matrix: K_m = 1×10^{-7} cm/s; S_{sm} = 3.00×10^{-3} cm^{-1}) were then utilized to simulate eight additional pumping tests at ports 3, 7, 12, 13, 15, 16, 18, and 19 at pumping rates ranging from 1 – 4 cm^3/s to obtain synthetic drawdown data that were later used for the THT analysis of synthetic data.

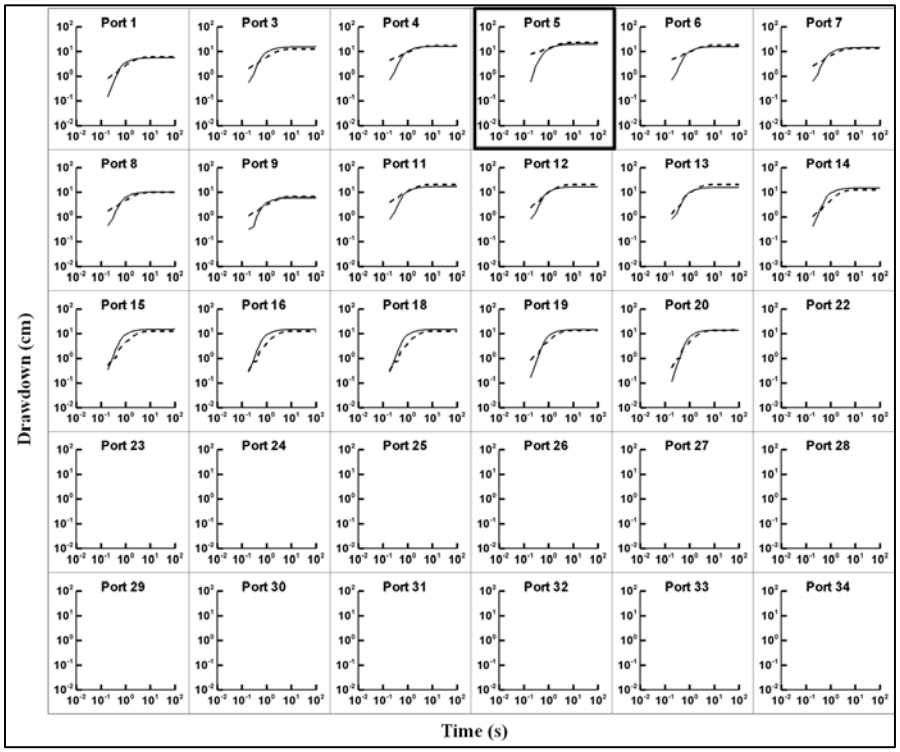

Figure 4.8.2.2: Observed (solid curve) and calibrated (dashed curve) drawdown curves using HGS during a pumping test at port 5.

4.8.2.4 Description of sequential pumping tests conducted in the fractured rock block

Upon completion of the flow-through tests and the synthetic simulations of pumping tests, 17 real pumping tests were conducted at each of the fracture ports on the fractured rock block (see Figure 4.8.2.1). A peristaltic pump was used to extract water from the pumping port and a pulse dampener was used between the pump and the pumped port to reduce the oscillations in the pumping rate. Thirty-one pressure transducers recorded pressure responses at different heights of the fractured domain and two of them recorded pressures in the constant head reservoirs during each test. Both reservoirs were fixed at the same level and the constant head was maintained throughout the test by putting the extracted water back to both reservoirs.

The duration of each pumping test ranged from 3 to 10 minutes. During each test, pressures were recorded at 30 to 31 ports located along the fractures, matrix and constant head reservoirs. Prior to conducting each pumping test, all pressure transducers were calibrated for three different reservoir heads as implemented by Illman et al. (2007, 2008, 2010) and Berg and Illman (2011a). To develop a static, initial condition, head data were recorded at each pressure transducer for several minutes prior to each pumping test. Then each pumping test was run until steady-state conditions which were visually confirmed by observing the stabilization of all head measurements on the datalogger connected to a computer. During all of the pumping tests, recorded pressures in ports completed on fractures reached steady-state within 2 to 3 seconds after the water extraction was started and no change in pressure was observed at any of the matrix ports, which was expected due to the very high contrast between the fracture and matrix *K*. A summary of all pumping tests conducted in the fractured rock block is provided in Table 4.8.2.2.

Table 4.8.2.2: Summary of pumping tests conducted on the fractured rock block.

Pumped Port	Pumping Rate (mL/s)	Duration (min)	Maximum Observed Drawdown (cm)	Port of Maximum Drawdown
Port 1	4	10	8	Port 3
Port 3	2.5	10	10	Port 15
Port 4	2.5	10	10.4	Port 3
Port 5	4	10	17.3	Port 11
Port 6	2.5	10	10	Port 11
Port 7	2.5	5	7.8	Port 19
Port 8	4	10	9.5	Port 7
Port 9	4	10	5.9	Port 8
Port 11	4	10	17	Port 13
Port 12	4	10	19.7	Port 13
Port 13	4	10	18.7	Port 12
Port 14	2.5	10	16.2	Port 15
Port 15	1.7	10	14.9	Port 16
Port 16	1	10	11.7	Port 15
Port 17	2.5	3	29.7	Port 18
Port 18	1.7	10	21.3	Port 17
Port 19	1	10	18.4	Port 18

4.8.2.5 Transient hydraulic tomography analyses of synthetic and real pumping test data

4.8.2.5.1 Inverse modeling approach

We then performed the stochastic inverse modeling of individual pumping tests and THT analysis using the Sequential Successive Linear Estimator (SSLE) developed by Zhu and Yeh (2005). The forward model included in SSLE is the VSAFT3 code (Yeh et al., 1993) which treats the fractured rock as a porous continuum. SSLE for THT evolved from the SSLE for steady state hydraulic tomography (Yeh and Liu, 2000). Both use the successive linear estimator (SLE) (Yeh et al., 1996) concept and successively include data sets, thus reducing the computational burden that would be encountered if all of the data sets were included simultaneously.

SLE starts with 1) cokriging if there are measurements of K and S_s (otherwise, kriging at sample locations) based on the covariance functions for the parameters to obtain conditional mean estimates of the parameter fields and to evaluate the conditional (or residual) covariance functions of the parameters (K and S_s) at every grid block of the inverse modeling domain. 2) Then, the conditional mean parameter fields are used to simulate the responses of the geologic formation (head) based on the governing flow equation. 3) The difference between the observed and simulated heads at head measurement points are subsequently used to improve the estimated parameters at every grid block of the domain. The improvement of the parameter at each block is the weighted sum of all the differences at all head measurement locations, similar to kriging. The weights are calculated based on the cross-covariance (residual) function between the head and the parameters similar to the solution to the kriging system equation. 4) The residual covariances of the estimated are parameters updated, which will be used to calculate the cross-covariance function for the next iteration. 5) If the difference is small than a given tolerance or other criteria are met, the iterative update is stopped. Otherwise, steps 2 through 5 are repeated. The algorithm of the sequential approach is similar to the SLE except it includes new pumping test data into the SLE.

SLE approach is different from the pilot point approach. SLE distributes information content in the observed head to every block of the aquifer domain according to the spatial cross-covariance (or cross-correlation) function between the head at observation locations and the parameters (K and S_s) at every location. This cross-correlation function is evaluated using the continuously updated parameter residual covariance functions and governing flow equation. They change according to the residual covariance functions of the parameters as well as the flow fields induced by different pumping tests. Estimated parameters at every block in the domain are thus improved if the observed heads have new information. This is the reason that SSLE is capable of mapping the heterogeneity over large area using a small number of observation points during HT. These points are discussed extensively in Huang et al. (2011).

While the simultaneous inversion of pumping tests is also possible with Zhu and Yeh's (2005) THT code extended by (Xiang et al., 2009), the computational requirements are significant for the analyses of our data. Therefore, at this time, we choose to sequentially analyze the pumping tests using the SSLE of Zhu and Yeh (2005).

4.8.2.5.2 Inverse model setup

The THT analysis of synthetic data (synthetic THT from now on) was first performed, before performing THT analysis with two sets of laboratory drawdown data (real THT cases 1 and 2 from now on) in order to investigate the capability of SSLE in imaging fractured rock

block by computing the K and S_s tomograms with noise-free data. The inversion of the synthetic data is important as it provides us with baseline results that one can expect from the number of pumping and monitoring points utilized in our synthetic and real experiments. These results will later be used to compare against the results from the real THT analysis.

Synthetic THT analysis was conducted by inverting three of the nine synthetic pumping tests conducted by HGS. Upon completion of the synthetic THT, two cases of the real THT were performed by inverting two different sets of pumping tests conducted in the fractured rock block enclosed in a flow cell. Each of the real THT cases 1 and 2 were conducted by inverting three laboratory pumping tests.

All stochastic inversions of individual pumping tests were performed using 30 to 32 processors for the synthetic case and 8 to16 processors for the real case on a PC-cluster (consisting of 1 master and 12 slaves each with Intel Q6600 Quad Core CPUs running at 2.4 GHz with 16 GB of RAM per slave) at the University of Waterloo. The operating system managing the cluster was CentOS 5.3 based on a 64-bit system.

A 91.5 cm by 60.5 cm and 5 cm (one element) thick domain was used for the inversion of both synthetic and laboratory data and the domain was composed of variably-sized rectangular elements. The domain was discretized into 14140 nodes and 6900 elements. The element size varied from 0.5 cm by 0.5 cm to 1.75 cm by 1.75 cm. The finer elements are located along the ports to match the port location and the element center and the coarser elements are located near the boundary. Figure E2 in Appendix E shows the computational grid used for both the synthetic and real THT analysis.

The boundary conditions were constant head for left and right boundaries and no flow for the remaining outer boundaries. The hydraulic head for both the left and right boundary of the model domain was set to 63.5 cm for the analysis of both synthetic and real data.

4.8.2.5.3 Input parameters

Inputs to the SSLE for the synthetic and real THT analyses include mean K and S_s values for the model domain, estimates or guesses of variances and the correlation scales for both parameters, volumetric discharge (Q) from each pumping test and observed pressure head data at various selected times per drawdown curve from each pumping tests. Here, the model was not conditioned with additional data, although point (small-scale) measurements of K and S_s can also be input to the model to condition the estimates.

One can estimate the mean values or initial homogeneous field of K and S_s in a number of ways. For example, literature values of effective hydraulic conductivity (K_{eff}) and specific storage (S_{seff}) that are considered reasonable for the fractured rock aquifer may be used as initial model input. An alternative could be estimating a geometric mean of the small-scale measurements (i.e., core, slug, and single-hole data), if small-scale data are available. The initial homogeneous K and S_s field can also be selected by obtaining equivalent hydraulic conductivity and specific storage estimates through the analysis of pumping test data by treating the medium to be homogeneous.

Here, the latter option was chosen and the initial homogeneous K and S_s were estimated by coupling PEST (Doherty, 2005) with the forward groundwater model in SSLE (Zhu and Yeh, 2005) and matching the drawdown responses at the pumping port. The homogeneous K and S_s for the fractured rock were estimated by matching the pumping port drawdown for 3 individual laboratory pumping tests conducted at Ports 3, 5 and 7. The model domain and the boundary conditions used for the parameter estimation were the same to those used for the inverse

modeling. Estimates of homogeneous K and S_s along with the corresponding 95% confidence intervals are presented in Table 4.8.2.3.

From Table 4.8.2.3, it is evident that the estimates of homogeneous K and S_s from all 3 cases were close to one another. Therefore, the geometric mean of the estimated homogeneous K and S_s ($K= 2.3 \times 10^{-2}$ cm/s and $S_s = 4.7 \times 10^{-3}$ cm^{-1}) were incorporated into SSLE as an initial guess for the inversion of the synthetic as well as the laboratory data. The model starts the inversion (for both synthetic and real THT) with these homogeneous estimates of K and S_s and updates them at the end of each iteration and the following iteration starts with these updated values of K and S_s. This process continues until the model goes through the last iteration of the last test.

SSLE also requires the estimates of the hydrogeologic structure (correlation length and the variances of the K and S_s) for inversion. One can assume correlation length and the variances or can conduct a geostatistical analysis of small scale data to estimate the variance and the correlation length. Here, a correlation length of 1 cm and a variance of 5 were assumed for both K and S_s. It is a well-known fact that it is difficult to estimate the variance and the correlation scale accurately and thus the estimation always involves some uncertainty. Here, a unit correlation length (1 cm) was used for the THT analyses, as larger correlation implies a homogeneous field of hydraulic properties. However, a previous numerical study conducted by Yeh and Liu (2000) has shown that the initial guesses of variance and correlation scales have negligible effects on the estimated K field based on hydraulic tomography, because hydraulic tomography utilizes a large number of head measurements, which already hold information of the detailed site-specific heterogeneity (Zhu and Yeh, 2005, 2006; Liu et al., 2007). Negligible effects of correlation scales on the estimate of fracture patterns in synthetic aquifers were also demonstrated by Hao et al. (2008).

The synthetic THT analysis was performed by inverting hydraulic head data from three synthetic pumping tests sequentially, which included the tests at ports 5, 7 and 3, in that order. The pumping tests utilized in the synthetic THT case were identical to the ones used in real THT case 1. For real THT case 2, we utilized pumping tests at ports 5, 16, and 19, to evaluate whether utilizing different pumping tests could have an impact on the estimated K and S_s tomograms.

The locations for the pumping tests were selected for their ability to stress the entire fractured block. For example, for all the synthetic and real THT cases, the pumping test at port 5 was included first in the inverse model followed by two additional tests with lower pumping rates. The reason for including pumping test at port 5 first was that the pumping test generated drawdown responses at all the ports located on fractures as it is located in the central portion of the fractured block and it had the highest flow rate, thus had the highest signal to noise ratio. Illman et al. (2008) showed that including the data with the highest signal-to-noise ratio first into inverse SSLE appeared to improve the results. Results not included here showed that the change in the order of the second (test at port 7) and the third pumping test (test at port 3) did not change the pattern of the resulting K and S_s tomograms significantly.

For the synthetic as well as real THT cases 1 and 2, four data points (at 0.5 s, 1 s, 3 s and 20 s) were extracted from each observation port (both fracture and matrix observation ports) to capture the entire drawdown curve. The total number of observed data points used from each pumping test ranged from 116 to 120. In total, 356 drawdown records from three different pumping tests were utilized to perform synthetic as well as real THT cases 1 and 2. The ports completed within the matrix did not show a response to any of the pumping tests. Therefore, zero

drawdown was input to the inverse model for each matrix observation port for both synthetic as well as real THT cases 1 and 2.

Table 4.8.2.3: Equivalent K and S_s estimated by PEST from pumping tests at ports 3, 5, and 7.

Pumped Port	Port 3	Port 5	Port 7
Estimated K (cm/s)	2.80×10^{-2}	1.40×10^{-2}	3.00×10^{-2}
Max K (cm/s)	3.90×10^{-2}	1.70×10^{-2}	4.00×10^{-2}
Min K (cm/s)	2.10×10^{-2}	1.10×10^{-2}	2.00×10^{-2}
Estimated S_s (/cm)	1.30×10^{-3}	2.00×10^{-2}	4.00×10^{-3}
Max S_s (/cm)	7.50×10^{-3}	4.00×10^{-2}	2.00×10^{-3}
Min S_s (/cm)	2.30×10^{-3}	1.00×10^{-2}	9.00×10^{-3}

4.8.2.6 Results from transient hydraulic tomography

4.8.2.6.1 Inverse modeling of synthetic data

Figure 4.8.2.3a-3c are the K tomograms obtained by inverting the synthetic transient head data one, two, and three pumping tests, respectively, while Figure 4.8.2.3d is the estimated ln K variance ($\sigma^2_{\ln K}$) map corresponding to the K tomogram of Figure 4.8.2.3c. On Figure 4.8.2.3a-d, the open black circle represents the pumped port location, while the solid black circles represent the ports which were monitored during the pumping tests. Thin dashed lines on Figure 4.8.2.3c indicate the locations of the horizontal and vertical fractures. Figure 4.8.2.3a shows that with only one pumping test, areas with higher K relative to the background that corresponds to a portion of the horizontal fracture and the vertical fracture in the central portion of the fractured rock block begin to emerge. As more tests are included into the SSLE algorithm, details to the high K zones corresponding to the fracture pattern emerges. In particular, the final K tomogram (Figure 3c) using three pumping tests reveals considerable detail to the fracture pattern and the connectivity of the features away from the two constant head boundaries. Less detail is available near the two constant head boundaries because the drawdowns induced near the boundaries are considerably less than the interior of the fractured rock block. In contrast, details to the fracture pattern are evident near the top and bottom no-flow boundaries where drawdowns tend to be magnified. The $\sigma^2_{\ln K}$ map on Figure 3d reveals that the lowest $\sigma^2_{\ln K}$ are found along the fracture and the highest within the matrix where the uncertainties are high.

Figures 4.8.2.4a-4c show the corresponding S_s tomograms that were estimated simultaneously. Similar to Figures 4.8.2.3a-3c, details to the fracture pattern where S_s values are lower than the background become more evident as more pumping test data are included into the inverse model. Figure 4.8.2.4d is the estimated ln S_s variance ($\sigma^2_{\ln S_s}$) map corresponding to the S_s tomogram of Figure 4.8.2.4c. Similar to Figure 4.8.2.3d, the $\sigma^2_{\ln S_s}$ map on Figure 4.8.2.4d reveals that the lowest $\sigma^2_{\ln S_s}$ are found along the fractures.

One should keep in mind that the synthetic data utilized to generate the synthetic K and S_s tomograms were obtained from forward simulations of pumping tests in the fractured rock block based on Figure E1 in Appendix E. In these forward simulations, we assigned uniform values of K and S_s for the fracture and matrix. According to Yeh et al. (2011), if drawdown data are available at every element, one should be able to estimate the K and S_s values perfectly for the

fracture and matrix. However, due to lack of drawdown data at all elements, we instead obtain a distribution of K and S_s, with high K and low S_s values appearing at fracture locations.

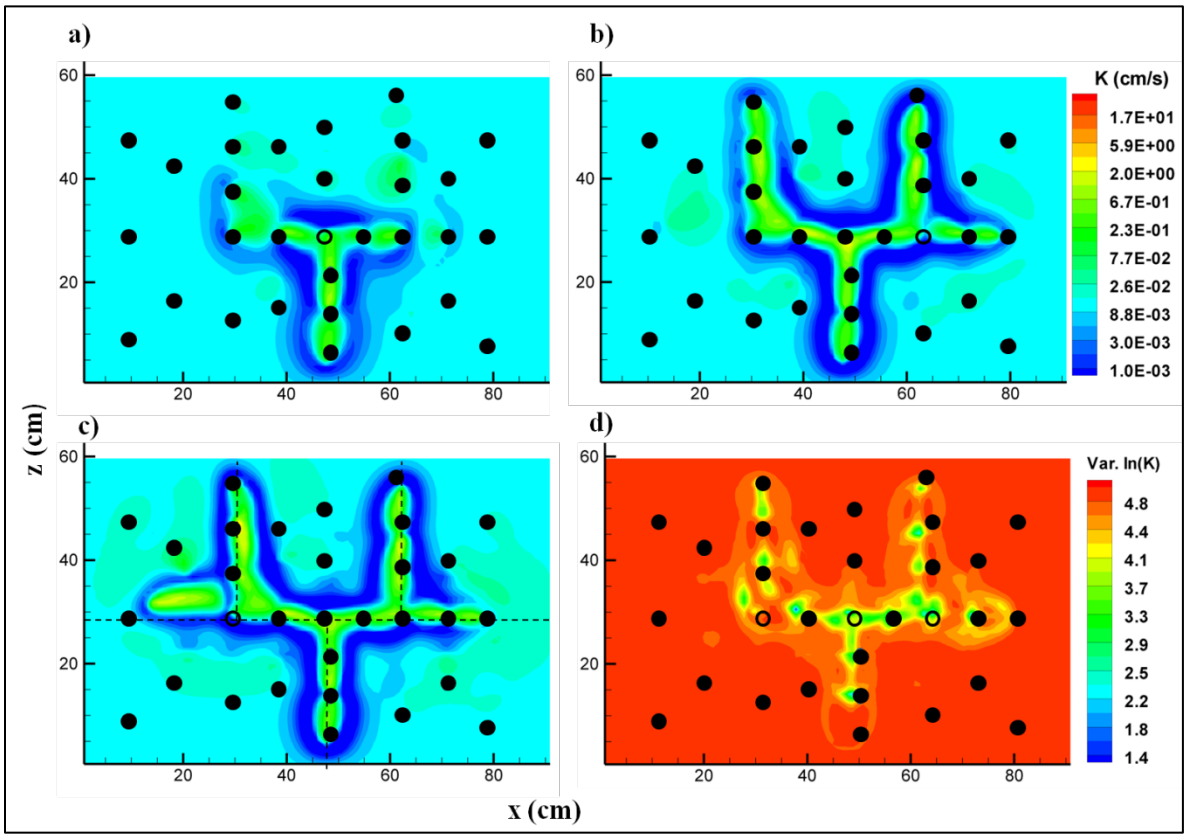

Figure 4.8.2.3: K tomograms (cm/s) computed using synthetic data from (a) one pumping test (port 5); (b) two pumping tests (ports 5, 7); (c) three pumping tests (ports 5, 7, 3); while (d) is the estimated ln K variance map associated with (c). Pumped locations are indicated by the open black circles, while observation intervals are indicated by solid black circles. Thin dashed lines on Figure 3c indicate the locations of the horizontal and vertical fractures. The image in each figure represents the x-z plane through the middle of the domain thickness.

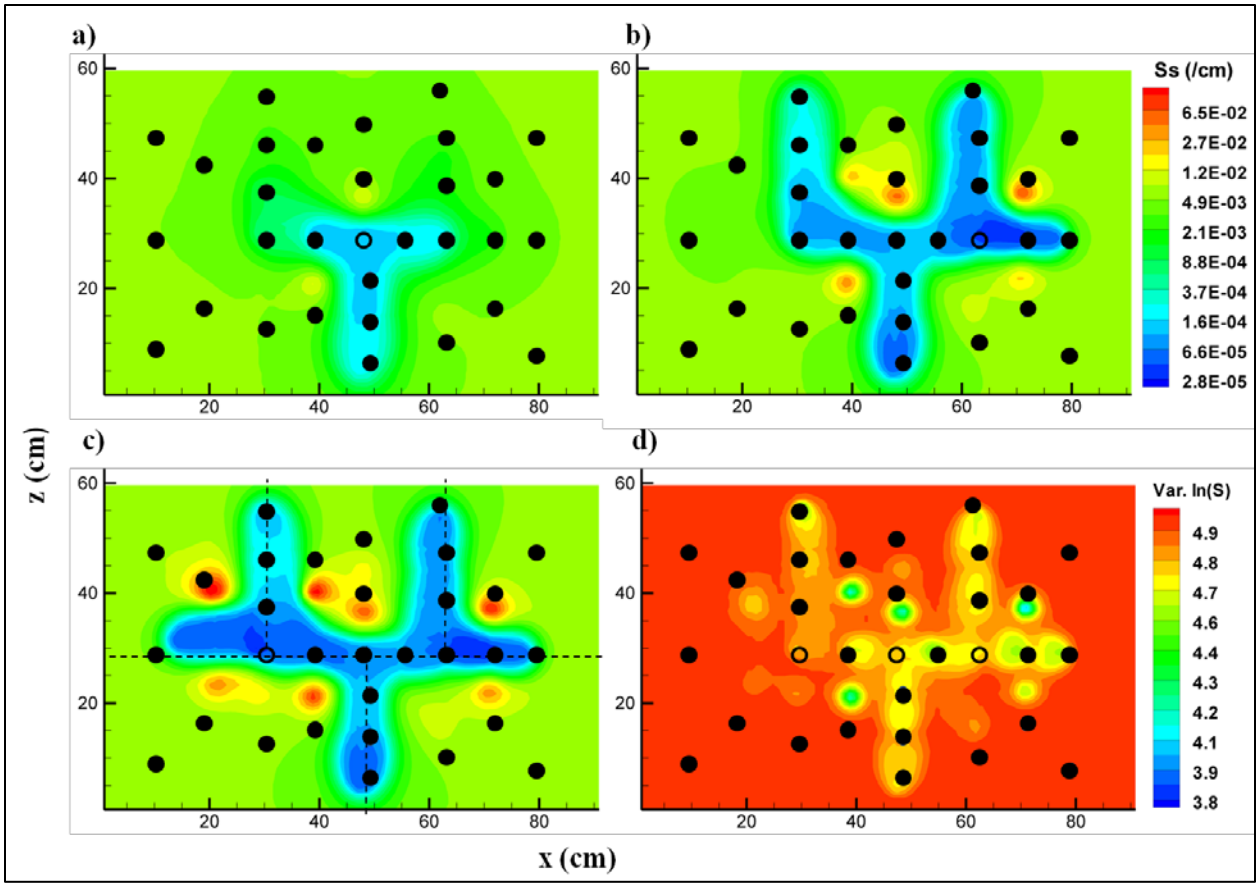

Figure 4.8.2.4: S_s tomograms (cm^{-1}) computed using synthetic data from (a) one pumping test (port 5); (b) two pumping tests (ports 5, 7); (c) three pumping tests (ports 5, 7, 3); while (d) is the estimated ln S_s variance map associated with (c). Pumped locations are indicated by the open black circles, while observation intervals are indicated by solid black circles. Thin dashed lines on Figure 4c indicate the locations of the horizontal and vertical fractures. The image in each figure represents the x-z plane through the middle of the domain thickness.

4.8.2.6.2 Inverse modeling of real data

We next examine the results from the inversion of real pumping test data obtained in identical fashion to the synthetic case. As in the synthetic case, the pumping tests took place at ports 5, 7, and 3 (real THT case 1). In reality, we do not know the true K and S_s distributions as in the synthetic case, although the locations of the fractures are visible on Figure 4.8.2.1. Figures 4.8.2.5a–5c and 4.8.2.6a-6c show the sequential improvement of the computed K and S_s tomograms as the number of pumping test data increases from one to three, while Figures 5d and 6d are the corresponding estimated ln K and ln S_s variances, respectively, after the inclusion of three pumping tests in the inverse model. The comparison of the K and S_s tomograms for the synthetic and real cases shows that the correspondence is very good. In particular, as in the synthetic case shown on Figure 4.8.2.3c and 4.8.2.4c, narrow regions of high K (Figure 4.8.2.5c) and low S_s (Figure 4.8.2.6c) zones that correspond with the actual fracture locations are identified with three pumping tests included in the inverse model. This is despite the fact that the SSLE treats the medium as a heterogeneous porous continuum.

The THT analysis of pumping tests at ports 5, 16, and 19 (real THT case 2) yielded similar K and S_s tomograms to results from real THT case 1 (Figures 4.8.2.5a-d; Figures 4.8.2.6a-d). Those results are included in the Supplementary Information section (see Figures S3 and S4). In both cases, the first pumping test included into the inverse algorithm was the test at port 5 located near the center of the fractured rock block. In case 1, the two other tests included were at ports 7 and 3, both of which were on the same horizontal fracture as in port 5. In real THT case 2, the latter two tests were located on ports 16 and 19 both of which were situated on the vertical fractures on the upper portion of the domain. This suggests that the pumping location may not be very sensitive to the final results as long as strong drawdown responses can be induced in the surrounding monitoring ports.

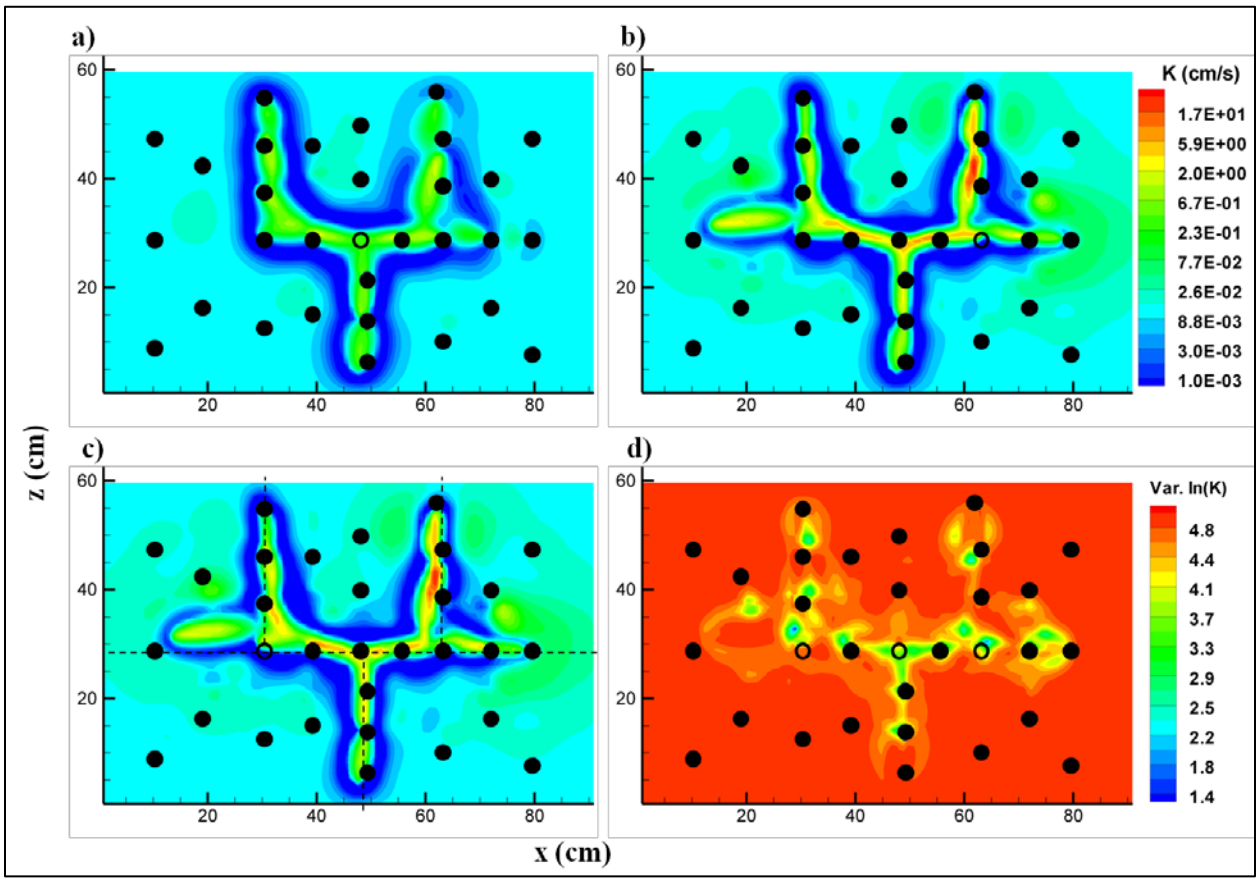

Figure 4.8.2.5: Case 1 K tomograms (cm/s) computed using real data from (a) one pumping test (port 5); (b) two pumping tests (ports 5, 7); (c) three pumping tests (ports 5, 7, 3); while (d) is the estimated ln K variance map associated with (c). Pumped locations are indicated by the open black circles, while observation intervals are indicated by solid black circles. Thin dashed lines on Figure 5c indicate the locations of the horizontal and vertical fractures. The image in each figure represents the x-z plane through the middle of the domain thickness.

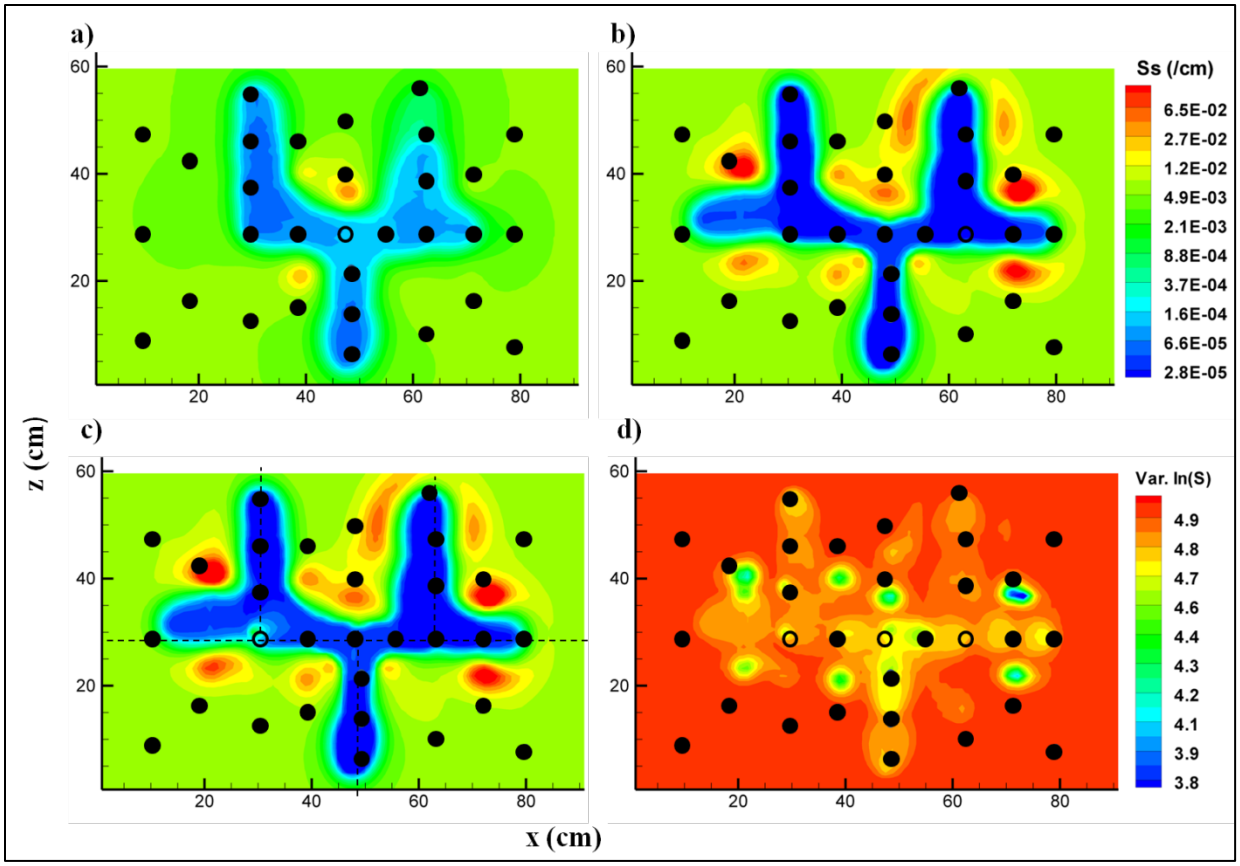

Figure 4.8.2.6: Case 1 S_s tomograms (cm^{-1}) computed using real data from (a) one pumping test (port 5); (b) two pumping tests (ports 5, 7); (c) three pumping tests (ports 5, 7, 3); while (d) is the estimated ln S_s variance map associated with (c). Pumped locations are indicated by the open black circles, while observation intervals are indicated by solid black circles. Thin dashed lines on Figure 6c indicate the locations of the horizontal and vertical fractures. The image in each figure represents the x-z plane through the middle of the domain thickness.

4.8.2.7. Discussion

4.8.2.7.1 Comparison of *K* and S_s tomograms obtained from synthetic versus real pumping test data

A visual comparison of the *K* and S_s tomograms generated by synthetic THT are compared to those generated by the real THT cases 1 and 2. This comparison is made to assess how the estimates from the inversion of noise-free synthetic data match the estimates from laboratory data that contains experimental noise. Our visual assessment reveals that the patterns of estimated *K* and S_s tomograms generated by the synthetic THT (Figures 4.8.2.3 and 4.8.2.4) and those estimated with real data (Figures 4.8.2.5, 4.8.2.6, E3, and E4) are quite similar suggesting the robustness of the estimates. Figures 4.8.2.7a and 4.8.2.7b represent the scatter plots of *K* and S_s values, respectively, obtained from the analysis of synthetic data (Figures 4.8.2.3c and 4.8.2.4c) to those obtained from the analysis of laboratory data (Figures 4.8.2.5c and 4.8.2.6c) for real THT case 1. The solid line represents the 1:1 line. Both figures 4.8.2.7a and 4.8.2.7b reveal that the data points cluster around the 1:1 line with some scatter suggesting generally good

correspondence between the two sets of tomograms. Similar results are obtained for the comparison between real and synthetic THT case 2 (Figure E5 in the Supplementary Information section).

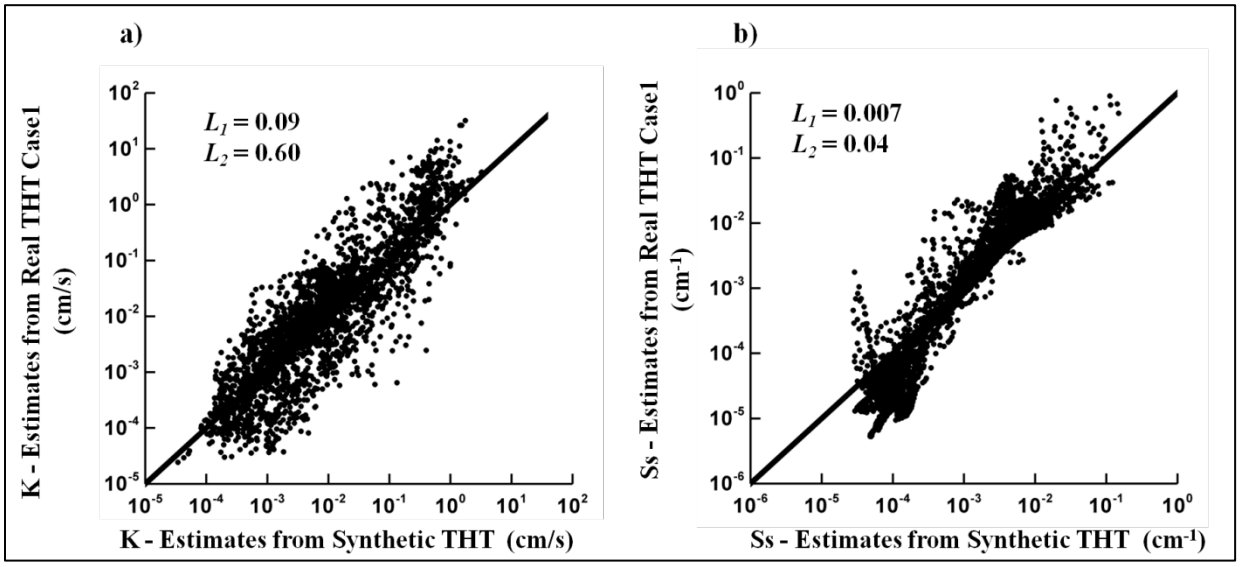

Figure 4.8.2.7: Scatter plots of (a) *K* and (b) S_s values from the inversion of real and synthetic data.

Two criteria, the mean absolute error (L_1) and mean squared error (L_2) norms were utilized to quantitatively evaluate the correspondence between the two sets of tomograms. Both L_1 and L_2 norms were calculated so that the mean absolute and mean squared errors can be compared. The L_1 and L_2 norms are computed as:

$$L_1 = \frac{1}{n}\sum_{i=1}^{n}\left|\chi_i - \hat{\chi}_i\right| \tag{4.8.2.4}$$

$$L_2 = \frac{1}{n}\sum_{i=1}^{n}\left(\chi_i - \hat{\chi}_i\right)^2 \tag{4.8.2.5}$$

where n is the total number of data, i indicates the data number, and χ_i and $\hat{\chi}_i$ represent the estimates from the two sets of data. To compute the L_1 and L_2 norms, we utilized the *K* and S_s values for each element from the tomograms estimated from the synthetic and real data.

The visual assessment of the scatter plots (Figures 4.8.2.7a and 4.8.2.7b) and the L_1 and L_2 norms suggest a good fit between these two sets of tomograms. This suggests that the THT analyses of the real pumping test data (real THT cases 1 and 2) yield results that are comparable to those from the synthetic data set for this fractured rock block.

4.8.2.7.2 Comparison of *K* and S_s tomograms from two real cases

The two sets of estimated *K* and S_s tomograms obtained from the inversion of pumping test data ports 5, 7, and 3 (real THT case 1) as well as ports 5, 16, and 19 (real THT case 2) are visually compared with the photograph of the fractured dolostone (Figure 4.8.2.1) to evaluate how well the fracture pattern is captured by THT analysis based on the SSLE code. The locations

of the horizontal and vertical fractures are also indicated as thin dashed lines on the final K and S_s tomograms. The visual comparison of snapshot of the fractured rock block (Figure 4.8.2.1) and the estimated K and S_s tomograms from the synthetic case (Figure 4.8.2.3c and 4.8.2.4c) as well as the real THT case 1 (Figure 4.8.2.5c and 4.8.2.6c) and real THT case 2 (Figure E3c and E4c) all reveal that the THT analysis of the laboratory pumping tests captured the fracture pattern and their connectivity quite well. In particular, the high K zones in Figures 4.8.2.3c, 4.8.2.5c, and E3c as well as the low S_s zones in Figure 4.8.2.4c, 4.8.2.6c, and E4c clearly show the fractures and their connectivity, although the high K and low S_s zone do not continue to the edge of the rock, which may be due to the boundary effect, as pointed out earlier.

A scatterplot of the K values from real THT cases 1 and 2 is shown on Figure 4.8.2.8a. A similar figure (Figure 4.8.2.8b) is shown to compare the S_s values. In both figures, the solid line represents the 1:1 line. Figures 4.8.2.8a reveals that while the scatter is large, the K values from the two cases cluster around the 1:1 line without much bias. On the other hand, examination of Figure 4.8.2.8b shows that the S_s values scatter around the 1:1 line, but there is a noticeable bias suggesting that there are some differences in the S_s values between real THT cases 1 and 2.

These results indicate that the changing the location of the second and third pumping tests did not significantly impact the K estimates from hydraulic tomography in this fractured rock block. However, the S_s estimates may be more sensitive to the location of the pumping tests based on Figure 4.8.2.8b. Here, the pumping test at port 5 was inverted first during both real THT cases 1 and 2. As described earlier, the pumping test at port 5 had the highest flow rate and stressed all the fractures more or less as it is located near the middle of the fractured rock block. Including the pumping test at port 5 in the inverse model followed the recommendation of Illman et al. (2008) that found that including the data with the highest signal-to-noise ratio first into the SSLE code improved the results when there is noise in data. The main reason behind this is that SSLE updates the K and S_s tomograms after each iteration and uses a weighted linear combination of the differences between the simulated and observed pressure heads to improve the estimates. Therefore, the K and S_s distribution estimated in the beginning of inversion process significantly impact the estimated tomograms. A version of the HT algorithm (SimSLE) that includes all data sets simultaneously for interpretation (Xiang et al., 2009), eliminates this ad hoc approach, although this approach can be significantly more computationally expensive.

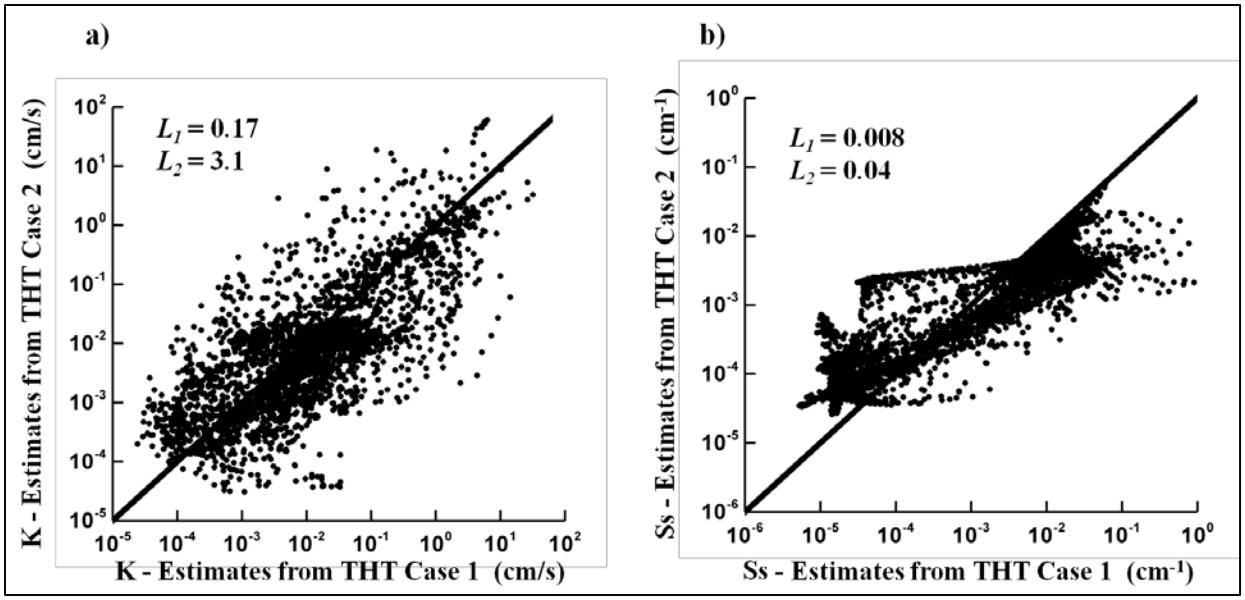

Figure 4.8.2.8: Scatter plots of (a) K and (b) S_s values from case 1 to case 2. The solid line represents the 1:1 line.

4.8.2.7.3 Comparison of estimated geometric mean of K from THT to those from the flow-through tests

To quantitatively compare the K estimates from the real THT cases 1 and 2 with the K_{eff} obtained from the flow-through tests, we calculated the geometric mean of K estimates obtained from case 1 ($K_G = 1.30 \times 10^{-2}$ cm/s) and case 2 ($K_G = 1.00 \times 10^{-2}$ cm/s). The values of K_{eff} obtained through the four separate flow-through tests yielded a range of 1.30×10^{-2} cm/s to 1.70×10^{-2} cm/s. This suggests that the K_G from the THT analysis somewhat underestimates the K_{eff} from the flow through tests. One potential reason for this is that the K tomograms from both cases 1 and 2 are smoothed out near the constant head boundary which could have lowered the mean conductivity.

4.8.2.7.4 Prediction of independent pumping tests

The K and S_s tomograms estimated for the real THT cases 1 and 2 were used to predict 5 pumping tests (ports 4, 6, 12, 15 and 18) that were not used in the construction of the tomograms. This is one form of validating the estimated K and S_s tomogram. Forward simulations are again performed using SSLE (Zhu and Yeh, 2005) with the same model domain used for the inversion.

Comparisons of observed (solid) and predicted (dashed) drawdown curves for real THT case 1 are presented in Figure 4.8.2.9 (test at port 12), while similar plots for the other ports are included in the Supplementary Information section (Figures E6 – E9). Plots comparing the observed and predicted drawdown curves for the same five pumping tests for real THT case 2 are included in the Supplementary Information section (Figure E10 – E14).

Examination of Figure 4.8.2.9 and Figures E6 – E9 reveals that, during the independent tests, the simulated drawdown matched the observed for most of the monitoring intervals, but there are some exceptions for ports near the pumped port due to excessive noise resulting from pumping. However, the simulated and observed drawdowns seem to match better at later time. At early time, many of the matches are poor and some are of intermediate to fair quality. The drawdown is primarily controlled by K at late time, while early time drawdown is controlled by

the diffusivity (α) of the rock ($\alpha = K/S_s$). As discussed earlier, wellbore storage may have played an important role in delaying the drawdown responses for the observed case which underscores the need to accurately represent borehole geometry. In addition, the estimated tomograms do not exactly replicate the actual values for the fractured rock, which may have led to these deviations between observed and predicted drawdowns especially at early time. However, there was no drawdown (real THT case 1) or a very small drawdown (real THT case 2) at the matrix ports for the simulated cases, which was consistent with the observed drawdowns.

Figure 4.8.2.10 shows the scatter plots of observed versus simulated drawdowns for the 5 independent pumping tests for real THT case 1. Each plot on Figure 4.8.2.10 represents the drawdown values from all the fracture and matrix observation intervals at 0.5, 1, 3, and 20 seconds since the corresponding pumping test began. The solid line is the 1:1 line indicating a perfect match. The dashed line is a best fit line, and the parameters describing this line, coefficient of determination (R^2) as well as L_2 norm for the corresponding tests are included on each plot. The R^2 values indicate the quality of match between the simulated and observed drawdowns, while the slope and the intercept of the linear model fit are the indication of bias. The L_2 norm was calculated using equation (4.8.2.5) with the χ_i and $\hat{\chi}_i$ now representing the observed and simulated drawdown from each monitoring port. Similar scatter plots for the independent pumping tests for real THT case 2 can be found in the Supplementary Information section (Figure S15).

From Figure 4.8.2.10, it can be seen that for most tests the data points cluster around the 1:1 line with some bias indicated by the slope of the linear model fit. The only exception is the pumping test at port 18, suggesting comparatively poor estimates for the pumping test at that port. In particular, the observed drawdown is somewhat higher than the simulated drawdown in some of the ports which suggests that the K estimates may be too high. The scatter plots for the independent tests for real THT case 2 provided in the Supplementary Information section (Figure E15) also show similar matches between the observed and simulated drawdowns.

4.8.2.7.5 Uniqueness of results

The THT analysis conducted with the SSLE code treats the fractured rock as a heterogeneous porous continuum, which makes it challenging to handle the high contrast between the fracture and matrix K and S_s values. Therefore, the estimated K and S_s values for the fractures and the matrix may not exactly correspond to actual values as shown by the results of the synthetic THT case (Figures 4.8.2.3c and 4.8.2.4c). Consequently, this will lead to the deviation of drawdown responses at the monitoring intervals when the tomograms are utilized for predicting pumping tests not used in the construction of the tomograms.

Despite this shortcoming, we found that by and large, the simulated drawdown responses captured the observed drawdown behaviors in the monitoring ports quite well, indicating the robustness of THT analysis of our laboratory data. In addition, the THT analysis of pumping tests revealed the fracture locations and their connectivity quite accurately which is highly encouraging. Based on the work of Illman et al. (2009) and this study, we feel that hydraulic tomography appears to be a promising tool to delineate the K and S_s distributions in fractured rocks, the dominant fracture patterns and their connectivity, both of which has been a challenge for decades. The advantage of hydraulic tomography is that, it does not require measurements of the fracture size, shape, aperture, detailed deterministic or statistical information of the geometry of fractured zone and the spatial distribution of these parameters which are not typically available between boreholes. In particular, Neuman (2005) noted that experience shows that the

density of fractures counted on surface outcrops is significantly different from those obtained from boreholes implying that information collected along surface outcrops may not be representative of conditions inside the rock mass. In addition, boreholes typically sample a small portion of the rock and the intersection of fractures with a given borehole may not be an indication of the geometry and density of fractures in the intact rock. Rather, hydraulic tomography relies on hydraulic tests conducted across boreholes, which result in the propagation of multiple drawdown signals across a large portion of the fractured rock that are relatively easy to collect. These drawdown signals carry direct information on hydraulic properties of both the fractures and matrix which cannot be obtained from mapping fractures. Thus, hydraulic tomography holds significant potential for characterizing fractured rocks.

Illman et al. (2007) discussed the issue of non-uniqueness of estimated K tomograms, as there could be an infinite number of solutions to the steady-state inverse problem for a heterogeneous K field, even when all of the forcing functions are fully specified. Similarly, non-uniqueness of computed heterogeneous K and S_s tomograms could also be an issue for the transient inverse problem. But according to some researchers (Yeh et al., 1996; Yeh and Liu, 2000; Liu et al., 2002; and Yeh and Simunek, 2002) when data are available at all estimated locations, the inverse problem becomes well-posed and ultimately lead to a unique and correct solution. More recently, Yeh et al. (2011) suggested that the non-uniqueness issue associated with highly parameterized problems arises from a lack of information required to make the problems well defined. They also suggested necessary conditions for an inverse model of groundwater flow to be well defined, which are: "the full specifications of 1) flux boundaries and source/sink, and 2) heads everywhere in the domain at least at three times (one of which is $t = 0$) and head change everywhere over the times must be nonzero for transient flow". Through numerical experiments, Yeh et al. (2011) showed that when the necessary conditions are fulfilled, the inverse problem results in a unique and correct solution.

We acknowledge that there are many possible K and S_s tomograms that can provide equally good matches between the simulated and observed hydrographs for the hydraulic tomography survey in the fractured rock because the conditions listed above for constraining a highly parameterized inverse problem are not fully given. Nevertheless, the SSLE algorithm constrains the estimates with specified mean and covariance function of the K and S_s parameters, and it seeks conditional unbiased mean estimates. That is, the estimates are unique in term of these constrains; they are the statistically unbiased estimates given all these non-redundant information from HT survey. They are, however, not necessarily the true fracture and matrix hydraulic conductivity and specific storage distributions. In spite of the uncertainty (or their deviation from the true), the estimates based on SSLE algorithm have been unequivocally shown to be capable of predicting responses of aquifers due to independent events which were not used in the analysis of hydraulic tomography by previous studies (e.g., Illman et al., 2007, 2008, 2009, 2010; Liu et al., 2007; Xiang et al., 2009; Berg and Illman, 2011a,b; Huang et al., 2011). Our study here further substantiates its robustness for hydraulic tomography survey of the fractured rock block.

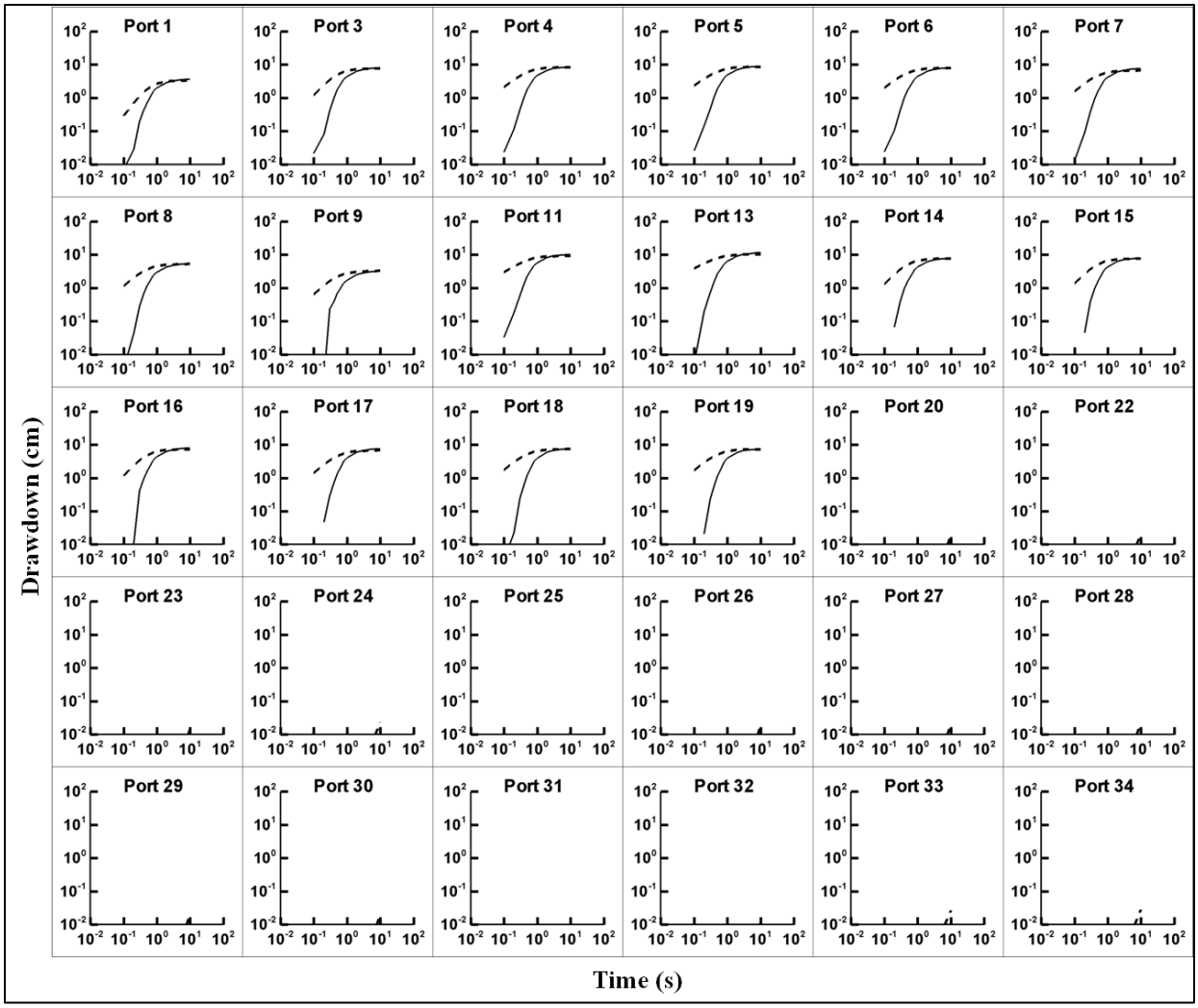

Figure 4.8.2.9: Drawdown versus time at the monitoring ports during the pumping test at port 12. The solid curve represents the observed drawdown curve while the dashed curve represents the predicted drawdown curve using the final K and S_s tomograms from case 1.

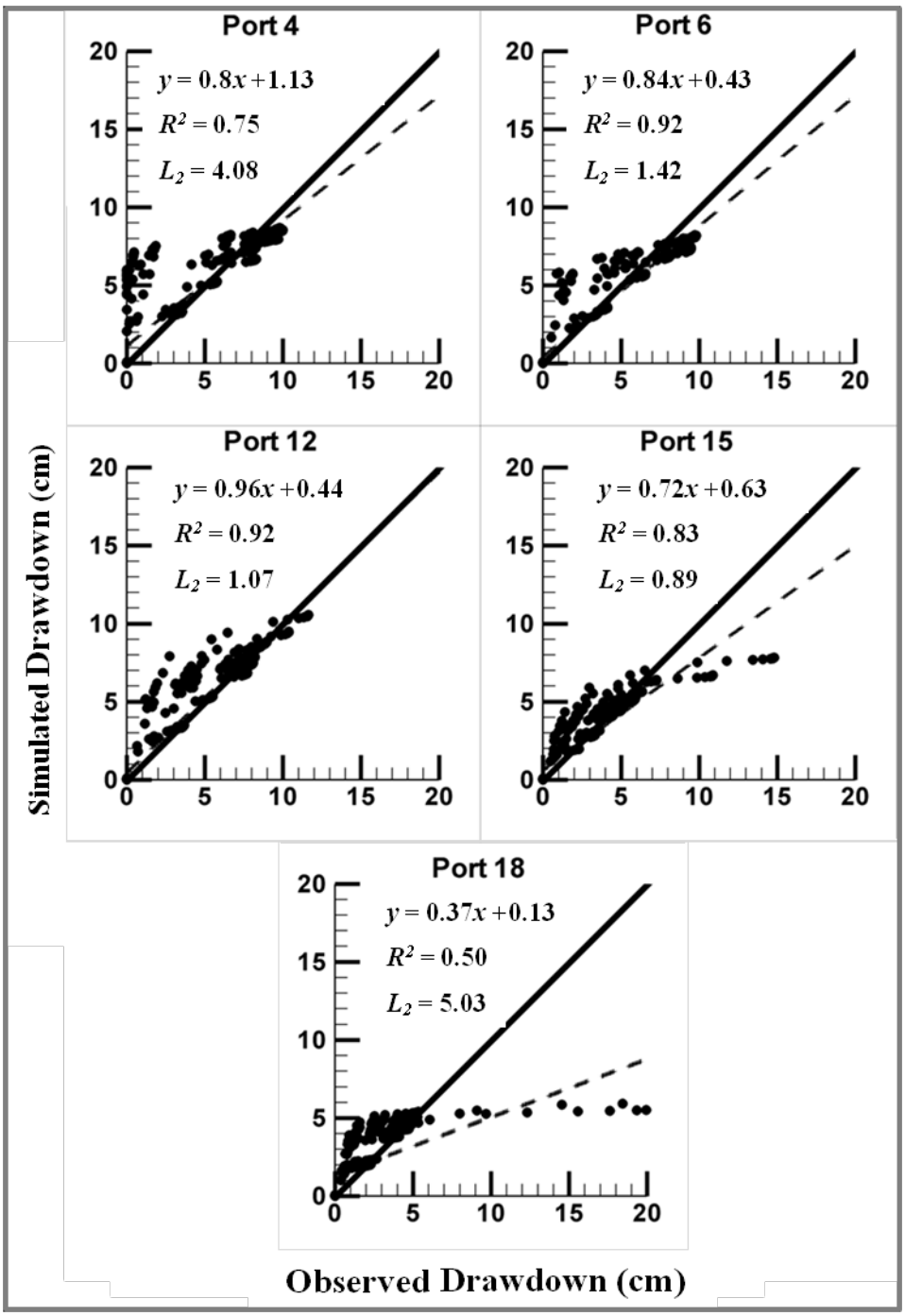

Figure 4.8.2.10: Scatter plots of 5 pumping tests using the estimated K and S_s fields from the THT analysis (case 1). The solid line is a 1:1 line indicating a perfect match. The dashed line is a best fit line, and the parameters describing this line as well as L_2 norm for the corresponding tests are on each plot.

4.8.3 Conservative tracer tests in a fractured dolostone rock block

4.8.3.1 Methods

Upon completion of the hydraulic tests, two tracer tests were conducted using bromide (Br^-) as conservative tracer to aid in the design of Trichloroethene (TCE) dissolution experiment. The tracer tests and the results obtained from the tests are described in this chapter.

The preparation of the flow cell has been described in section 4.8.2. Tracer tests were conducted by fixing the hydraulic gradient across the rock sample. The hydraulic gradient was fixed by setting drip points at the end reservoirs at different heights. A peristaltic pump was used to supply water continuously into the influent reservoir and the drip point was maintaining constant head in the influent and effluent reservoirs. Figure 4.8.3.1 represents the schematic diagram of the experimental set-up for the tracer experiments, where injection and all the sampling ports are indicated. Figure 4.8.3.2a shows the photograph of the flow cell and in Figure 4.8.3.2b injection and sampling ports on the horizontal fracture are indicated on the photograph with rectangular white box.

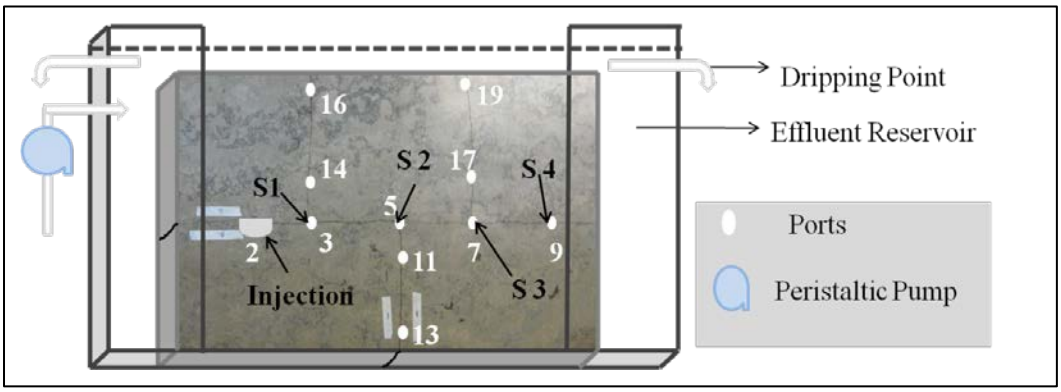

Figure 4.8.3.1: Schematic Diagram of the Experimental Set-up for the Tracer Experiments. The white ovals indicate the sampling ports. S1, S2, S3 and S4 are the four sampling ports.

Before injecting the tracer a steady flow field was established by fixing the hydraulic gradient across the rock sample and the flow rate was measured at the effluent dripping point. Once the flow field became stable, 100 mg/L bromide (Br^-) solution was injected into a hole below the flow path marked as “injection” (port 2) in Figure 4.8.3.1. The hole was made and filled with sand prior to the enclosure of the fractured block into the flow cell. Before the hole was filled with sand, the porosity and hydraulic conductivity of the sand were measured in the laboratory, which were approximately 0.1 cm/s and 0.4 – 0.5 respectively. A brass fitting was placed on the rock to cover the hole using titanium putty (Devcon, Danvers, MA, USA). To hold the sand in place, a stainless steel mesh was placed underneath the brass fitting. The injection and sampling ports were equipped with Swagelok fittings (brass Swagelok tube fitting bored-through male connector, 1/16 in. Tube OD x 1/8 in. Male NPT) in order to hold the stainless steel needle used for injection or sample collection and a one-way luer stopcock to prevent any fluid loss while injecting or sampling. The bromide (Br^-) solution was injected into the sand filled hole (marked as port 2 in Figure 4.8.3.1) using a peristaltic pump connected to the needle at a known rate by opening the stopcock. After a certain time, the injection was stopped and the stopcock was closed. Each sampling port was also equipped with a Swagelok fitting to hold the

needle used to collect the sample and a one-way luer stopcock to prevent any fluid loss while sampling. Deionised (DI) water used for all the tracer experiments.

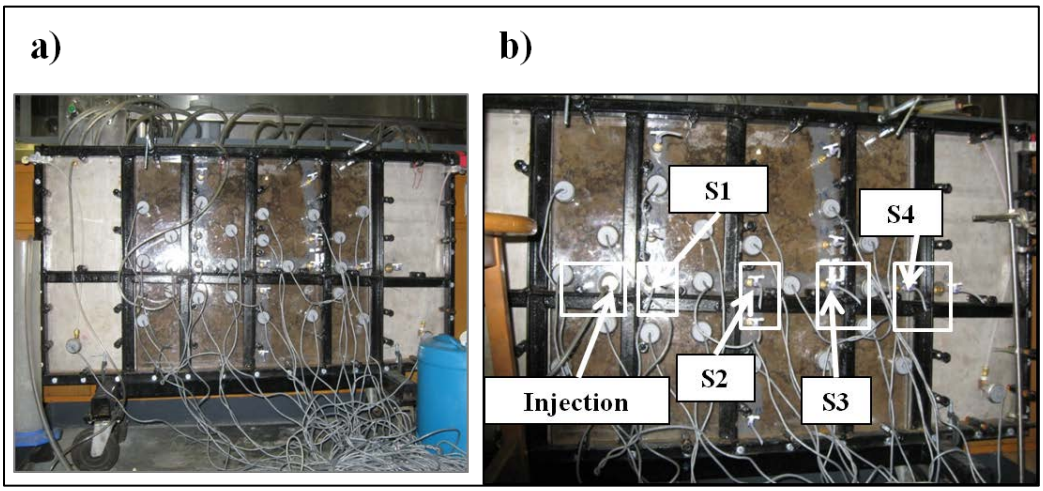

Figure 4.8.3.2: a) Photograph of the Experimental block and b) Injection and sampling ports. Injection and sampling ports are indicated in the flow cell with white rectangular box. S1, S2, S3 and S4 are the four sampling ports.

During each tracer test, the ambient flow rate was approximately 2.7 mL/min. After the flow field was established, a tracer solution with bromide (Br^-) at a concentration of 100 mg/L was injected into port 2 (Figure 4.8.3.1) at a rate of 15 mL/min during the 1st test and 14 mL/min during the 2nd tests for 60 seconds. The down gradient monitoring ports 3, 5, 7, 9 indicated in Figure 4.8.3.1 were sampled periodically. During sampling each cycle, port 3 was sampled first, as it was the closest to the source (injection port) and then port 5, 7 and 9 (Figure 4.8.3.1) were sampled respectively. The duration of the experiment was approximately 23 minutes and 36 minutes for the 1st and 2nd tracer experiments, respectively. Each of the 4 sampling ports was sampled 10 times during the 1st test, while each of them was sampled 15 times during the 2nd test. In total 40 and 60 samples were collected during the 1st and 2nd tracer experiment respectively.

Samples were collected using 1.5mL vials, which were filled to the top to avoid volatilization and mass loss in the head space. Water samples taken during each tracer test were chilled in a refrigerator at 4°C until they were analyzed. A Dionex ICS-2000 Ion Chromatograph (IC) equipped with an Ion-Eluent Generator and conductivity detector was used to determine the bromide concentrations.

4.8.3.2 Results and discussion

Similar results were obtained from both tracer experiments. Bromide breakthrough curves at the monitoring ports 3, 5, 7 and 9 (indicated in Figure 4.8.3.1) from tracer experiment 1 and 2 are presented in Figure 4.8.3.3 and Figure 4.8.3.4, respectively. The solid black line parallel to the vertical axis in Figure 4.8.3.3 and Figure 4.8.3.4 shows the time when injection was stopped. The pattern of the break through curve at a specific monitoring port obtained from each test was identical. Vertical fracture ports 11, 13, 14, 16, 17, 19 (indicated in Figure 4.8.3.1) were also sampled once at the end of each experiment and no bromide was detected.

Examination of Figure 4.8.3.3 and Figure 4.8.3.4 shows that the bromide concentration reached its peak at all of the monitoring ports within a few second of injection. In both tracer

experiments, the volume of injected solution was larger than the hole, used for injection. Therefore, the bromide mass reached flow path (horizontal fracture) as soon as it was injected, leading to the peak concentration at the monitoring ports within a few seconds of injection. This was the reason why the highest bromide concentration was found at port 3 (closest to the source) during the 1st sample. The peak arrival time at ports 5, 7 and 9 (indicated in Figure 4.8.3.1) increased as the distance from the source increased. A quick calculation revealed that the peak arrival time at the monitoring ports roughly matched the flow velocity.

Similarly, from Figure 4.8.3.3 and Figure 4.8.3.4 it can be found that the peak concentration was the highest for port 3, decreased gradually for ports 5, 7 and 9. Thus, the breakthrough curve became broader along the flow path. During each test, the highest peak concentration was found at the monitoring port (port 3) that was sampled 1st in each cycle. The peak concentration went down gradually along the flow path, as the sampling port move further from the source.

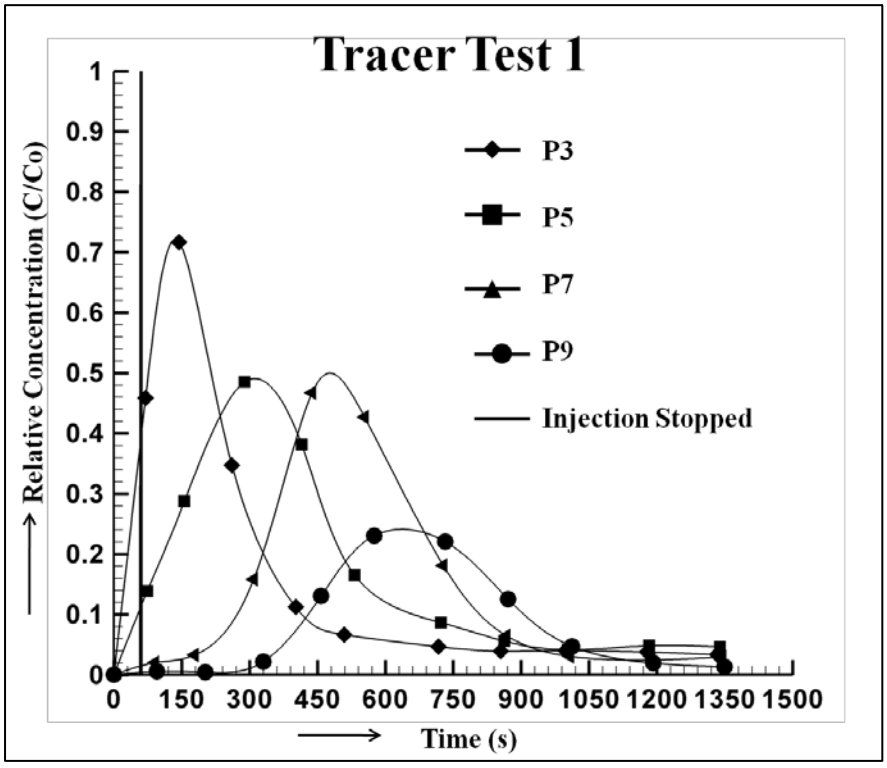

Figure 4.8.3.3: Bromide Breakthough Curves at the Monitoring Port during Tracer Test 1. The black vertical line indicates the injection stop time.

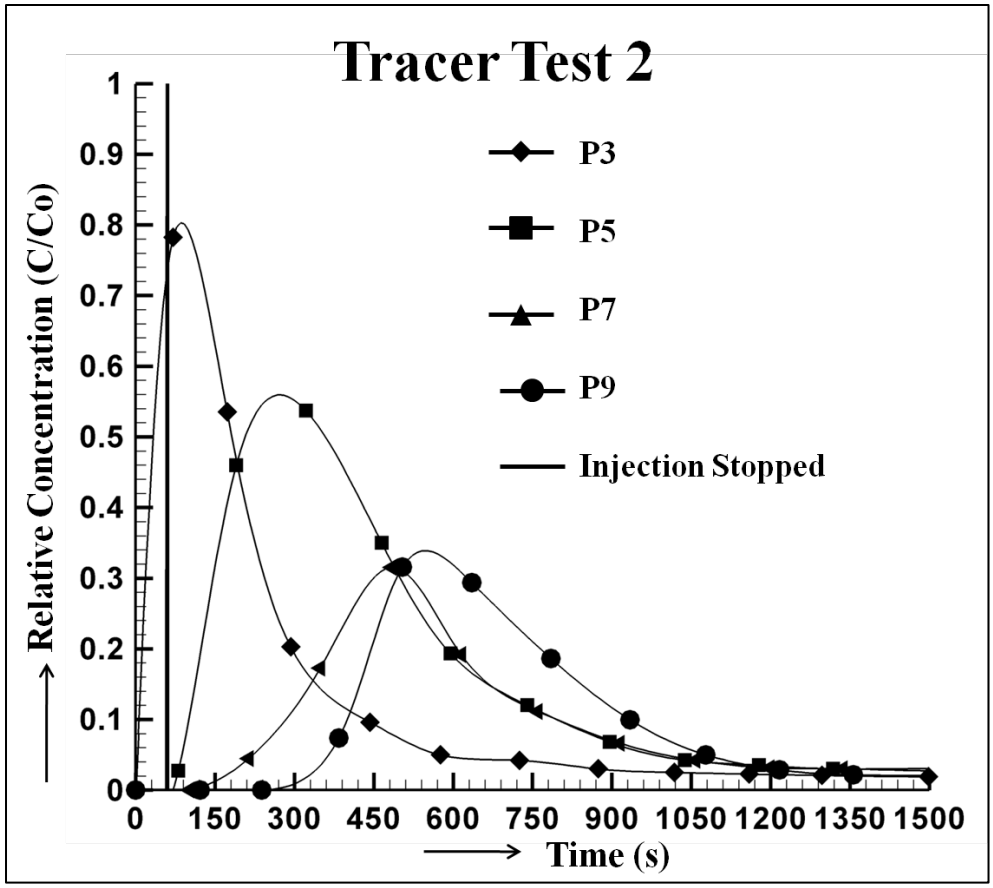

Figure 4.8.3.4: Bromide Breakthough Curves at the Monitoring Port during Tracer Test 2. The black vertical line indicates the injection stop time.

Table 4.8.3.1: Injected Mass and the Mass Crossing Sampling Ports during Tracer Test 1.

Injected Mass		Mass Crossing Sampling Ports	
Port	Mass (mg)	Port	Mass (mg)
2	1.5	3 5 7 9	0.9 0.98 0.87 0.5

Table 4.8.3.2: Injected Mass and the Mass Crossing Sampling Ports during Tracer Test 2.

Injected Mass		**Mass Crossing Sampling Ports**	
Port	**Mass (mg)**	**Port**	**Mass (mg)**
2	1.4	3	0.95
		5	1.2
		7	0.71
		9	0.72

The mass crossing each sampling port during each tracer experiment was estimated from the bromide breakthrough curves using trapezoidal rule. Tables 4.8.3.1 and 4.8.3.2 summarize the injected mass as well as the mass crossing the sampling ports during tracer experiment 1 and 2 respectively.

From Tables 4.8.3.1 and 4.8.3.2, it is evident that there is a significant difference in the injected mass and the mass crossing the sampling ports. During both tests, mass crossing port 5 is the closest to the injected. Although highest peak was found at port 3, mass crossing port 3 was less than the one that past port 5. Port 3, being the closest to the injection port, we assume, we missed the peak at port 3 where the bromide concentration reached its peak as soon as it was injected. The difference between injected mass and the mass that passed the sampling port became larger for port 7 and 9, as the sampling port moves further from the source. This difference is attributed to the bromide mass lost in samples collected at the ports closer to the source.

From the experience of the tracer experiments we decided to inject a TCE volume less than the pore volume of the sand that was used to fill the source hole, so that it does not overflow the hole and reach the flow path (horizontal fracture) as soon as it is injected, allowing us to capture entire breakthrough curve. Regarding sampling, we decided to sample only one down gradient monitoring port (port 9) during the trichloroethene (TCE) dissolution experiment instead of sampling 4 ports to prevent the mass loss. Port 9 was chosen to collect samples because it was the closet to the effluent reservoir.

4.8.4 TCE dissolution experiments in a fractured dolostone rock block: Introduction

After completing the tracer experiments, a known volume of Trichloroethene (TCE) was injected into a small reservoir to create a well characterized source zone. A constant flow field was established to conduct TCE dissolution experiment. In this chapter, the TCE dissolution experiment and the results obtained from the experiment are discussed.

4.8.4.1 Experimental Set-up and Description

The experimental set-up for the TCE dissolution experiment was same as the one used for the tracer experiments, described in section 4.8.3. Figure 4.8.4.1 represents the schematic diagram of the experimental set-up for the TCE dissolution experiment, where the injection and sampling ports are indicated as “Injection” and “Sample” respectively. Figure 4.8.4.2a is a photograph of the flow cell and in Figure 4.8.4.2b, the injection and sampling ports are indicated on the photograph with rectangular white box. All parts of the experimental system that would be in contact with water in the tank were constructed or sealed with inert materials. For example, the influent and effluent reservoirs were made of stainless steel. As mentioned in section 4.8.2, titanium putty (Devcon, Danvers, MA, USA) was used to attach the brass fittings (that were used as ports) to the front surface of the rock and sealed around it as well as to seal along the length of the fractures. Similar to the tracer tests, injection and sampling ports were equipped with Swagelok fittings to hold the stainless steel needle used for injection or sample collection and a one-way luer stopcock to prevent any fluid loss while injecting or sampling. Deionised (DI) water was used for the TCE dissolution experiment.

Before injecting TCE into the fractured rock, a steady flow field was established by fixing the hydraulic gradient across the rock sample and the flow rate was measured at the effluent drip point using graduated cylinder. Hydraulic head of the left and right reservoirs were approximately 60cm and 59 cm respectively, although they varied quite a bit. Once the flow field was stable, 2.25mL (3.3 gm) of pure phase (99%) TCE (Sigma Aldrich, St. Louis, MO, USA) was injected in a small reservoir using a syringe into the flow cell to create a source zone. The source zone was created by injecting the TCE into the sand filled hole below the flow path marked as “Injection” in Figure 4.8.4.1. The volume of injected TCE was selected based on the porosity of the sand (F-35 Bag sand, US Silica, Frederick, MD, USA) that was used to fill the hole. The sand porosity was measured at the laboratory which was 40% to 50%. We injected 2.25 mL TCE assuming the pore volume to be 35%, so that it does not overflow the reservoir. It is assumed that injected TCE occupies the bottom part of the reservoir. The source hole, where the TCE was injected has been described in section 4.8.3.

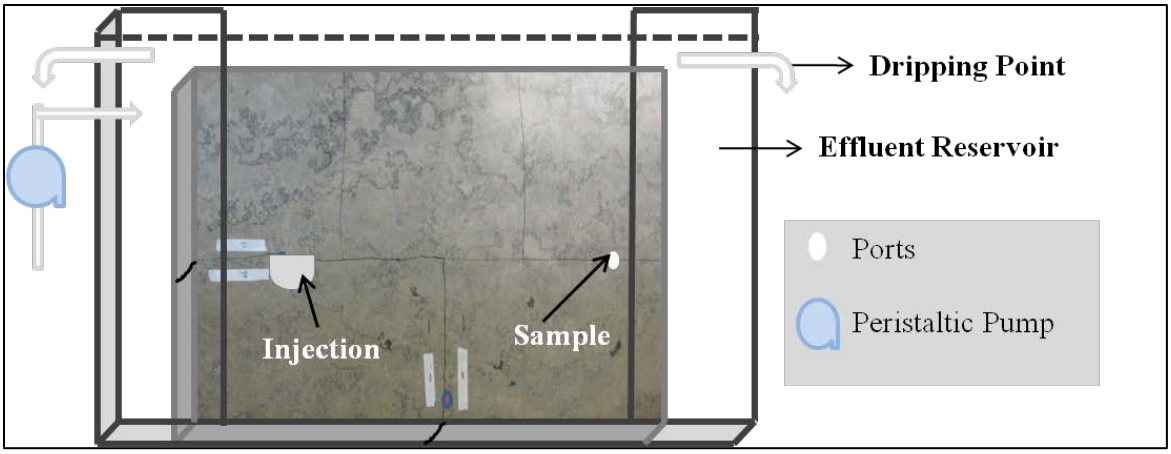

Figure 4.8.4.1: Schematic Diagram of the experimental set-up for the TCE dissolution experiment. The white oval indicates the sampling port.

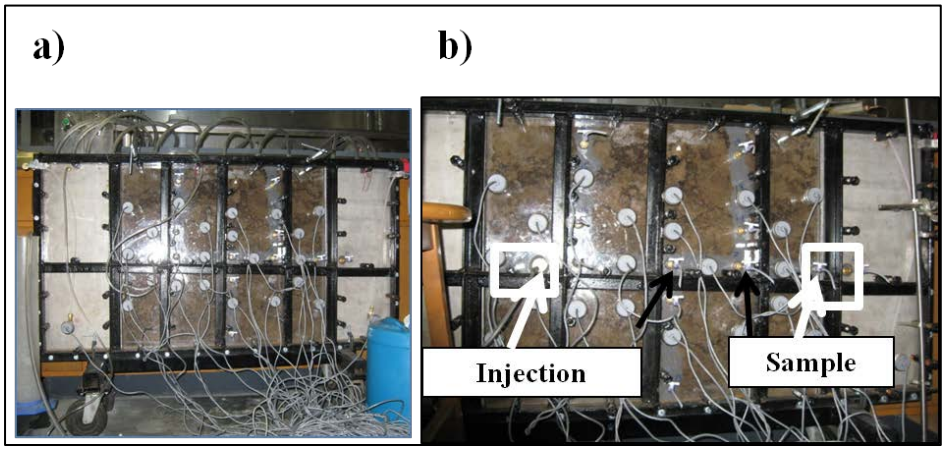

Figure 4.8.4.2: a) Photograph of the experimental block and b) Injection and sampling ports. Injection and sampling ports are indicated in the flow cell with white rectangular box.

After the injection, the down gradient monitoring port indicated as "Sample" in Figure 4.8.4.1 was sampled periodically using a needle for 86 days to monitor the TCE breakthrough curve. In total, 175 samples were withdrawn during the first 86 days referred to as the"1st part" of the TCE dissolution experiment. To monitor the TCE breakthrough in the fractured rock sample, only one down gradient monitoring port was sampled to reduce the mass loss that was discussed earlier. The rate of flow through the fracture was also measured periodically at the effluent dripping point throughout the experiment.

To conduct the 2nd part of the dissolution experiment, after 86 days of injection, flow through the fractured domain was shut off over a period of three weeks to let TCE diffuse into the flow path. After this period of flow shutoff, water flow through the fractured rock block was resumed and sampling continued for another two weeks to observe the anticipated rebound in concentration at the monitoring port.

Samples were collected in 2 mL vials and they were filled to the top to avoid volatilization and mass loss in the head space. Each water sample withdrawn during the dissolution experiment was chilled in a refrigerator at 4°C until they were analyzed. TCE concentrations

were determined using a Hewlett Packard 5890 Series II gas chromatograph (GC) equipped with a Ni63 ECD detector.

4.8.4.2 Results and discussion

Figure 4.8.4.3 shows the TCE breakthrough curve over 86 days which is also plotted along with the flow rate through the fractured rock block. In Figure 4.8.4.3, the left axis shows the TCE concentration and the right axis shows the flow rate. The solid black circles represent the TCE concentration, while the black rectangles represent the flow rate over time.

Examination of Figure 4.8.4.3 reveals that the flow rate was mostly stable throughout the experiment, with an exception at early time. The measured flow rate at the effluent drip point varied in between 2 mL/min to 3 mL/min except at very early time. At very early time flow rate went down to 1mL/min to 1.2mL/min due top very frequent sampling. Very frequent sampling (every 15 minutes) following the injection of TCE was likely responsible for this early time fluctuation of flow rate, as it became stable when the sampling was slowed down.

From the TCE concentration profile in Figure 4.8.4.3 it can be seen that at the monitoring port, TCE concentration reached its peak after 20 to 25 hours of injection which was about 67 ppm and declined gradually to 1ppm after 12 days and 0.1 ppm after 86 days of injection.

TCE mass removed through dissolution was estimated from the TCE concentration profile using trapezoidal rule which revealed that only 21% of the injected mass was recovered in 86 days. Therefore, TCE concentration at the monitoring port reached its tailing stage instead of staying at the peak, although the source was not depleted completely. One potential explanation may be the physical diffusive phenomenon due to the development of a concentration gradient over time between the source zone and the flow path. As the injected TCE was sitting at the bottom of the sand filled hole below the flow path, a layer of dissolved TCE developed in between the source zone and the flow path within a few hours of injection. Thus, after a few hours of injection, TCE had to diffuse from the source zone to the flow path through this dissolved layer, which was the anticipated phenomenon behind the TCE concentration going down gradually at the monitoring port before the complete depletion of the source zone. To investigate this, flow through the fractured domain had been shut off for three weeks and the 2nd part of the dissolution experiment (TCE rebound) was conducted.

During the 2nd part of the dissolution experiment, the flow through the fractured domain was turned off to investigate whether an increase in TCE concentration due to TCE diffusion through the dissolved layer to the flow path is observed or not. The flow was resumed after three weeks and the down gradient monitoring port was being sampled again for another two weeks to examine if there is any rebound in TCE concentration at the monitoring port.

Figure 4.8.4.4a represents the TCE concentration profile over 121 days (1st and 2nd part of the dissolution experiment) and a portion of the breakthrough curve, indicated by a rectangular box in Figure 4.8.4.4a has been expanded in Figure 4.8.4.4b for ease of visualization. Similar to Figure 4.8.4.3, in Figure 4.8.4.4a and b, the left axis shows the TCE concentration and the right axis shows the flow rate. The solid black circles represent the TCE concentration, while the black rectangles represent the flow rate over time.

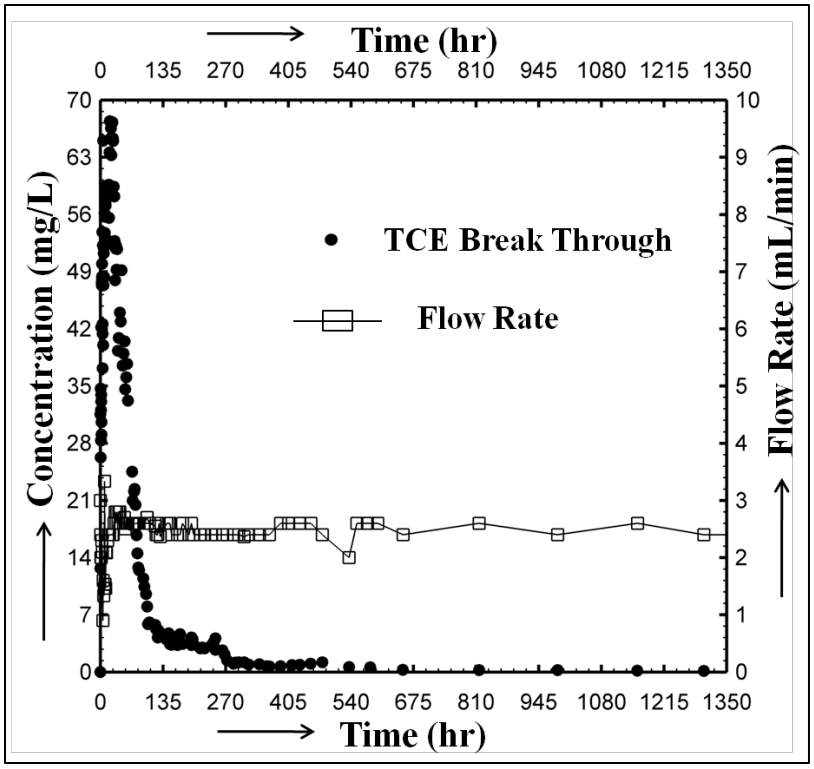

Figure 4.8.4.3: TCE Breakthrough Curve from the 1st part of Dissolution Experiment and Flow Rate over Time. Solid black circles represent the TCE concentration while the black rectangles represent the flow rate over time.

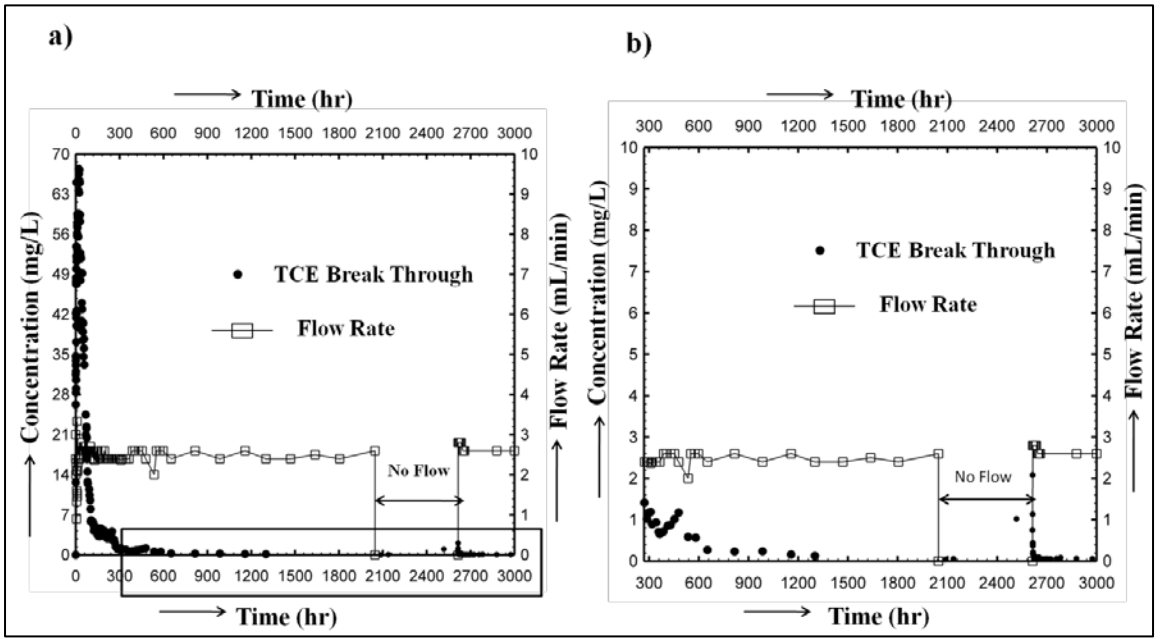

Figure 4.8.4.4: a) TCE Concentration Over 121 Days and b) Rebound in TCE Concentration. Solid black circles represent the TCE concentration while the black rectangles represent the flow rate over time.

Examination of Figure 4.8.4.4a and b reveal that, a slight rebound was observed in TCE concentration. TCE concentration increased to 2 ppm from 0.1 ppm and started to decrease again within a few minutes of starting the flow. In 121 days, the total dissolved mass was estimated to be 21.2 % of the injected mass.

To examine whether the rest of the mass diffused into the matrix, TCE concentration that could be diffused into the matrix in 121 days (to different distances from the fracture) was calculated using 1-D diffusion equation given by equation (4.8.4.1)

$$C_i\,(x,t) = C_0 erfc[\frac{x}{2\sqrt{tD_d}}] \qquad (4.8.4.1)$$

where, *Ci* is the TCE concentration at a distance *x* from the fracture at time *t*, *Co* is the initial concentration and *erfc*[*y*] is the complementary error function. In equation (4.8.4.1), D_d is the effective diffusion coefficient given by $D_d = D_0\tau$, where, D_0 is the free solution diffusion coefficient and τ is tortuosity. The free solution diffusion coefficient (D_0) and tortuosity (τ) values used for the calculation were 1.0×10^{-5} cm^2/s (i.e., Perry, 1984; Pankow and Cherry, 1996) and 0.1 respectively.

Estimated diffusive TCE front is shown in Figure 4.8.4.5 and the calculated concentration at corresponding distances are listed in Table 4.8.4.1. From Figure 4.8.4.5 and Table 4.8.4.1 it is evident that TCE penetrated about 0.1 cm (1 mm) into the rock matrix. Penetrated TCE mass into the rock matrix (both side of the horizontal fracture) was then estimated by multiplying the average concentration (arithmetic mean of all 9 concentrations given in Table 4.8.4.1) by the penetration volume. Penetration volume and estimated penetrated TCE mass into the rock matrix are also presented in Table 4.8.4.1. From Table 4.8.4.1, it is evident that approximately 0.02 gm of TCE could be penetrated into the rock matrix, which is only 0.61% of total injected mass. Therefore, the rest of the TCE mass is probably still present at the bottom of the hole.

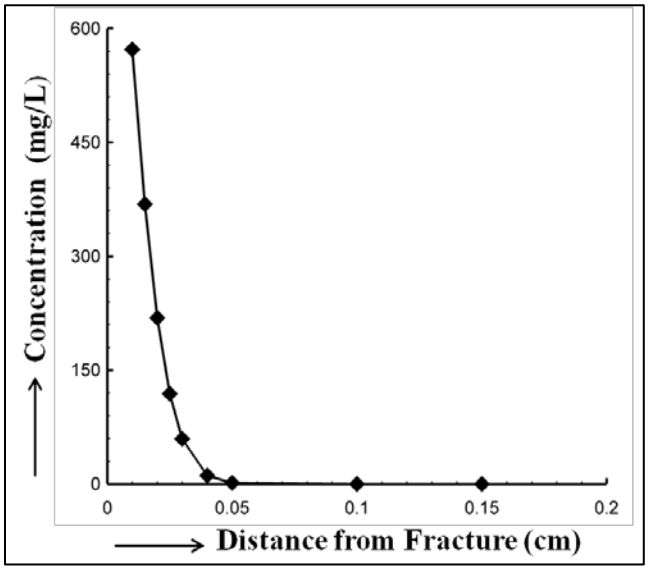

Figure 4.8.4.5: The Profile of Estimated Diffusing TCE Front into the Rock Matrix.

Table 4.8.4.1: Estimated TCE concentration and Diffused Mass in the Rock Matrix.

Distance From Fracture (cm)	Concentration (mg/L)	Average Concentration (mg/L)	Volume (cm^3)	Mass (gm)
0.01	5.72E+02	1.50E+02	68.63	0.02
0.015	3.68E+02			
0.02	2.18E+02			
0.025	1.19E+02			
0.03	5.92E+01			
0.04	1.11E+01			
0.05	1.44E+00			
0.1	1.42E-07			
0.15	0.00E+00			

The dissolution experiment in the laboratory helped to understand the TCE dissolution behavior in a fractured rock environment. Upon completion of the laboratory experiment, the transport of aqueous phase TCE originating from the source zone was modeled using: 1) assumed hydraulic properties of the fractured block based on the discrete fracture network modeling concept and, 2) the estimated K distribution obtained from the THT analysis of cross-hole pumping tests. This modeling effort is described in the next chapter.

4.8.5 Numerical modeling of aqueous phase TCE transport

Upon completion of the laboratory TCE dissolution experiment, Hydrogeosphere (HGS) was used to simulate the 1st portion (0 – 86 days) of the aqueous phase TCE breakthrough curve. The aqueous phase TCE was simulated using two approaches: 1) discrete fracture network modeling approach and 2) stochastic continuum approach. The goal of theses modeling study was to capture the pattern breakthrough curve as well as to compare the results from these two approaches.

4.8.5.1: Discrete Fracture Network Modeling Approach: Model setup

In the discrete fracture network modeling approach, a discretely fractured domain, with known geometry of fractures of the laboratory fractured block was used for the simulation. A uniform aperture thickness estimated from the flow-through tests were assigned to all fractures and a very low hydraulic conductivity (*K*) was assigned to the matrix.

A model domain, 91.5 cm in length, 60.5 cm in height and 1 cm thick (one element thick) was used for the dissolution modeling using the discrete fracture network modeling approach. The model domain was the same as the one used for simulating the pumping tests using HGS, described in section 4.8.2.3, with the only exception that the thickness of the model domain is different. The model domain used for simulating TCE dissolution was of unit thickness and composed of variably-sized rectangular elements. The element size varied from 0.05 cm by 0.01 cm to 1.375 cm by 1.375 cm. The finer elements are located along the fracture and the coarser elements are located near the boundary.

Figure 4.8.5.1a shows the mesh used for simulating the aqueous phase TCE transport, where the location of the source is indicated with a black circle and Figure 4.8.5.1b shows the fracture faces. The model domain was very finely discretized around the source zone indicated in Figure 4.8.5.1a, to account for the steep concentration gradient, expected to develop from the source zone into the flow path. The darker areas in Figure 4.8.5.1 indicate the highly refined areas of the model domain.

The flow boundary conditions were constant head for left and right boundaries and no flow for the remaining outer boundaries. Equilibrium dissolution from the immobile phase was simulated for the source zone. For equilibrium dissolution, aqueous phase concentration is same as the contaminant solubility. The boundary condition assigned at the source zone assumes that an immobile liquid phase dissolves into water until all dissolvable material is exhausted. In this transport boundary condition, each chosen nodes is assigned a first-type concentration value which is equal to the mass of dissolvable material per unit volume of porous medium and the concentration is maintained until all the material associated with a node is dissolved (Therrien et al., 2009). Equation (4.8.5.1) describes the transport boundary condition.

$$\int_0^{T_0} \int_{Vn_i} -\nabla[qC - D\nabla C]\, dV_{ni} dt = Mo_{ini} \qquad (4.8.5.1)$$

$$C = Co, \text{ when } 0 \leq t < To$$

where, *To* is the dissolution time, Vn_i is the volume associated with node n_i, Mo_{ini} initial mass stored at node n_i, q is the Darcy flux, *C* is the concentration, *Co* is the aqueous phase solubility, and *D* is the dispersivity.

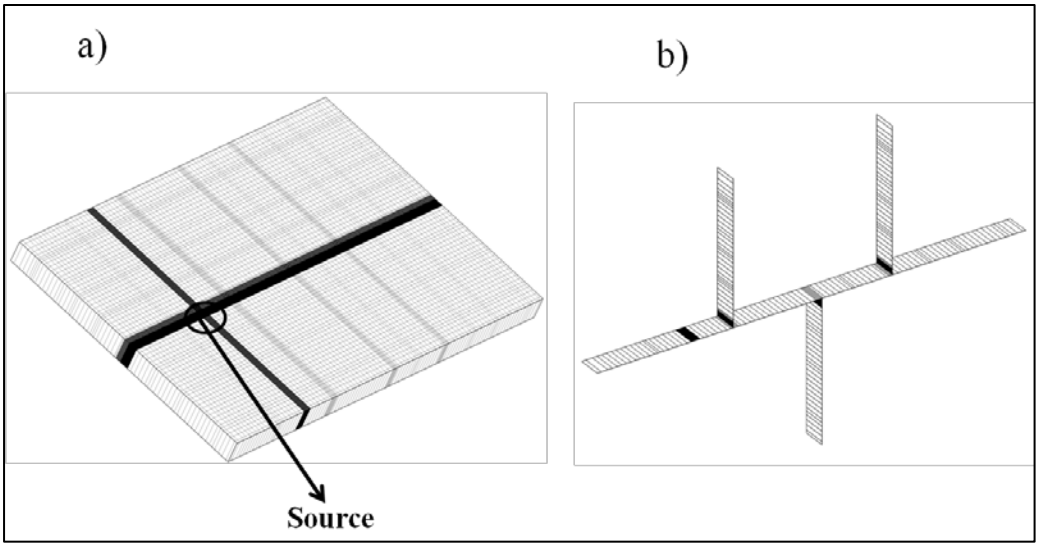

Figure 4.8.5.1: a) Mesh Used for TCE Dissolution Modeling using Discrete Fracture approach and b) Fracture Faces.

4.8.5.2 Model input

A uniform aperture value, obtained from flow-through tests was assigned to the fractures and a very low hydraulic conductivity (1.0×10^{-7} cm/s) was assigned to the matrix to simulate aqueous phase TCE transport. As described in section 4.8.2.3, HGS calculates the fracture hydraulic conductivity (K_f) from the aperture thickness. The matrix hydraulic conductivity (K_m) used for the transport modeling was determined through manual calibration of pumping test at port 5, simulated using HGS to match the simulated drawdown with the observed, described in section 4.8.2.3. The experimental rock is representative of Guelph formation. Therefore, a porosity value representative of the Guelph formation obtained from Zheng (1999) was used as matrix porosity. According to Zheng (1999), the bulk porosity of Guelph dolomite can range from 0.1% to 14.4%. Here the matrix porosity was chosen to be 0.1% as the experimental rock seems to be quite tight.

To simplify the transport modeling, a model domain having a unit thickness was used for the simulation, by scaling down the thickness by a factor of 5. Before conducting transport simulations, the flow through the fractured domain was simulated by fixing the hydraulic gradient across the model domain to match the experimental flow velocity. As the domain thickness was scaled down by a factor of 5, the fluid flux through the domain, volume of the source zone and the injected mass were also reduced by the same factor.

The source zone was assigned the hydraulic conductivity of sand that was measured in the laboratory using the falling head method. The porosity of the sand was also measured in the laboratory which was used as the source zone porosity for dissolution modeling. TCE solubility to water at room temperature (20°C) was obtained from literature (e.g., Russel et al., 1992; Pankow and Cherry, 1996). Initially we started with the literature value (1.0×10^{-5} cm^2/s) (i.e., Perry, 1984; Pankow and Cherry, 1996 etc.) for the free solution diffusion coefficient of TCE, but the manual calibration resulted in a higher value (3.1×10^{-3} cm^2/s) than the literature value to match the break-through curve. Other transport parameters used for dissolution modeling such as tortuosity and dispersivity were also determined through trial and error. The simulation was

conducted several times by varying each of these parameters manually until a good match between the observed and simulated break-through curves was obtained. Among the transport parameters, dispersivity was found to affect the pattern of the breakthrough curve most. Table 4.8.5.1 summarizes the flow and transport parameters used to obtain the simulated breakthrough curve presented here.

Table 4.8.5.1: Flow and Transport Parameters Used for TCE Dissolution Modeling in Discrete Fracture Approach.

Parameters Used			Source
Fracture	Aperture (cm)	0.049	Flow-through tests
	Fracture Hydraulic Conductivity, K_f (cm/s)	17.5	Calculated by HGS
	Longitudinal Dispersivity (cm)	1.96	
	Transverse Dispersivity (cm)	0.176	
Matrix	Matrix Hydraulic Conductivity, K_m (cm/s)	1.0×10^{-7}	*De Marsily*, 1986; *Domenico and Schwatrz*, 1997; *Schwartz and Zhang*, 2003 etc. (1.0×10^{-7} cm/s to1.0×10^{-4} cm/s)
	Matrix Porosity	0.1%	*Zheng*, 1999 (0.1% – 14.4%)
	Source Hydraulic Conductivity, K_s (cm/s)	0.1	Hydraulic conductivity of sand (used to fill the source hole) measured in the laboratory.
Source	Source Porosity	50%	Porosity of sand (used to fill the source hole) measured in the laboratory.
	Tortuosity	0.65	
	Free Solution Diffusion Coefficient (cm^2/s)	3.1×10^{-3}	*Perry*, 1984; *Pankow and Cherry*, 1996. (1.0×10^{-5} cm^2/s)
TCE	Solubility (mg/L)	1000	*Russel et al*., 1992; *Pankow and Cherry*, 1996. (1000 mg/L – 1100 mg/L)

4.8.5.3 Stochastic Continuum Modeling approach: Model setup

In the stochastic continuum modeling approach, the model domain was treated as a porous medium and the hydraulic conductivity (*K*) field obtained from Transient Hydraulic Tomography (THT) was utilized for simulating aqueous phase TCE transport using HGS.

A model domain, 91.5 cm in length, 60.5 cm in height and 5 cm thick (one element thick) was used for the transport modeling using the stochastic continuum approach. The model domain was same as the one used for transient hydraulic tomography (THT) analysis using SSLE, described in section 4.8.2.5. The model domain was composed of variably-sized rectangular elements and it was discretized into 14140 nodes and 6900 elements. The element size varied from 0.5 cm by 0.5 cm to 1.75 cm by 1.75 cm. The finer elements are located along the ports to match the port location and the element center and the coarser elements are located near the boundary.

Figure 4.8.5.2 shows the mesh used for simulating TCE dissolution using the stochastic continuum approach, where the location of the source is indicated with a black circle. Here the model domain used for the simulation was same as the one used for inversion, as the *K*-tomogram obtained from the THT analysis was used for dissolution modeling. Therefore, in this case, the model domain was not finely discretized around the source zone like the discrete fracture approach described earlier, although it would have been useful to deal with the concentration gradient, expected to develop from the source zone into the high *K* zone.

The flow boundary conditions were constant head for left and right boundaries and no flow for the remaining outer boundaries. The transport boundary condition, assigned to the source zone was same as the one described earlier.

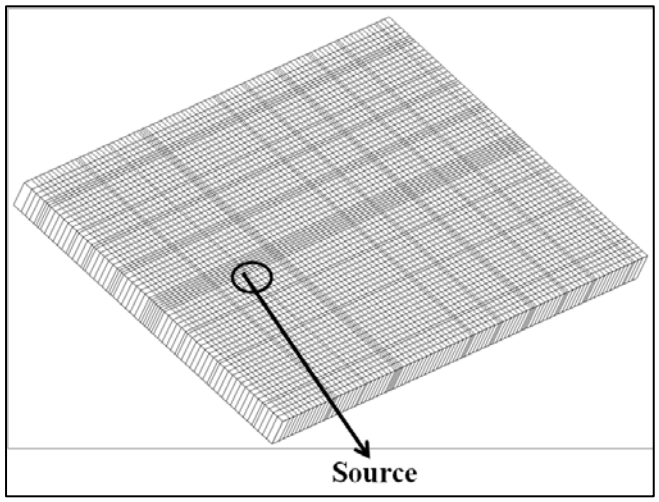

Figure 4.8.5.2: Mesh Used for TCE Dissolution Modeling using Stochastic Continuum Approach.

4.8.5.2: Model input

In this case, to simulate the transport of aqueous phase TCE, each element of the model domain was assigned a hydraulic conductivity (*K*) obtained from the THT analysis (case 1), described in section 4.8.2. All the elements in the model domain were also assigned a bulk

porosity value. (The experimental rock is representative of Guelph formation. Therefore, a porosity value representative of the Guelph formation obtained from Zheng (1999) was used for the model domain. According to Zheng (1999), the bulk porosity of Guelph dolomite can range from 0.1% to 14.4%. Here the bulk porosity was chosen to be 1%. Before conducting transport simulations, the flow through the porous medium was simulated by fixing the hydraulic gradient across the model domain to match the experimental flow velocity.

Table 4.8.5.2: Flow and Transport Parameters Used for TCE Dissolution Modeling in Stochastic Continuum Approach (Case 1).

Parameters Used			Source
Porous Medium	Hydraulic Conductivity, *K* (cm/s)	*K*-Tomogram Obtained from THT analysis (Case 1)	THT analysis of laboratory pumping Tests (Case 1)
	Longitudinal Dispersivity (cm)	91	
	Transverse Dispersivity (cm)	5.76	
	Vertical Transverse Dispersivity (cm)	6.76	
	Porosity	1%	*Zheng*, 1999 (0.1% – 14.4%)
	Tortuosity	0.65	
TCE	Free Solution Diffusion Coefficient (cm^2/s)	1.00×10^{-7}	*Perry*, 1984; *Pankow and Cherry*, 1996. (1.0×10^{-5} cm^2/s)
	Solubility (mg/L)	1000	*Russel et al*., 1992 (US EPA Ground Water Issue, 1992); *Pankow and Cherry*, 1996; (1000 mg/L – 1100 mg/L)

Similar to the discrete fracture approach, here TCE solubility to water at room temperature (20°C) was obtained from literature (e.g., Russel et al., 1992; Pankow and Cherry, 1996). Initially we started with the literature value (i.e., Perry, 1984; Pankow and Cherry, 1996) for the free solution diffusion coefficient of TCE, but the manual calibration resulted in values (1×10^{-7} cm^2/s in case 1 and 1×10^{-6} cm^2/s in case 2) little lower than the literature value to match the break-through curve. Other transport parameters used for dissolution modeling such as tortuosity

and dispersivity were also determined through trial and error. The simulation was conducted several times by varying each of these parameters manually until a good match between the observed and simulated break-through curves was obtained. Among the transport parameters, dispersivity was found to affect the pattern of the breakthrough curve most. Two best cases simulated using different transport parameters are presented here. Tables 4.8.5.2 and 4.8.5.3 summarize the flow and transport parameters utilized to simulate TCE dissolution in case 1 and case 2 respectively using stochastic continuum approach.

Table 4.8.5.3: Flow and Transport Parameters Used for TCE Dissolution Modeling in Stochastic Continuum Approach (Case 2).

Parameters Used			Source
Porous Medium	Hydraulic Conductivity, *K* (cm/s)	*K*-Tomogram Obtained from THT analysis (Case 1)	THT analysis of laboratory pumping Tests (Case 1)
	Longitudinal Dispersivity (cm)	91	
	Transverse Dispersivity (cm)	6.76	
	Vertical Transverse Dispersivity (cm)	6.76	
	Porosity	1%	*Zheng*, 1999 (0.1% – 14.4%)
	Tortuosity	0.65	
TCE	Free Solution Diffusion Coefficient (cm^2/s)	1.0×10^{-6}	*Perry*, 1984; *Pankow and Cherry*, 1996. ($1.0E\times10^{-5} cm^2/s$)
	Solubility (mg/L)	1100	*Russel et al*., 1992 (US EPA Ground Water Issue, 1992); *Pankow and Cherry*, 1996; (1000 mg/L – 1100 mg/L)

4.8.5.5 Results and discussion: Discrete Fracture Network Modeling approach

Comparison of the observed and simulated TCE concentration profiles (simulated using the discrete fracture network modeling approach) is presented in Figure 4.8.5.3a. In Figure 4.8.5.3b, the selected portion of the breakthrough curve, indicated with the black rectangular box (in Figure 4.8.5.3a), has been expanded to examine how the simulated concentration matched the

observed data at early time. The solid black circles represent the observed TCE concentration from the laboratory experiment, while the diamonds represent the simulated concentration using the discrete fracture network modeling approach.

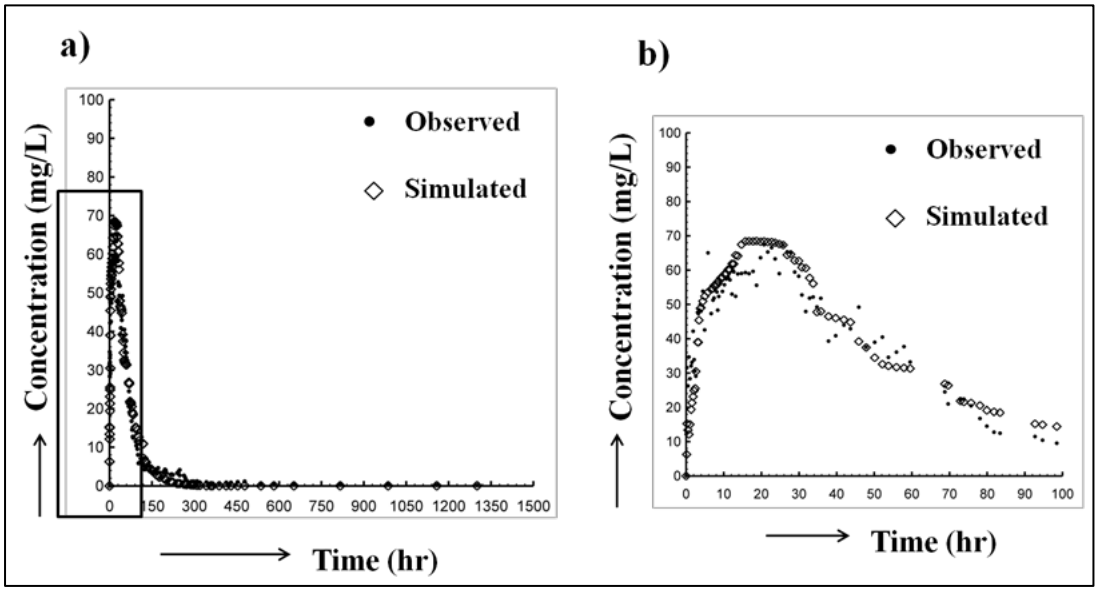

Figure 4.8.5.3: a) Observed and Simulated Breakthrough Curves (using discrete fracture network modeling approach) and b) Observed and Simulated Breakthrough Curves at Early Time. The solid black circles represent the observed TCE concentration in the laboratory experiment while the diamonds represent the simulated concentration.

From Figure 4.8.5.3, it can be seen that a good match was obtained between the observed and simulated breakthrough curves using the discrete fracture network modeling approach indicating that this approach can capture the TCE breakthrough curve quite well.

The time stepping is probably responsible for the steps or plateaus in simulated concentration in Figure 4.8.5.3b. The convergence criteria of the model was set in a way that, if the change in estimated concentration was below the convergence criteria (a previously set threshold), a previously set time-step multiplier came into effect leading to a larger time-step. This process continued until the change in estimated concentration was below the convergence criteria. Once the change in estimated concentration was above the previously set threshold, the time step was cut down by the same factor leading to a smaller time-step. This back and forth adjustment of time-step was probably responsible for the steps or plateaus in simulated concentration in Figure 4.8.5.3b.

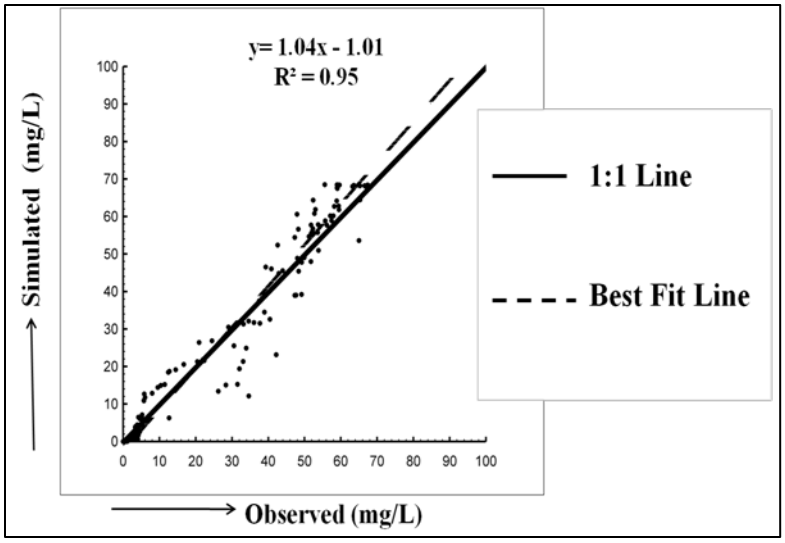

Figure 4.8.5.4: Scatter Plot of Observed and Simulated TCE Concentration (using the discrete fracture network modeling approach). The solid line is a 1:1 line indicating a perfect match. The dashed line is a best fit line, and the parameters describing this line are on the plot.

Figure 4.8.5.4 is a scatter plot comparing simulated and observed TCE concentration at the sampling port. The solid line is a 1:1 line indicating a perfect match. The dashed line is a best fit line, and the parameters describing this line are included on the plot. The scatter plot is presented as an assessment of how well the simulated breakthrough curve was able to capture the observed. The R^2 value indicates the Correlation between the simulated and observed values. The correspondence between the simulated versus the observed concentration values can be considered to be good when the data set clusters around the 1:1 line and the R^2 value is close to 1. The slope and the intercept of the linear model fit are the indication of bias. From Figure 4.8.5.4, it is seen that the data points cluster around the 1:1 line indicating a good match between the observed and simulated breakthrough curve. The R^2 value was also very close to 1 (0.95) indicating that simulated concentration profile captured the observed pattern quite well.

As mentioned earlier, the simulation was conducted several times changing some of the parameters such as dispersivity and free solution diffusion coefficient until a good match between the observed and simulated breakthrough curves was obtained and the simulated breakthrough curve shown here is the one that best matched the observed. The set of parameters used to produce the simulated breakthrough curve are listed in Table 4.8.5.1. Note that, a similar match can be obtained using a different combination of transport parameters such as dispersivity and free solution diffusion coefficient, which suggest non-uniqueness of the parameters.

The purpose of modeling the TCE breakthrough curve using the discrete fracture network modeling approach was to investigate whether the TCE breakthrough curve can be captured in a fractured rock environment when the fracture geometry, fracture aperture and the flow through the system are well known. In this case, the geometry of the fractured rock, fracture aperture and the flow through the system were well characterized through the hydraulic and tracer tests conducted ahead of the dissolution experiment. The fracture geometry of the numerical model closely resembles the fracture patterns in the rock block in the laboratory. Also, the mesh was very finely refined around the source zone to deal with concentration gradient expected to develop over time from the source zone into the flow path. Finally, result shows that it is

possible to capture the pattern of TCE dissolution in a fractured rock environment using discrete fracture network modeling approach.

4.8.5.6 Results and discussion: Stochastic Continuum Modeling approach

In this case, the hydraulic conductivity (*K*) field obtained from "Real THT analysis Case 1" was used and the model domain was treated as a porous medium to simulate the transport of aqueous phase TCE. The simulation was conducted several times by varying the parameters until a good match between the observed and simulated breakthrough curves was attained and the two best cases are presented here.

A comparison of observed and simulated TCE concentration profiles (stochastic continuum modeling approach) for case 1 is presented in Figure 4.8.5.5a. In Figure 4.8.5.5b a selected portion of the breakthrough curve indicated with the black rectangular box (in Figure 4.8.5.5a) has been expanded to examine how the simulated concentration matched the observed at early time. A similar comparison of observed and simulated breakthrough curves for case 2 is presented in Figures 4.8.5.7a and 4.8.5.7b. The solid black circles represent the observed TCE concentration from the laboratory experiment, while the diamonds represent the simulated concentration using the stochastic continuum modeling approach.

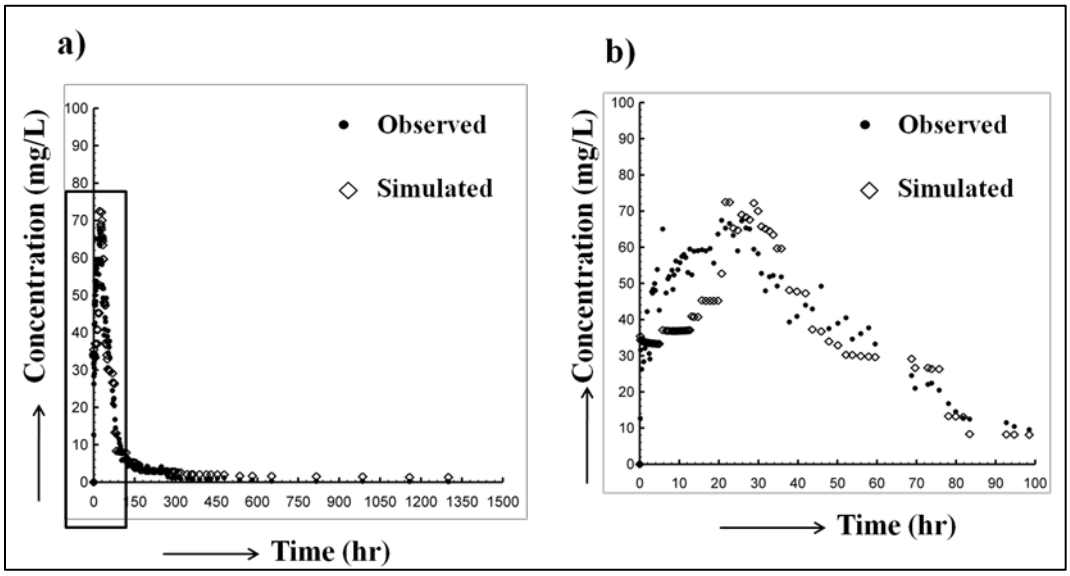

Figure 4.8.5.5: a) Observed and Simulated Breakthrough Curves in Case 1 (using the stochastic continuum modeling approach) and b) Observed and Simulated Breakthrough Curves at Early Time. The solid black circles represent the observed TCE concentration in the laboratory experiment while the diamonds represent the simulated concentration.

Examination of Figure 4.8.5.5 reveals that the match between the observed and simulated concentration profiles in case 1 is fair except at early time (0 – 20 hours). At early time, the simulated concentration was lower than the observed in case 1 (Figure 4.8.5.5b). On the other hand, from Figure 4.8.5.7 it can be seen that at early time, simulated concentrations matched the observed quite well for case 2. But in case 2 (Figure 4.8.5.7b) the simulated peak concentration was much higher than observed and the peak arrived earlier in the simulated case than the observed. In case 2 (Figure 4.8.5.7a), the simulated TCE concentration was found to be a little

higher than the observed at the tailing stage too, which was expected as the peak concentration was much higher than the observed in this case.

There could be couple of reasons behind the deviation of the simulated TCE breakthrough curve from one observed one:

- In the stochastic continuum modeling approach, the mesh was not finely discretized around the source zone what was done for the discrete fracture network modeling approach to deal with the concentration gradient expected to developed overtime from the source zone into the high *K* zone.
- The estimated hydraulic conductivity (*K*) field from the THT analysis used to simulate the aqueous phase TCE transport might play a role behind this deviation. The estimated hydraulic conductivity (*K*) values may not exactly replicate actual *K* values for the fractured block.
- At early time of the dissolution experiment in the laboratory, flow through the fractured rock fluctuated quite a bit due to very frequent sampling, while in the synthetic case the flow rate was stable throughout the duration of the simulation. Therefore, the flow rate for the synthetic case did not exactly match the observed at early time, which may have caused the discrepancy between the observed and simulated concentration.

However, the overall the pattern of the TCE breakthrough curve was captured using the stochastic continuum modeling approach for both cases 1 and 2. However, it was difficult to match both the peak arrival time and the peak concentration simultaneously.

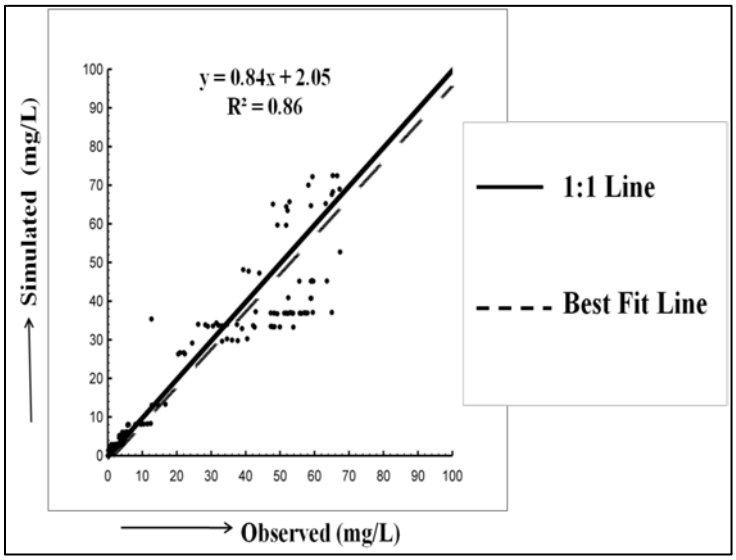

Figure 4.8.5.6: Scatter Plot of Observed and Simulated TCE Concentration in Case 1 (using the stochastic continuum modeling approach). The solid line is a 1:1 line indicating a perfect match. The dashed line is a best fit line, and the parameters describing this line are on the plot.

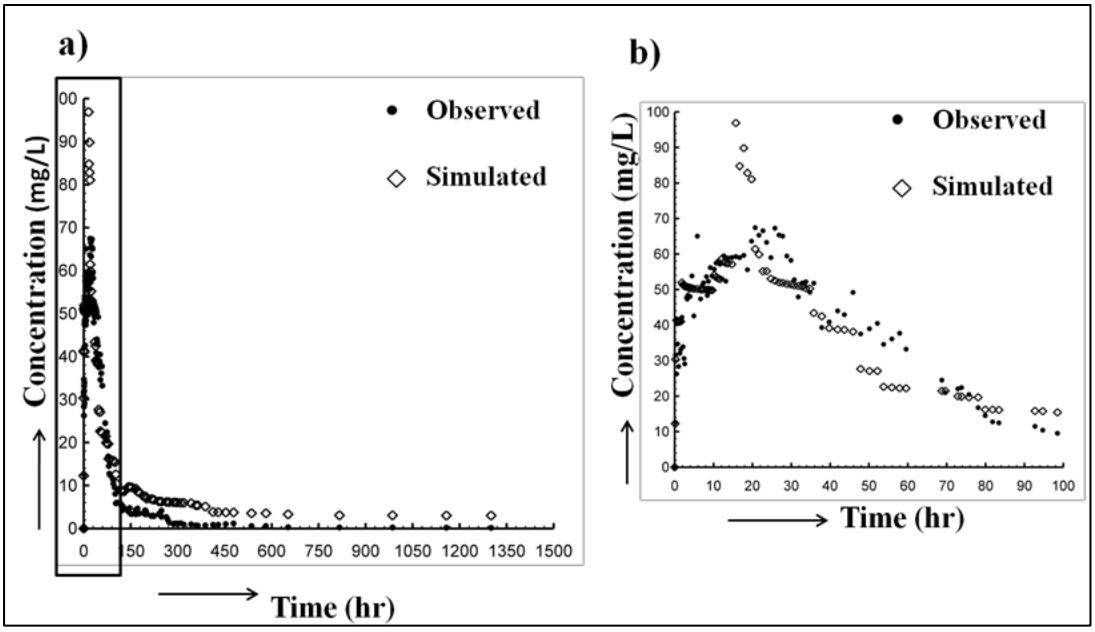

Figure 4.8.5.7: a) Observed and Simulated Breakthrough Curves in Case 2 (using the stochastic continuum modeling approach) and b) Observed and Simulated Breakthrough Curves at Early Time. The solid black circles represent the observed TCE concentration in the laboratory experiment while the diamonds represent the simulated concentration.

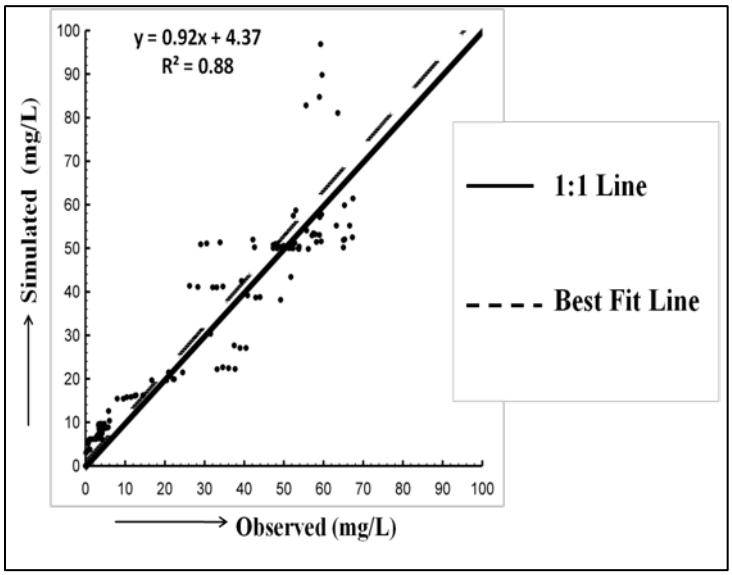

Figure 4.8.5.8: Scatter Plot of Observed and Simulated TCE Concentration in Case 2 (using the stochastic continuum modeling approach). The solid line is a 1:1 line indicating a perfect match. The dashed line is a best fit line, and the parameters describing this line are on the plot.

Figures 4.8.5.6 and 4.8.5.8 are the scatter plots comparing simulated and observed TCE concentrations at the sampling port in cases 1 and 2 respectively. The solid line is a 1:1 line indicating a perfect match. The dashed line is a best fit line, and the parameters describing this line are included on each plot. From Figures 4.8.5.6 and 4.8.5.8, it is seen that the data points

cluster around the 1:1 line, indicating a fair match between the observed and simulated breakthrough curves, although some bias is evident due to the deviation of simulated concentrations from the observed values, which has been discussed above. The R^2 values were close to 1 in both cases (0.86 in case 1 and 0.88 in case 2) indicating a good correspondence between the simulated and observed TCE concentration in both cases.

The set of parameters used to produce the simulated breakthrough curves in case 1 (Figure 4.8.5.5) and case 2 (Figure 4.8.5.7) are listed in Tables 4.8.5.2 and 4.8.5.3, respectively. As mentioned earlier, the simulation was conducted several times changing some of the transport parameters such as dispersivity and free solution diffusion coefficient until a good match between the observed and simulated break through curves was obtained. The simulated breakthrough curves represented here are the ones that best matched the observed. Note that, similar matches can be obtained using a different combination of transport parameters such as dispersivity and free solution diffusion coefficient, suggesting the non-uniqueness of the parameters.

TASK 7: FIELD STUDIES

4.9 Application of compound specific analyses to characterize natural attenuation of TCE in a fractured bedrock aquifer

4.9.1 Introduction

The release of Dense Non-Aqueous Phase Liquids (DNAPLs) is a significant cause of groundwater contamination at industrial and military sites throughout the world. DNAPL source zones and plumes of aqueous phase contaminants resulting from DNAPL release can contribute to long-term groundwater contamination, potentially for centuries. Therefore, their management and remediation is of critical importance (Pankow and Cherry, 1996). Over the past two decades, considerable advances have been achieved in understanding the fundamental processes controlling the fate of DNAPLs spilled or released in heterogeneous unconsolidated geologic materials. In spite of these efforts, it is widely recognized that few, if any, sites contaminated by DNAPLs have been fully remediated in terms of either the dissolved contaminants contained in the aqueous phase or the removal of the DNAPL source (Alvarez and Illman, 2006). Contaminated sites with complex geology, including fractured rock, often require large amounts of physical analyses and chemical data collection for characterizing the source zones and the corresponding contaminant plumes. Due to the difficulty in actively remediating a chlorinated solvent site, biodegradation and natural attenuation have been proposed as another method for site remediation. Illman and Alvarez (2009) have summarized some of the commonly utilized performance assessment techniques for determining whether biodegradation is occurring at a site or not. Thus, while progress has been made in understanding DNAPL migration and fate in heterogeneous unconsolidated deposits, there remains a paucity of knowledge on the behavior of DNAPLs in fractured bedrock environments.

Trichloroethene (TCE) is a DNAPL that tends to be resistant to degradation once released to the groundwater system. This combined with repeated release into the natural environment has made it one of the most ubiquitous organic contaminants in industrial nations. Tests show that through chemical degradation reactions, TCE can be transformed into a small number of different compounds and it is known that these reactions are often catalyzed by microbes (Chapelle and Bradley, 2003). Due to the different chemical processes affecting the degradation of TCE in addition to a variety of natural field conditions, complex plumes consisting of many different organic solvents can develop from TCE spills (Huang et al., 1999). Documented loss of contaminant mass, formation of degradation byproducts, and applied microcosm data have been used as evidence for degradation (Illman and Alvarez, 2009; EPA 1999). However, these methods on their own are limited and often cannot be used to fully verify whether degradation is occurring or determine the degree of degradation. Therefore, the gathering of multiple lines of evidence to determine whether biodegradation is occurring or not at a given site is advocated by Alvarez and Illman (2006).

In recent years, isotopic techniques have been developed not only as a tool to determine the physical and chemical processes affecting TCE transport and degradation, but also to better understand those processes, especially at complex field sites. These isotopic methods, when combined with other methods, have led to promising advances in characterizing the organic degradation of TCE (Freedman and Gossett, 1989; Holliger et al., 1998; Bloom et al., 2000; Chapelle and Bradley, 2003; Meckenstock et al., 2004). These techniques depend on the fact

that many processes, including sorption and volatilization, do not significantly fractionate the isotopes of TCE. However, degradation does impart a significant fractionation in the carbon and chlorine isotope ratios of reactants and products.

TCE from different manufacturers and different methods of production may vary significantly in isotopic composition. Thus, determining the source of TCE is one potential application of isotopic analyses. Methods relying on isotopic data have also been used to verify the occurrence of TCE degradation. Isotopic analyses have been studied alongside chemical analyses as a tool to estimate the degree of TCE degradation (Meckenstock et al., 2004). Analysis of the isotopic composition of TCE at a given field site has also been identified as a means of potentially determining the mechanisms of degradation at that site. Isotopic data has been particularly useful in studying reductive dechlorination.

In this study, we employed compound-specific isotopic analyses to better understand the geochemical evolution of TCE and its degradation products in a fractured dolomitic bedrock aquifer at a former industrial waste disposal facility, near Smithville, Ontario, Canada. The site is actively being remediated via a pump-and-treat system placed around a known source zone. A previous study by McLaren et al (2012) using a numerical model revealed that the pump-and-treat system has neither been effective in stabilizing the plume nor removing a significant amount of contaminant mass, but that the stability of the plume is instead due to first-order degradation. The chemical and isotopic analysis presented in the current study aims to support this conclusion. Both chlorine and carbon isotopic analyses, in conjunction with more common chemical methods, were employed to identify TCE degradation. In addition, the application of compound specific isotopic analyses of TCE and DCE to determine the mechanism and degree of TCE degradation was attempted. However, due to the development of a complex flow regime from pumping of multiple wells in a fractured rock environment, additional analyses will be required for the improved interpretation of isotopic fractionation effects. Despite the complexity of the flow regime, this is the first study to employ a dual isotopic approach to the characterization of TCE degradation in fractured rock.

4.9.2 Site history

The Chemical Waste Management Limited (CWML) operated an industrial waste storage facility between 1970 and 1985 near the town of Smithville, Ontario, Canada. It is estimated that about 434,000 L of liquid wastes, comprising an estimated 266,000 L (61% of the total volume) of polychlorinated Biphenyls (PCBs), 57,000 L (13%) of other organic chlorinated solvents, as well as acids, alkalis, and other inorganic waste sludge (Golder Associates Ltd., 1999) was received during its operating life. In 1980, the Ontario Ministry of the Environment (MOE) installed five test wells to the north and south of the CWML compound to monitor the site. Soil and water samples collected from these wells did not contain detectable levels of PCB or other organic contaminants. However, in 1985, there was a discovery of PCB and other solvents penetrating into the overburden and infiltrating the upper portions of the local bedrock. This discovery caused the shutdown of a nearby municipal water supply well. The extent of the TCE plume in 1988, as inferred from on-site investigations (Smithville Phase IV Bedrock Remediation Program, 2000) is shown in Fig. 4.9.1. As part of the cleanup operations, eight pumping wells (R1 – R8) were constructed, and groundwater at the site has been pumped

continuously with pumped water treated on-site. These production wells influence the local groundwater flow regime and remove contaminants from the subsurface environment.

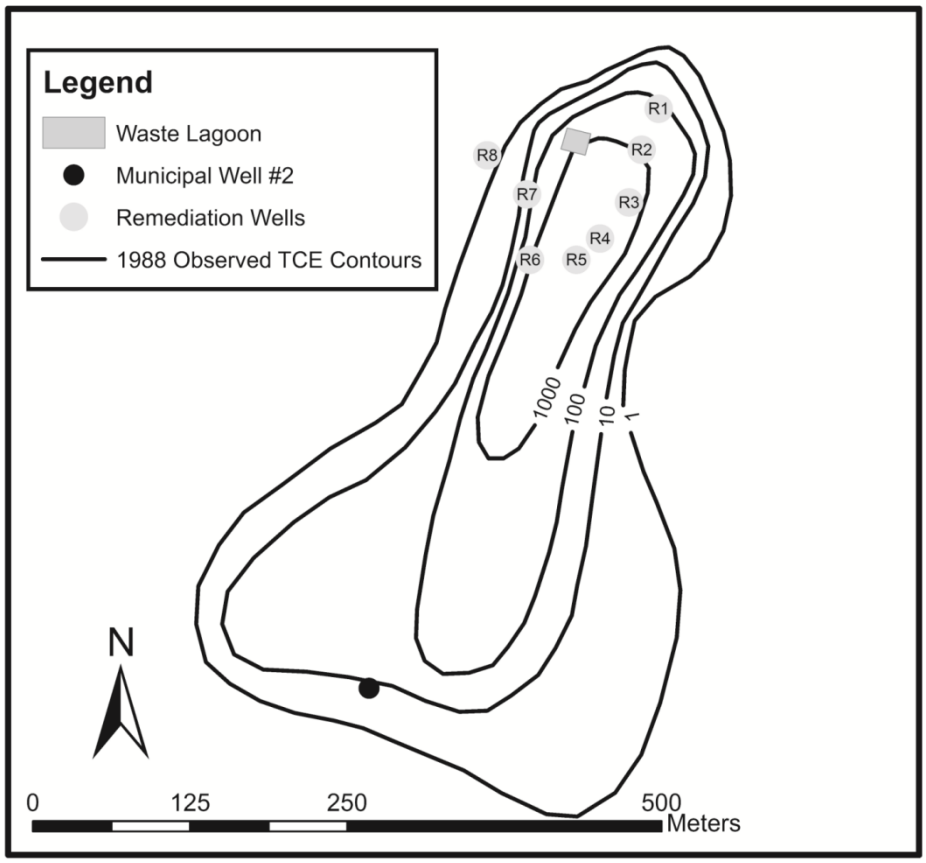

Figure 4.9.1: Observed TCE plume with concentration in μg/L based on data from 1988 (after McLaren et al., 2012).

4.9.3 Site hydrogeology

The upper soil layer at the Smithville site is topographically flat-lying glaciolacustrine clay plain. This glacial till covers the bedrock in the local area and extends over much of the Niagara Peninsula in Southern Ontario (Willis et al., 1992; Johnson et al., 1992). The overburden clay layer has significant fracturing throughout its entire depth that made it possible for fluids to penetrate this layer and migrate to lower layers (Slough et al., 1997). Directly underlying the overburden is a series of sedimentary carbonate rocks layers. This study focuses primarily on bedrock material and contamination below the overburden due to the fact that much of the overburden and surface material has been removed or remediated. The bedrock units contain various joints, fractures, and vugs that permit groundwater flow. The physical flow of water through this complex fractured network allows for DNAPLs to be transported along with the groundwater and mixing of contaminants to occur.

The geological layers of most interest in the shallow subsurface are in the uppermost geological unit, the Lockport Formation which is a relatively horizontally layered carbonate unit.

The top layer of the Lockport Formation, the Eramosa Member, is characterized as a bituminous and argillaceous fine-crystalline dolostone. The bedding in this layer is thin to medium (Telford, 1978; Johnson et al., 1992). In the local area the Eramosa Member is 11-15 meters thick and dips to the south by about 2 degrees. This uppermost bedrock layer contains many fractures and is weathered, making it very important in the context of the organic contamination at the site (Golder Associates, 1999).

Since the discovery, over 50 observation wells were installed in the local area between 1985 and 1990 with many of these wells being screened at multiple levels for detailed three-dimensional characterization of the site (Golder Associates, 1994). Cores were collected and photographed for fifteen of the boreholes drilled at the site. The frequency, size and orientation of fractures in the Lockport Formation were recorded. These fractures were classified as bedding plane fractures, vertical fractures, or broken-core zones (Lapcevik et al., 1997). Site characterization also included 1597 constant-head hydraulic tests in 23 boreholes (Golder Associates Ltd., 1995; Novakowski et al., 1999; Zanini et al., 2000). For these boreholes, test intervals of 2 m were isolated using pneumatic packers. For 12 boreholes, an additional 824 tests with 0.5 meter test intervals were conducted.

Local geological characterization of the Eramosa Member and numerous packer tests indicate a highly heterogeneous aquifer with fracture frequency. The results of hydraulic testing of the Eramosa Member reveal that this layer is quite conductive and is a large potential aquifer (Lapcevik et al., 1997). The estimated hydraulic conductivity values are orders of magnitude larger than the corresponding values for the underlying layer (the Upper Vinemount Member), thus it is considered to be isolated from deeper layers by this locally confining unit (Golder Associates, 1999). Furthermore, the Eramosa Member is very important because domestic wells in this area of southern Ontario normally draw their water from this formation. Therefore, the contamination in this layer is the primary focus of the geochemical investigation of the site. The groundwater flow direction in the Eramosa Member based on historical water level data is shown in Figure 4.9.2. The fourteen wells labeled in Figure 4.9.2 have screen intervals that are in the upper 5 meters of the Eramosa Member, these wells were chosen for additional chemical analyses.

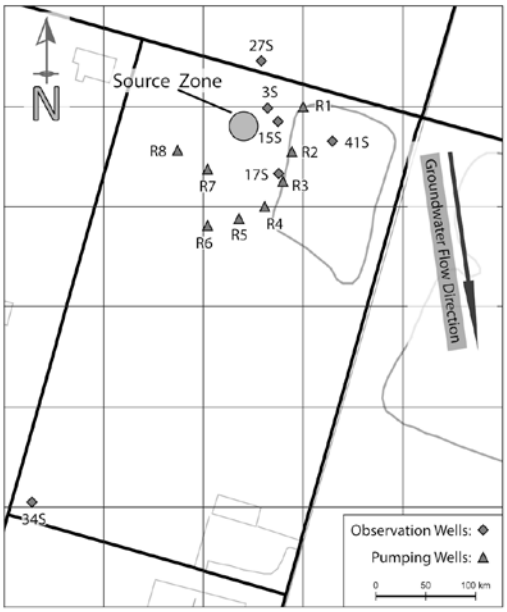

Figure 4.9.2: Site map showing wells sampled for geochemical and isotopic analysis.

4.9.4 Methods

Monitoring of the chemical composition of groundwater underlying the Smithville site has been undertaken since 1988. Nearly fifty screened well intervals at the Smithville site are currently sampled as part of the ongoing quarterly sampling routine. Consistent sampling for many species of VOCs has been maintained since 1996. Chemical concentration analyses of ethane and ethane were only completed for the 14 wells near the source zone from December 2008 until April 2010.

The process of reductive dechlorination degrades TCE to less chlorinated byproducts, specifically DCE, VC, ethene and ethane. Therefore, studying the concentration of TCE and its potential products of degradation, especially chlorinated ethenes, often helps to form a general understanding of the geochemical evolution of a TCE contaminated aquifer. TCE has been consistently observed in many of the sampled wells at the Smithville site. However, TCE has been found almost entirely in the Eramosa Member and the Vinemount Member. The majority of chemical analyses completed in the units below the Eramosa Member (results not shown) have shown concentrations of chlorinated solvents below the limits of detection.

Based on historical chemical data, 14 wells in the upper part of the Eramosa Member were selected for additional sampling from December 2008 until April 2010 to further characterize the subsurface geochemistry of the site (Figure 4.9.1). Samples from the 14 wells discussed in the previous section were collected during quarterly sampling events in December 2008, March 2009, June 2009, September 2009, January 2010 and April 2010. Three of these wells - wells 3S, 17S, and 19S - were not included in regular quarterly sampling, but were selected due to proximity to the source zone. The chemical samples taken were collected from wells screened in

the upper part of the Eramosa Member and all field samples were collected after removing three well volumes.

In the field measurements of temperature, pH and E_h were taken through the use of a flow through cell. Unfiltered samples with no preservatives were collected from some sample intervals for nitrate analyses via the cadmium reduction flow injection method (SM 4500 NO3, I) and nitrite analysis via an ultraviolet spectrophotometric screening method (method SM 4500 NO2, B). Samples were also collected for spectrophotometry for chloride (automated colourimetry, method SM 4500 Cl, E) and sulfate (turbidimetry, method EPA 375.4). Ion chromatography of samples with no preservatives was used to analyze the concentration of acetic acid (Maxxan method CAM SOP-00431). TCE, dichloroethene (DCE), vinyl chloride (VC) and various other VOC analyses were completed by gas chromatograph – mass spectrograph (GC-MS) (method SM 847). Hydrochloric acid was used for preservation of these samples. Analyses of ethene, ethane, methane and propane concentrations were completed on samples collected without preservatives with the use of gas chromatograph - flame ionization detection (GC-FID). Additional details to the analytical method used for GC-FID is provided in Kampbell and Vandergrift (1998).

For isotopic analyses trisodium phosphate (Na_3PO_4) was used to preserve samples collected in the field. Chlorine stable isotopes of TCE and cis-1, 2-DCE (cDCE) were determined by the means of a Continuous Flow - Isotope Ratio Mass Spectrometry (CF-IRMS) following the procedure described in Shouakar-Stash et al. (2006). Organic compounds were extracted and concentrated by Solid Phase Micro Extraction (SPME). The extracted compounds were injected on a GC column to separate the various compounds and only the desired compounds were directed to the IRMS to be analyzed for their isotopic compositions. The chlorine isotopic compositions are reported in per mil (‰) deviation from isotopic standard reference material using the conventional δ notation shown in Equation 4.9.1.

$$\delta = ((R_{sample}/R_{standard}) - 1) \cdot 1000\ \% \qquad (4.9.1)$$

For chlorine isotopic analyses ($\delta^{37}Cl$) the ratios R_{sample} and $R_{standard}$ are $^{37}Cl/^{35}Cl$ of a given sample and $^{37}Cl/^{35}Cl$ of a standard reference material, respectively. The $\delta^{37}Cl$ values were calibrated and reported relative to the reference material Standard Mean Ocean Chloride (SMOC) (Kaufmann et al., 1984). The standard deviation for chlorine isotopic analyses of TCE ranges from .01 ‰ to .2 ‰; for chlorine isotopic analyses of cDCE it ranges from .01 ‰ to .27 ‰.

To determine the $\delta^{13}C$ values of TCE and cDCE, a purge and trap system was used (PT-GC-IRMS). The system used is a Tekmar 3000 purge-and-trap unit (Tekmar Company, Cincinatti, Ohio). For Gas Chromatography, a Trace GC (Thermo Finnigan, San Jose, CA) with a GC-Combustion III interface was used. For separations, a 60 meter long DB-624 column with .32mm internal diameter and 1.8μm film thickness was used. The IRMS used was the Delta^{plus} XL isotope ratio mass spectrometer (Thermo Finnigan MAT, Bremen, Germany). The carbon isotopic compositions were reported in permil deviation from isotopic standard reference material using the conventional delta notation, shown above. The sample and standard ratios were $^{13}C/^{12}C$ for carbon isotopic analyses. The $\delta^{13}C$ values were calibrated and reported relative to the reference material Vienna Pee Dee Belemnite (VPDB) (Clark and Fritz, 1997). The standard deviation for chlorine isotopic analyses of TCE and cDCE using this method was reported to be approximately .5 ‰.

4.9.5 Results and discussion

Data collected from wells on site indicated that the groundwater contamination by TCE was found almost entirely in the Eramosa Member and the Vinemount Member. Many of the wells in the proximity of the Smithville site that were screened within the upper part of the Eramosa Member returned continuously high TCE concentrations. The majority of chemical analyses completed in the units below the Eramosa Member returned concentrations of chlorinated solvents at or below the limits of detection.

The chemical reactions that potentially affect TCE biodegradation, both biotic and abiotic, are favorable within certain ranges of redox conditions. Thus, characterization of the redox conditions of a given site is an important undertaking. A previous study characterized the redox conditions of the native uncontaminated groundwater underlying Smithville (Zanini et al., 1997). The results of analyses completed on multilevel wells sampled in February, July and November of 1997 indicated that the Eramosa Member had waters that were suboxic to reducing, with even more highly reducing conditions in underlying layers.

Chemical analyses on the wells shown in Table 4.9.1 were completed in April of 2010 in addition to analyses of redox indicators other than methane. All wells tested for nitrate in April of 2010 had concentrations below detectable limits. Nitrite was present in low quantities in wells 3S and R6. Sulfate analyses are less useful in carbonate rocks as an indicator of redox conditions. Analyses of E_h indicate that some areas of the site, especially near wells R1 – R5 and 17S, are more reducing than might be expected based on historical values and recently collected data for the upper part of the Eramosa Member. The results of methane sample analyses from the six sampled dates are shown in Table 4.9.2. This data indicates that methanogenesis is occurring at this site. Data collected shows high methane concentrations in wells 15S and 17S from the majority of samples collected. Concentrations above the detection limit were also found in wells R2 – R5 and R7.

The analyses of redox parameters show that reducing environments have formed in the upper part of the Eramosa Member. Historical analysis and recently collected field data indicate that the native uncontaminated groundwater in this zone of the Eramosa Member is suboxic, with little evidence of significant reduction of organic matter. In this area, sulfate reduction is most likely a dominant terminal electron accepting process and methanogenesis is not significant. The well closest to the contaminant source zone (well 3S) also did not show significant evidence of enhanced organic matter reduction. However, samples collected from wells screened near the top of the Eramosa Member within the proximity of the source zone - particularly wells R2 – R5, R7, 15S and 17S - were more reducing. Samples collected in this area indicated an increased rate in the reduction of organic matter. In these areas of this layer sulfate reduction and methanogenesis likely both are significant terminal electron accepting processes.

Figure 4.9.3a-d shows the results of analyses of ethane and chlorinated ethenes collected between December 2008 and January 2010 from 4 of the wells near the source zone. Chemical data collected reveals that the highest concentrations of chlorinated ethenes were found in wells 3S8 and R7. Data from wells 17S9 and 15S9 also show consistently high chlorinated ethene concentrations. Well 3S8, which is closest to the source zone, shows high TCE values but the concentration of products of degradation was not significant. Wells R7 and 15S9 have shown significant concentrations of less chlorinated byproducts, however in samples collected from these wells TCE still makes up a large percentage of the total mass of ethenes and ethane. The

data collected from well 17S9 show low concentrations of TCE with a large percentage of the total mass of degradation products as VC, ethene and ethane. Analyses completed on this well indicate that significant degradation of TCE does occur in this zone of the aquifer. Though this formation of byproducts does support the case for biodegradation, documenting the loss of contaminant mass in a complex fractured bedrock network is not easily accomplished. Applied microcosm studies have not been completed at this site, thus additional verification of degradation is problematic at this site and, potentially, others like it.

Table 4.9.1: Data pertaining to the redox conditions of the Smithville site, samples collected in April of 2010.

Well ID	NO_3	NO_2	Sulphate	Eh(field)
units -->	(mg/L)	(mg/L)	(mg/L), SO_4	mV
RWS1	-	-	-	25
RWS2	< 0.1	< .01	770	36
RWS3	< 0.1	< .01	680	30
RWS4	< 0.1	< .01	650	24
RWS5	< 0.1	< .01	780	37
RWS6	< 3.1	0.03	750	51
RWS7	< 4.1	< .01	820	58
RWS8	-	-	-	67
17S	< 0.1	< .01	1200	26
15S	< 2.1	< .01	650	63
3S	< 1.1	0.04	370	86
34S	< 0.1	< .01	520	84
27S	-	-	-	356
41S	-	-	-	125

Table 4.9.2: Methane data for samples collected from the Smithville site.

Well ID	Dec-08	Mar-09	Jun-09	Sep-09	Jan-10	Apr-10
RWS1	374	1450	< 0.1	< 0.1	-	< 0.1
RWS2	39.9	262	< 0.1	18.4	1.4	< 0.1
RWS3	17.85	109.3	< 0.1	4.7	1.7	< 0.1
RWS4	19.5	46.3	< 0.1	0.9	1.7	1.4
RWS5	9.7	13.3	< 0.1	15.7	1.3	< 0.1
RWS6	15.9	67.1	< 0.1	< 0.1	-	10.9
RWS7	53.1	281	< 0.1	17	2.55	2.6
RWS8	-	-	-	4	1.6	5.4
17S9	63.8	580	< 0.1	378	1.4	1322.4
15S9	84.14	410	< 0.1	2.5	< 0.1	418.7
3S8	< 0.1	4.6	< 0.1	< 0.1	2.1	4.3
27S7	< 0.1	0	< 0.1	< 0.1	-	5.6
41S10	-	-	-	-	-	0.4
34S12	0.8	8.7	< 0.1	< 0.1	< 0.1	8.6

a)

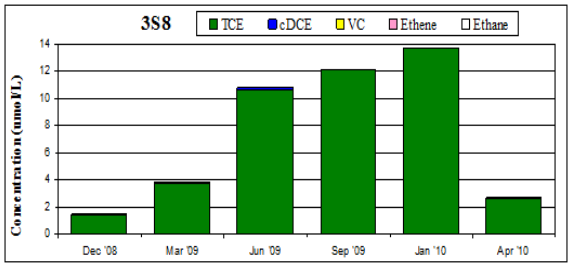

b)

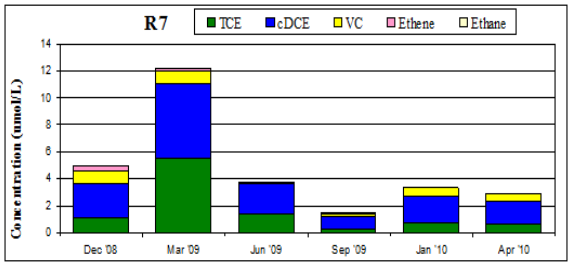

c)

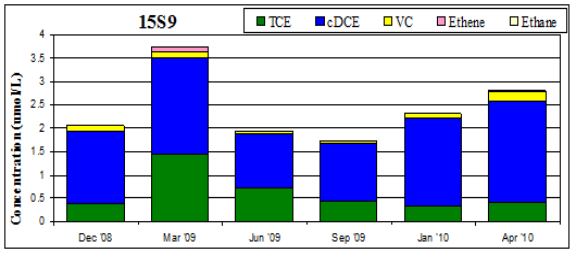

d)

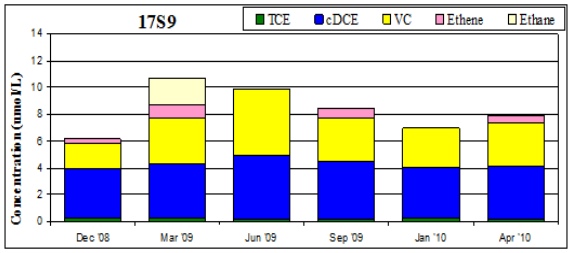

Figure 4.9.3: Concentrations of chlorinated ethenes, ethene and ethane for wells a) 3S8, b) R7, c) 15S9, and d) 17S9. All data presented in units of μmol/L.

TCE isotopic data pertaining to the 4 wells that were discussed above are presented below in Figure 4.9.4. The isotopic data are presented as a $\delta^{37}Cl_{TCE}$ vs $\delta^{13}C_{TCE}$ plot. Degradation of TCE by reductive dechlorination has been shown to impart an increase in the $\delta^{37}Cl_{TCE}$ and $\delta^{13}C_{TCE}$ of the reactant TCE (Meckenstock et al., 2004). Thus, in Figure 4.9.4, lower values represent TCE that has undergone less degradation. There is much variability in the isotopic data collected from wells on site. Some of this variation may be attributed to sorption and volatilization of TCE, but these are generally negligible when compared to the isotopic change imparted by degradation. The data collected from well 3S8 indicate that the least amount of biodegradation of TCE has occurred at this location. Data from wells 15S and R7 generally show generally higher isotopic ratios than well 3S. The high isotopic values observed in well 17S indicate a high degree of TCE degradation.

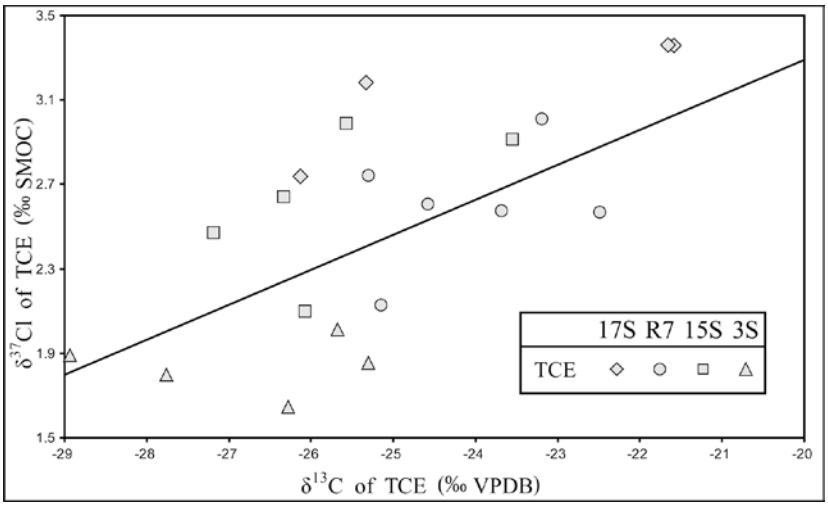

Figure 4.9.4: Carbon and chlorine isotopic TCE data pertaining to wells 3S, 15S, R7 and 17S.

The isotopic ratios of cDCE are presented in Figure 4.9.5. The chemical concentrations of cDCE were not high enough to analyze the carbon cDCE isotopes of samples collected from wells 3S. Indeed, quantification limits are a big challenge in some cases. However, there are advancements in the field. For example, our current capabilities are limited to headspace injection and solid phase micro extraction (SPME). However, a purge and trap is another option that can improve the quantification limits. Long term sorption followed by a thermal desorption is also being tested and verified for isotope analysis. Once it is validated and available it can improve the available quantification limits to researchers and consultants.

The cDCE isotopic data also show much variability in the samples collected. Degradation of TCE often produces DCE with lower isotopic ratios. However, further degradation of DCE can impart an increase in $\delta^{37}Cl_{cDCE}$ and $\delta^{13}C_{cDCE}$ values. The carbon isotopic ratios of cDCE are generally higher than the corresponding $\delta^{13}C_{TCE}$ values.

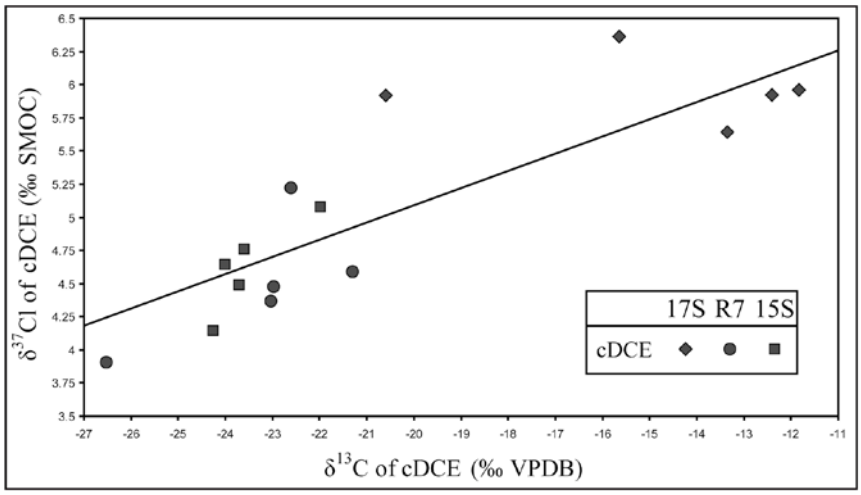

Figure 4.9.5: Carbon and chlorine cDCE isotopic data pertaining to wells 15S, R7 and 17S.

The lowest isotopic ratios of the 4 wells discussed in detail above were found in well R7. The variability of analytical results in this well does indicate that the degradation of TCE and subsequently cDCE can be quite different seasonally. This was expected due to variable pumping rates and the nature of groundwater flow in an area with large amounts of precipitation. The analyses of cDCE isotopes show less variability in the isotopic ratios observed in well 15S, though the values are in the same general range as those observed in well R7. Well 17S, in contrast, had consistently higher $\delta^{37}Cl_{cDCE}$ and $\delta^{13}C_{cDCE}$ values. In this well, the carbon isotopes of TCE show as much as a 17 ‰ difference between the lowest $\delta^{13}C_{TCE}$ values observed in well 3S and the highest $\delta^{13}C_{cDCE}$ values from well 17S.

The redox conditions at the Smithville site have been characterized by previous research. These data along with the data pertaining to redox conditions indicate that the native uncontaminated groundwater in the upper part of the Eramosa Member aquifer is suboxic, but that methanogenesis is not a significant terminal electron accepting process in this zone. Redox data indicate that electrochemical conditions are highly variable throughout the site, including an area near the source zone that is less reducing. Some of the wells within the area of the TCE plume on site have much more reducing environments. These environments have especially evolved in the outside of the TCE contaminant plume where concentrations of TCE are relatively high but not at a maximum. This may be due to the fact that significant concentrations of certain organic contaminants, including TCE, may substantially inhibit microbial activity necessary to generate more reducing groundwater environments. The more reducing environments formed in wells further from the center of the contaminant mass is consistent with other research in which a mixing zone at the edges of the plume has been observed.

The results of chemical analyses of chlorinated ethenes and ethane yielded a dataset that was useful in determining which wells may be affected by the degradation of TCE. Production of DCE in significant amounts, above 1.0 ppb, was observed in multiple wells after 2003. The additional production of high concentrations of DCE, VC, ethene, and ethane indicates that degradation was a significant process removing TCE contaminants from the groundwater system underlying the Smithville site. Given the production of the degradation byproducts, the redox conditions of the site, as well as the isotopic evidence, reductive dechlorination in the presence of microbial catalysts is most likely the dominant degradation process at the site based on multiple lines of evidence. DCE data observed indicates that the dominant product is DCE in the form of the cis-1,2-DCE isomer. This is a further indication that microbes most likely mediate the dechlorination process that forms DCE from TCE. In April 2010, analyses of acetic acid were completed on 10 of the wells at the site, revealing that the concentrations were below the analytical limits (1-10 mg/L). This also supports the case for biodegradation due to the fact that acetic acid can be produced as a result of abiotic degradation of TCE in reducing areas.

When combined with the chemical data above, isotopic data can often be used to further assess TCE degradation. The isotopic data had a high range in both carbon and chlorine isotopes as well as much variability even in samples collected from the same well sampling interval. Given the geological characteristics of the groundwater aquifer material, the variability in chemical and isotopic data is a likely result. However, the range in isotopic data does indicate that degradation is occurring at the Smithville site. On the other hand, we note that the TCE concentrations in well 3S are extremely high and the isotopic data indicates that not much degradation has occurred at this sampling location. This data from samples collected near the source zone may indicate the presence of an active TCE source. Wells sampled closer to the

edges of the TCE contaminant plume, including wells R7 and 15S, show a significant production of degradation products as well as higher $\delta^{37}Cl_{TCE}$ and $\delta^{13}C_{TCE}$ values than those observed at well 3S. Redox data, formation of chemical degradation products and isotopic data all indicate that further degradation of TCE does occur in the vicinity of well 17S.

Compound specific isotopic analysis of DCE is a useful tool to characterize the degradation of DCE. The analyses of cDCE isotopes indicate that transformation of cDCE to more degraded compounds is occurring. The $\delta^{37}Cl_{cDCE}$ and $\delta^{13}C_{cDCE}$ values in wells R7 and 15S are generally much higher than corresponding TCE isotopic values. This indicates that continued degradation of cDCE is occurring within the contaminant plume. Both the carbon and chlorine isotopes of cDCE in well 17S tend to be more enriched in heavier isotopes than samples collected in other wells. Given that the values for TCE chlorine and carbon isotopic analyses from well 17S are also high, cDCE is forming and continued degradation is a significant process at this location.

The results of isotopic analyses and chemical data have been shown to be useful in estimating the degree of degradation of TCE and DCE in certain field sites. In addition, numerical simulation studies of McLaren et al. (2012) suggest that the stability of the plume is due to first-order degradation. However, given the variability of chemical and isotopic data, a quantitative calculation of the degree of biodegradation cannot be reliably estimated. Increased sampling on site may aid in understanding the degree of biodegradation. Applied microcosm studies along with isotopic analyses from samples collected at the site may aid in using this data to estimate the degree of biodegradation. Microcosm data may also provide a more specific determination of the biological processes affecting degradation. Finally, the application of a numerical groundwater flow and transport model that can account for isotope fractionation (e.g., Huang et al., submitted manuscript) may shed additional insights on biodegradation and natural attenuation at this site.

TASK 8: NUMERICAL MODELING OF LAB AND FIELD DATA

4.10 Numerical simulation of DNAPL emissions and remediation in a fractured dolomitic aquifer

4.10.1 Introduction

Chlorinated solvents are the most prevalent contaminants at industrial sites and military installations (Pankow and Cherry, 1996), and are released as Dense Nonaqueous Phase Liquids (DNAPLs). DNAPL release history is often poorly documented, and the movement of pure-phase DNAPL in heterogeneous geologic environments is complex and difficult to predict, which leads to considerable uncertainty in their fate in the subsurface. Because pure-phase DNAPL sources can contribute to long-term groundwater contamination for decades to centuries, their remediation and or management is of high importance.

Over the past decade, considerable effort has been expended towards understanding the behaviour of DNAPLs released in heterogeneous unconsolidated geologic materials, and progress has been made with respect to understanding the processes operating in these environments, including the role played by heterogeneity on the movement and dissolution mechanisms of pure-phase DNAPL and the migration of the aqueous-phase. However, it is widely recognized that few, if any, contaminated sites have been remediated with respect to either the pure-phase DNAPL source or the aqueous-phase plume.

The difficulty involved in remediating DNAPL sites has led to an increase in interest in passive or natural attenuation (e.g., Wiedemeier et al., 1999; Alvarez and Illman, 2006; Illman and Alvarez, 2009). This approach requires the knowledge of dissolution mechanisms that control the partitioning of pure-phase DNAPL into the aqueous phase. Research in this area has shown that dissolution of DNAPLs can be a slow process resulting in plumes that can persist for very long timeframes. There is also considerable debate on whether dissolution/mass transfer can be modeled as an equilibrium or kinetic process (e.g., Miller et al., 1990; Powers et al., 1992, 1994a,b; Geller and Hunt, 1993; Imhoff et al., 1994a,b; Unger et al., 1998; Frind et al., 1999; Saba and Illangasekare, 2000; Nambi and Powers, 2000; Maji and Sudicky, 2008). For example, Frind et al. (1999) examined the dissolution and mass transfer of multiple organics under field conditions through numerical simulations of the Borden emplaced source experiment conducted by Rivett et al. (1994, 2001). In particular, Frind et al. (1999) were successful in matching the simulated results to the actual plume data by considering declining solubility and flow bypassing effects. The simulations also showed that mass transfer at this site is equilibrium controlled during the 1000-day observation period and that the apparent tailing of one of the organic components is due to declining solubility, rather than mass transfer kinetics. However, Frind et al. (1999) noted that the Borden aquifer is mildly heterogeneous (Sudicky, 1986; Woodbury and Sudicky, 1991) and that the plume from the emplaced source was only observed over 1000 days. Mild heterogeneity and short experimental duration may have contributed to the applicability of the equilibrium assumption in describing the mass transfer behavior at Borden. However, research in the literature suggests that kinetic conditions can prevail in a more heterogeneous aquifer (Mayer and Miller, 1996) and when longer durations of mass transfer are considered (Powers et al., 1994a,b).

Research on DNAPL mobilization, dissolution, and plume transport has progressed significantly for porous media, but there is still paucity of information in terms of fractured geologic media, partly due to the complexity of such systems. For example, in a fractured low-permeability material (e.g., igneous and metamorphic rocks), DNAPL will preferentially enter

and remain within the fracture network, because the DNAPL entry pressure is generally lower in the fractures than the porous matrix. Because the fracture void space is commonly on the order of 10^{-3} or less of the bulk rock volume, even small DNAPL releases can spread over large rock volumes and depths relative to a similar spill volume in granular media. Because determining the maximum vertical and lateral extent of the pure-phase DNAPL source zone is of primary importance when assessing source-zone remediation options and aqueous-phase plume containment, the characterization of the fracture network properties becomes a vital task although it remains one fraught with uncertainty.

It is well known that the diffusion of dissolved contaminants from fracture to matrix can retard the movement of aqueous-phase solute plumes (see, e.g., Tang et al., 1980, Sudicky and Frind, 1982). It has also been shown by Parker et al. (1994) that the concomitant processes of DNAPL dissolution and matrix diffusion can cause the disappearance of the pure phase from DNAPL-saturated fractures in a high porosity matrix material in a relatively rapid time frame. More recently, Slough et al. (1999a) performed a suite of numerical experiments employing the multiphase compositional model CompFlow (Unger et al., 1995, 1996, 1998), enhanced to handle DNAPL migration in discrete fracture networks embedded in a porous rock matrix. They showed that matrix diffusion can cause both the eventual disappearance of DNAPL, and also affect the rate and extent of DNAPL migration in the fracture network. Further work by Slough et al. (1999b) demonstrated for the first time that the entry pressure of DNAPL to the rock matrix could play a critical role on the distribution of pure-phase DNAPL in fractured rock. For example, a low entry pressure, typically the case in moderate-porosity carbonates, will enhance the movement of the pure-phase DNAPL into the rock matrix. While this tends to limit the vertical and lateral extent of the pure-phase DNAPL source zone, Slough et al. (1999b) concluded that attempts to clean up the source by "flushing" (e.g., surfactant or chemical oxidant flushing, water flooding, etc.) could be thwarted by the preferential flow of the flushing fluid through the fracture network, thereby limiting contact with DNAPL stored in the rock matrix. To date, the mechanism of DNAPL uptake by the rock matrix has not been explored in the field or laboratory studies, and the scope of the numerical experiments is limited to quantifying uncertainties and defining the range of fracture-matrix conditions under which it can occur.

It is now widely accepted (e.g., Sale and McWhorter, 2001; Rao and Jawitz, 2003) that complete DNAPL source reduction (i.e., 100% by mass) is not achievable in heterogeneous geologic media. Consequently, cleanup strategies based on partial source-zone removal and natural attenuation of the aqueous-phase plume are becoming popular amongst groundwater practitioners and regulators. The salient question is then, how much source mass must be removed such that a down-gradient compliance goal can be achieved for final site closure? Rao and Jawitz (2003) and others showed that a significant reduction in the aqueous-phase contaminant flux at a downstream boundary could be achieved *via* partial source-zone mass reduction, and that a flux-based metric is more suitable for gauging the performance of partial source-zone remediation than a concentration-based metric. Nevertheless, all of these analyses were constrained to unconsolidated geologic materials and used simple analytical models. To our knowledge, the relative benefits of partial DNAPL source-zone remediation on either mass flux or concentration reduction in fractured porous rock have not yet been explored.

Unger et al. (1998) conducted an extensive numerical analysis of the effects of different DNAPL mass transfer models on source depletion rates under natural-gradient conditions in synthetically constructed heterogeneous granular aquifers, and found that the strength of the contaminant source and the resulting aqueous-phase plume concentration are largely controlled

by how the dissolution process is represented. Although the discretization was relatively coarse and fine-scale heterogeneities could therefore not be accommodated, their multi-realization analysis revealed that using the equilibrium versus a kinetic dissolution model had a more profound effect on source-zone depletion times and contaminant emissions from the source than the degree of heterogeneity of the aquifer permeability. More recently, Maji and Sudicky (2008) incorporated a full suite of published kinetic dissolution models into CompFlow and carried out a high-resolution stochastic analysis of the impact of source-zone depletion on aqueous-phase concentration and mass flux reduction.

Research conducted to quantitatively understand pure-phase DNAPL movement and aqueous-phase plume development in fractured-rock environments has mainly been limited to computational (e.g., Huyakorn et al., 1994; Rubin et al., 1997; Slough et al., 1999a,b; Reynolds and Kueper, 2003; Rubin et al., 2008) and laboratory studies (e.g., Schwille, 1988; Reitsma and Kueper, 1994; Longino and Kueper, 1999; Dickson and Thomson, 2003; Shaefer et al., 2009). For example, Dickson and Thomson (2003) examined the dissolution of entrapped DNAPLs in variable-aperture fractures in the laboratory and developed an empirical model for mass transfer rates. Schaefer et al. (2009) conducted laboratory experiments in discretely fractured sandstone blocks to evaluate residual DNAPL architecture and dissolution. While these studies have advanced the understanding of dissolution behaviour of DNAPLs in fractured rocks at the laboratory scale, a comprehensive study that examines the relationship between the DNAPL source zone, its aqueous phase plume and remediation in a field setting is lacking.

This study focuses on the fate of various chlorinated solvents that have penetrated the fractured dolomitic bedrock at the Smithville site in Ontario, Canada, where a large aqueous-phase plume has developed over the last several decades. A pump-and-treat remediation program has been in operation since 1989 with the aim of hydraulically stabilizing the plume. First, a review of the available field data is presented to improve our understanding of the relevant flow and contaminant transport processes operating at the site, and to assess the performance of the pump-and-treat remediation program in terms of contaminant mass recovery, which has not been quantified to date. We then present the results of CompFlow simulations of the development of a pure-phase DNAPL source zone, which is then used to define the source term for a HydroGeoSphere (HGS) (Therrien et al., 2005) simulation of the transport of aqueous-phase trichloroethene (TCE) in the regional groundwater flow system, both prior to pump-and-treat remediation, and after the system is in operation.

4.10.2 Site location and history

Between 1979 and 1985, Chemical Waste Management Limited (CWML) operated a storage facility for industrial wastes located approximately one kilometre northeast of the town of Smithville, Ontario, about 15 km south of Lake Ontario on the Niagara Escarpment (Figure 4.10.1).

The facility was filled to capacity by 1983, and it is estimated that about 434,000 liters of liquid wastes, comprising an estimated 266,000 liters (60% of the total volume) of Polychlorinated Biphenyls (PCBs), 57,000 liters (13%) of other organic chlorinated solvents, as well as acids, alkalis, and other inorganic waste sludge (Golder, 1999) were received during its operating life.

In 1980, the Ontario Ministry of the Environment (MOE) installed five test wells to the north and south of the CWML compound to monitor the site. Soil and water samples collected from these wells did not contain detectable levels of PCB or other organic contaminants.

However, in 1985, it was discovered that PCB and other solvents had penetrated the overburden and infiltrated the upper portions of the local bedrock. This discovery caused the shutdown of a nearby municipal water supply well. The extent of the TCE plume in 1988, as inferred from on-site investigations (Smithville Phase IV Bedrock Remediation Program, 2000) is shown in Figure 4.10.2.

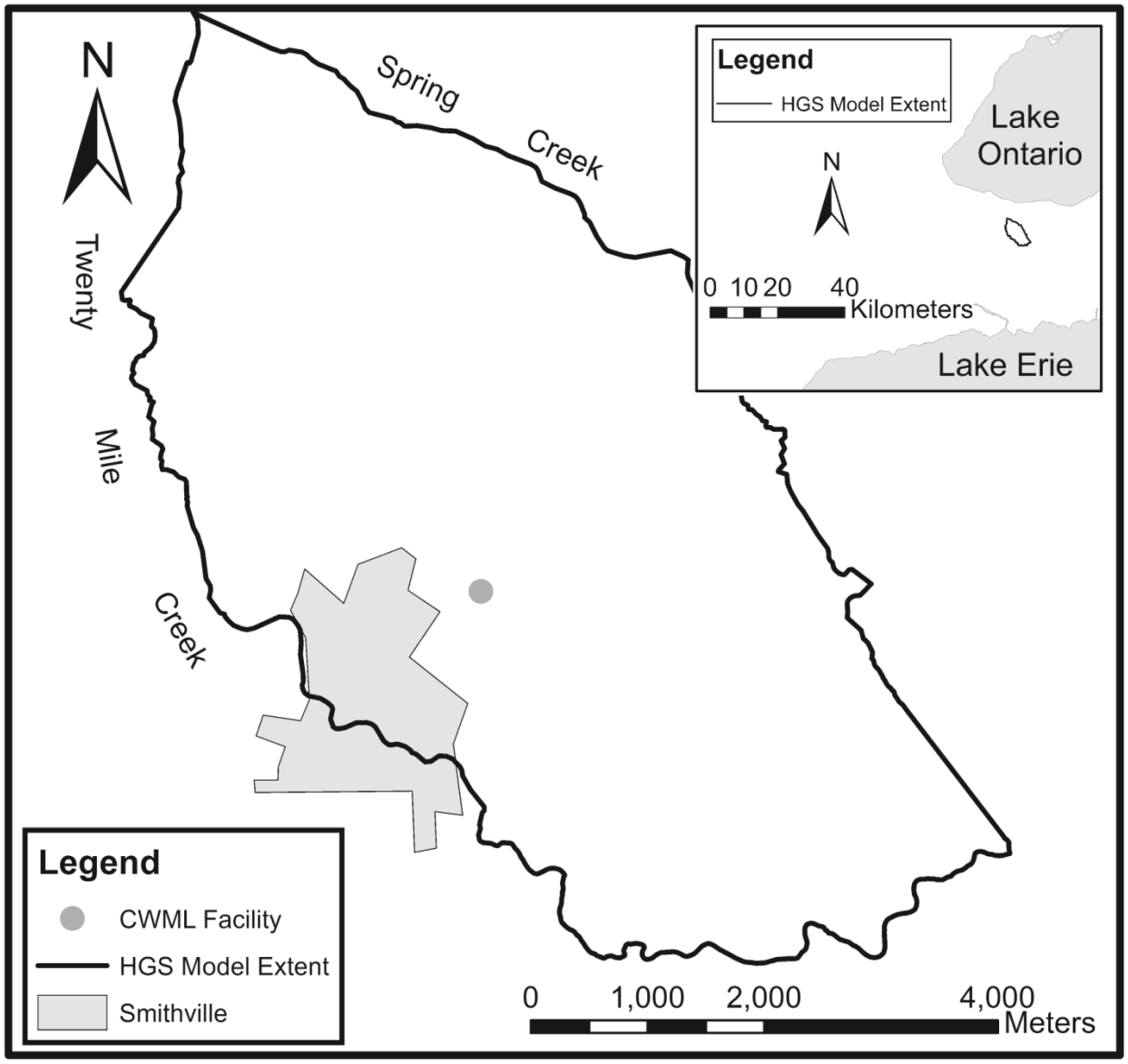

Figure 4.10.1: Regional and watershed scale maps showing the Smithville site location, Ontario, Canada.

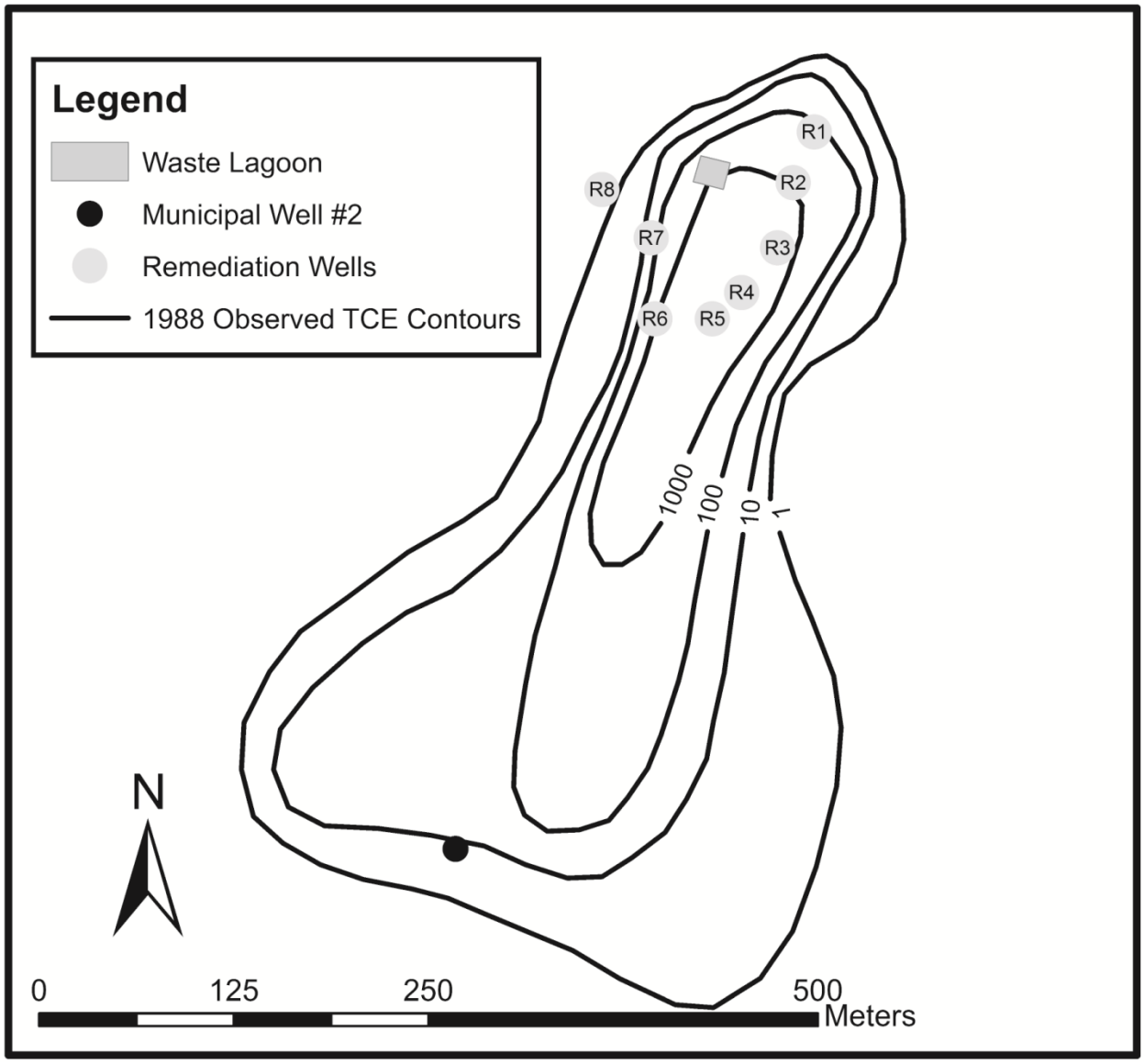

Figure 4.10.2: Observed TCE plume with concentration in μg/L based on data from 1988.

4.10.3 Site hydrogeology and remediation system in place

4.10.3.1 Site geology

The Smithville site is blanketed with about 5-10 m of glacial till and lacustrine sediments. This layer has a low hydraulic conductivity (10^{-9} to 10^{-11} m/s) (Zanini et al., 2000), but significant fracturing has been observed throughout its entire thickness, which could allow contaminants to penetrate and move into the underlying bedrock relatively easily (Golder Associates, 1995; Slough et al., 1997).

Rock cores logged in an onsite drilling program were used to characterize the local bedrock units. The uppermost bedrock layer is the Lockport Formation. Locally, the Lockport

Formation dips at about 0.5% to the South. This formation can be divided into 4 members, which are, in descending order, the Eramosa, Vinemount, Goat Island, and Gasport. The Eramosa is a dolostone that has been characterized as fine-crystalline, bituminous, and argillaceous. It contains many fractures, is weathered (Golder, 1999), and is 11-15 metres thick in the local area. The contact between the Eramosa and the underlying Vinemount is gradational. The Vinemount has been divided into upper and lower units in local well logs (Golder, 1999), with the upper unit being a shaly dolostone that is highly weathered and is 4-6 metres thick, and the lower unit also being a shaly dolostone, but not as weathered, and with tighter bedding and a thickness of 3-5 metres. The Goat Island is a dark to light grey, and crystalline (very fine to micro crystalline) dolostone. It tends to be mineralized with calcite, selenite, sphalerite, galena, and pyrite (Golder, 1999), and is 6-8 meters thick, with thick and irregular bedding. The Gasport is a light grey, generally coarse-grained, dolomitic limestone and is locally 8-11 metres thick. Underlying the Gasport is the Decew Formation, which is a very fine-crystalline argillaceous dolostone that tends to be dark grey in color and is 2 metres thick in the local area. Beneath the Decew Formation is the Rochester Formation, which is a dark grey to black, calcareous shale and siltstone with abundant carbonate interbeds of approximately 17 metres in thickness.

4.10.3.2: Site hydrogeology

To study the hydrogeology of the area, over 50 observation wells were installed between 1985 and 1990. Cores were collected and photographed for fifteen of the boreholes drilled at the site. The frequency, size and orientation of fractures in the Lockport Formation were recorded. These fractures were classified as bedding plane fractures, vertical fractures, or broken-core zones (Lapcevic et al., 1997). Site characterization also included 1597 constant-head hydraulic tests in 23 boreholes (Golder Associates, 1994; Novakowski et al., 1999; Zanini et al., 2000). For these boreholes, test intervals of 2 meters were isolated using pneumatic packers. For 12 boreholes, an additional 824 tests with 0.5 meter test intervals were conducted. Table 4.10.1 presents a summary of K values grouped by individual bedrock units estimated from the constant-head hydraulic tests.

Table 4.10.1: Hydraulic conductivity estimated using constant-head hydraulic tests for various geological units at the Smithville site.

Unit	Number of tests	Geometric mean of K (m/s)	Mean ln K (m/s)
Eramosa	70	2.14×10^{-6}	-13.05
Upper Vinemount	15	8.71×10^{-7}	-13.95
Lower Vinemount	295	1.10×10^{-8}	-18.33
Goat Island	227	8.06×10^{-8}	-16.33
Gasport	148	1.21×10^{-6}	-13.62
Decew	173	9.66×10^{-8}	-16.15
Rochester	676	2.73×10^{-9}	-19.72

Ground water flow at the site is generally to the southeast, following the stratigraphic dip of the geological units (Golder Associates 1995). Previously conducted studies of the Lockport Formation at this site and in surrounding areas have revealed that ground water flow is primarily controlled by laterally extensive bedding plane fractures that have limited vertical connectivity (Novakowski and Lapcevic 1988; Riechart 1992; Golder Associates 1995; Zanini et al., 2000). Site investigations (Golder Associates 1995) conducted previously reveal that fractures in the upper portion of the Lockport formation could be laterally connected over a distance of 1 km. This observation is based on the transport of contaminants from the DNAPL source zone. The hydraulic gradient in the upper portion of the Lockport formation has been estimated to be on the order of 0.02 with estimates of ground water velocity ranging from 20 to 6000 m/yr. In contrast, hydraulic gradients of the units beneath the upper portion of the Lockport formation were estimated to range between 0.001 to 0.007 (Golder Associates 1995; Zanini et al., 2000).

4.10.3.3 Contamination history and remediation system

The exact mass, composition, date and location of contaminant released at the Smithville site are not known. However, the surficial location of the vast majority of released contaminants has been identified and is indicated as the Waste Lagoon in Figure 4.10.2. Slough et al. (1997) deduced that fractures and macropores within the till can allow for the downward migration of DNAPLs released at the ground surface. It has been estimated that 30,000 - 40,000 liters of a poorly characterized mix of DNAPLs were released to the bedrock aquifer (Golder Associates, 1999). As part of the remediation program, 8 pumping wells (see Remediation Wells, Figure 2) were installed around the source zone and connected to a treatment system. These remediation wells are intended to hydraulically stabilize the contaminant plume and remove aqueous-phase contaminants from the subsurface.

Water samples collected from both shallow and deep wells from November 1987 to December 2007 reveal that TCE concentration values have been continuously decreasing in all recovery wells except R7, and vary significantly from well to well. For example, TCE concentrations in R7 are relatively high (typically greater than 250 µg/L) while the concentrations are much less in R8 (usually below 5 µg/L).

The TCE mass recovered through the pump-and-treat wells was estimated based on the pumping rate and TCE concentration from each recovery well. Figure 4.10.3 shows the total TCE mass removed by the eight remediation wells. TCE mass removed varies from year to year and from well to well due to temporal variations in the pumping rate. In general, we observe that as the total pumping rate increases, the total mass of TCE recovered through the wells also increases.

Table 4.10.2 summarizes the average rate of TCE mass removed and total TCE mass removed from each well during the period March 14, 1995 to December 15, 2004 (Illman et al., 2012). In terms of TCE removal, wells R1, R5, and R8 have been less efficient compared to the other recovery wells, while well R7 has been the most efficient. The estimated average rate of TCE mass removed for this period is 73.2 g/day (based on 21 data samples) while in total for the 8 recovery wells, 15.9 kg of TCE has been removed. This suggests that pump-and-treat systems may not be very effective in removing TCE in heterogeneous aquifers, in particular, in fractured rock environments.

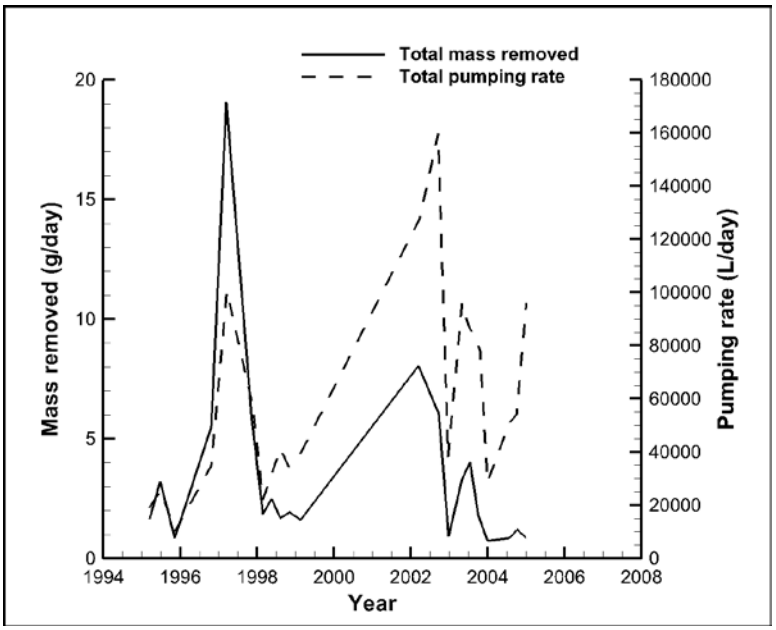

Figure 4.10.3: Total TCE mass removed from all recovery wells with respect to total pumping rate (after Illman et al., 2012).

Table 4.10.2: TCE mass removed from recovery wells (March 14, 1995 - December 15, 2004) (after Illman et al., 2012).

Recovery Well	TCE Mass Removed (g/day)	Total TCE mass Removed (kg)
R1	1.5	0.2
R2	8.5	2.1
R3	10.8	1.5
R4	7.6	1.2
R5	1.0	0.2
R6	5.2	0.8
R7	37.3	9.6
R8	1.3	0.2
Total	73.2	15.9

4.10.4 Regional groundwater flow modeling

To improve our understanding of groundwater flow, contaminant transport, and the pump-and-treat remediation performance, we utilize HydroGeoSphere (HGS), a physically based, surface/variably saturated subsurface flow model to a 32 km^2 watershed which includes the Smithville site (see Figure 4.10.1). HGS is capable of simulating water flow and solute transport in surface water bodies and in the variably-saturated subsurface. The two-dimensional form of the nonlinear diffusion-wave equation, together with Manning's equation to compute overland flow velocities, is employed on the surface, while Richards' equation and Darcy's law are assumed to hold in the subsurface. Full coupling of the surface and subsurface flow regimes is accomplished by simultaneously solving one system of non-linear discrete equations arising from the control volume finite element method to describe flow and solute transport in both flow regimes, as well as the water and solute fluxes between continua. Details concerning the theory, numerical solution techniques and example applications using HGS are given in Therrien et al. (2005).

A 10-m Digital Elevation Model (DEM) obtained from the Ontario Ministry of Natural Resources (2009) was used to identify the lateral extents of the watershed as well as define a two-dimensional triangular-element mesh representing the top of the model domain (ground surface). Elevations from the DEM were mapped onto an unstructured finite element mesh generated for HGS. The base of the domain coincides with the top of the Rochester formation, which is of relatively low permeability. The lateral boundaries of the numerical model were chosen to coincide with rivers or surface water flow divides as shown in Figure 4.10.1. Twenty-mile Creek and Spring Creek form much of the southwestern and northeastern boundaries, respectively.

The finite-element mesh used to conduct the flow and transport simulations is shown in Figure 4.10.4. The zone of dense mesh refinement is extensive enough to include the source zone, remediation well field and Municipal well #2 (Figure 4.10.2). The 3D finite-element mesh contains 512,337 nodes and 974,010 6-node prism elements. Elements range in size from about 100 m down to 10 m in the zone of refinement. The 2D surface flow domain and its corresponding finite-element mesh are coincident with the top of the model domain shown in Figure 4.10.4.

Flow boundary conditions are assigned for both the surface and subsurface domains. For the surface domain, the entire outer boundary was assigned a critical depth condition, which allows surface water to flow freely out of the domain if ponding occurs. The interior regions of the surface flow domain were assigned a specified flux boundary condition with the flux value (6.0 cm/year) being calibrated for the observed regional flow system. This value represents a net effective precipitation rate (P_{eff} = P - R - ET) and reflects the low permeability of the clay/till overburden. It is representative of the relatively small amount of the total precipitation that recharges (i.e. reaches) the water table, the remainder being lost to runoff and evapotranspiration processes. By including the surface flow domain in the model, we avoid the possibility of unrealistically high heads that may develop when the recharge water is forced into the subsurface domain as an applied flux.

Initial values of hydraulic and transport properties, including hydraulic conductivity (K) and porosity (ϕ) were taken from reports and previous modeling studies. Although fractures are common at the site, the subsurface domain was treated as an equivalent porous medium in the HGS model, and so the K input reflects the bulk nature of the combined porous matrix and fracture network system. These values, along with the net effective precipitation rate, were

calibrated by comparing model results to the inferred regional piezometric surface within the upper Eramosa provided in Pockar (1999), which was based on water well records obtained from the Ontario Ministry of the Environment (Well Record Data, 1899-2010). Although there exists a large database of observed water levels that were taken as part of numerous on-site investigations at the Smithville site, these were mostly collected after the establishment of the pump-and-treat system, and so do not reflect undisturbed conditions.

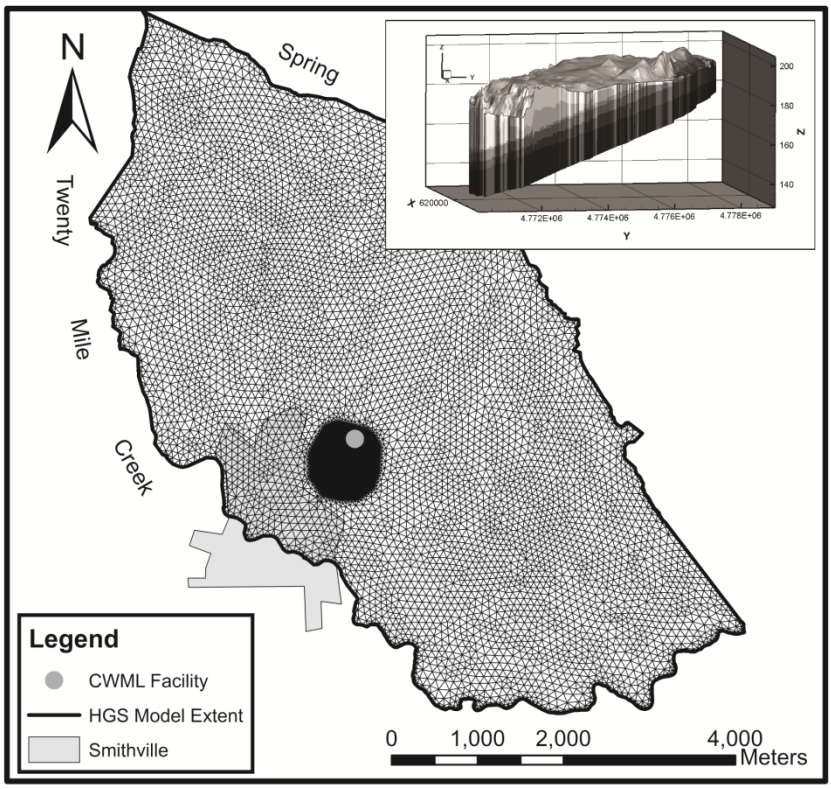

Figure 4.10.4: Finite-element mesh for the study area. Inset shows stratigraphic layering (note that north is oriented parallel to the y-axis).

The final hydraulic parameter values used to obtain the calibrated steady-state flow solution are given in Table 4.10.3. The final net effective precipitation rate used in the model was 6 cm/year. Figure 4.10.5 compares the observed piezometric surface in the Eramosa formation (Pockar, 1999) and the simulated hydraulic head from HGS. According to Pockar (1999), the potentiometric surface given in Figure 4.10.5 was obtained from water well drilling records archived by the Ontario Ministry of the Environment and Energy (OMOEE, 1986). Although the accuracy of the reported potentiometric surface is unknown, the surface is judged to be reasonable as it reflects surface topography. A measure of the accuracy of the flow solution is given in Figure 4.10.6, which was constructed by extracting simulated hydraulic head values along the isocontours of Pockar (1999) and plotting them against the observed values. Error bars represent the standard deviation of the head values extracted along the isocontours (i.e. an estimate of the error) and are nowhere greater than +/- 1.2 metres. Figures 4.10.5 and 4.10.6 indicate that the regional flow direction and hydraulic gradient can be simulated reasonably well with the numerical model. This suggests that the conceptualization of flow through the fractured rock as an equivalent porous medium is adequate at this regional scale.

The fluid exchange flux between the surface and subsurface was around -6 cm/year (negative values indicate recharge) over most of the domain, which is equal to the net effective precipitation value. Zones of discharge are mostly located along the edges of the domain near Spring Creek and Twenty Mile Creek.

Table 4.10.3: Calibrated hydraulic parameter values.

Hydrostratigraphic Unit	***K* (m/s)**	***ϕ***
Overburden	1.5×10^{-8}	0.50
Eramosa	2.1×10^{-4}	0.06
Upper Vinemount	8.7×10^{-5}	0.03
Lower Vinemount	1.1×10^{-8}	0.03
Goat Island	8.1×10^{-8}	0.08
Gasport	1.2×10^{-6}	0.09

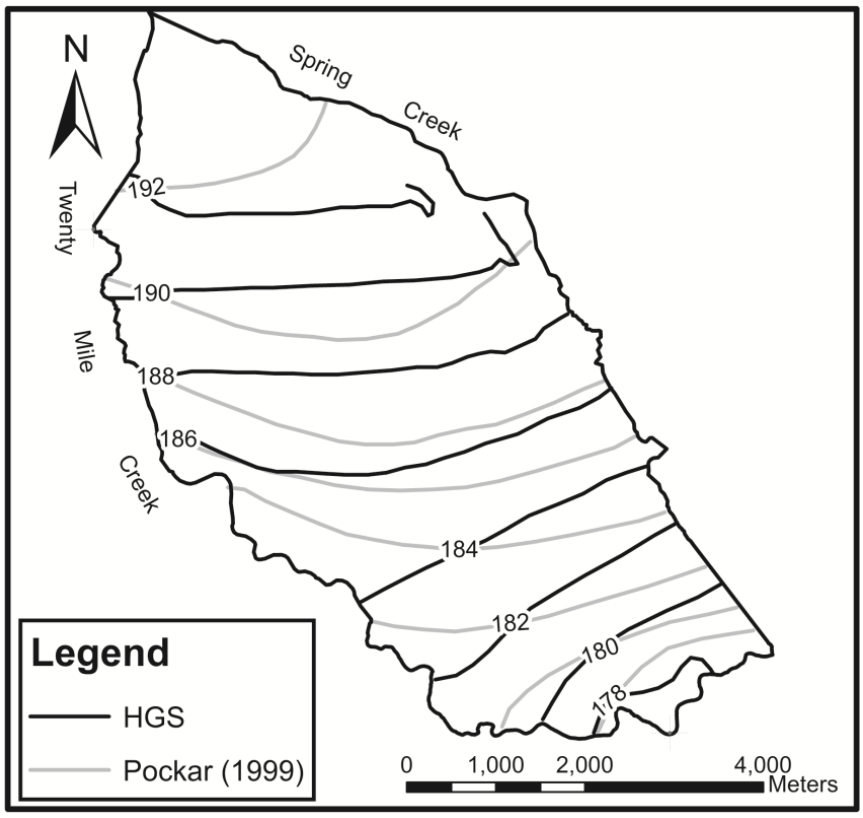

Figure 4.10.5: Inferred piezometric head (m) (Pockar, 1999) and simulated hydraulic head (m) (HGS) in the Eramosa formation.

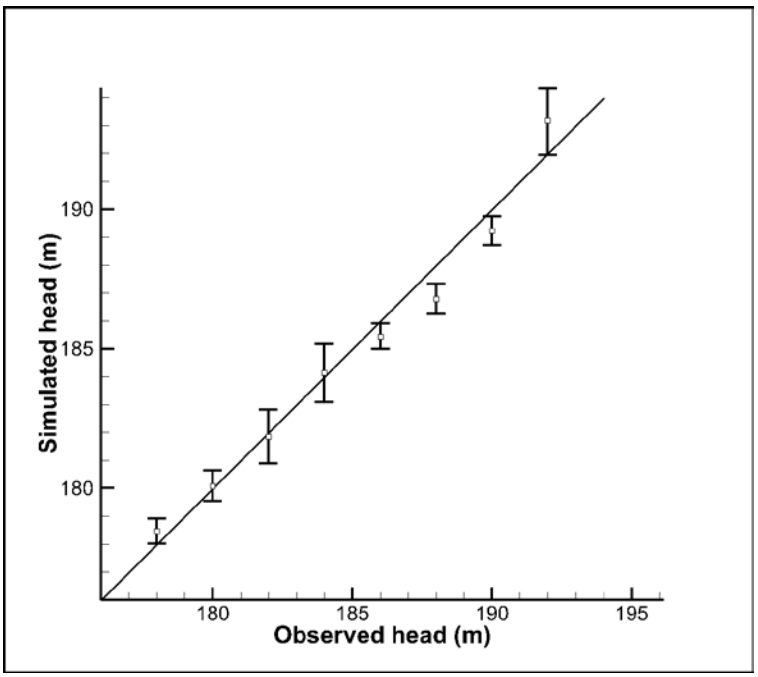

Figure 4.10.6: Simulated versus observed [inferred piezometric surface within Eramosa formation (Pockar, 1999)] hydraulic head. Mean heads, (indicated by squares) were extracted from the simulated head solution at 100 evenly spaced points along each isocontour of observed head. Error bars represent the standard deviation of the extracted head values.

4.10.5 Source zone modeling

For regional scale transport simulations of aqueous phase organic contaminants in fractured geologic media, it is necessary to describe the DNAPL distributions within the source zones. The subsurface movement of DNAPL in fractured rocks is a complex process and the final distribution depends largely on the hydraulic properties and the capillary pressure-saturation relationships of both the fractures and the matrix of the geologic medium. The result is an uneven but essentially stable distribution of DNAPL 'pools' which dissolve slowly over time. A multiphase flow and multispecies reactive transport model, Compflow (Unger et al., 1995, 1996, and 1998), can simultaneously simulate both aqueous (groundwater) and nonaqueous phase (DNAPL) flow, dissolution, and aqueous phase transport in fractured porous media and it can be used to characterize the DNAPL source distribution at a contaminated site.

DNAPL source simulations at the Smithville site are based on the hydrogeological conceptualization suggested by Slough et al. (1999b). Hydrostratigraphy at the Smithville site is comprised of 5-m of overburden, 1-m thick sandy till, 17-m thick permeable dolostone (Eramosa), 3-m vuggy dolostone (upper Vinemount), 2-m tight dolostone (lower Vinemount), and 15-m permeable dolostone (Goat Island) from ground surface to depth (Figure 4.10.7a). Fracture logs at the site indicate that the permeable dolostone is highly fractured, while the vuggy and tight dolostones are relatively moderately fractured. It is assumed that surface overburden and sandy till units are dominated by more permeable vertical fractures (Figure 4.10.7b). Statistical characteristics for fracture location, frequency, length, and aperture are based on the data from borehole survey (Golder, 1999; MOE, 2010) and previous modeling studies

(Slough et al., 1999b) and described in Table 4.10.4. For the fracture network generation, all fracture attributes are assumed to follow a simplistic uniform distribution for given minimum and maximum values and the generation of each fracture is independent (a Poisson process). The permeability for each fracture is calculated based on the cubic law (i.e., $k = (2b)^2/12$ where $2b$ is the fracture aperture) and hydrogeological properties of each stratigraphic unit and fluid properties are described in Table 4.10.5. The retention relations for the fractures of different openings and matrix blocks are given in Figure 4.10.8.

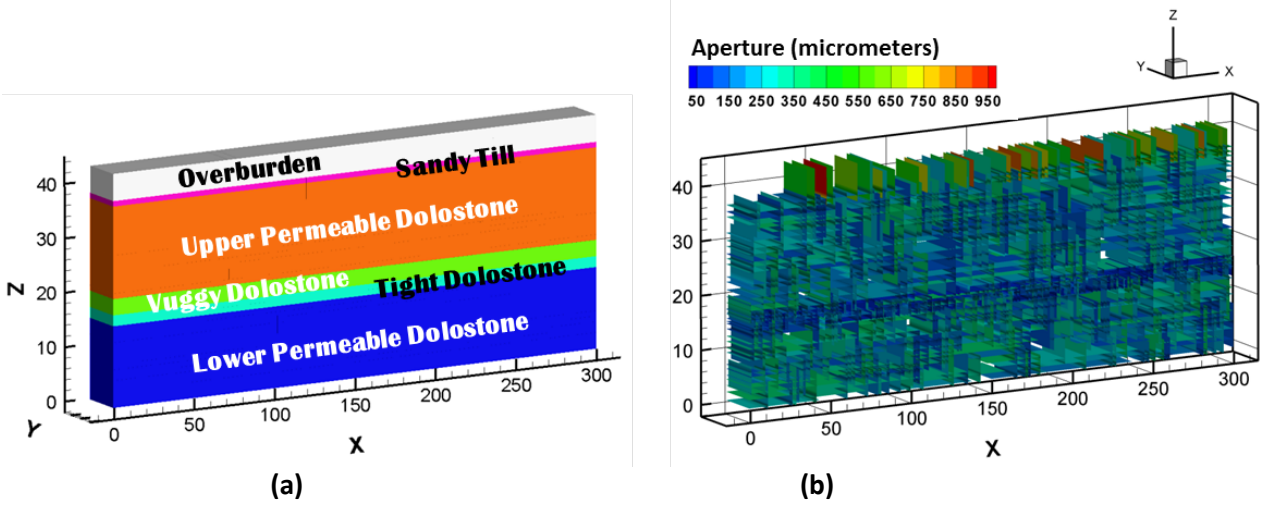

Figure 4.10.7: (a) Hydrostratigraphy and (b) an example of a fracture network at the Smithville site.

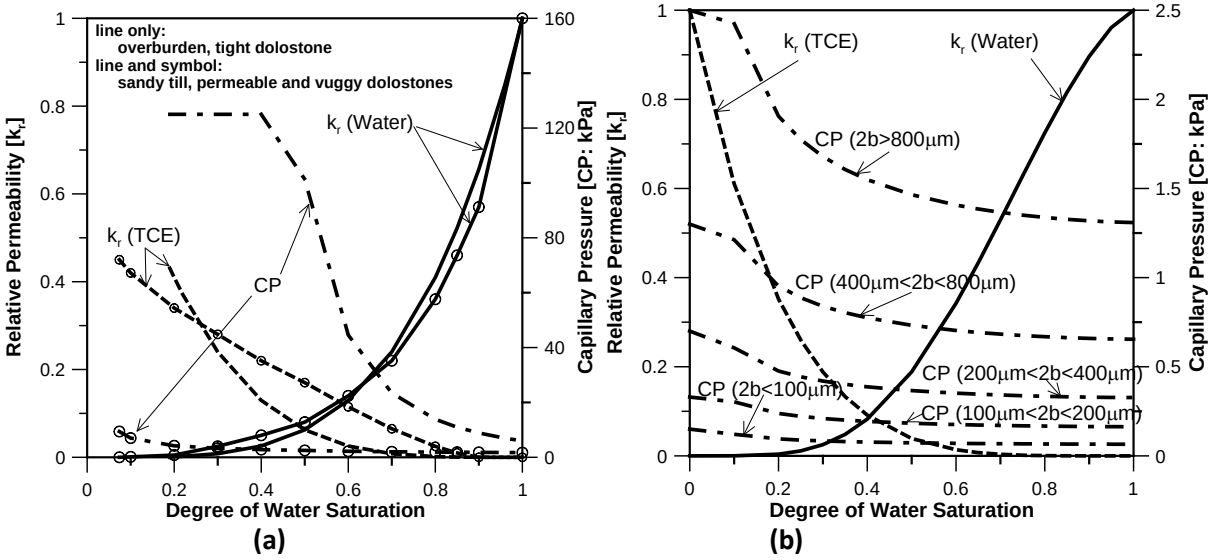

Figure 4.10.8: Retention relations among water saturation, relative permeability (k_r), and capillary pressure (CP) used for (a) matrix and (b) fracture.

Table 4.10.4: Statistical characteristics for fracture location, frequency, length, and aperture distributions. Location, length, and aperture are assumed to follow a uniform distribution.

Fracture Attribute \ Hydrostratigraphic Unit		Overburden /Sandy Till	Upper Permeable Dolostone	Vuggy and Tight Dolostone	Lower Permeable Dolostone
Location	x_{min}[m], x_{max}[m]	[0,300]	[0,300]	[0,300]	[0,300]
	z_{min}[m], z_{max}[m]	[38.5,38.5]	[16,38]	[14,18]	[0,16]
Vertical fracture					
Frequency	1/m	0.2	1.3	0.91	1.43
Length	l_{min}[m], l_{max}[m]	[5,5]	[5,15]	[30,90]	[30,90]
Aperture	$2b_{min}$[μm], $2b_{max}$[μm]	[200,1000]	[100,400]	[50,200]	[100,400]
Horizontal fracture					
Frequency	1/m	NA	1.25	1.9	1.25
Length	l_{min}[m], l_{max}[m]	NA	[60,120]	[2,4]	[5,10]
Aperture	$2b_{min}$[μm], $2b_{max}$[μm]	NA	[100,400]	[50,200]	[100,400]

Table 4.10.5: Parameters used for COMPFLOW simulations of DNAPL infiltration [modified after Slough et al., (1999a and b)].

Material Properties							
	Overburden	Sandy Till	Upper Permeable Dolostone (Eramosa)	Vuggy Dolostone (upper Vinemount)	Tight Dolostone (lower Vinemount)	Lower Permeable Dolostone (Goat Island)	Fractures
Permeability [m^2]	1.76×10^{-15}	1.76×10^{-15}	1.43×10^{-13}	5.69×10^{-13}	1.0×10^{-15}	1.43×10^{-13}	$(2b)^2/12$
Porosity [-]	0.5	0.5	0.0624	0.03	0.03	0.0624	1.00
Fluid Properties							
	Water		TCE			Air	
Compressibility [1/kPa]	3.0×10^{-6}		4.3×10^{-7}			8.3×10^{-3}	
Molar Density [$mole/m^3$]	5.55×10^{4}		41.05			1.11×10^{4}	
Molecular Weight [kg/mole]	1.80×10^{-2}		1.31×10^{-1}			2.90×10^{-2}	
Viscosity [centipoise]	1.0		0.77			0.75	
Equilibrium Partitioning	Mole fraction in Water/Mole fraction in TCE				Liquid/Solid Partitioning		
	1.92×10^{-4}				0.0		

Conceptual models of DNAPL contamination at Smithville have been developed from field and laboratory studies and are summarized in the Smithville Phase IV Bedrock Remediation Program report (2000). The DNAPL is a complex mixture of many components: ~60% of a typical mixture being composed of polychlorinated biphenyl (PCB, 37 to 47% by weight), chlorobenzene compounds (CB, 9 to 13% by weight) and trichloroethene (TCE, 2 to 3% by weight). TCE, being the most soluble, has been sampled and studied extensively and was used as the chemical constituent in the Compflow and HGS transport simulations.

In a simplified two-dimensional domain in Figure 4.10.7a ($0 < x < 300$ m; $0 < z < 43$ m; $0 < y < 5$ m), pure-phase TCE and groundwater flow, equilibrium dissolution of TCE into groundwater, and aqueous TCE transport was simulated for the TCE spill period of two years for the 3000 L of TCE at the surface spill zone (50-m by 5-m: $30 < x < 80$ m; $z = 43$ m; $0 < y < 5$m). This amount of TCE (3000 L) released into the subsurface was approximated from the estimated total amount of liquid waste (30,000 - 40,000 L over about 50-m by 50-m surface disposal area; Golder Associates, 1999). Before releasing TCE, a steady-state groundwater flow field was established to derive ambient groundwater flow from left to right constant pressure boundaries (no-flow conditions at the top and bottom) with an approximate natural hydraulic gradient of 0.0083 (2.5-m over 300-m) at the site. Both fluids and dissolved TCE contaminant were allowed to leave the system at the right constant pressure boundary.

Figure 4.10.9 shows the TCE saturation distributions after 2 years of TCE spill based on four example fracture network realizations. They indicate that spilled TCE flows predominantly downwards and also in the direction of groundwater flow until it reaches the less permeable, moderately fractured, dolostone unit. It then flows horizontally above this tight unit or downward through it slowly. DNAPL arriving at the bottom of the domain can flow horizontally in the direction of groundwater flow.

Table 4.10.6 summarizes the location of the center of mass (C_x, C_z) and the mean total volume of TCE DNAPL for each hydrostratigraphic unit. It also shows the amount of TCE in the fracture and matrix domains in each hydrostratigraphic unit averaged over the results obtained using ten fracture network realizations. It indicates that DNAPL imbibes into and is stored in the matrix domain while flowing predominantly through fractures. In addition, results in Table 4.10.6 indicate that of the initial 3000 L of pure-phase TCE that was spilled, 507 L (17%) has turned into aqueous-phase TCE by dissolution over a period of two years.

Table 4.10.6: Location of center of mass (C_x, C_z) and mean volume of TCE DNAPL for each stratigraphic unit: total in the fracture and matrix domains and in the fracture domain only as values presented in parentheses.

Hydrostratigraphic Unit	**C_x [m]**	**C_z [m]**	**Volume [L]**	**% in volume**
Overburden	74.8 (74.8)	40.7 (40.6)	4.0 (4.0)	0.16 (2.6)
Sandy till	76.3 (76.3)	37.5 (37.5)	2.2 (2.2)	0.09 (1.4)
Eramosa	81.8 (86.2)	30.0 (29.0)	1609.6 (69.8)	64.6 (44.4)
Upper Vinemount (vuggy)	93.0 (96.8)	18.3 (18.4)	141.0 (14.4)	5.66 (9.1)
Lower Vinemount (tight)	105 (105)	16.2 (16.2)	22.0 (22.0)	0.88 (14.0)
Goat Island	107 (110)	8.93 (9.74)	714.3 (44.8)	28.70 (28.5)
Total			2493.1 (157.1)	100 (100)

4.10.6 Contaminant transport modeling of TCE plume and pump-and-treat remediation at the Smithville site

The eight remediation wells shown in Figure 4.10.2 were pumped at variable rates beginning around 1989. Figure 4.10.3 shows the cumulative pumping rate and chemical concentration data from the eight remediation wells over the period of March 14, 1995 to December 15, 2004. Although we have detailed records of pumping rates for all wells it would be computationally burdensome to apply these temporal variations in HGS (i.e. forced small time steps), thus the cumulative pumping rates for all wells, shown in Figure 4.10.3, were used instead. This cumulative pumping rate was equally distributed to each of the eight pump-and-treat wells.

The solubility of pure TCE is about 1100 mg/L, but this value would be lessened in the presence of the other components in the DNAPL mixture. In the HGS transport simulations, it is assumed that this effective solubility of TCE can be calculated by multiplying the pure-phase solubility by the mole fraction of TCE in the mixture. Note that it is understood that variations in activity coefficients occur during multicomponent dissolution, and including these processes may lead to a better representation of the dissolution of the DNAPL mixture (Lee and Chrysikopoulos, 1995, 2006; Chrysikopoulos and Lee, 1998).

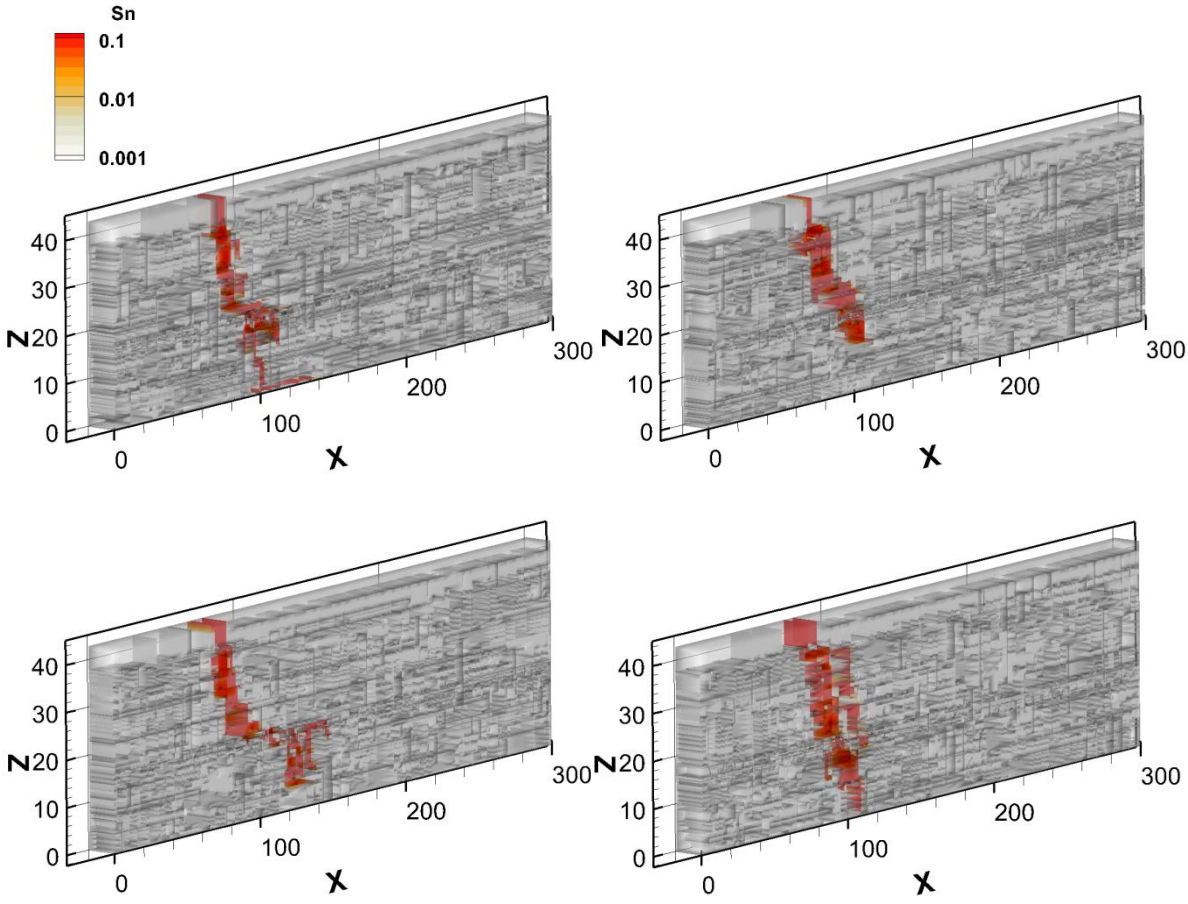

Figure 4.10.9: TCE saturation (S_n) distributions after 2 years of TCE spill based on four example fracture network realizations.

Table 4.10.7 summarizes the parameters used in the HGS transport simulations. The source volume represents the total amount of DNAPL that was estimated to have been spilled at the site (Golder, 1995). The free-solution diffusion coefficient is a value that is typical for major ions in groundwater (e.g. Freeze and Cherry, 1979). The decay coefficient represents the degradation of TCE as a first-order reaction process (Suarez and Rifai, 1999). The DNAPL was assumed to have three components: PCB, CB and TCE, whose properties (Kueper et. al., 2003) are provided in Table 4.10.8. Although CB is soluble, for the purposes of this study, only TCE dissolution was considered.

Table 4.10.7: Parameters for the HGS transport simulations.

DNAPL volume in the source zone	40,000 L
Free-solution diffusion coefficient	0.0315 m^2/year
Decay coefficient for dissolved TCE	1.1 $year^{-1}$
Decay coefficient for DNAPL source	0.0 $year^{-1}$ (i.e. no decay)
Longitudinal dispersivity	10 m
Transverse dispersivity	1 m
Tortuosity	0.1

Table 4.10.8: Chemical properties of the various DNAPL components.

Component	**Density(kg/L)**	**Molecular Weight (g/mole)**	**Solubility (mg/L)**
PCB	1.38	267.9	0
TCE	1.46	131.4	1100
CB	1.11	112.6	500

Table 4.10.9: Three separate DNAPL compositions considered in the transport simulations.

	Pure TCE		**4% TCE**		**2% TCE**	
Component	**Weight %**	**Mole Fraction**	**Weight %**	**Mole Fraction**	**Weight %**	**Mole Fraction**
PCB	0	0	75.59	0.572	87	0.742
TCE	100	1	4.37	0.067	2	0.034
CB	0	0	20.04	0.361	11	0.223
Total DNAPL Mass Kg	58,400		52,754		53,818	

Given the total DNAPL volume of 40,000 L and the density of each component in the mixture, we can compute the total DNAPL mass for each mixture, and from the molecular weight of each component we can compute its mole fraction.

Table 4.10.9 gives the weight percent and mole fraction of each component in three hypothetical DNAPL mixtures (pure TCE, 4% TCE and 2% TCE by volume) and the total DNAPL mass of each mixture.

In HGS, the pure-phase DNAPL source is represented as a mass of immobile, immiscible liquid, which dissolves at the solubility limit (i.e., equilibrium assumption). Given the amount of

DNAPL in each layer (Table 4.10.6, % in volume) and the total DNAPL mass in each mixture, we can compute the amount of pure-phase DNAPL in the source in each layer. We then use the mole fraction of each component in the mixture to compute the effective solubility of TCE. For example, in the case of pure TCE, the concentration of the source nodes is fixed at the pure-phase TCE solubility of 1100 mg/L, and this is maintained until the mass is exhausted. For the 4% TCE and 2% TCE sources, the concentration of the source nodes is computed as a product of the pure-phase solubility and the mole fraction of TCE at a source node. As dissolution of TCE proceeds, the mole fraction declines and so too does the effective solubility and fixed concentration.

Using the calibrated steady-state flow system as the initial condition, the transport model was first run from 1969 to 1985, with Municipal well 2 pumping at a rate of 650 m^3/day. The HGS model was then restarted with the emplaced TCE dissolution source and run from 1985 until 2011, with Municipal well #2 being shut off in 1987, and the remediation wells starting up in 1989. For the period between 1989 and that shown in Figure 4.10.3, the remediation wells were pumped at a total rate of 56,000 L/day (Golder, 1995).

Figure 4.10.10 compares the TCE mass removed by the pump-and-treat system for the various DNAPL source compositions to the observed data shown in Figure 4.10.3. For pure TCE as simulated by HGS, a large amount of mass is removed at early time and the mass removal curve is very steep, with the later time peaks being much lower than the observed values. This behavior is most likely due to the high solubility of pure TCE, which rapidly depletes the source mass. For the 4% and 2% TCE cases, the mass is removed more slowly (shallower curve) and the peak values match those observed more closely except at later time when they are too low, perhaps because dissolution is still depleting the source too rapidly.

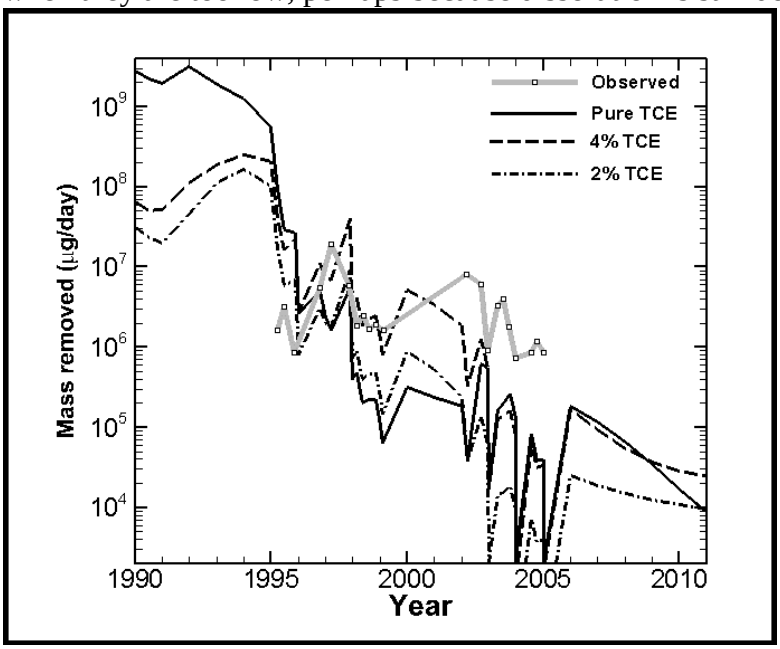

Figure 4.10.10: Total mass of TCE removed by pump-and-treat wells.

Figs. 4.10.11 through 4.10.13 show the simulated TCE plume in 1988 in plan-view for the various DNAPL source compositions. For comparison, the observed 1988 plume (Figure 4.10.2) is also shown. For pure TCE, the plume is very extensive and of relatively high concentration, reflecting the high pure-phase solubility of TCE. The other two cases yield more reasonable

results, with the 1000 μg/L isocontour being of approximately the same shape and extent as was observed, particularly for the 2% TCE case.

In 2005, the predicted concentrations were far below those observed in the field, even for the 4% and 2% TCE cases. One possible explanation for the persistence of the observed TCE plume is that the surface area of the source available for contaminant dissolution is limited. The HGS model allows groundwater to flow freely through the source zone, whereas in reality, it may flow preferentially around DNAPL 'pools'. In order to test the impact of preferential flow, a single run was carried out in which the *K* in the DNAPL source region of the Eramosa member is reduced by two orders of magnitude to 2.1×10^{-6} m/s.

Figure 4.10.14 shows that this change in *K* causes the mass removal curve to be shallower, and the later time peak values now match the observed peak values more closely. At very late times, the mass removal curve for the reduced *K* case is very shallow, and the simulated plume persists much longer.

In order to gauge the impact of TCE decay versus remediation well pumping on the extent of the TCE plume, two additional simulations were carried out. The 4% TCE source case with the original hydraulic conductivity values in the source zone was used as a base case for these simulations, but in the first case the TCE decay rate was set to zero, while in the second the pumping wells were turned off. The resulting change in the position of the 10 μg/L TCE contour is shown in Figure 4.10.15 for the base case (solid line), the case with no TCE decay (dashed line) and the case with no pumping (dashed-dotted line). It is evident that TCE decay has a much more profound influence on the extent of the TCE plume than does remediation well pumping. This is borne out by the results of Illman et al. (2012), who computed that approximately 16 kg of TCE had been removed by the remediation wells between 1995 and 2004. This represents a very small percentage of the estimated TCE source mass.

The HGS model results indicate the possibility that a component of the DNAPL mixture which had a relatively low rate of decay as compared to TCE existed, then it could bypass the remediation well system and contaminate a much larger area of the flow system than is indicated by the observed TCE plume.

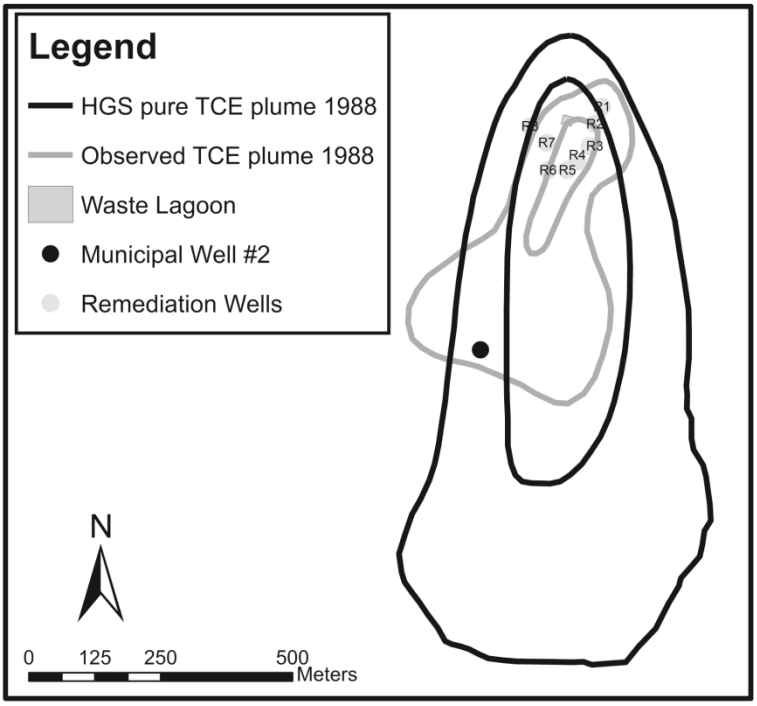

Figure 4.10.11: Observed and simulated (Pure TCE source) 1000 and 1 μg/L TCE contours for the Eramosa Member, 1988.

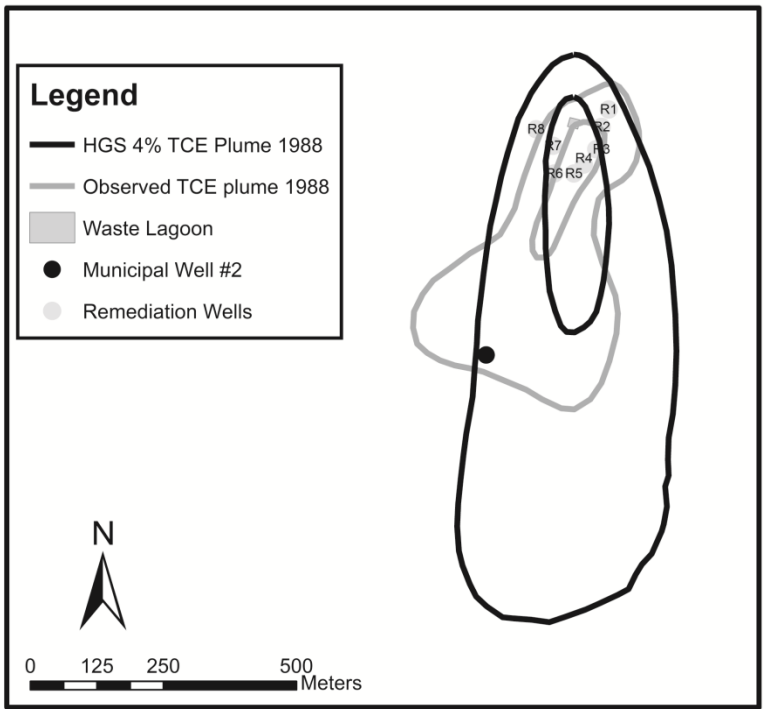

Figure 4.10.12: Observed and simulated (4% TCE source) 1000 and 1 μg/L TCE contours for the Eramosa Member, 1988.

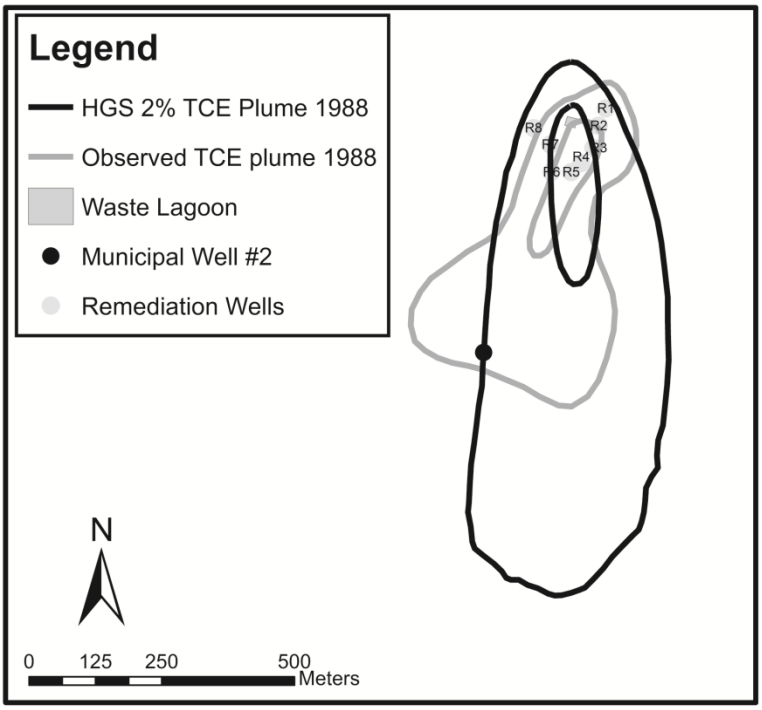

Figure 4.10.13: Observed and simulated (2% TCE source) 1000 and 1 μg/L TCE contours for the Eramosa Member, 1988.

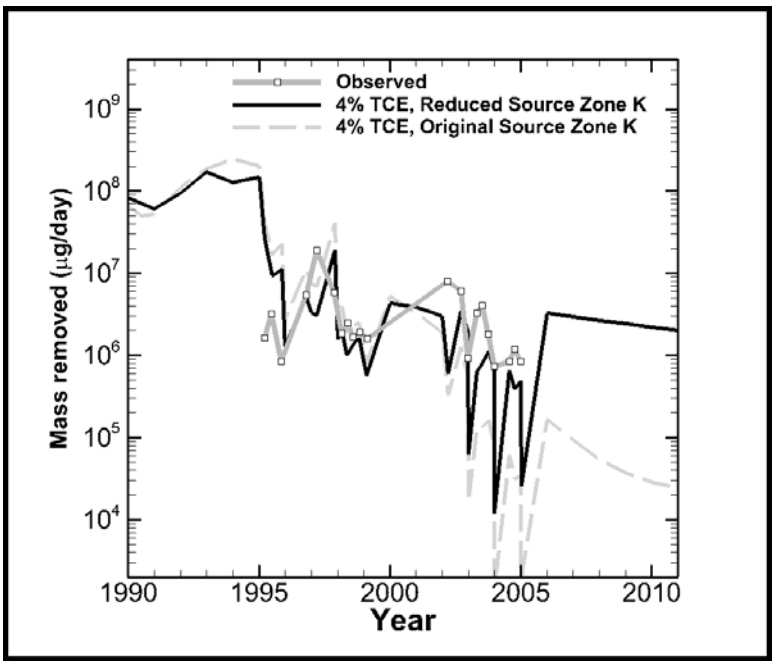

Figure 4.10.14: Effect of reduced source zone *K* on total mass of TCE removed by pump-and-treat wells.

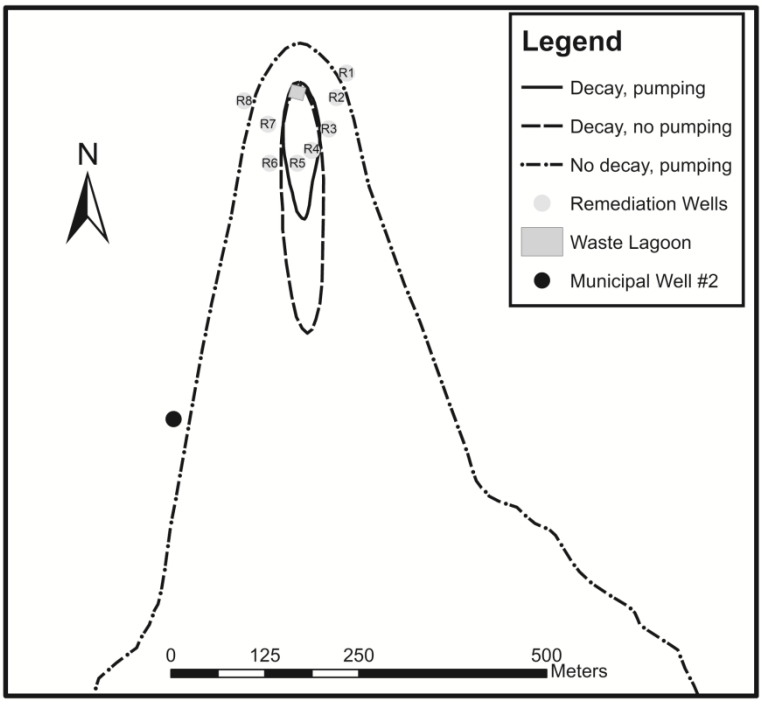

Figure 4.15: Simulated 10 μg/L TCE contours in the Eramosa Member at time 2004 showing the combined effects of TCE decay and remediation well pumping.

4.10.7 Discussion

The transfer of mass from the nonaqueous to the aqueous phase is a process of central importance when considering the remediation of DNAPL contaminated site, as it underpins the estimation of cleanup times and whether partial source zone removal can be effective in achieving a down-gradient compliance goal for final site closure. Improving the understanding of mass transfer will likely require an accurate knowledge of DNAPL source zone architecture and mass stored in the source zones. While methods are in development for quantifying DNAPL source zone architectures (e.g., Sciortino et al., 2000; Zhang and Graham, 2001; Datta-Gupta et al., 2002; Yeh and Zhu, 2007; Illman et al., 2010) for unconsolidated deposits, such methods have not been developed for fractured geologic media to date.

Given the concerns over mobilization of DNAPLs due to drilling and aggressive characterization practices, alternative methods may be needed to estimate the DNAPL architecture in fractured rocks. One such alternative is to estimate the DNAPL penetration and distribution in the source area through a multiphase compositional model such as CompFlow that explicitly accounts for discrete fractures and exchanges between fractures and matrix. Slough et al (1999) have previously shown that such simulations are computationally feasible for field scale scenarios in two dimensions, but a recent study (e.g., Walton et al., 2012) has shown that a three-dimensional analysis for a field scale problem, while technically possible, may be too time-consuming with existing computational resources. This suggests that the application of multiphase compositional models such as CompFlow to realistic field scale problems may not be feasible at this time.

Given the need for field scale simulations, we adopted a two-step approach in which CompFlow is first applied to simulate the migration of DNAPLs in a discretely fractured porous medium for hydrostratigraphy representing the Smithville site. Results from the CompFlow simulation are used to define the pure-phase DNAPL source zones in the discrete fractures and matrix. In the second step, the CompFlow results are employed to define the source term for a regional-scale transport simulation using HydroGeoSphere (HGS) by treating the layered fractured dolomitic rocks as an equivalent porous continuum. While the Smithville site is known to be highly heterogeneous, we elect to conduct our simulations by treating the fractured rock to be uniform for a given stratigraphic unit. However, variability in hydrogeologic parameters is accounted for in different layers. Considering that the groundwater flow and contaminant transport simulations are conducted over a regional scale, we feel that the treatment of the fractured rock as an equivalent porous medium, and in which the DNAPL is distributed across different units in the source zone is justified. Comparison of simulated and observed regional water levels shown in Figures 4.10.5 and 4.10.6 suggests that the observed regional flow direction and hydraulic gradient can be replicated with the model and thus the conceptualization of flow through fractured rock as an equivalent porous medium is adequate at this regional scale.

Transport simulation results revealed poor agreement with observed mass removal data and TCE plume extent when a pure TCE source was considered. However, the match was improved (Figures 4.10.10 and 4.10.13) when a DNAPL that was a mixture of various components was considered. In this case, the effective solubility of each component is lower than in the pure phase and can be estimated as a function of mole fraction using Raoult's law. Because each compound has a different solubility, dissolution of DNAPL in the source zone results in the preferential removal of contaminants with higher solubility. This process changes the DNAPL composition over time along with the effective solubilities of the remaining compounds and accounting for it has led to improved agreement when considering the total mass of TCE removed by pump-and treat wells at the Smithville site.

Additional improvements (Figure 4.10.14) were also achieved through a reduction of the hydraulic conductivity of the source zone by two orders of magnitude. Frind et al. (1999) achieved a similar result when modeling the emplaced source experiment at Borden by reducing the hydraulic conductivity of the source zone. The hypothesis is that the presence of pure-phase DNAPL in the fractures and matrix reduces the permeability of the formation to water flow.

5. Conclusions and implications for future research

A multiphase flow and multispecies reactive transport model for DNAPL-involved Compound Specific Isotope Analysis

We have presented a model that can simulate multiphase and multi-component flow and transport with isotope fractionation. The model is verified for DNAPL-aqueous phase equilibrium partitioning, aqueous phase multi-chain and multi-component reactive transport, and aqueous phase multi-component transport with isotope fractionation. For the verification of DNAPL-aqueous phase equilibrium partitioning, simulation results for a simplistic system consisting of two nodes are compared to two analytical solutions representing diffusion-dominant and advection-dominant cases. Specifically, from the viewpoint of mass conservation, the dissolution rate at the source cell should be equilibrated with the accumulation in the receptor cell for the diffusion-dominant case or be equilibrated with the advective flux at the receptor cell for the advection-dominant case. The simulation results match well with analytical solutions for both cases. For the verification of reactive multi-chain and multi-component transport, simulation results obtained from a case involving a one-dimensional homogeneous column are compared with a semi-analytical solution [*Sudicky et al., 2013*]. The simulation results for transport with multispecies chain degradation show an excellent match with those in Hunkeler et al. (2009) and the semi-analytical solutions. For the verification of multi-component transport with isotope fractionation, simulation results are compared with those of Hunkeler et al. (2009) and show that the difference is less than 10^{-3}. Based on the verification results, our model can be considered reasonable and robust from two points of view: fitting well with analytical solutions and demonstrating physically reasonable trends of the delta values.

To investigate the effect of DNAPL spill rates, degradation rate constants, and enrichment factors on the temporal and spatial distribution of the isotope signatures of CAHs, four one-dimensional simulations were performed: a scenario based on Hunkeler et al. (2009) (case 1), increased degradation rate constants only (case 2), increased enrichment factors only (case 3), and both increased degradation rate constants and enrichment factors (case 4). Additionally, each case was simulated using a low and a high PCE DNAPL release rate. When a DNAPL phase is formed and flows along with the groundwater, concentrations of CAHs and their isotopic signature in the source zone are shown to be influenced by the amount of DNAPL being introduced into the system and the rates of degradation and isotope enrichment, as well as the heterogeneities and groundwater flow system characteristics. The results clearly indicate that the isotope signature can be significantly influenced by multiphase flow. It is also illustrated that degradation and isotope enrichment compete with dissolution to determine the isotope signatures in the source zone: isotopic ratios remain the same as those of the source if dissolution dominates the reaction, while heavy isotopes are enriched in reactants along flow paths when degradation becomes dominant. It is shown that DNAPL composition can change with distance from the DNAPL source zone due to the partitioning of components between the aqueous and NAPL phases even when degradation is not allowed in NAPL phase.

Three-phase flow in discretely fractured rock

The purpose of this section was to introduce the framework for a practical way of modeling three-phase flow in fractured porous media. Our formulation couples the discrete fracture network and PM using physically based relationships parameterized by measurable physical quantities. Asperity contact bridged flow across fracture planes is incorporated in this model.

Our approach allows for construction of an irregular mesh to incorporate fractures at the density of interest while keeping the number of CVs in the numerical system as small as possible. Then, simplifying assumptions are made so that small volume nodes at the intersections of fractures can be algebraically eliminated, thus removing undue constraints on the time step size. We demonstrate the utility of our mesh generation technique in a relatively large-scale simulation based on the Smithville, Ontario, DNAPL contamination site. In the given example, the node bisection technique is effective in creating a mesh with fewer nodes than traditional discretization schemes.

A semi-analytical solution for simulating contaminant transport subject to chain-decay reactions

We presented a set of new, semi-analytical solutions to simulate three-dimensional contaminant transport subject to first-order chain-decay reactions and equilibrium sorption. The analytical solutions can treat the transformation of contaminants into daughter products by first-order decay and the increasing concentrations of transformation species, leading to decay chains consisting of multiple contaminant species and various reaction pathways. The solutions in their current forms are capable of accounting for up to seven species and four decay levels. Complex branching transformation pathways can be accomodated using branching ratios to account for decay stoichiometry. Besides advection, dispersion, bio-chemical or radioactive decay and daughter product formation, the model also accounts for sorption of contaminants on the aquifer solid phase with each species being allowed to have a different retardation factor. The solutions are obtained by exponential Fourier, finite Fourier cosine and Laplace transforms. Limiting forms of the solutions, such as steady state cases, can be obtained analytically, but we evaluate most of the solutions by numerically inverting the analytical solutions in Laplace space and by integrating the exponential Fourier transforms by Gauss quadrature.

The semi-analytical solutions were verified by comparing the results from three different test cases to those generated by the HydroGeoSphere numerical model. In general, we conclude that the agreement between the two approaches is very good suggesting the high accuracy of the semi-analytical model. While the comparison was very good, minor discrepancies between the semi-analytical and HydroGeoSphere models arose in certain situations. We note that to improve the accuracy of the numerical solutions, we took the following steps: 1) reducing grid sizes based on the Peclet number, 2) assigning upstream weighting and fully implicit conditions, and 3) setting small transport solver convergence criteria (i.e. 10^{-10}). Therefore, we attribute the minor discrepancies to slight difficulties in evaluating the semi-analytical solutions near the contaminant source.

The advent of numerical models (e.g., Simunek et al., 1994; Clement, 1997; Zheng and Wang, 1999; Widdowson et al., 2002; Therrien et al., 2005; Yu et al., 2009) and the development of user-friendly interfaces have accelerated the use of these models to capture contaminant transport behavior and once captured, utilized in predictive modes. Numerical models are considered to be more flexible than analytical solutions such as those presented here because they can handle complexities associated with natural systems such as the space- and time-varying nature of forcing functions and subsurface heterogeneity. However, while there are a number of comprehensive numerical models that account for such complexities, analytical solutions are still necessary to verify these numerical models. In addition, accurate solutions from analytical models can be computed efficiently are thus useful as screening tools for the assessment of contaminant plume behaviour (e.g., Illman and Alvarez, 2009), and the analysis of permeable reactive barriers (e.g., Rabideau et al., 2005; Park and Zhan, 2009; Mieles and Zhan,

2012). In particular, the ability of this model to consider decay chains consisting of multiple contaminant species, various reaction pathways, unique branching ratios, and retardation factors for different members makes it ideal for use in these screening studies.

Impact of Source Mass Depletion at the Compliance Boundary in Fractured- Porous Media

A set of numerical experiments of non-aqueous phase and dissolved aqueous TCE migration for the conceptual model of the Smithville site were performed to analyze the effects of fractures and rock matrix characteristics on the source-zone architecture and the efficiency of partial source-zone remediation. Results indicate that simulated TCE concentration and mass flux at the downstream compliance boundary and the source depletion (dissolution) are strongly related. The relation between fractional source reduction and reduction of mass flux can be generally quantified as the following: while the mass flux in the downstream can be significantly lowered by the depletion of a small portion of TCE source (e.g., 10%), the reduction of mass flux under a certain level can be extremely difficult until the most source (e.g., 99%) is depleted. From the set of simulations, it is clear that statistics of fracture network geometry and hydraulic characteristics of fracture and matrix can significantly influence the non-aqueous phase and dissolved TCE migration patterns. With the increase in matrix permeability, NAPL TCE can migrate vertically further with more imbibition into the matrix domain and aqueous phase TCE can transport further downstream by increasing the connectivity among fractures. The effect of the increase in fracture permeability is relatively minor and mainly for the migration distance from the source zone to the downstream. It is concluded from the results that DNAPL source architecture and the partitioning of the source between the fracture and matrix domains are mainly functions of statistics of fracture network geometry and hydraulic characteristics of fracture/matrix; source depletion and the rate of DNAPL migration to downstream are closely related; and the downstream mass flux, however, is extremely difficult to be lowered under a certain level with a very small portion of remaining source in most fractured porous media.

Refinement of analytical techniques to analyze compound-specific hydrogen of chlorinated solvents

The current CSIA method introduced in this study offers the opportunity to utilize the hydrogen compound-specific isotope parameter in wide range environmental studies that investigates different chlorinated compounds such as TCE and cis-DCE. The method shows high accuracy and precision (better than 7‰ (1σ)). The quantification limit of the method is as low as 400 µg/L.

The Effect of Sorption on ^{37}Cl and ^{13}C Isotope Fractionation

The effect of sorption and desorption of TCE in porous media was examined through three individual column experiments with different materials containing different amount of organic carbon since soil organic carbon has an important role in sorption of TCE; the Ottawa silica sand without organic carbon content, the Borden sand with an average organic carbon content of 0.02% (MacKay et al. 1986); and the Borden sand with 0.28% activated carbon content. Results from ^{37}Cl CSIA indicate that sorption and desorption processes can cause noticeable isotope fractionation. Results show that the solution is depleted in^{37}Cl and ^{13}C isotopes indicating that the sorbed light isotopes were re-entered the solution. Nonetheless, isotope results for both sorption and desorption experiments indicate higher fractionation of ^{37}Cl isotopes than ^{13}C

isotopes. In conclusion, we should consider the effect of sorption and desorption mechanisms on isotope fractionation especially in the soils with high organic carbon content.

Laboratory Column Experiment: The Effect of Biodegradation on ^{37}Cl and ^{13}C Isotope Fractionation

The high TCE concentration of 500 mg/L was inhibitory to nitrate reducing bacteria which caused an increase in the oxidation-reduction potential of the column. Once ORP increased, dechlorinating bacteria became inactive since the production of cis-DCE decreased and VC production terminated. The cis-DCE production was started to increase once the concentration of TCE was decreased to about 120 mg/L. However, VC has not been detected in the effluent samples. It can be concluded that the type of bacteria responsible for degrading TCE to cis-DCE survived in the oxic environment but the type of bacteria responsible for degrading cis-DCE to VC and subsequently ethene was sensitive to oxygen and killed in the period when ORP became positive. This is an ongoing project and future data might change the conclusions.

Transient hydraulic tomography in fractured dolostone

The accurate characterization of fractured geologic medium, imaging of fracture patterns and their connectivity have been a challenge for decades. Recently, hydraulic tomography has been proposed as a new method for imaging the hydraulic conductivity (K) and specific storage (S_s) distributions of fractured geologic media. While encouraging results have been obtained in the field, the method has not been rigorously assessed in a controlled laboratory setting. In this study, we have assessed the performance of transient hydraulic tomography (THT) in a fractured rock block. The block is characterized through flow-through tests and multiple pumping tests. These pumping test data were then analyzed using the Sequential Successive Linear Estimator (SSLE) code of *Zhu and Yeh* [2005] to conduct THT to image the fracture patterns and their connectivity through the delineation of K and S_s distributions (or tomograms). Results show that the THT analysis of pumping tests yields high K and low S_s zones that capture the fracture pattern and their connectivity quite well and those patterns become more vivid as additional pumping test data are added to the inverse model. This study leads to the following major findings and conclusions:

1) It is possible to delineate permeable fracture zones, their pattern and connectivity through the THT analysis of multiple pumping tests along with the inverse code SSLE developed by *Zhu and Yeh* [2005]. From the estimated K and S_s tomograms obtained from THT analysis of synthetic and laboratory data, it is evident that THT captured the fracture pattern quite well and they became more distinct with additional pumping tests.

2) Based on the THT analysis of synthetic data, the estimated K and S_s values for the fractures and the matrix may not exactly replicate the actual values, but the model also provides uncertainty estimates associated with the resulting K and S_s tomograms, which are given in the corresponding variance maps. However, the purpose of the study was to capture the fracture pattern (the pattern of K and S_s tomograms) using THT, which has been achieved here. The high K and low S_s zones clearly show the fractures and their connectivity, although the high K and low S_s zones do not continue to the edge of the rock, which could be due to the boundary effect.

3) Two cases of THT analysis were performed using the laboratory pumping tests by changing the location of 2nd and 3rd pumping tests to examine if there was any significant impact of these later pumping tests locations on the pattern of resulting K and S_s. Results showed that the patterns of estimated K and S_s tomograms in real THT cases 1 and case 2 were similar,

although the pumped locations (2^{nd} and 3^{rd} test) utilized for the inversion were different for two cases. A closer inspection of scatterplots comparing the K values from the two cases revealed that while the scatter is large, the K values cluster around the 1:1 line without much bias. It indicates that, changing the location of 2^{nd} and 3^{rd} pumping tests does not significantly impact the K estimates for this fractured rock block. On the other hand, the S_s values from the two cases scattered around the 1:1 line, but there was a noticeable bias suggesting some differences in the S_s values between the two cases.

4) Five independent pumping tests not included during the inversion were simulated using estimated K and S_s tomograms generated by each of the two real THT cases to evaluate to what extent they can predict independent pumping tests. For most cases, the predicted drawdown responses from the independent pumping tests captured the observed behavior at later time, while at early time predicted drawdown deviated from the observed for some tests. All the inverse simulations were run for 20 seconds and the matrix ports had no drawdown (in real THT case 1) or a very small drawdown (in real THT case 2) for all the calibrated and predicted cases, which was consistent with the observed data. SSLE being a porous media code, it is difficult for the model to handle the high contrast between the fracture and matrix K and S_s values. Thus, estimated K and S_s values may not exactly replicate the actual values for the fractured rock, which could have led to some discrepancies between the observed and simulated drawdown values. But overall, simulated drawdown responses captured the observed behaviors both at the fracture and matrix ports quite well, indicating that the K and S_s tomograms estimated using THT successfully captured fracture pattern and their connectivity.

5) We conclude that the results from this study are encouraging in that the patterns of K and S_s tomograms generated by THT analysis based on the inverse algorithm SSLE, are consistent with the fracture pattern of the rock sample. THT appears to be a promising approach in delineating fractures and their connectivity in the subsurface. This is significant because existing methods of fractured rock characterization typically relies on detailed field mapping of fracture geometry through outcrops and boreholes. However, mapping of such features between boreholes is currently not possible. Geophysical techniques may also provide information on fractures and their connectivity but they do not provide direct information on the hydraulic characteristics, which hydraulic tomography does. However, the development of hydraulic tomography in fractured rocks is still at the early stage given that this study was conducted in the laboratory in a controlled environment. More experiments are needed at the field scale in a variety of fractured rock environments.

TCE dissolution experiments in a fractured dolostone rock block

The purpose of the transport modeling was to investigate whether it is possible to capture the pattern of the observed TCE breakthrough curve in a fractured rock block using:

- the discrete fracture network modeling approach, in which the fracture geometry and the flow through the system were exact replica of the experimental block and
- the stochastic continuum modeling approach, in which the model domain was treated as a porous medium.

The discrete fracture network modeling approach captured the pattern of the TCE breakthrough curve based on the experiments in this fractured rock block quite well. On the other hand, the stochastic continuum modeling approach also captured the overall pattern of TCE breakthrough curve despite some early time deviation.

These studies are still at the early stage and were conducted under laboratory conditions in a controlled environment. The experimental block and the flow through the system were well characterized through the hydraulic and tracer experiments. Thus small scale field experiment is required to validate these approaches to predict DNAPL plume behavior in the field. However, it would be very expensive and time consuming to model TCE dissolution in the field using the discrete fracture approach, as it requires detailed deterministic and statistical information of the geometry of fractured zone and the spatial distribution of fracture apertures, which information are not available between boreholes. On the other hand, stochastic continuum approach could be comparatively less expensive and time consuming, as it does not require these detail information about the spatial distribution of fractures.

Application of compound specific analyses to characterize natural attenuation of TCE in a fractured bedrock aquifer

Chlorinated solvents are one of the most prevalent classes of contaminants at industrial sites throughout the world. Isotopic data have been recently used in various studies as a means of identifying degradation of chlorinated ethenes and potentially determining the mechanisms affecting degradation. This study used compound specific carbon and chlorine isotopic analyses as a tool to understand the geochemical evolution of TCE. DCE isotopes were also analyzed as a means of assessing the further transformation of the primary product of TCE degradation at this site.

Along with redox and chemical data, the isotopic data from the site support the fact that biodegradation of TCE is occurring at the Smithville site. In addition, numerical simulation studies of McLaren et al. (2012) suggest that the stability of the plume is due to first-order degradation. The dominant process is most likely reductive dechlorination of TCE. The further conversion of DCE to more degraded compounds is also supported by chemical and isotopic data. Due to the fact that isotopic analyses are a direct indicator of the transformation of TCE, these data are useful for verification of degradation. At this field site natural attenuation as a removal process for TCE has been verified by the application of this method. This has important site management implications since the formation of degradation products of TCE (especially VC) can be even more toxic than TCE. Degradation of TCE to ethene and ethane can considerably clean a site. In addition, if natural attenuation is already occurring by means of native microbial communities, biostimulation may serve to enhance the rates of bioremediation.

Numerical simulation of DNAPL emissions and remediation in a fractured dolomitic aquifer

The knowledge of Dense Nonaqueous Phase Liquid (DNAPL) source zone architecture and corresponding emissions is necessary in quantifying the efficacy of partial source zone removal on site closure and corresponding cleanup time estimation. Research on these areas has revealed important insights in porous media, but knowledge on the movement and dissolution mechanisms of pure-phase DNAPL and the migration of the aqueous-phase plumes is quite limited in fractured geologic media. This study focusses on the numerical modeling of various chlorinated solvents that have penetrated the fractured dolomitic bedrock at the Smithville site in Ontario, Canada, where a large aqueous phase plume has developed over the last several decades and since 1989 has been hydraulically influenced by a pump-and-treat remediation system. We adopt a two-step procedure in which a multiphase compositional model CompFlow is first applied to simulate the migration of DNAPLs in a discretely fractured porous medium with

hydrostratigraphy representing the Smithville site. Results from the CompFlow simulation include the pure-phase DNAPL source zone distribution in the discrete fractures and matrix. In the second step, the CompFlow results are employed to define the source term for a regional-scale transport simulation using HydroGeoSphere (HGS) by treating the layered fractured dolomitic rocks as an equivalent porous continuum. Transport simulations are conducted both prior to and after the operation of the pump-and-treat system. Our results lead to the following conclusions:

1. CompFlow simulations suggest that DNAPL penetration from the fracture into the matrix can take place in the carbonate units at the Smithville site. Imbibition is controlled by the capillary-saturation curves of the units. The penetration of DNAPL from the fracture into the matrix is different from the phenomenon of aqueous-phase contaminants diffusing from the DNAPL in the fracture into the matrix.

2. The HGS model was successfully applied to simulate the surface/subsurface flow system at Smithville. The final calibrated flow solution shows considerable agreement with the inferred piezometric surface in the Eramosa presented in Pockar (1995).

3. The calibrated flow system was then used to simulate the transient response due to pumping and the transport of TCE which dissolves from an emplaced DNAPL source. Substantial agreement with observed mass removal data and TCE plumes was achieved by modifying the composition of the DNAPL source and also by reducing the hydraulic conductivity in the source region of the Eramosa member.

4. In this study, the use of bulk properties and an equivalent porous medium approach reproduced the observed characteristics of the flow system and dissolved TCE plume in a reasonably accurate manner.

5. Transport model results support the conceptual model of TCE contamination which posits a mixed source (2 to 4% TCE) of pure DNAPL with somewhat limited contact to actively flowing groundwater that is undergoing equilibrium dissolution.

6. Model results support earlier estimates that indicated that the pump-and-treat system has only recovered a small volume of TCE. It also suggests that the pump-and-treat system has been ineffective in controlling the plume and the stability of the plume is due to first-order degradation. Results from site geochemical and stable isotope analysis presented in Illman et al. (2012) suggests that biodegradation is a possible mechanism for removing aqueous phase chlorinated solvents away from the source zone.

7. Given the concerns over mobilization of DNAPLs due to drilling and aggressive characterization practices, alternative methods may be needed to estimate the DNAPL architecture in fractured rocks. One such alternative is to estimate the DNAPL penetration and distribution in the source area through a multiphase compositional model such as CompFlow that explicitly accounts for discrete fractures and exchanges between fractures and matrix. Slough et al (1999) have previously shown that such simulations are computationally feasible for field scale scenarios in two dimensions, but a recent study (e.g., Walton et al., 2012) has shown that a three-dimensional analysis for a field scale problem, while technically possible, may be too time-consuming with existing computational resources. This suggests that the application of multiphase compositional models such as CompFlow to realistic field scale problems may not be feasible at this time.

6. Papers in preparation, submitted, and published

Clark, J., S. K. Frape, and W. A. Illman, Application of geochemical and compound specific isotope analyses to assess TCE biodegradation in fractured dolomitic aquifer, in preparation.

Hwang, H.-T., Y.-J. Park, E. A. Sudicky, A. J.A. Unger, W. A. Illman, S. K. Frape and O. Shouakar-Stash. 2013a. Use of a multiphase flow and multispecies reactive transport model for DNAPL-involved compound specific isotope analysis, Advances in Water Resources, 59, 111-122, http://dx.doi.org/10.1016/j.advwatres.2013.05.009.

Hwang, H.-T., S.-W. Jeen, E. A. Sudicky, W. A. Illman, Y.-J. Park, 2013b, Parameter estimation of the chlorinated ethylene and chlorinated acetylene reduction model by Zero-Valent Iron, in preparation.

Hwang, H.-T., E. A. Sudicky, W. A. Illman, S.-W. Jeen, Y.-J. Park, 2013c, Monte Carlo simulations for designing an effective Zero-Valent Iron permeable reactive barrier. In preparation.

Sudicky, E. A., H.-T. Hwang, W. A. Illman, Y.-S. Wu, J. B. Kool, and P. Huyakorn, A semi-analytical model for simulating groundwater fate and transport of contaminants subject to chained-decay reactions, *Journal of Contaminant Hydrology*, 144(1), 20-45.

Maji, R. and E. A. Sudicky. 2008. Influence of mass transfer characteristics for DNAPL source depletion and contaminant flux in a highly characterized glaciofluvial aquifer, *Journal of Contaminant Hydrology*, 102, 105-119.

McLaren, R., E. A. Sudicky, Y.-J. Park, and W. A. Illman (2012), Numerical simulation of DNAPL emissions and remediation in a fractured dolomitic aquifer, *Journal of Contaminant Hydrology*, 136-137, 56-71. http://dx.doi.org/10.1016/j.jconhyd.2012.05.002.

Park, Y.-J., Sudicky, E.A., Illman, W.A., Uncertainty analysis of the influence of fracture and rock matrix characteristics on the source-zone architecture, migration patterns of aqueous phase contaminants, and remediation design at a DNAPL contaminated site, in preparation.

Sharmeen, R., W. A. Illman, S. J. Berg, T.-C. J. Yeh, Y.-J. Park, E. A. Sudicky, and K. Ando (2012), Transient hydraulic tomography in fractured dolostone: Laboratory rock block experiments, *Water Resour. Res., 48,* W10532, doi:10.1029/2012WR012216.

Sudicky, E. A., H.-T. Hwang, W. A. Illman, Y.-S. Wu, J. B. Kool, P. Huyakorn. 2013. A semi-analytical computer model for simulating groundwater fate and transport of contaminants subject to chain decay reactions, *Journal of Contaminant Hydrology*, 144(1), 20-45.

Vakili, F., O. Shouakar-Stash, J. M. Passmore-Niemi, W. A. Illman, E. A. Sudicky, and S. K. Frape. The isotopic fractionations of 37Cl and 13C associated with sorption and desorption of TCE in porous media, in preparation.

Walter, K. M., A. J. A.Unger, and E. A. Sudicky, Three-phase flow in discretely fractured rock: Part 1 Model Development, in preparation

7. Literature Cited

Abe, Y., R. Aravena, J. Zopfi, O. Shouakar-Stash, E. Cox, J. D. Roberts, D. Hunkeler, Carbon and Chlorine Isotope Fractionation during Aerobic Oxidation and Reductive Dechlorination of Vinyl Chloride and cis-1,2-Dichloroethene. Environmental Science & Technology. 43 (2008) 101-7.

Abriola L, Pinder G. A multiphase approach to the modeling of porous-media contamination by organic-compounds .1. Equation development. Water Resources Research 1985;21(1):11-18.

Alvarez, P. J., Illman, W. A., 2006. Bioremediation and Natural Attenuation: Process Fundamentals and Mathematical Models, John Wiley & Sons, 609 pp.

Andersson, J., and B. Dverstorp (1987), Conditional Simulations of Fluid Flow in Three-Dimensional Networks of Discrete Fractures, Water Resour. Res., 23(10), 1876–1886.

Ando K., A. Kostner, and S. P. Neuman (2003) Stochastic continuum modeling of flow and transport in a crystalline rock mass: Fanay-Augères, France, revisited, Hydrogeol. J., 11(5): 521-535.

Aravena, R., W. D. Robertson, Use of Multiple Isotope Tracers to Evaluate Denitrification in Ground Water: Study of Nitrate from a Large-Flux Septic System Plume. Ground Water. 36 (1998) 975-82.

Atteia, O., M. Franceschi, A. Dupuy, Validation of Reactive Model Assumptions with Isotope Data: Application to the Dover Case. Environmental Science & Technology. 42 (2008) 3289-95.

Balfour DJ. Evaluation of lateral solute migration in surficial weathered clayey till [master's thesis]. [Ontario, Canada]: University of Waterloo; 1991.

Barenblatt GI, Zheltov IP, Kochina IN. Basic concepts in the theory of homogeneous liquids in fissured rocks. J. Appl. Math. Mech. Engl. Transl. 1960;24(5):1286-1303.

Bauer, B., Attinger S., Kinzelbach, W., 2001. Transport of a decay chain in homogenous porous media: analytical solutions, Journal of Contaminant Hydrology, 49(3-4), 217–239.

Bear, J. (1972), Dynamics of Fluids in Porous Media, Dover Publications, Inc., 764 pp.

Bear, J., 1979. Groundwater Hydraulics. McGraw-Hill, New York.

Beneteau, K. M., R. Aravena, S. K. Frape, Isotopic characterization of chlorinated solvents--laboratory and field results. Organic Geochemistry. 30 (1999) 739-53.

Benke R, and S. Painter (2003) Modeling conservative tracer transport in fracture networks with a hybrid approach based on the Boltzmann transport equation. Water Resour. Res., 39(11), 1324, doi:10.1029/2003WR001966.

Beranger, S. C., B. E. Sleep, B. S. Lollar, and F. P. Monteagudo (2005), Transport, biodegradation and isotopic fractionation of chlorinated ethenes: modeling and parameter estimation methods," Advances In Water Resources, vol. 28, no. 1, pp. 87-98.

Berg, S. J., and W. A. Illman (2011a), Capturing aquifer heterogeneity: Comparison of approaches through controlled sandbox experiments. Water Resour. Res., 47(9), W09514, doi:10.1029/2011WR010429.

Berg, S. J., and W. A. Illman (2011b), Three-dimensional transient hydraulic tomography in a highly heterogeneous glaciofluvial aquifer-aquitard system, Water Resour. Res., 47(10), W10507, doi: 10.1029/2011WR010616.

Bibby, R. (1981), Mass transport of solutes in dual-porosity media. Water Resour. Res., 17(4):1075–1081.

Bloom, Y., Aravena, R., Hunkeler, D., Edwards, E., and Frape, S.K. 2000. Carbon Isotope Fractionation During Microbial Dechlorination of Trochloroethene, cis-1,2-Dichloroethene, and Vinyl Chloride: Implications for Assessment and Natural Attenuation. Environmental Science and Technology, 34, 2768-2772.

Bohling, G. C., X. Zhan, J. J. Butler Jr., and L. Zheng (2002), Steady shape analysis of tomographic pumping tests for characterization of aquifer heterogeneities, Water Resour. Res., 38(12), 1324, doi:10.1029/2001WR001176.

Bohling, G. C., J. J. Butler, X. Zhan, and M. D. Knoll (2007), A field assessment of the value of steady shape hydraulic tomography for characterization of aquifer heterogeneities, Water Resour. Res., 43, W05430, doi:10.1029/2006WR004932.

Brauchler, R., R. Liedl, and P. Dietrich (2003), A travel time based hydraulic tomographic approach, Water Resour. Res., 39(12), 1370, doi:10.1029/2003WR002262.

Brauchler, R., R. Hu, P. Dietrich, and M. Sauter (2011), A field assessment of high resolution aquifer characterization based on hydraulic travel time and hydraulic attenuation tomography, Water Resour. Res., 47, W03503, doi:10.1029/2010WR009635.

Cacas, M. C., E. Ledoux, G. de Marsily, A. Barbreau, P. Calmels, B. Gaillard, and R. Margritta, (1990), Modeling fracture flow with a stochastic discrete fracture network: Calibration and validation, 1, The flow model, Water Resour. Res., 26(3), 479-489.

Cardiff, M., W. Barrash, P. K. Kitanidis, B. Malama, A. Revil, S. Straface, and E. Rizzo (2009), A Potential-Based Inversion of Unconfined Steady-State Hydraulic Tomography, Ground Water, 47(2), 259-270.

Cardiff, M., and W. Barrash (2011), 3-D transient hydraulic tomography in unconfined aquifers with fast drainage response, Water Resour. Res., 47, W12518, doi:10.1029/2010WR010367.

Cardiff, M., W. Barrash, and P. K. Kitanidis (2012), A field proof-of-concept of aquifer imaging using 3-D transient hydraulic tomography with modular, temporarily-emplaced equipment, Water Resour. Res., 48, W05531, doi:10.1029/2011WR011704.

Castagna, M., and A. Bellin (2009), A Bayesian approach for inversion of hydraulic tomographic data, Water Resour. Res., 45, W04410, doi:10.1029/2008WR007078.

Castagna, M., M. Becker, and A. Bellin (2011), Joint estimation of transmissivity and storativity in a bedrock fracture, Water Resour. Res., 47, W09504, doi:10.1029/2010WR009262.

Chapelle, F., Bradley, P. 2003. Redox Conditions and the Reductive/Oxidative biodegradation of Chlorinated Ethenes in Groundwater Systems. In Dehalogenation: Microbial Processes and Environmental Applications. Springer US.

Chartrand, M. M. G., Morrill, P. L., Lacrampe-Couloume, G., Lollar, B. S., 2005. Stable isotope evidence for biodegradation of chlorinated ethenes at a fractured bedrock site. Environmental Science & Technology. 39, .

Chen, G., W.A. Illman, D.L. Thompson, V.V. Vesselinov, and S.P. Neuman (2000), Geostatistical, type curve and inverse analyses of pneumatic injection tests in unsaturated fractured tuffs at the Apace Leap Research Site near Superior, Arizona. In: Faybishenko, B., P.A., Witherspoon, S.M., Benson (Eds.), Dynamics of Fluids in Fractured Rocks, Geophysical Monograph 122, AGU, Washington, DC, pp. 73-98.

Cho, C.M., 1971. Convective transport of ammonium with nitrification in soil. Canadian Journal of Soil Science 51(3), 339–350.

Churchill, R. V., 1972. Operational Mathematics, McGraw-Hill, Inc., New York, 481 pp.

Chrysikopoulos, C.V., and Lee, K.Y., 1998. Contaminant transport resulting from multicomponent nonaqueous phase liquid pool dissolution in three-dimensional subsurface formations, Journal of Contaminant Hydrology, 31(1-2), 1-21.

Clark, I. D. And P. Fritz. 1997. Environmental Isotopes in Hydrogeology. CRC Press.

Clement, T., (2001), Generalized solution to multispecies transport equations coupled with a first-order reaction network, Water Resources Research, vol. 37, no. 1, pp. 157-163.

Clement, T.P., 1997. RT3D—A Modular Computer Code for Simulating Reactive Multi-Species Transport in 3-Dimensional Groundwater Aquifers. Richland, Wash.: Pacific Northwest National Laboratory.

Cokuner G, Hyde T. Homogeneous equivalents of naturally fractured porous media for miscible fluid displacements. Journal of Petroleum Science and Engineering 1998 March;19(3-4):145-157.

Coniglio, M., Q. Zheng, and T. Carter, (2003), Dolomitization and recrystallization of middle Silurian reefs and platformal carbonates of the Guelph Formation, Michigan Basin, southwestern Ontario. Bulletin of Canadian Petroleum Geology, v. 51, p. 177-199.

Coniglio, M., R. Frizzell, and B. R. Pratt, (2004), Reef-capping laminites in the Upper Silurian carbonate-evaporite transition, Michigan Basin, southwestern Ontario. Sedimentology, v. 51, p. 653-668.

Cooper, H. H., Jr., and C. E. Jacob (1946), A generalized graphical method for evaluating formation constants and summarizing well-field history, Eos Trans., AGU, 27(4), 526–534.

Coplen, T.B., 1996. New guidelines for reporting stable hydrogen, carbon, and oxygen isotope-ratio data. Geochim. Cosmochim. Acta 60, 3359–3360.

Cvetkovic V, S. Painter, N. Outters, and J. O. Selroos (2004) Stochastic simulation of radionuclide migration in discretely fractured rock near the Äspö Hard Rock Laboratory. Water Resour. Res., 40, W02404, DOI:10.1029/2003WR002655.

Datta-Gupta, A., Yoon, S., Vasco, D. W., Pope, G. A., 2002. Inverse modeling of partitioning interwell tracer tests: A streamline approach, Water Resour. Res., 38(6), 1079, doi:10.1029/2001WR000597.

Day-Lewis, F. D., J. W. Lane, Jr., J. M. Harris, and S. M. Gorelick (2003), Time-lapse imaging of saline-tracer transport in fractured rock using difference-attenuation radar tomography, Water Resour. Res., 39(10), 1290, doi:10.1029/2002WR001722.

de Hoog, F.R., Knight, J. H., Stokes, A. N., 1982. An improved method for numerical inversion of Laplace transforms. SIAM Journal on Scientific and Statistical Computing 3(3), 357–366.

Dejam M, Hassanzadeh H. Formation of Liquid Bridges Between Porous Matrix Blocks. AICHE Journal 2011 February;57(2):286-298.

Dershowitz, W. S., and H. H. Einstein, (1988), Characterizing rock joint geometry with joint system models, in Rock Mechanics and Rock Engineering, 21, 21-51, Springer-Verlag, New York.

Dickson, S. E.; Thomson, N. R. Dissolution of entrapped DNAPLs in variable aperture fractures: Experimental data and empirical model. Environ. Sci. Technol. 2003, 37, 4128–4137.

Doherty, J. (2005), PEST Model-Independent Parameter Estimation User Manual, 5th ed., Watermark Numerical Computing, Brisbane, Australia.

Duguid, J. O. and P. C. Y. Lee, (1977), Flow in fractured porous media, Water Resour. Res., 13(3), 558-566.

Dverstrop, B., and J. Andersson (1989), Application of the discrete fracture network concept with field data: Possibilities of model calibration and validation, Water Resour. Res., 25(3), 540– 550.

Dverstrop, B., J. Andersson, and W. Nordqvist (1992), Discrete fracture network interpretation of field tracer migration in sparsely fractured rock, Water Resour. Res., 28, 2327– 2343.

Elsner, M., D. Hunkeler, Evaluating Chlorine Isotope Effects from Isotope Ratios and Mass Spectra of Polychlorinated Molecules. Analytical Chemistry. 80 (2008) 4731-40.

Environmental Protection Agency. (1999). Use of monitored natural attenuation at Superfund, RCRA corrective action, and underground storage tank sites. Washington, DC: Office of Solid Waste and Emergency Response, OSWER Directive Number 9200.4–17P.

Eykholt, G. R., Elder, C. R., Benson, C. H. 1999. Effects of aquifer heterogeneity and reaction mechanism uncertainty on a reactive barrier, J. Hazard. Materials, 68(1-2), 73–96.

Fienen, M. N., T. Clemo, and P. K. Kitanidis (2008), An interactive Bayesian geostatistical inverse protocol for hydraulic tomography, Water Resour. Res., 44, W00B01, doi:10.1029/2007WR006730.

Firoozabadi A, Markeset T. Laboratory Studies in Fractured Porous-Media Part .1. Reinfiltration for Gas-Liquid Systems. In Situ 1995;19(1):1-21.

Forsyth P, Shao BY. Numerical simulation of gas venting for NAPL site remediation. Advances in Water Resources 1991;14(6):354-367.

Forsyth P. A Control Volume Finite-Element Approach to NAPL Groundwater Contamination. SIAM Journal On Scientific And Statistical Computing 1991 September;12(5):1029-1057.

Forsyth P. A Positivity Preserving Method for Simulation of Steam Injection for Napl Site Remediation. Advances in Water Resources 1993;16(6):351-370.

Frampton, A., and V. Cvetkovic (2010), Inference of field-scale fracture transmissivities in crystalline rock using flow log measurements, Water Resour. Res., 46, W11502, doi:10.1029/2009WR008367.

Freedman, D. and Gossett J. 1989. Biological Reductive Dechlorination of Tetrachloroethylene and Trichloroethylene to Ethylene Under Methanogenic Conditions. Applied Environmental Microbiology. 55:9, 2144-2151.

Geiger S, Matthaei S, Niessner J, Helmig R. Black-Oil Simulations for Three-Component, Three-Phase Flow in Fractured Porous Media. SPE Journal 2009 June;14(2):338-354.

Geller, J. T., Hunt, J. R., 1993. Mass transfer from nonaqueous phase organic liquids in water-saturated porous media. Water Resour. Res. 29 (4), 833–845.

Golder Associates Ltd. 1994. Hydrogeological Data Compilation and Assessment CWML Site, Smithville Ontario. Project Number 94-106.

Golder Associates Ltd. 1999. Assessment of Extent of PCB plume at CWML Site Smithville, Ontario. MOE Smithville Documents.

Gottlieb, J., and P. Dietrich (1995), Identification of the permeability distribution in soil by hydraulic tomography, Inverse Probl., 11(2), 353–360.

Grisak G, Pickens J. Solute transport through fractured media .1. The effect of matrix diffusion. Water Resources Research 1980;16(4):719-730.

Guerrero, J. S. P., Skaggs, T. H., van Genuchten, M. T., 2010. Analytical solution for multi-species contaminant transport in finite media with time-varying boundary conditions, Transport in Porous Media 85(1), 171-188, DOI: 10.1007/s11242-010-9553-4.

Guerrero, J. S. P., Skaggs, T. H., van Genuchten, M. T., 2009. Analytical solution for multi-species contaminant transport subject to sequential first-order decay reactions in finite media, Transport in Porous Media 80(2), 373-387, DOI: 10.1007/s11242-009-9368-3.

Guzman, A. G., A. M. Geddis, M. J. Henrich, C. F. Lohrstorfer, and S. P. Neuman (1996), Summary of air permeability data from single-hole injection tests in unsaturated fractured tuffs at the Apache Leap Research Site: Results of steady-state test interpretation, Rep. NUREG/CR-6360, U.S. Nucl. Regul. Comm., Washington, D. C.

Hantush, M. S. 1960, Modification of the theory of leaky aquifers, J Geophys. Res.65(11), 3713-3725.

Hao, Y., T.-C. J. Yeh, J. Xiang, W. Illman, K. Ando, K.-C. Hsu, and C.-H. Lee (2008), Hydraulic tomography for detecting fracture zone connectivity, Ground Water, 46(2), 183–192.

Hirschorn, S. K., A. Grostern, G. Lacrampe-Couloume, E. A. Edwards, L. MacKinnon, C. Repta, D. W. Major, B. Sherwood Lollar, Quantification of biotransformation of chlorinated hydrocarbons in a biostimulation study: Added value via stable carbon isotope analysis. Journal of Contaminant Hydrology. 94 (2007) 249-60.

Holliger, C., Wohlfarth, G., Diekert, G. 1999. Reductive Dechlorination in the Energy Metabolism of Anaerobic Bacteria. FEMS Microbiology Reviews. 22, 383-398.

Hoteit H, Firoozabadi A. An efficient numerical model for incompressible two-phase flow in fractured media. Advances in Water Resources 2008b June;31(6):891-905.

Hoteit H, Firoozabadi A. Multicomponent fluid flow by discontinuous Galerkin and mixed methods in unfractured and fractured media. Water Resources Research 2005 November 10;41(11).

Hoteit H, Firoozabadi A. Compositional modeling of discrete-fractured media without transfer functions by the discontinuous Galerkin and mixed methods. SPE Journal 2006 September;11(3):341-352.

Hoteit H, Firoozabadi A. Numerical modeling of two-phase flow in heterogeneous permeable media with different capillarity pressures. Advances in Water Resources 2008a January;31(1):56-73.

Hsieh, P. A., S. P. Neuman, G. K. Stiles, and E. S. Simpson (1985), Field determination of the three-dimensional hydraulic conductivity tensor of anisotropic media 2: Methodology and application to fractured rocks, Water Resour. Res., 21(11), 1667–1676, doi:10.1029/WR021i011p01667.

Huang, L., Sturchio, N., Abrajano, T., Heraty, L., and Holt, B. 1999. Carbon and Chlorine Isotope Fractionation of Chlorinated Aliphatic Hydrocarbons by Evaporation. Organic Geochemistry. 30, 777-785.

Huang, S.-Y., J.-C. Wen, T.-C. J. Yeh, W. Lu, H.-L. Juan, C.-M. Tseng, J.-H. Lee, and K.-C. Chang (2011), Robustness of joint interpretation of sequential pumping tests: Numerical and field experiments, Water Resour. Res., 47(10), W10530, doi:10.1029/2011WR010698.

Hunkeler, D., and R. Aravena., 2000. Determination of compound-specific carbon isotope ratios of chlorinated methanes, ethanes, and ethenes in aqueous samples. Environmental Science & Technology 34 (13), 2839-44.

Hunkeler, D., R. Aravena, Evidence of substantial carbon isotope fractionation between ubstrate, inorganic carbon, and biomass during aerobic mineralization of 1,2-dichloroethene by Xanthobacter autotrophicus. Applied and Environmental Microbiology. 66 (2000) 4870–6.

Hunkeler, D., N. Andersen, R. Aravena, S. M. Bernasconi, B. J. Butler, Hydrogen and Carbon Isotope Fractionation during Aerobic Biodegradation of Benzene. Environmental Science & Technology. 35 (2001) 3462-7.

Hunkeler, D., N. Chollet, X. Pittet, R. Aravena, JA Cherry, and BL Parker. 2004. Effect of source variability and transport processes on carbon isotope ratios of TCE and PCE in two sandy aquifers. Journal of Contaminant Hydrology 74 (1-4) (OCT): 265-82.

Hunkeler, D., B. M. Van Breukelen, M. Elsner, Modeling Chlorine Isotope Trends during Sequential Transformation of Chlorinated Ethenes. Environmental Science & Technology. 43 (2009) 6750-6.

Huyakorn, P.S., Panday, S., Wu, Y.S., 1994. A three-dimensional multi-phase flow model for assessing NAPL contamination in porous and fractured media: 1. Formulation. J. Contam. Hydrol. 16, 109–130.

Huyakorn, P. S., Y.-S. Wu, N. S. Park, An improved sharp-interface model for assessing NAPL contamination and remediation of groundwater systems. Journal of Contaminant Hydrology. 16 (1994) 203-34.

Hwang, H.-T., Park, Y.-J., Sudicky, E.A., Unger, A.J.A., Frape, S., Shouakar-Stash, O., and Illman, W.A., Use of a multiphase flow and multiphase transport model for DNAPL-involved compound specific isotope analysis, (in preparation).

Illman, W. A., and S. P. Neuman (2000), Type curve interpretation of multirate single-hole pneumatic injection tests in unsaturated fractured rock, Ground Water, 38(6), 899–911.

Illman, W. A. and S. P. Neuman (2001), Type curve interpretation of a cross-hole pneumatic injection test in unsaturated fractured tuff, Water Resour. Res., 37(3), 583-603.

Illman, W. A. and S. P. Neuman (2003), Steady-state analysis of cross-hole pneumatic injection tests in unsaturated fractured tuff, J Hydrol, 281(1-2), 36-54.

Illman, W. A. (2005), Type curve analyses of pneumatic single-hole tests in unsaturated fractured tuff: Direct evidence for a porosity scale effect, Water Resour. Res., 41, W04018, doi:10.1029/2004WR003703.

Illman, W. A. and D. M. Tartakovsky (2005a), Asymptotic analysis of three-dimensional pressure interference tests: Point source solution, Water Resour. Res., 41, W01002, doi:10.1029/2004WR003431.

Illman, W. A. and D. M. Tartakovsky (2005b), Asymptotic analysis of cross-hole pneumatic injection tests in unsaturated fractured tuff, Adv. Water Resour., 28(11), 1217 – 1229, doi:10.1016/j.advwatres.2005.03.011.

Illman, W. A. and D. L. Hughson (2005), Stochastic simulations of steady state unsaturated flow in a three-layer, heterogeneous, dual continuum model of fractured rock, Journal of Hydrology, 307(1-4), 17-37.

Illman,W. A. (2006), Strong field evidence of directional permeability scale effect in fractured rock, J. Hydrol., 319(1 – 4), 227 – 236, doi:10.1016/j.jhydrol.2005.06.032.

Illman, W. A., X. Liu, and A. Craig. 2007, Steady-state hydraulic tomography in a laboratory aquifer with deterministic heterogeneity: Multi-method and multiscale validation of hydraulic conductivity tomograms, J. of Hydrol., 341(3-4), 222-234.

Illman, W. A., A. J. Craig, and X. Liu. 2008, Practical issues in imaging hydraulic conductivity through hydraulic tomography, Ground Water, 46(1), 120-132.

Illman, W. A., X. Liu, S. Takeuchi, T. J. Yeh, K. Ando, and H. Saegusa. 2009, Hydraulic tomography in fractured granite: Mizunami Underground Research site, Japan, Water Resour. Res., 45, W01406, doi:10.1029/2007WR006715.

Illman, W. A., Alvarez, P. J., 2009. Performance assessment of bioremediation and natural attenuation, Critical Reviews in Environmental Science and Technology 39(4), 209-270, doi: 10.1080/10643380701413385.

Illman, W. A., J. Zhu, A. J. Craig, and D. Yin. 2010a, Comparison of aquifer characterization approaches through steady state groundwater model validation: A controlled laboratory sandbox study, Water Resour. Res., 46, W04502, doi:10.1029/2009WR007745.

Illman, W. A., S. J. Berg, X. Liu, A. J. Craig and A. Massi. 2010b, Hydraulic/partitioning tracer tomography for trichloroethene source zone characterization: Small-scale sandbox experiments, Environ. Sci. Technol., 44(22), pp. 8609-8614, doi: 10.1021/es101654j.

Illman, W. A., S. J. Berg, and T.-C. J. Yeh (2011), Comparison of approaches for predicting solute transport: Sandbox experiments, Ground Water, 50(3), 421-431, DOI: 10.1111/j.1745-6584.2011.00859.x.

Illman, W. A., Sudicky, E. A., Frape, S. K., 2012, Field and computational investigations of contaminant plume response to DNAPL source zone architecture and depletion at the Smithville site, Final Project Report, Ontario Ministry of Environment, 174 pgs.

Imhoff, P.T., Jaffé, P.R., Pinder, G.F., 1994a. An experimental study of complete dissolution of a nonaqueous phase liquid in saturated porous media. Water Resour. Res. 30 (2), 307–320.

Imhoff, P.T., Jaffé, P.R., Pinder, G.F., 1994b. Correction to “An experimental study of complete dissolution of a nonaqueous phase liquid in saturated porous media,”. Water Resour. Res. 30 (10), 2871.

Ji, S.-H., M. J. Nicholl, R. J. Glass, and K.-K. Lee (2006), Influence of simple fracture intersections with differing aperture on density-driven immiscible flow: Wetting versus nonwetting flows, Water Resour. Res., 42, W10416, doi:10.1029/2006WR004953.

Johnson, M., Armstrong, D., Sanford, B., Telford, P., Rutka1, M. Paleozoic and Mesozoic Geology of Ontario. 1992. In "Geology of Ontario". Thurston, P., Williams, H., Sutcliffe, R., Stott, G. Ontario Geological Survey. Special Volume 4, Part 1.

Jorgensen P, McKay L, Spliid N. Evaluation of chloride and pesticide transport in a fractured clayey till using large undisturbed columns and numerical modeling. Water Resources Research 1998 April;34(4):539-553.

Kaluarachchi J, Parker J. An Efficient Finite-Element Method for Modeling Multiphase Flow. Water Resources Research 1989 January;25(1):43-54.

Kampbell, D.H. and S.A. Vandergrift. 1998. “Analysis of Dissolved Methane, Ethane, and Ethylene in Ground Water by a Standard Gas Chromatographic Technique.” Journal of Chromatographic Science, Vol. 36, 253-256.

Kazemi H. Pressure Transient Analysis of Naturally Fractured Reservoirs with Uniform Fracture Distribution. Society of Petroleum Engineers Journal 1969;9(4):451-462.

Kazemi H, Gilman JR. In: Bear J, Tsang CF, de Marsily G, editors. Flow and Contaminant Transport in Fractured Rock. Academic Press; 1993.

Khandelwal, A., Rabideau, A. J., 1999. Transport of sequentially decaying reaction products influenced by linear nonequilibrium sorption, Water Resources Research 35(6), 1939–1945.

Knudby, C., and J. Carrera (2005), On the relationship between indicators of geostatistical, flow and transport connectivity, Adv. Water Resour., 28(4), 405– 421, doi:10.1016/j.advwatres.2004.09.001.

Knudby, C., and J. Carrera (2006), On the use of apparent hydraulic diffusivity as an indicator of connectivity, J. Hydrol., 329(3– 4), 377– 389, doi:10.1016/j.jhydrol.2006.02.026.

Kueper, B.H., Wealthall, G.P., Smith, J.W.N., Leharne, S.A and D.N, Lerner, 2003. An illustrated handbook of DNAPL transport and fate in the subsurface, The Environment Agency, Bristol, UK.

Lapcevik, P., Novakowski, K., Bickerton, G., Voralek, J. 1997. Hydraulic Characterization of the Fracture Framework in Carbonate Rock Underlying CWML Site, Smithville, Ontario. Air & Waste Management Association's 90th Anual Meeting & Exhibition, June 8-13, Toronto, Ontario, Canada.

Le Borgne, T., O. Bour, F. L. Paillet, and J. P. Caudal (2006), Assessment of preferential flow path connectivity, and hydraulic properties at single borehole and cross-borehole scales in a fractured aquifer, J. Hydrol., 328(1– 2), 347–359, doi:10.1016/j.jhydrol.2005.12.029.

Lee R, Ketelle R, Bownds J, Rizk T. Aquifer Analysis and Modeling in a Fractured, Heterogeneous Medium. Ground Water 1992 July-August;30(4):589-597.

Lee, K.Y., and Chrysikopoulos, C.V., 1995. Numerical modeling of three-dimensional contaminant migration from dissolution of multicomponent NAPL pools in saturated porous media, Environmental Geology, 26(3), 157-165.

Lee, K.Y., and Chrysikopoulos, C.V., 2006. Dissolution of a multicomponent DNAPL pool in an experimental aquifer, Journal of Hazardous Materials, 128 (2-3), 218-226.

Lesinigo M, D'Angelo C, Quarteroni A. A multiscale Darcy-Brinkman model for fluid flow in fractured porous media. Numerische Mathematik 2011 April;117(4):717-752.

Li, W., W. Nowak, and O. A. Cirpka (2005), Geostatistical inverse modeling of transient pumping tests using temporal moments of drawdown, Water Resour. Res., 41, W08403, doi:10.1029/2004WR003874.

Li, W., A. Englert, O. A. Cirpka, and H. Vereecken (2008), Three-dimensional geostatistical inversion of flowmeter and pumping test data, Ground Water, 46(2), 193-201.

Liu H, Doughty C, Bodvarsson G. An active fracture model for unsaturated flow and transport in fractured rocks. Water Resources Research 1998 October;34(10):2633-2646.

Liu, S., T. -C. J. Yeh, and R. Gardiner. 2002, Effectiveness of hydraulic tomography: sandbox experiments. Water Resour. Res. 38(4): 10.1029/2001WR000338.

Liu, X., W. A. Illman, A. J. Craig, J. Zhu, and T.-C. J. Yeh. 2007, Laboratory sandbox validation of transient hydraulic tomography, Water Resour. Res., 43, W05404, doi:10.1029/2006WR005144.

Liu, X., and P. K. Kitanidis (2011), Large-scale inverse modeling with an application in hydraulic tomography, Water Resour. Res., 47(2), W02501.

Lollar, B. S., Slater, G. F., Ahad, J., Sleep, B., Spivack, J., Brennan, M., MacKenzie, P., 1999. Contrasting carbon isotope fractionation during biodegradation of trichloroethylene and toluene: Implications for intrinsic bioremediation. Organic Geochemistry. 30, .

Lollar, B. S., Slater, G. F., Sleep, B., Witt, M., Klecka, G. M., Harkness, M., Spivack, J., 2001. Stable carbon isotope evidence for intrinsic bioremediation of tetrachloroethene and trichloroethene at area 6, Dover Air Force Base. Environmental Science & Technology. 35, .

Long, J. C. S., J. S. Remer, C. R. Wilson, and P. A. Witherspoon (1982), Porous media equivalents for networks of discontinuous fractures, Water Resour. Res., 18(3), 645– 658.

Longino, B., Kueper, B. H., 1999. Nonwetting Phase Retention and Mobilization in Rock Fractures, Water Resour. Res., 35(7), 2085-2093.

Lu X. J., Sun, Y. W., 2008. A solution of transport in porous media with equilibrium and kinetic reactions, Transport in Porous Media, 72(2), 199-206.

Lunn, M., Lunn, R. J., Mackay, R., 1996. Determining analytic solutions of multiple species contaminant transport with sorption and decay. Journal of Hydrology 180(1-4), 195–210.
Mackay, D. M., J. A. Cherry, Groundwater contamination: pump-and-treat remediation. Environmental Science & Technology. 23 (1989) 630-6.
Maji, R., Sudicky, E. A. 2008, Influence of mass transfer characteristics for DNAPL source depletion and contaminant flux in a highly characterized glaciofluvial aquifer, J. Contam. Hydrol. 102, 105-119.
Makurat A. Laboratory experiments of fracture flow and fracture cross flow. In: Jha, PC and Gupta, RN editors. Proceedings of the Site Characterisation Practice; 2000. p. 271-284.
Mariotti, A., et al. (1981), Experimental determination of nitrogen kinetic isotope fractionation: Some principles; illustration for the denitrification and nitrification processes, Plant and Soil, vol. 62, no. 3, pp. 413-430.
Mariotti, A., A. Landreau, B. Simon, 15N isotope biogeochemistry and natural denitrification process in groundwater: Application to the chalk aquifer of northern France. Geochimica et Cosmochimica Acta. 52 (1988) 1869-78.
Mayer, A. S., Miller, C.E. 1996, The influence of mass transfer characteristics and porous media heterogeneity on nonaqueous phase dissolution, Water Resour. Res., 32(6), 1551–1567.
McDermott C. I., M. Sauter, and R. Liedl (2003), New experimental techniques for pneumatic tomographical determination of the flow and transport parameters of highly fractured porous rock samples, J. Hydrol., 278 (1-4), 51-63.
McDermott C, Kolditz O. Geomechanical model for fracture deformation under hydraulic, mechanical and thermal loads. Hydrogeology Journal 2006 April;14(4):485-498.
McKay L, Gillham R, Cherry J. Field experiments in a fractured clay till .2. Solute and colloid transport. Water Resources Research 1993 December;29(12):3879-3890.
McKenna S. A. , L. C. Meigs, R. Haggerty (2001) Tracer tests in a fractured dolomite, 3. Double-porosity, multiple-rate mass transfer processes in convergent flow tracer tests. Water Resour. Res., 37(5):1143–1154.
McLaren, R. G., P. A. Forsyth, E. A. Sudicky, J. E. VanderKwaak, F. W. Schwartz, J. H. Kessler (2000), Flow and transport in fractured tuff at Yucca Mountain: numerical experiments on fast preferential flow mechanisms, J. Contam. Hydrol., 43(304) 211-238, DOI: 10.1016/S0169-7722(00)00085-1.
McLaren, R., E. A. Sudicky, Y.-J. Park, and W. A. Illman (2012), Numerical simulation of DNAPL emissions and remediation in a fractured dolomitic aquifer, Journal of Contaminant Hydrology, 136-137, 56-71. http://dx.doi.org/10.1016/j.jconhyd.2012.05.002.
Meckenstock, R., Morasch, B., Griebler, C., and Richnow, H. 2004. Stable Isotope Fractionation Analysis as a Tool to Monitor Biodegradation in Contaminated Acquifers. Journal of Contaminant Hydrology. 75, 215-255.
Melander, L., Isotope effects on reaction rates. The Ronald press company, New York. (1960).
Mercer, J. W., R. M. Cohen, A review of immiscible fluids in the subsurface: Properties, models, characterization and remediation. Journal of Contaminant Hydrology. 6 (1990) 107-63.
Mieles, J., Zhan, H., 2012. Analytical solutions of one-dimensional multispecies reactive transport in a permeable reactive barrier-aquifer system. Journal of Contaminant Hydrology, 134-135, 54-68. http://dx.doi.org/10.1016/j.jconhyd.2012.04.002.
Miles, B., R. Maji, E. A. Sudicky, G. Teutsch, A. Peter, A pragmatic approach for estimation of source-zone emissions at LNAPL contaminated sites. Journal of Contaminant Hydrology. 96 (2008) 83-96.

Miller, C.T., Poirier-McNeill, M.M., Mayer, A.S., 1990. Dissolution of trapped nonaqueous phase liquids: mass transfer characteristics. Water Resour. Res. 26(11), 2783–2796.

Moench, A. F. (1984) Double-porosity models for a fissured groundwater reservoir with fracture skin, Water Resour. Res., 20(7), 831–846.

Moortgat J, Sun S, Firoozabadi A. Compositional modeling of three-phase flow with gravity using higher-order finite element methods. Water Resources Research 2011 May 11;47(W05511).

Morrill, P. L., G. Lacrampe-Couloume, G. F. Slater, B. E. Sleep, E. A. Edwards, M. L. McMaster, D. W. Major, and B. S. Lollar. 2005. Quantifying chlorinated ethene degradation during reductive dechlorination at kelly AFB using stable carbon isotopes. Journal of Contaminant Hydrology 76 (3-4) (FEB 2005): 279-93.

Morrill, P. L., B. E. Sleep, D. J. Seepersad, M. L. McMaster, E. D. Hood, C. LeBron, D. W. Major, B. Sherwood Lollar, Variations in expression of carbon isotope fractionation of chlorinated ethenes during biologically enhanced PCE dissolution close to a source zone., Journal of Contaminant Hydrology. 110 (2009) 60-71.

Nambi, I.M., Powers, S.E., 2000. NAPL dissolution in heterogeneous systems: an experimental investigation in a simple heterogeneous system. J. Contam. Hydrol. 44, 161–184.

Narasimhan T. Multidimensional Numerical-Simulation of Fluid-Flow in Fractured Porous-Media. Water Resources Research 1982;18(4):1235-1247.

National Research Council (NRC) (1996), Rock Fractures and Fluid Flow: Contemporary Understanding and Applications, Natl. Acad. Press, Washington, D.C.

Neuman, S. P. (1987), Stochastic continuum representation of fractured rock permeability as an alternative to the REV and fracture network concepts, pp. 533-561, Rock Mechanics: Proceedings of the 28th U.S. Symposium, Tucson, Arizona, edited by I.W. Farmer, J.J.K. Daemen, C.S. Desai, C.E. Glass, and S.P. Neuman, A.A. Balkema, Rotterdam, 1240 p.

Neuman, S. P. (2005), Trends, prospects and challenges in quantifying flow and transport through fractured rocks, Hydrogeol. J., 13(1), 124–147, doi:10.1007/s10040-004-0397-2.

Neville, C. J., Ibaraki, M., Sudicky, E. A., 2000. Solute transport with multiprocess nonequilibrium: a semi-analytical solution approach, Journal of Contaminant Hydrology 44(2), 141-159.

Ni, C.-F. and T.-C. J. Yeh (2008), Stochastic inversion of pneumatic cross-hole tests and barometric pressure fluctuations in heterogeneous unsaturated formations, Adv. Water Resour., 31(12), 1708-1718.

Noorishad J, Ayatollahi M, Witherspoon P. A Finite-Element Method for Coupled Stress and Fluid-Flow Analysis in Fractured Rock Masses. International Journal of Rock Mechanics and Mining Sciences 1982;19(4):185-193.

Novakowski, K.S., and P. A. Lapcevic. 1988. Regional hydrogeology of the Silurian and Ordovician sedimentary rock underlying Niagara Falls, Ontario, Canada. Journal of Hydrology 104, 211-236.

Numata, M., N. Nakamura, H. Koshikawa, Y. Terashima, Chlorine Isotope Fractionation during Reductive Dechlorination of Chlorinated Ethenes by Anaerobic Bacteria. Environmental Science & Technology. 36 (2002) 4389-94.

Ontario Ministry of the Environment and Energy (OMOEE), 1986, Water Well Drillers Reports Database.

Ontario Ministry of Natural Resources, 2009, Natural Resources and Values Information System. Toronto, Ontario.

Pankow, J. F., Cherry, J. A., 1996, Dense Chlorinated Solvents and other DNAPLs in Groundwater, Waterloo Press.

Parker, B. L., R.W. Gillham, R. W., Cherry, J. A., 1994, Diffusive disappearance of immiscible phase organic liquids in fractured geologic media. Ground Water, 32(5): 805-820.

Park Y.-J., J.-R. de Dreuzy, K.-K. Lee, and B. Berkowitz (2001b), Transport and intersection mixing in random fracture networks with power law length distributions. Water Resour. Res., 37(10), 2493–2501.

Park Y.-J., K.-K. Lee, B. Berkowitz (2001a) Effects of junction transfer characteristics on transport in fracture networks. Water Resour. Res., 37(4), 909–923.

Park Y.-J., K.-K. Lee, G. Kosakowski, B. Berkowitz (2003) Transport behavior in three-dimensional fracture intersections. Water Resour. Res., 39(8), 1215, DOI:10.1029/2002WR001801.

Park, Y.-J., E. A. Sudicky, R. G. McLaren, and J. F. Sykes (2004), Analysis of hydraulic and tracer response tests within moderately fractured rock based on a transition probability geostatistical approach, Water Resour. Res., 40, W12404, doi:10.1029/2004WR003188.

Park, Y.-J., Sudicky, E.A., Illman, W.A., Uncertainty analysis of the influence of fracture and rock matrix characteristics on the source-zone architecture, migration patterns of aqueous phase contaminants, and remediation design at a DNAPL contaminated site, (in preparation).

Park, E., Zhan, H.B., 2009. One-dimensional solute transport in a permeable reactive barrier-aquifer system. Water Resources Research 45, W07502. http://dx.doi.org/10.1029/2008WR007155.

Peters R., E. A. Klavetter (1988) A continuum model for water movement in an unsaturated fractured rock mass. Water Resour. Res., 24(3), 416–430.

Pockar, R.M., 1999, Development of a Regional-Scale Numerical Model of Groundwater Flow and a Local-Scale Numerical Model of Groundwater Flow and Solute Transport at the Former CWML Storage Facility at Smithville, Ontario. Thesis in Earth Sciences, University of Waterloo, Waterloo, Ontario, Canada, 162 pp.

Poulson, S. R., J. I. Drever, Stable Isotope (C, Cl, and H) Fractionation during Vaporization of Trichloroethylene. Environmental Science & Technology. 33 (1999) 3689-94.

Powers, S. E., Abriola, L. M., Weber Jr., W. J., 1992. An experimental investigation of nonaqueous phase liquid dissolution in saturated subsurface systems: steady state mass transfer rates. Water Resour. Res. 28(10), 2691–2705.

Powers, S. E., Abriola, L. M.,Weber Jr.,W. J., 1994a. An experimental investigation of nonaqueous phase liquid dissolution in saturated subsurface systems: transient mass transfer rates. Water Resour. Res. 30 (2), 321–332.

Powers, S .E., Abriola, L. M., Dunkin, J.S., Weber Jr., W.J., 1994b. Phenomenological models for transient NAPL-water mass-transfer processes. J. Contam. Hydrol. 16, 1–33.

Pruess K., J. S. Y. Wang, and Y. W. Tsang (1990) On thermohydrologic conditions near high-level nuclear waste emplaced in partially saturated fractured tuff: 2. Effective continuum approximation. Water Resour. Res., 26(6), 1249–1261.

Quezada, C. R., Clement, T. P., Lee, K. K., 2004. Generalized solution to multi-dimensional, multi-species transport equations coupled with a first-order reaction network involving distinct retardation factors, Advances in Water Resources 27(5), 507-520.

Rabideau, A.J., Suribhatla, R., Craig, J.R., 2005. Analytical models for the design of iron-based permeable reactive barriers. ASCE Journal of Environmental Engineering 131 (11), 1589–1597. http://dx.doi.org/10.1061/(ASCE)0733-9372(2005) 131:11(1589).

Rao, P. S. C., Jawitz, J. W., 2003, Comment on "Steady state mass transfer from single-component dense nonaqueous phase liquids in uniform flow fields", Water Resour. Res., 39(3), 1068.

Reimus P., G. Pohll, T. Mihevc, J. Chapman, M. Haga, B. Lyles, S. Kosinski, R. Niswonger, and P. Sanders, (2003) Testing and parameterizing a conceptual model for solute transport in a fractured granite using multiple tracers in a forced gradient test. Water Resour. Res., 39(12), 1356, DOI:10.1029/2002WRR001597.

Reiss L. The Reservoir Engineering Aspects of Fractured Formations. Gulf Publishing Co.; 1980.

Reitsma, S., Kueper, B.H., 1994. Laboratory measurement of capillary pressure–saturation relationships in a rock fracture. Water Resour. Res. 30(4), 865–878.

Reynolds, D. A., Kueper, B. H., 2003. Effective constitutive properties for dense nonaqueous phase liquid (DNAPL) migration in large fracture networks: A computational study, Water Resour. Res., 39, 1254, doi:10.1029/2002WR001684.

Reynolds DA, Kueper BH. Multiphase flow and transport through fractured heterogeneous porous media. Journal of Contaminant Hydrogeology 2004;71:89-110.

Riechart, T. M. 1992. Influence of vertical fractures in horizontally stratified rocks. Unpublished M.Sc. thesis, Department of Earth Sciences, University of Waterloo, Ontario.

Rivett, M.O., S. Feenstra, and J.A. Cherry. 2001. A controlled field experiment on groundwater contamination by a multicomponent DNAPL: creation of the emplaced-source and overview of dissolved plume development. Journal of Contaminant Hydrology 49, no. 1–2: 111–149.

Rivett, M.O., S. Feenstra, and J.A. Cherry. 1994. Transport of a dissolved phase plume from a residual solvent source in a sand aquifer. Journal of Hydrology 159, no. 1–4: 27–41.

Romm, E. S. (1966), Flow characteristics of fractured rocks (in Russian), Nedra, Moscow.

Rubin, H., Rathfelder, K., Abriola, L.M., 1997. Modeling quasi-steady NAPL dissolution in permeable fractured media. ASCE Journal of Environmental Engineering 123 (3), 205–216.

Rubin, H., Yaniv, S., Spiller, M., Köngeter, J., 2008. Parameters that control the cleanup of fractured permeable aquifers. Jour. Contam. Hydrol., 96(1-4), 128-149.

Saba, T., Illangasekare, T.H., 2000. Effect of groundwater flow dimensionality on mass transfer from entrapped nonaqueous phase liquid contamination. Water Resour. Res. 36 (4), 971–979.

Saidi A. Reservoir Engineering of Fractured Reservoirs-Fundamentals and Practical Aspects. Paris: Total Edition Press; 1987.

Samper-Calvete J., Yang, C., 2007. A semi-analytical solution for linearized multicomponent cation exchange reactive transport in groundwater, Transport in Porous Media, 69(1), 67-88.

Sale, T. C., McWhorter, D. B., 2001, Steady state mass transfer from single- component dense nonaqueous phase liquids in uniform flow fields, Water Resour. Res., 37(2), 393-404.

Sarma P, Aziz K. New transfer functions for simulation of naturally fractured reservoirs with dual-porosity models. SPE Journal 2006 September;11(3):328-340.

Schaefer, C. E., Callaghan, A. V., King, J. D., and McCray, J. E., 2009, Dense nonaqueous phase liquid architecture and dissolution in discretely fractured sandstone blocks, Environmental Science & Technology, 43(6), 1877-1883.

Schmidt, T., L. Zwank, M. Elsner, M. Berg, R. Meckenstock, S. Haderlein, Compound-specific stable isotope analysis of organic contaminants in natural environments: a critical review of the state of the art, prospects, and future challenges. Analytical and Bioanalytical Chemistry. 378 (2004) 283-300.

Schöniger, A., W. Nowak, and H.-J. Hendricks Franssen (2012), Parameter estimation by ensemble Kalman filters with transformed data: Approach and application to hydraulic tomography, Water Resour. Res., 48, W04502, doi:10.1029/2011WR010462.

Schuth, C., H. Taubald, N. Bolano, and K. Maciejczyk. 2003. Carbon and hydrogen isotope effects during sorption of organic contaminants on carbonaceous materials. Journal of Contaminant Hydrology 64 (3-4) (JUL 2003): 269-81.

Schwartz, F. W. and H. Zhang (2003), Fundamentals of Ground Water, John Wiley & Sons, 764 pp.

Schwartz, F. W., L. Smith, and A. S. Crowe (1983), A stochastic analysis of macroscopic dispersion in fractured media, Water Resour. Res., 19(5), 1253 – 1265.

Schwille, F., 1988. Dense Chlorinated Solvents in Porous and Fractured Media. Lewis Publishers, Chelsea, MI. translated by J.F. Pankow.

Sciortino, A., Harmon, T. C., Yeh, W. W.-G., 2000. Inverse modeling for locating dense nonaqueous pools in groundwater under steady flow conditions, Water Resour. Res., 36(7), 1723– 1736.

Sherwood Lollar, B., G. F. Slater, B. Sleep, M. Witt, G. M. Klecka, M. Harkness, J. Spivack, Stable Carbon Isotope Evidence for Intrinsic Bioremediation of Tetrachloroethene and Trichloroethene at Area 6, Dover Air Force Base. Environmental Science & Technology. 35 (2000) 261-9.

Shouakar-Stash, O., Drimmie, R. J., Morrison, J., Frape, S. K., Heemskerk, A. R., and Mark, W. A. (2000) On-line D/H analysis for water, natural gas and organic solvents by manganese reduction. Analytical Chemistry. vol. 72, No. 11, 2664-2666.

Shouakar-Stash, O., Frape, S. K., Drimmie, R. J. (2003) Stable hydrogen, carbon and chlorine isotope measurements of selected chlorinated organic solvents. Journal of Contaminant Hydrology. Vol. 60, 211-228.

Shouakar-Stash, O., RJ Drimmie, M. Zhang, and SK Frape. 2006. Compound-specific chlorine isotope ratios of TCE, PCE and DCE isomers by direct injection using CF-IRMS. Applied Geochemistry 21 (5) (MAY): 766-81.

Simunek, J., Vogel, T., Van Genuchten, M. Th., 1994. The SWMS 2D Code for Simulating Water Flow and Solute Transport in Two-Dimensional Variably Saturated Media. Version 1.21. Research Report No. 132. Riverside, Calif.: U.S. Salinity Laboratory, Agricultural Research Service, U.S. Department of Agriculture.

Singhal, B. B., and R. P. Gupta (2010), Applied Hydrogeology of Fractured Rocks, Springer, 408 pp.

Slater, G. F., J. M. E. Ahad, B. Sherwood Lollar, R. Allen-King, B. Sleep, Carbon Isotope Effects Resulting from Equilibrium Sorption of Dissolved VOCs. Analytical Chemistry. 72 (2000) 5669-72.

Slater, G. F., Lollar, B. S., Sleep, B. E., Edwards, E. A., 2001. Variability in carbon isotopic fractionation during biodegradation of chlorinated ethenes: Implications for field applications. Environmental Science & Technology. 35, .

Slough, K.J., Sudicky, E.A., Forsyth, P.A., 1999a. Numerical simulation of multiphase flow and phase partitioning in discretely-fractured geologic media, Jour. Contam. Hydrol., 40(2), 107-136.

Slough, K.J., Sudicky, E.A., Forsyth., P.A., 1999b. Importance of rock matrix entry pressure on DNAPL migration in fractured geologic materials, Ground Water, 37(2), 237-244.

Slough K, Sudicky E, Forsyth P. Grid refinement for modeling multiphase flow in discretely fractured porous media. Advances in Water Resources 1999 November 1;23(3):261-269.

Slough, K., Sudicky, E., and Forsyth, P. Simulation of NAPL migration and persistence in the overburden and fractured bedrock at Smithville, Ontario. 1997. Proceedings of the Air & Waste Management Association's Annual Meeting & Exhibition.

Smith, L., and F. W. Schwartz (1984), An analysis of the influence of fracture geometry on mass transport in fractured media, Water Resour. Res., 20(9), 1241– 1252.

Smithville Phase IV Bedrock Remediation Program 2000. Alternatives Report & Preliminary Site Conceptual Model (1997) Report.

Srinivasan, V.,Clement, T. P., 2008a. Analytical Solutions for Sequentially Coupled One-Dimensional Reactive Transport Problems - Part I: Mathematical Derivations, Advances in Water Resources 31(2), 203-218.

Srinivasan, V., Clement, T. P., 2008b. Analytical Solutions for Sequentially Coupled One-Dimensional Reactive Transport Problems - Part II: Special Cases, Implementation and Testing, Advances in Water Resources 31(2), 219-232.

Straface, S., T.-C. J. Yeh, J. Zhu, S. Troisi, and C. H. Lee (2007), Sequential aquifer tests at a well field, Montalto Uffugo Scalo, Italy, Water Resour. Res., 43, W07432, doi:10.1029/2006WR005287.

Sturchio, N. C., Clausen, J. L., Heraty, L. J., Huang, L., Holt, B. D., Abrajano, T. A., 1998. Chlorine isotope investigation of natural attenuation of trichloroethene in an aerobic aquifer. Environmental Science & Technology. 32, .

Suarez, M. P., Rifai, H. S., 1999, Biodegradation Rates for Fuel Hydrocarbons and Chlorinated Solvents in Groundwater, Bioremediation Journal, 3(4): 337-362.

Sudicky, E.A. and Frind, E.O., 1982. Contaminant transport in fractured porous media: Analytical solutions for a system of parallel fractures. Water Resour. Res., 18(3), 1634 1642.

Sudicky, E. A., 1986. A natural-gradient experiment on solute transport in a sand aquifer: Spatial variability of hydraulic conductivity and its role in the dispersion process, Water Resour. Res., 22(13), 2069–2082

Sudicky, E. A., 1991. CMM: A semi-analytical computer model for simulating ground water fate and transport of contaminants subject to chained-decay reactions, unpublished report prepared for Dr. Zubair Saleem, US EPA Office of Solid Waste, Hydrogeologic Inc., Contract No. 68-WO-0029.

Sudicky, E. A., H.-T. Hwang, W. A. Illman, Y.-S. Wu, J. B. Kool, P. Huyakorn, A semi-analytical solution for simulating contaminant transport subject to chain-decay reactions. Journal of Contaminant Hydrology. 144 (2013) 20-45.

Sun, Y., Clement, T. P., 1999. A generalized decomposition method for solving coupled multi-species reactive transport problems, Transport in Porous Media, 37(3), 327-346.

Sun, Y., Petersen, J. N., Clement, T. P., Skeen, R. S., 1999a. Development of analytical solutions for multi-species transport with serial and parallel reactions, Water Resources Research 35(1), 185-190.

Sun, Y., Petersen, J. N., Clement, T. P., 1999b. Analytical solution for multiple species reactive transport in multiple dimensions, Journal of Contaminant Hydrology (35)4, 429-440.

Tang, D.H., Frind, E.O., Sudicky, E.A., 1980, Contaminant transport in fractured porous media: Analytical solution for a single fracture. Water Resour. Res., 17(33), 555 564.

Telford, P. 1978. Silurian Stratigraphy of the Niagara Escarpment, Niagara Falls to the Bruce Peninsula. In "Toronto '78, Field Trips Guidebook". Currie, A., Mackasey, W. Carswell Printing, Toronto.

Therrien, R., R. G. McLaren, E. A. Sudicky, and S. M. Panday (2009), HydroGeoSphere: A Three-dimensional Numerical Model Describing Fully-integrated Subsurface and Surface Flow and Solute Transport, edited, Groundwater Simulations Group, Waterloo, Ontario, Canada.

Tsang, Y. W., C. F. Tsang, F. V. Hale, and B. Dverstorp (1996), Tracer Transport in a Stochastic Continuum Model of Fractured Media, Water Resour. Res., 32(10), 3077–3092.

Tunnicliffe, B. S., Thomson, N. R., 2004. Mass removal of chlorinated ethenes from rough-walled fractures using permanganate, Jour. Contam. Hydrol., 75(1-2), 91-114.

Unger A, Mase C. Numerical study of the hydromechanical behaviour of two rough fracture surfaces in contact. Water Resources Research 1993 July;29(7):2101-2114.

Unger, A. J. A., P. A. Forsyth, E. A. Sudicky, Variable spatial and temporal weighting schemes for use in multi-phase compositional problems. Advances in Water Resources. 19 (1996) 1-27.

Unger, A. J. A., P. A. Forsyth, E. A. Sudicky, Influence of alternative dissolution models and subsurface heterogeneity on DNAPL disappearance times. Journal of Contaminant Hydrology. 30 (1998) 217-42.

Unger AJA, Bodvarsson GS, Simmons AM. Simulating infiltration in unsaturated basalt for the Large-Scale Aquifer Pumping and Infiltration Test at INEEL [Simulation de l'infiltration dans des basaltes non-saturş pour des tests à grande échelle de pompage et d'infiltration à l'INEEL]. Journal of Hydraulic Research 2004;42(Extra Issue):105-113.

Unger, A. J. A., E. A. Sudicky, P. A. Forsyth, Mechanisms Controlling Vacuum Extraction Coupled With Air Sparging for Remediation of Heterogeneous Formations Contaminated by Dense Nonaqueous Phase Liquids. Water Resour Res. 31 (1995) 1913-25.

Van Warmerdam, E. M., S. K. Frape, R. Aravena, R. J. Drimmie, H. Flatt, J. A. Cherry, Stable chlorine and carbon isotope measurements of selected chlorinated organic solvents. Applied Geochemistry. 10 (1995) 547-52.

Van Breukelen, B. M., D. Hunkeler, F. Volkering, Quantification of Sequential Chlorinated Ethene Degradation by Use of a Reactive Transport Model Incorporating Isotope Fractionation. Environmental Science & Technology. 39 (2005) 4189-97.

Van Breukelen, B. M., Quantifying the Degradation and Dilution Contribution to Natural Attenuation of Contaminants by Means of an Open System Rayleigh Equation. Environmental Science & Technology. 41 (2007) 4980-5.

Van Breukelen, B. M., H. Prommer, Beyond the Rayleigh Equation: Reactive Transport Modeling of Isotope Fractionation Effects to Improve Quantification of Biodegradation. Environmental Science & Technology. 42 (2008) 2457-63.

van Genuchten, M.T., 1985. Convective–dispersive transport of solutes involved in sequential first-order decay reactions. Computers & Geosciences 11(2), 129–147.

vanWarmerdam, E. M., S. K. Frape, R. Aravena, R. J. Drimmie, H. Flatt, and J. A. Cherry. 1995. Stable chlorine and carbon isotope measurements of selected chlorinated organic solvents. Applied Geochemistry 10 (5) (SEP 1995): 547-52.

Vasco, D. W., H. Keers, and K. Karasaki (2000), Estimation of reservoir properties using transient pressure data: An asymptotic approach, Water Resour. Res., 36(12), 3447–3465, doi:10.1029/2000WR900179.

Vesselinov, V., S. P. Neuman, and W. A. Illman (2001), Three-Dimensional Numerical Inversion of Pneumatic Cross-Hole Tests in Unsaturated Fractured Tuff 2. Equivalent Parameters, High-Resolution Stochastic Imaging and Scale Effects, Water Resour. Res., 37(12), 3019-3041.

Walsh R, McDermott C, Kolditz O. Numerical modeling of stress-permeability coupling in rough fractures. Hydrogeology Journal 2008 June;16(4):613-627.

Walton, K. M., A. J. A. Unger, E. Sudicky, Three-phase flow in discretely fractured rock: Part 1 model development (submitted).

Walton, K. M., A. J. A. Unger, M. A. Ioannidis, B. L. Parker, Three-phase flow in discretely fractured rock: Part 2. validation and verification exercises (submitted).

Wang J, Narasimhan T. Unsaturated Flow in Fractured Porous Media. In: Bear J, Tsang CF, de Marsily G, editors. Flow and Contaminant Transport in Fractured Rock. Academic Press; 1993. p. 325-394.

Warren J, Root P. The Behavior of Naturally Fractured Reservoirs. Society of Petroleum Engineers Journal 1963;3(3):245-255.

Well Record Data 1899-2010. ON: Ministry of the Environment, Available FTP: http://www.ene.gov.on.ca/environment/en/resources/collection/data_downloads/index.htm #Well Records.

Widdowson, M.A., Waddill, D.A., Brauner, J.S., Chapelle, F.H., and Bradley, P.M., 2002. SEAM3D–A Numerical Model for Three-Dimensional Solute Transport Coupled to Sequential Electron Acceptor-Based Biological Reaction in Groundwater. Blacksburg, Va.: The VA Department of Civil and Environmental Engineering, Virginia Polytechnic Institute and State University.

Wiedemeier, T.H., Rifai, H.S., Newell, C.J., and Wilson, J.T., 1999, Natural Attenuation of Fuels and Chlorinated Solvents in the Subsurface. New York: JohnWiley & Sons.

Williams, J. H., and F. L. Paillet (2002), Using flowmeter pulse tests to define hydraulic connections in the subsurface: A fractured shale example, J. Hydrol., 265(1 – 4), 100 – 117, doi:10.1016/S0022- 1694(02)00092-6.

Woodbury, A., Sudicky, E. A., 1991. The geostatistical characteristics of the Borden aquifer, Water Resour. Res., 27(4), 533–546.

Wu Y.-S., W. Zhang, L. Pan, J. Hinds, and G. B. Bodvarsson (2002) Modeling capillary barriers in unsaturated fractured rock. Water Resour. Res., 38(11), 1253, DOI:10.1029/2001WR000852.

Wu, C.-M., T.-C. J. Yeh, J. Zhu, T. H. Lee, N.-S. Hsu, C.-H. Chen, and A. F. Sancho (2005), Traditional analysis of aquifer tests: Comparing apples to oranges?, Water Resour. Res., 41, W09402, doi:10.1029/2004WR003717.

Xiang, J., T.-C. J. Yeh, C.-H. Lee, K.-C. Hsu, and J.-C. Wen (2009), A simultaneous successive linear estimator and a guide for hydraulic tomography analysis, Water Resour. Res., 45, W02432, doi:10.1029/2008WR007180.

Yaws, C. L., Yaws' handbook of thermodynamic and physical properties of chemical compounds Knovel, 2003.

Yeh, T.-C. J., R. Srivastava, A. Guzman, and T. Harter (1993), A numerical model for water flow and chemical transport in variably saturated porous media, Ground Water, 31, 634–644.

Yeh, T.-C. J., A. L. Gutjahr, and M. H. Jin (1995), An iterative cokriging-like technique for ground water flow modeling, Ground Water, 33(1), 33– 41.

Yeh, T.-C., M. Jin, and S. Hanna (1996), An iterative stochastic inverse method: Conditional effective transmissivity and hydraulic head fields, Water Resour. Res., 32(1), 85–92, doi:10.1029/95WR02869.

Yeh, T.-C. J., and S. Liu (2000), Hydraulic tomography: Development of a new aquifer test method, Water Resour. Res., 36(8), 2095– 2105.

Yeh, T.-C. J., and J. Simunek (2002), Stochastic fusion of information for characterizing and monitoring the vadose zone, Vadose Zone J., 1, 207–221, doi:10.2113/1.2.207.

Yeh, T.-C. J., Zhu, J., 2007. Hydraulic/partitioning tracer tomography for characterization of dense nonaqueous phase liquid source zones, Water Resour. Res., 43, W06435, doi:10.1029/2006WR004877.

Yeh, T.-C. J., D. Mao, L. Wan, K.-C. Hsu, J.-C. Wen, and C.-H. Lee (2011), Uniqueness, Scale, and Resolution Issues in Groundwater Model Parameter Identification, Technical Report, Dept. of Hydrology and Water Resources, The University of Arizona.

Yu S, Unger AJA, Parker B. Simulating the fate and transport of TCE from groundwater to indoor air. Journal of Contaminant Hydrogeology 2009 July 21;107(3-4):140-161.

Yu, S., Freitas, J.G., Unger, A.J.A., Barker, J.F., and Chatzis, J., 2009. Simulating the evolution of an ethanol and gasoline source zone within the capillary fringe. Journal of Contaminant Hydrology, 105, 1–17.

Zanini, L., Novakowski, K.S., Lapcevic, P., Bickerton, G.S., Talbot, C. 1997. Inorganic Geochemistry of the Groundwater at the CWML site, Smithville, Ontario - Phase II and Phase III investigation. NWRI publications, No, 98-243

Zanini L., Novakowski, K. S., Lapcevic, P., Bickerton, G. S., Voralek, J., and Talbot, C., 2000, Groundwater flow in a fractured carbonate aquifer inferred from combined hydrogeological and geochemical measurements, Ground Water 38(3), 350-360.

Zhang, Y., Graham, W. D., 2001. Spatial characterization of a hydrogeochemically heterogeneous aquifer using partitioning tracers: Optimal estimation of aquifer parameters, Water Resour. Res., 37(8), doi:10.1029/2000WR900377.

Zheng, C., Wang, P.P., 1999. MT3DMS, A Modular Three-Dimensional Multi-Species Transport Model for Simulation of Advection, Dispersion and Chemical Reactions of Contaminants in Groundwater Systems: Documentation and User's Guide. Contract Report SERDP-99-1. Vicksburg, Miss.: U.S. Army Engineer Research and Development Center, 202 pp.

Zhu, J., and T.-C. J. Yeh (2005), Characterization of aquifer heterogeneity using transient hydraulic tomography, Water Resour. Res., 41, W07028, doi:10.1029/2004WR003790.

Zhu, J., and T.-C. J. Yeh (2006), Analysis of hydraulic tomography using temporal moments of drawdown recovery data, Water Resour. Res., 42, W02403, doi:10.1029/2005WR004309.

Zimmerman R.W., G. Chen, T. Hadgu, G. S. Bodvarsson (1993) A numerical dual-porosity model with semianalytical treatment of fracture/matrix flow. Water Resour. Res., 29(7):2127–2137.

Appendix A: Nomenclature for 4.1: DNAPL transport model for CSIA

Symbol	
CV	Control Volume
$\mathbf{D}_l$	Hydrodynamic dispersion tensor for phase l [L^2T^{-1}]
d_l	Molecular diffusion of all components in phase l [L^2T^{-1}]
g	Gravitational acceleration [LT^{-2}]
K	Intrinsic permeability of porous media [L^2]
k_{rl}	Relative permeability of phase l [-]
KIE_p	Kinetic isotope effect of component p [-]
l	Phase of component; $l = \{g, q, n\}$
M_l	Molar density of phase l [mole L^{-3}]
p	Component; $p = \{w, a, c_1 ... c_n\}$
P_l	Pressure of phase l [ML^{-2}]
${}^H P_p$	Probability of component p that a heavy isotope is in a reactive position [-]
$Q_{p,l}$	Source (+ve) or sink (-ve) term for component p in phase l [mol $L^{-3}T^{-1}$]
R_C	Ratios in the amount of heavy and light carbons in a sample [-]
R_{Cl}	Ratios in the amount of heavy and light chlorines in a sample [-]
R_C^0	Reference isotope ratios for carbon compound [-]
R_{Cl}^0	Reference isotope ratios for chlorine compound [-]
$Re_{p,l}$	Multi-chain reactive term for component p in phase l [mol $L^{-3}T^{-1}$]
S_l	Saturation of phase [-]
$\mathbf{v}_l$	Darcy flux of phase l [LT^{-1}]
$\lvert\mathbf{v}_l\rvert$	Magnitude of darcy flux of phase l [LT^{-1}]
$X_{p,l}$	Mole fraction of component p in phase l [-]
$Z_{p,gn}$	Equilibrium partitioning coefficients of component p between phase g phase n [-]
$Z_{p,gq}$	Equilibrium partitioning coefficients of component p between phase g phase q [-]
α_L^l	Longitudinal dispersivity of phase l [L]
α_T^l	Transverse dispersivity of phase l [L]
δ_{ij}	Kronecker delta
$\delta^{13}C$	Isotopic signature of carbon compound [-]
$\delta^{37}Cl$	Isotopic signature of chlorine compound [-]
ε_p^C	Enrichment factor of carbon for component p [-]
ε_p^{Cl}	Enrichment factor of chlorine for component p [-]
$\lambda_{p_{Dg}}^{Dg}$	First-order decay rate of daughter component p [T^{-1}]
$\lambda_{p_{pr}}^{pr}$	First-order decay rate of parent component p [T^{-1}]

λ_p Bulk degradation rate constant for species p [T^{-1}]

μ_l Viscosity of phase l [$ML^{-2}T$]

ρ_l Mass density of phase l [ML^{-3}]

τ Tortuosity of porous media [-]

ϕ Porosity of porous media [-]

$\omega_{p_{Dg}}$ Splitting factor for component p [-]

$\omega_{p_{pr}}$ Splitting factor for parent component p [-]

Appendix B: Analytical solution for 3-D transport of a straight and branching chain of decaying solutes in groundwater

Consider the straight decay chain 1 → 2 → 3 → 4 → ,... and the following problem geometry (Figure B.1), where c_{pi} is the source peak concentration, S_i is the source standard deviation in y-direction for a Gaussian-shaped source in the y-direction, v is the average linear groundwater velocity, n is porosity, D_x, D_y, D_z are the dispersion coefficients in the x, y, and z directions, R_i is the retardation factor, λ_i is the decay constant, γ_i is the source decay constant (can equal λ_i or 0). Note that the subscript i in the above definitions refer to the i^{th} member of the chain and assume that

$$D_{x_i} = D_x$$
$$D_{y_i} = D_y$$
$$D_{z_i} = D_z$$

That is, all species have the same dispersion coefficient, which implies the same mechanical dispersion and molecular diffusion coefficient.

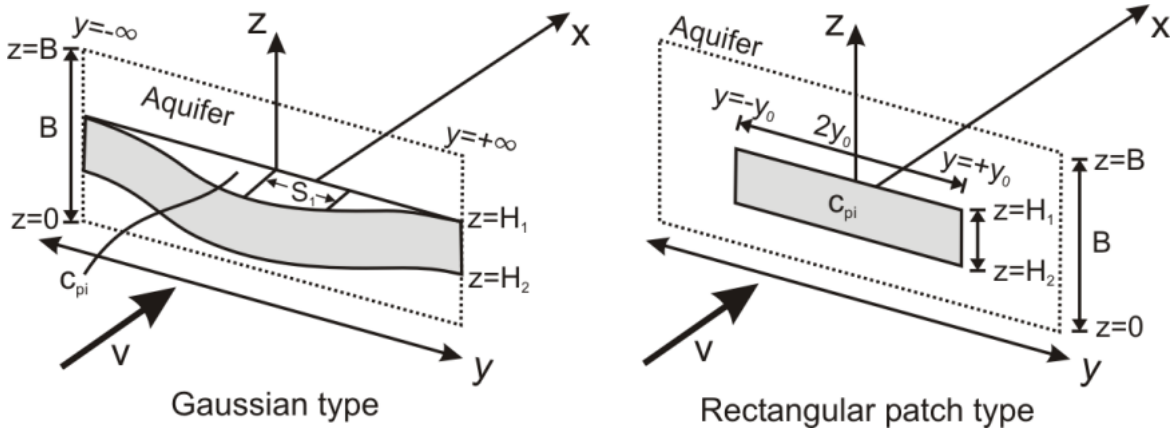

Figure B.1: Problem geometry for the analytical solution for three-dimensional transport of straight and branching chains of decaying solutes in groundwater.

Species 1:

The boundary value problem governing the reactive transport of species 1 is:

$$R_1 \frac{\partial c_1}{\partial t} + v \frac{\partial c_1}{\partial x} - D_x \frac{\partial^2 c_1}{\partial x^2} - D_y \frac{\partial^2 c_1}{\partial y^2} - D_z \frac{\partial^2 c_1}{\partial z^2} - \lambda_1 R_1 c_1 = 0 \qquad \text{(B1)}$$

$$c_1(x, y, z, 0) = 0 \qquad \text{(B2a)}$$

$$\frac{\partial c_1}{\partial t}(0, y, z, t) + \gamma_1 c_1(0, y, z, t) = 0 \qquad \text{(B2b)}$$

$$c_1(0, y, z, 0) = c_{p_1} \varpi_1(y) \left[H(z - H_1) - H(z - H_2) \right] \qquad \text{(B2c)}$$

where

$$\varpi_1(y)=\begin{cases}\exp\left(-\dfrac{y^2}{2S_1^2}\right) & \text{Gaussian type}\\ \left[H\left(y+y_0\right)-H\left(y-y_0\right)\right] & \text{Rectangular patch type}\end{cases}$$

$$H\left(y-y_0\right)=\begin{cases}0 & y<y_0\\ 1 & y>y_0\end{cases}$$

$$H\left(z-H_i\right)=\begin{cases}0 & z<H_i\\ 1 & z>H_i\end{cases}$$

$$c_1\left(\infty,y,z,t\right)=0 \tag{B2d}$$

$$c_1\left(x,\pm\infty,z,t\right)=0 \tag{B2e}$$

$$\frac{\partial c_1}{\partial z}\left(x,y,0,t\right)=0 \tag{B2f}$$

$$\frac{\partial c_1}{\partial z}\left(x,y,B,t\right)=0 \tag{B2g}$$

Define the Fourier transform in *y* as

$$\mathscr{F}\left[c_1\left(x,y,z,t\right)\right]=\overline{c}_1\left(x,\alpha,z,t\right)=\int_{-\infty}^{\infty}e^{-i\alpha y}c_1dy \tag{B3}$$

and apply it to (B1), and associated conditions (B2), to get

$$R_1\frac{\partial\overline{c}_1}{\partial t}+v\frac{\partial\overline{c}_1}{\partial x}-D_x\frac{\partial^2\overline{c}_1}{\partial x^2}+\alpha^2D_y\overline{c}-D_z\frac{\partial^2\overline{c}_1}{\partial z^2}-\lambda_1R_1\overline{c}_1=0 \tag{B4}$$

subject to

$$\overline{c}_1\left(x,\alpha,z,0\right)=0 \tag{B5a}$$

$$\frac{\partial\overline{c}_1}{\partial t}\left(0,\alpha,z,t\right)+\gamma_1\overline{c}_1\left(0,\alpha,z,t\right)=0 \tag{B5b}$$

$$\overline{c}_1\left(0,\alpha,z,0\right)=c_{p_1}\zeta_1(\alpha)\cdot\left[H\left(z-H_1\right)-H\left(z-H_2\right)\right] \tag{B5c}$$

$$\overline{c}_1\left(\infty,\alpha,z,t\right)=0 \tag{B5d}$$

$$\frac{\partial\overline{c}_1}{\partial z}\left(x,\alpha,0,t\right)=0 \tag{B5e}$$

$$\frac{\partial\overline{c}_1}{\partial z}\left(z,\alpha,B,t\right)=0 \tag{AB5f}$$

where $\zeta(\alpha)$ is the the Fourier transform of the source type function ($\varpi(y)$). $\zeta(\alpha)$ can be expressed according to the source type:

Gaussian-type can be transformed using [*Churchill*, 1972, p.472]:

$$\mathscr{F}\left[\exp\left(-\frac{y^2}{2S_1^2}\right)\right]=\left(2\pi\right)^{1/2}S_1\exp\left(-\frac{S_1^2\alpha^2}{2}\right) \tag{B6a}$$

The rectangular patch type, which is the boxcar function, in *y* is defined as:

$$\mathscr{F}\left[H\left(y+y_0\right)-H\left(y-y_0\right)\right]=\frac{2}{\alpha}\sin(\alpha y_0) \tag{B6b}$$

Now apply the finite Fourier cosine transform in *z*, defined as:

$$\mathscr{F}_c\left[\overline{c}_1\left(x,\alpha,z,t\right)\right]=\overline{\overline{c}}_1\left(x,\alpha,n,t\right)=\int_0^B \overline{c}_1\cos\left(\frac{n\pi z}{B}\right)dz \tag{B7}$$

To get:

$$R_1\frac{\partial\overline{\overline{c}}_1}{\partial t}+v\frac{\partial\overline{\overline{c}}_1}{\partial x}-D_x\frac{\partial^2\overline{\overline{c}}_1}{\partial x^2}+\left(\alpha^2D_y+\frac{n^2\pi^2}{B^2}D_z+\lambda_1R_1\right)\overline{\overline{c}}_1=0 \tag{B8}$$

$$\overline{\overline{c}}_1\left(x,\alpha,n,0\right)=0 \tag{B9a}$$

$$\frac{\partial\overline{\overline{c}}_1}{\partial t}\left(0,\alpha,n,t\right)+\gamma_1\overline{\overline{c}}_1\left(0,\alpha,n,t\right)=0 \tag{B9b}$$

$$\overline{\overline{c}}_1\left(0,\alpha,n,0\right)=c_{p_1}\zeta_1(\alpha)\times\begin{cases}\left(H_2-H_1\right) & n=0\\ \dfrac{B}{n\pi}\left[\sin\left(\dfrac{n\pi H_2}{B}\right)-\sin\left(\dfrac{n\pi H_1}{B}\right)\right] & n>0\end{cases} \tag{B9c}$$

where:

$$\zeta_1(\alpha)=\begin{cases}\left(2\pi\right)^{1/2}S_1\exp\left(-\dfrac{S_1^2\alpha^2}{2}\right) & \text{Gaussian type}\\ \dfrac{2}{\alpha}\sin(\alpha y_0) & \text{Rectangular patch type}\end{cases} \tag{B9d}$$

$$\overline{\overline{c}}_1\left(\infty,\alpha,n,t\right)=0 \tag{B9e}$$

Finally, apply the Laplace transform in *t* defined as:

$$\mathscr{L}\left[\overline{\overline{c}}_1\left(x,\alpha,n,t\right)\right]=\overline{\overline{\overline{c}}}_1\left(x,\alpha,n,p\right)=\int_0^\infty \overline{\overline{c}}_1e^{-pt}dt \tag{B10}$$

to obtain:

$$\frac{d^2\overline{\overline{\overline{c}}}_1}{dx^2}-\frac{v}{D_x}\frac{d\overline{\overline{\overline{c}}}_1}{\partial x}-\frac{1}{D_x}\left[R_1\left(p+\lambda_1\right)+\alpha^2D_y+\frac{n^2\pi^2D_z}{B^2}\right]\overline{\overline{\overline{c}}}_1=0$$

or

$$\frac{d^2\overline{\overline{\overline{c}}}_1}{dx^2}-\phi\frac{d\overline{\overline{\overline{c}}}_1}{dx}-\omega_1\left(\alpha,n,p\right)\overline{\overline{\overline{c}}}_1=0 \tag{B11}$$

$$\overline{\overline{\overline{c}}}_1\left(0,\alpha,n,p\right)=c_{p_1}\zeta_1\left(\alpha\right)\kappa_1\left(n\right)\cdot\frac{1}{p+\gamma_1} \tag{B12a}$$

$$\overline{\overline{\overline{c}}}_1\left(\infty,\alpha,n,p\right)=0 \tag{B12b}$$

where

$$\phi=\frac{v}{D_x}$$

$$\omega_1\left(\alpha,n,p\right)=\frac{1}{D_x}\left[R_1\left(p+\lambda_1\right)+\alpha^2D_y+\frac{n^2\pi^2D_z}{B^2}\right]$$

$$\kappa_1(n)=\begin{cases}(H_2-H_1) & n=0\\ \dfrac{B}{n\pi}\left[\sin\left(\dfrac{n\pi H_2}{B}\right)-\sin\left(\dfrac{n\pi H_1}{B}\right)\right] & n>0\end{cases} \tag{B12c}$$

The general solution to (B11), subject to (B12a, b) is easily shown to be

$$\overline{\overline{\overline{c}}}_1=\frac{c_{p_1}\zeta_1(\alpha)\kappa_1(n)}{p+\gamma_1}\exp\left\{b_1^-(\alpha,n,p)x\right\} \tag{B13}$$

where

$$b_1^-(\alpha,n,p)=\frac{\phi}{2}\left[1-\left\{1+\frac{4\omega_1(\alpha,n,p)}{\phi^2}\right\}^{1/2}\right]$$

The task that remains is the inversion of the transforms. Analytical inversion steps and the form of $c_1(x, y, z, t)$ is given in Appendix B. However, here we will follow a different approach to yield a solution for the Laplace-transformed solution $\overline{c}_i(x,y,z,p)$ that will be inverted numerically. We do this because it facilitates the determination of $c_i(x, y, z, t)$ for $i > 1$. First, we define the inverse Fourier cosine transform:

$$\begin{aligned}\mathcal{F}_c^{-1}\left[\overline{\overline{\overline{c}}}_1(x,\alpha,n,p)\right]&=\overline{\overline{c}}_1(x,\alpha,z,p)\\ &=\frac{\overline{\overline{\overline{c}}}_1(x,\alpha,n=0,p)}{B}+\frac{2}{B}\sum_{n=1}^{\infty}\overline{\overline{\overline{c}}}_1(x,\alpha,n,p)\cos\left(\frac{n\pi z}{B}\right)\end{aligned} \tag{B14}$$

Now let's invert the exponential Fourier transform using the general formula:

$$\begin{aligned}\mathcal{F}^{-1}\left[\overline{f}(\alpha)\right]&=\frac{1}{2\pi}\int_{-\infty}^{\infty}e^{i\alpha y}\overline{f}(\alpha)d\alpha=f(y)\\ &=\frac{1}{2\pi}\int_{-\infty}^{\infty}\left[\cos(\alpha y)+i\sin(\alpha y)\right]\overline{f}(\alpha)d\alpha\end{aligned} \tag{B15}$$

If $f(y)$ is an even function in y then (B15) reduces to:

$$f(y)=\frac{1}{\pi}\int_0^{\infty}\cos(\alpha y)\,\overline{f}(\alpha)d\alpha \tag{B16}$$

since $\sin(\alpha y)$ is odd and $\cos(-\alpha y) = \cos(\alpha y)$. Given that $c_i(x, y, z, t)$ is even (i.e., $c_i(x, -y, z, t) = c_i(x, y, z, t)$), we obtain, by applying (B16) to (B14)

$$\overline{c}_1(x,y,z,p)=\frac{1}{\pi B}\int_0^{\infty}\left[\overline{\overline{\overline{c}}}_1(x,\alpha,n=0,p)+2\sum_{n=1}^{\infty}\overline{\overline{\overline{c}}}_1(x,\alpha,n,p)\cos\left(\frac{n\pi z}{B}\right)\right]\cos(\alpha y)d\alpha \tag{B17}$$

with $\overline{\overline{\overline{c}}}_1(x,\alpha,n,p)$ given by (B13). Caution should be taken to ensure that the appropriate form of $\kappa(\alpha,n,p)$ given by (AB12c) is used since its form for $n = 0$ is different from that for $n > 0$. Finally, denoting $\mathcal{L}^{-1}$ as the inverse Laplace transform operator, we can write

$$c_1(x,y,z,t)=\mathcal{L}^{-1}\left[\overline{c}_1(x,y,z,p)\right] \tag{B18}$$

This step can be efficiently and accurately performed using the de Hoog et al. [1982] numerical algorithm.

Species 2:

$$R_2\frac{\partial c_2}{\partial t}+v\frac{\partial c_2}{\partial x}-D_x\frac{\partial^2 c_2}{\partial x^2}-D_y\frac{\partial^2 c_2}{\partial y^2}-D_z\frac{\partial^2 c_2}{\partial z^2}+\lambda_2 R_2 c_2-\lambda_1 R_1 c_1=0 \tag{B19}$$

$$c_2\left(x,y,z,0\right)=0 \tag{B20a}$$

$$\frac{\partial c_2}{\partial t}\left(0,y,z,t\right)+\gamma_2 c_2\left(0,y,z,t\right)-\gamma_1 c_1\left(0,y,z,t\right)=0 \tag{B20b}$$

$$c_2\left(0,y,z,0\right)=c_{p_2}\varpi_2(y)\cdot\left[H\left(z-H_1\right)-H\left(z-H_2\right)\right] \tag{B20c}$$

$$c_2\left(\infty,y,z,t\right)=0 \tag{B20d}$$

$$c_2\left(x,\pm\infty,z,t\right)=0 \tag{B20e}$$

$$\frac{\partial c_2}{\partial z}\left(x,y,0,t\right)=0 \tag{B20f}$$

$$\frac{\partial c_2}{\partial z}\left(x,y,B,t\right)=0 \tag{B20g}$$

Similar to species 1, the source type function can be expressed as:

$$\varpi_2(y)=\begin{cases}\exp\left(-\dfrac{y^2}{2S_2^2}\right) & \text{Gaussian type}\\ \left[H\left(y+y_0\right)-H\left(y-y_0\right)\right] & \text{Rectangular patch type}\end{cases} \tag{B20h}$$

In solving or c_2, we will follow exactly the same steps as we did for c_1. The only difference is the nonhomogeneous term involving $\lambda_1 R_1 c_1$ in (B19) which is easily accommodated. We must also take care of the integral transformations of (B20b) subject to initial condition (B20c). After applications of the Fourier transforms $\mathscr{F}$ and $\mathscr{F}_c$, they become:

$$\frac{\partial \bar{\bar{c}}_2}{\partial t}\left(0,\alpha,n,t\right)+\gamma_2\bar{\bar{c}}_2\left(0,\alpha,n,t\right)-\gamma_1\bar{\bar{c}}_1\left(0,\alpha,n,t\right)=0 \tag{B21}$$

subject to:

$$\bar{\bar{c}}_2\left(0,\alpha,n,0\right)=c_{p_2}\zeta_2\left(\alpha\right)\kappa_2\left(n\right)$$

where:

$$\zeta_2(\alpha)=\begin{cases}\left(2\pi\right)^{1/2}S_2\exp\left(-\dfrac{S_2^2\alpha^2}{2}\right) & \text{Gaussian type}\\ \dfrac{2}{\alpha}\sin(\alpha y_0) & \text{Rectangular patch type}\end{cases} \tag{B22a}$$

$$\kappa_2(n)=\begin{cases}\left(H_2-H_1\right) & n=0\\ \dfrac{B}{n\pi}\left[\sin\left(\dfrac{n\pi H_2}{B}\right)-\sin\left(\dfrac{n\pi H_1}{B}\right)\right] & n>0\end{cases} \tag{B22b}$$

Application of the Laplace transform to (B21) gives:

$$\begin{aligned}\overline{\overline{\overline{c}}}_2(0,\alpha,n,p) &= \frac{c_{p_2}\zeta_2(\alpha)\kappa_2(n)}{p+\gamma_2} + \frac{\gamma_1}{p+\gamma_2}\overline{\overline{\overline{c}}}_1(0,\alpha,n,p) \\ &= \frac{c_{p_2}\zeta_2(\alpha)\kappa_2(n)}{p+\gamma_2} + \frac{\gamma_1}{p+\gamma_2}\cdot\frac{c_{p_1}\zeta_1(\alpha)\kappa_1(n)}{p+\gamma_1}\end{aligned} \tag{B23}$$

where (B12a) has been substituted for $\overline{\overline{\overline{c}}}_1(0,\alpha,n,p)$.

We obtain the following ordinary differential equation describing $\overline{\overline{\overline{c}}}_2(x,\alpha,n,p)$:

$$\frac{d^2\overline{\overline{\overline{c}}}_2}{dx^2} - \phi\frac{d\overline{\overline{\overline{c}}}_2}{dx} - \omega_2(\alpha,n,p)\overline{\overline{\overline{c}}}_2 = \beta_1\overline{\overline{\overline{c}}}_1 \tag{B24}$$

$$\overline{\overline{\overline{c}}}_2(0,\alpha,n,p) = \frac{c_{p_2}\zeta_2(\alpha)\kappa_2(n)}{p+\gamma_2} + \frac{c_{p_1}\gamma_1\zeta_1(\alpha)\kappa_1(n)}{(p+\gamma_2)(p+\gamma_1)} \tag{B25a}$$

$$\overline{\overline{\overline{c}}}_2(\infty,\alpha,n,p) = 0 \tag{B25b}$$

where $\phi = v/D_x$ as before and

$$\omega_2(\alpha,n,p) = \frac{1}{D_x}\left[R_2(p+\lambda_2) + \alpha^2 D_y + \frac{n^2\pi^2 D_z}{B^2}\right]$$

$$\beta_1 = -\frac{\lambda_1 R_1}{D_x}$$

Upon substituting (B13) for $\overline{\overline{\overline{c}}}_1$ into (AB21) and using the result given in Appendix D, the general solution to (B21) is

$$\begin{aligned}\overline{\overline{\overline{c}}}_2 &= A\exp\{b_2^-(\alpha,n,p)x\} + B\exp\{b_2^+(\alpha,n,p)x\} \\ &\quad + \frac{\beta_1 c_{p_1}\zeta_1(\alpha)\kappa_1(n)}{p+\gamma_1}\cdot\frac{1}{\omega_1-\omega_2}\exp\{b_1^-(\alpha,n,p)x\} \\ &= A\exp\{b_2^- x\} + B\exp\{b_2^+ x\} + \frac{\beta_1}{\omega_1-\omega_2}\cdot\overline{\overline{\overline{c}}}_1(x,\alpha,n,p)\end{aligned} \tag{B26}$$

$$b_2^{\pm} = \frac{\phi}{2}\left[1 \pm \left\{\frac{4\omega_2}{\phi^2}\right\}^{1/2}\right]$$

provided that

$$\omega_1 \neq \omega_2 \quad (i.e., R_1\lambda_1 \neq R_2\lambda_2)$$

Requiring that the solution be bounded according to (B25b) implies that *B = 0*. Making use of (B25a) yields:

$$\frac{c_{p_2}\zeta_2(\alpha)\kappa_2(n)}{p+\gamma_2} + \frac{c_{p_1}\gamma_1\zeta_1(\alpha)\kappa_1(n)}{(p+\gamma_1)(p+\gamma_2)} = A + \frac{\beta_1 c_{p_1}\zeta_1(\alpha)\kappa_1(n)}{p+\gamma_1}\cdot\frac{1}{\omega_1-\omega_2}$$

or

$$A = \frac{c_{p_2}\zeta_2(\alpha)\kappa_2(n)}{p+\gamma_2} + \frac{c_{p_1}\gamma_1\zeta_1(\alpha)\kappa_1(n)}{(p+\gamma_1)(p+\gamma_2)} - \frac{c_{p_1}\beta_1\zeta_1(\alpha)\kappa_1(n)}{p+\gamma_1}\cdot\frac{1}{\omega_1-\omega_2} \tag{B27}$$

Thus, substituting for *A* and *B* in (B26) gives

$$\begin{aligned}\overline{\overline{\overline{c}}}_2 &= \left[\frac{c_{p_2}\zeta_2(\alpha)\kappa_2(n)}{p+\gamma_2}+\frac{c_{p_1}\gamma_1\zeta_1(\alpha)\kappa_1(n)}{(p+\gamma_2)(p+\gamma_1)}\right]\exp\left\{b_2^-(\alpha,n,p,x)\right\}\\ &+\frac{c_{p_1}\zeta_1(\alpha)\kappa_1(n)}{p+\gamma_1}\cdot\beta_1\cdot\frac{1}{\omega_1-\omega_2}\left[\exp\left\{b_1^-(\alpha,n,p)x\right\}-\exp\left\{b_2^-(\alpha,n,p)x\right\}\right]\end{aligned} \tag{B28}$$

or

$$\begin{aligned}\overline{\overline{\overline{c}}}_2 &= \left[\frac{c_{p_2}\zeta_2(\alpha)\kappa_2(n)}{p+\gamma_2}+\left\{\frac{\gamma_1}{p+\gamma_2}-\frac{\beta_1}{\omega_1-\omega_2}\right\}\overline{\overline{\overline{c}}}_1(0,\alpha,n,p)\right]\exp\left\{b_2^-x\right\}\\ &+\frac{\beta_1}{\omega_1-\omega_2}\overline{\overline{\overline{c}}}_1(x,\alpha,n,p)\end{aligned} \tag{B28a}$$

provided that

$$\omega_1 \neq \omega_2 \quad (i.e.,\ R_1\lambda_1 \neq R_2\lambda_2)$$

It can be seen that the first term on the right-hand side of (B25) involving c_{p_2} is of the same form as (B13) for $\overline{\overline{\overline{c}}}_1$. If we have the special case that $\omega_1 = \omega_2 \quad (i.e.,\ R_1\lambda_1 = R_2\lambda_2)$, then a modified general solution must be used (Appendix D, Eq. D8), which yields:

$$\begin{aligned}\overline{\overline{\overline{c}}}_2 &= \left[\frac{c_{p_2}\zeta_2(\alpha)\kappa_2(n)}{p+\gamma_2}+\frac{c_{p_1}\gamma_1\zeta_1(\alpha)\kappa_1(n)}{(p+\gamma_2)(p+\gamma_1)}\right]\exp\left\{b_2^-(\alpha,n,p)x\right\}\\ &+\frac{xc_{p_1}\beta_1\zeta_1(\alpha)\kappa_1(n)}{(p+\gamma_1)\left(b_2^+-b_2^-\right)}\exp\left\{b_2^-(\alpha,n,p)x\right\}\end{aligned} \tag{B29}$$

for the case $\omega_1 = \omega_2$ or

$$\begin{aligned}\overline{\overline{\overline{c}}}_2 &= \left[\frac{c_{p_2}\zeta_2(\alpha)\kappa_2(n)}{p+\gamma_2}+\frac{\gamma_1}{p+\gamma_2}\overline{\overline{\overline{c}}}_1(0,\alpha,n,p)\right]\exp\left\{b_2^-x\right\}\\ &-\frac{\beta_1 x}{b_2^+-b_2^-}\overline{\overline{\overline{c}}}_1(x,\alpha,n,p)\end{aligned} \tag{B29a}$$

Finally, making use of the inversion results (B17) and (B18), we can write:

$$c_2(x,y,z,t) = \mathscr{L}^{-1}\left[\frac{1}{\pi B}\int_0^\infty\left[\overline{\overline{\overline{c}}}_2(x,\alpha,n=0,p)+2\sum_{n=1}^{\infty}\overline{\overline{\overline{c}}}_1(x,\alpha,n,p)\cos\left(\frac{n\pi z}{B}\right)\right]\cos(\alpha y)\,d\alpha\right] \tag{B30}$$

where either (B28a) or (B29a) is substituted.

Species 3:

$$R_3\frac{\partial c_3}{\partial t}+v\frac{\partial c_3}{\partial x}-D_x\frac{\partial^2 c_3}{\partial x^2}-D_y\frac{\partial^2 c_3}{\partial y^2}-D_z\frac{\partial^2 c_3}{\partial z^2}+\lambda_3 R_3 c_3-\lambda_2 R_2 c_2 = 0 \tag{B31}$$

$$c_3(x,y,z,0) = 0 \tag{B32a}$$

$$\frac{\partial c_3}{\partial t}(0,y,z,t)+\gamma_3 c_3(0,y,z,t)-\gamma_2 c_2(0,y,z,t) = 0 \tag{B32b}$$

$$c_3(0,y,z,0) = c_{p_3}\varpi(y)\cdot\left[H(z-H_1)-H(z-H_2)\right] \tag{B32c}$$

$$c_3(\infty,y,z,t) = 0 \tag{B32d}$$

$$c_3(x,\pm\infty,z,t) = 0 \tag{B32e}$$

$$\frac{\partial c_3}{\partial z}(x,y,0,t) = 0 \tag{B32f}$$

$$\frac{\partial c_3}{\partial z}(x,y,B,t) = 0 \tag{B32g}$$

Application of the Fourier transforms $\mathscr{F}$ and $\mathscr{F}_c$ and the Laplace transform $\mathscr{L}$ to the system (B31) and (B32) leads to

$$\frac{d^2\overline{\overline{\overline{c}}}_3}{dx^2} - \phi\frac{d\overline{\overline{\overline{c}}}_3}{dx} - \omega_3(\alpha,n,p)\overline{\overline{\overline{c}}}_3 = \beta_2\overline{\overline{\overline{c}}}_2 \tag{B33}$$

$$(p+\gamma_3)\overline{\overline{\overline{c}}}_3(0,\alpha,n,p) = c_{p_3}\zeta_3(\alpha)\kappa_3(n) + \gamma_2\overline{\overline{\overline{c}}}_2(0,\alpha,n,p) \tag{B34}$$

$$\overline{\overline{\overline{c}}}_3(0,\alpha,n,p) = \frac{c_{p_3}\zeta_3(\alpha)\kappa_3(n)}{p+\gamma_3} + \frac{\gamma_2}{p+\gamma_3}\left[\frac{c_{p_2}\zeta_2(\alpha)\kappa_2(n)}{p+\gamma_2} + \frac{c_{p_1}\gamma_1\zeta_1(\alpha)\kappa_1(n)}{(p+\gamma_2)(p+\gamma_1)}\right] \tag{B35a}$$

$$\overline{\overline{\overline{c}}}_3(\infty,\alpha,n,p) = 0 \tag{B35b}$$

where:

$$\omega_3(\alpha,n,p) = \frac{1}{D_x}\left[R_3(p+\lambda_3) + \alpha^2 D_y + \frac{n^2\pi^2 D_z}{B^2}\right]$$

$$\beta_2 = -\frac{\lambda_2 R_2}{D_x}$$

$$\zeta_3(\alpha) = \begin{cases} (2\pi)^{1/2} S_3 \exp\left(-\dfrac{S_3^2\alpha^2}{2}\right) & \text{Gaussian type} \\ \dfrac{2}{\alpha}\sin(\alpha y_0) & \text{Rectangular patch type} \end{cases}$$

$$\kappa_3(n) = \begin{cases} (H_2 - H_1) & n = 0 \\ \dfrac{B}{n\pi}\left[\sin\left(\dfrac{n\pi H_2}{B}\right) - \sin\left(\dfrac{n\pi H_1}{B}\right)\right] & n > 0 \end{cases}$$

The general solution of (B33) after substituting for $\overline{\overline{\overline{c}}}_2$ using (B28a) is (again using the results of Appendix C):

$$\overline{\overline{\overline{c}}}_3 = A\exp\left\{b_3^-(\alpha,n,p)x\right\} + B\exp\left\{b_3^+(\alpha,n,p)x\right\}$$
$$+\frac{\beta_2}{\omega_2-\omega_3}\left[\frac{c_{p_2}\zeta_2(\alpha)\kappa_2(n)}{p+\gamma_2}+\left\{\frac{\gamma_1}{p+\gamma_2}-\frac{\beta_1}{\omega_1-\omega_2}\right\}\overline{\overline{\overline{c}}}_1(0,\alpha,n,p)\right]\exp\left\{b_2^-(\alpha,n,p)x\right\} \quad \text{(B36)}$$
$$+\frac{\beta_1\beta_2}{(\omega_1-\omega_2)(\omega_1-\omega_3)}\overline{\overline{\overline{c}}}_1(x,\alpha,n,p)$$

provided that

$$\omega_1 \neq \omega_2, \omega_1 \neq \omega_3, \omega_2 \neq \omega_3$$

The parameters b_3^- and b_3^+ are defined analogously to those for species 1 or 2 defined earlier except that λ_3 and R_3 are substituted. Boundary condition (B35b) gives $B = 0$ and (B35a) yields:

$$A = \frac{c_{p_3}\zeta_3(\alpha)\kappa_3(n)}{p+\gamma_3}+\frac{\gamma_2}{p+\gamma_3}\overline{\overline{\overline{c}}}_2(0,\alpha,n,p)$$
$$-\frac{\beta_2}{\omega_2-\omega_3}\left[\frac{c_{p_2}\zeta_2(\alpha)\kappa_2(n)}{p+\gamma_2}+\left\{\frac{\gamma_1}{p+\gamma_2}-\frac{\beta_1}{\omega_1-\omega_2}\right\}\overline{\overline{\overline{c}}}_1(0,\alpha,n,p)\right] \quad \text{(B37)}$$
$$-\frac{\beta_1\beta_2}{(\omega_1-\omega_2)(\omega_1-\omega_3)}\overline{\overline{\overline{c}}}_1(0,\alpha,n,p)$$

Now, substitute (B37) into (B36) to get

$$\overline{\overline{\overline{c}}}_3 = \left[\begin{array}{l}\frac{c_{p_3}\zeta_3(\alpha)\kappa_3(n)}{p+\gamma_3}+\frac{\gamma_2}{p+\gamma_3}\overline{\overline{\overline{c}}}_2(0,\alpha,n,p)\\ -\frac{\beta_2}{\omega_2-\omega_3}\left(\frac{c_{p_2}\zeta_2(\alpha)\kappa_2(n)}{p+\gamma_2}+\left\{\frac{\gamma_1}{p+\gamma_2}-\frac{\beta_1}{\omega_1-\omega_2}\right\}\overline{\overline{\overline{c}}}_1(0,\alpha,n,p)\right)\\ -\frac{\beta_1\beta_2}{(\omega_1-\omega_2)(\omega_1-\omega_3)}\overline{\overline{\overline{c}}}_1(0,\alpha,n,p)\end{array}\right]\exp\left\{b_3^-x\right\}$$
$$+\frac{\beta_2}{\omega_2-\omega_3}\left[\frac{c_{p_2}\zeta_2(\alpha)\kappa_2(n)}{p+\gamma_2}+\left\{\frac{\gamma_1}{p+\gamma_2}-\frac{\beta_1}{\omega_1-\omega_2}\right\}\overline{\overline{\overline{c}}}_1(0,\alpha,n,p)\right]\exp\left\{b_2^-x\right\} \quad \text{(B38)}$$
$$+\frac{\beta_1\beta_2}{(\omega_1-\omega_2)(\omega_1-\omega_3)}\overline{\overline{\overline{c}}}_1(x,\alpha,n,p)$$
$$\omega_1 \neq \omega_2, \omega_1 \neq \omega_3, \omega_2 \neq \omega_3$$

If on the other hand $\omega_2 = \omega_3$ (i.e., $R_2\lambda_2 = R_3\lambda_3$) but then we have $\omega_2 \neq \omega_3$ using (C8) in Appendix C:

$$\begin{aligned}\overline{\overline{\overline{c}}}_3 &= A\exp\left\{b_3^- x\right\} + B\exp\left\{b_3^- x\right\} \\ &\quad -\beta_2\left[\frac{c_{p_2}\zeta_2(\alpha)\kappa_2(n)}{p+\gamma_2} + \left\{\frac{\gamma_1}{p+\gamma_2} - \frac{\beta_1}{\omega_1-\omega_2}\right\}\overline{\overline{\overline{c}}}_1(0,\alpha,n,p)\right] \\ &\quad \cdot\left[\frac{1}{b_3^+ - b_3^-} + x\right]\frac{1}{b_3^+ - b_3^-}\exp\left(b_3^- x\right) \\ &\quad + \frac{\beta_1\beta_2}{(\omega_3-\omega_1)(\omega_2-\omega_1)}\overline{\overline{\overline{c}}}_1(x,\alpha,n,p) \\ &\qquad \omega_1 \neq \omega_2, \omega_1 \neq \omega_3, \omega_2 = \omega_3\end{aligned} \tag{B39}$$

Application of the boundary conditions (B34 or B35a) and (B35b) gives *B = 0* and

$$\begin{aligned}A &= \frac{c_{p_3}\zeta_3(\alpha)\kappa_3(n)}{p+\gamma_3} + \frac{\gamma_2}{p+\gamma_3}\overline{\overline{\overline{c}}}_2(0,\alpha,n,p) \\ &\quad + \beta_2\left[\frac{c_{p_2}\zeta_2(\alpha)\kappa_2(n)}{p+\gamma_2} + \left\{\frac{\gamma_1}{p+\gamma_2} - \frac{\beta_1}{\omega_1-\omega_2}\right\}\overline{\overline{\overline{c}}}_1(0,\alpha,n,p)\right. \\ &\quad \left.\cdot\frac{1}{\left(b_3^+ - b_3^-\right)^2}\right] - \frac{\beta_1\beta_2}{(\omega_3-\omega_1)(\omega_2-\omega_1)}\overline{\overline{\overline{c}}}_1(0,\alpha,n,p)\end{aligned} \tag{B40}$$

Substituting (B40) into (B39) for A and letting B = 0 gives:

$$\begin{aligned}\overline{\overline{\overline{c}}}_3 &= \left[\begin{array}{l}\dfrac{c_{p_3}\zeta_3(\alpha)\kappa_3(n)}{p+\gamma_3} + \dfrac{\gamma_2}{p+\gamma_3}\overline{\overline{\overline{c}}}_2(0,\alpha,n,p) \\ -\dfrac{\beta_1\beta_2}{(\omega_3-\omega_1)(\omega_2-\omega_1)}\overline{\overline{\overline{c}}}_1(0,\alpha,n,p)\end{array}\right]\exp\left\{b_3^- x\right\} \\ &\quad -\frac{\beta_2 x}{b_3^+ - b_3^-}\left[\frac{c_{p_2}\zeta_2(\alpha)\kappa_2(n)}{p+\gamma_2} + \left\{\frac{\gamma_1}{p+\gamma_2} - \frac{\beta_1}{\omega_1-\omega_2}\right\}\overline{\overline{\overline{c}}}_1(0,\alpha,n,p)\right]\exp\left\{b_3^- x\right\} \\ &\quad + \frac{\beta_1\beta_2}{(\omega_3-\omega_1)(\omega_2-\omega_1)}\overline{\overline{\overline{c}}}_1(x,\alpha,n,p)\end{aligned} \tag{B41a}$$

or

$$\begin{aligned}\overline{\overline{\overline{c}}}_3 &= \left[\begin{array}{l}\dfrac{c_{p_3}\zeta_3(\alpha)\kappa_3(n)}{p+\gamma_3} + \dfrac{\gamma_2}{p+\gamma_3}\overline{\overline{\overline{c}}}_2(0,\alpha,n,p) \\ -\dfrac{\beta_1\beta_2}{(\omega_3-\omega_1)(\omega_2-\omega_1)}\overline{\overline{\overline{c}}}_1(0,\alpha,n,p)\end{array}\right]\exp\left\{b_3^- x\right\} \\ &\quad -\frac{\beta_2 x}{b_3^+ - b_3^-}\left[\overline{\overline{\overline{c}}}_2(x,\alpha,n,p) - \frac{\beta_1}{\omega_1-\omega_2}\overline{\overline{\overline{c}}}_1(x,\alpha,n,p)\right] \\ &\quad + \frac{\beta_1\beta_2}{(\omega_3-\omega_1)(\omega_2-\omega_1)}\overline{\overline{\overline{c}}}_1(x,\alpha,n,p)\end{aligned} \tag{B41b}$$

where

$$\omega_3 = \omega_2, \omega_2 \neq \omega_1, \omega_3 \neq \omega_1$$

and (B28a) is used to express the second term in (B41a).

If we have $\omega_3 \neq \omega_1$,then using (B29a) for $\overline{\overline{\overline{c}}}_3$ in (B33) leads to:

$$\begin{aligned}\overline{\overline{\overline{c}}}_3 &= A\exp\left\{b_3^- x\right\} + B\exp\left\{b_3^+ x\right\} \\ &+ \frac{\beta_2}{\omega_2-\omega_3}\left[\frac{c_{p_2}\zeta_2(\alpha)\kappa_2(n)}{p+\gamma_2} + \frac{\gamma_1}{p+\gamma_2}\overline{\overline{\overline{c}}}_1(0,\alpha,n,p)\right]\exp\left\{b_2^- x\right\} \\ &- \frac{\beta_1\beta_2}{\omega_1-\omega_3}\cdot\frac{1}{b_2^+-b_2^-}\left[x - \frac{1}{b_2^- - b_3^+}\right]\overline{\overline{\overline{c}}}_1(x,\alpha,n,p) \qquad \text{(B42)} \\ &= A\exp\left\{b_3^- x\right\} + B\exp\left\{b_3^+ x\right\} \\ &+ \frac{\beta_2}{\omega_2-\omega_3}\left[\overline{\overline{\overline{c}}}_2(x,\alpha,n,p) + \frac{\beta_1\overline{\overline{\overline{c}}}_1(0,\alpha,n,p)}{\left(b_2^+-b_2^-\right)\left(b_2^- - b_3^+\right)}\right]\end{aligned}$$

$$\omega_2 = \omega_1, \omega_3 \neq \omega_1, \omega_2 \neq \omega_3$$

where use has been made of the result (C11) in Appendix C and also (B29a). Application of the boundary conditions yields $B = 0$ and

$$\begin{aligned}A &= \frac{c_{p_3}\zeta_3(\alpha)\kappa_3(n)}{p+\gamma_3} + \frac{\gamma_2}{p+\gamma_3}\overline{\overline{\overline{c}}}_2(0,\alpha,n,p) \\ &- \frac{\beta_2}{\omega_2-\omega_3}\left[\overline{\overline{\overline{c}}}_2(0,\alpha,n,p) + \frac{\beta_1\overline{\overline{\overline{c}}}_1(0,\alpha,n,p)}{\left(b_2^+-b_2^-\right)\left(b_2^- - b_3^+\right)}\right]\end{aligned} \qquad \text{(B43)}$$

Using (B43) in (B442) gives

$$\begin{aligned}\overline{\overline{\overline{c}}}_3 &= \left[\begin{array}{l}\dfrac{c_{p_3}\zeta_3(\alpha)\kappa_3(n)}{p+\gamma_3} + \left(\dfrac{\gamma_2}{p+\gamma_3} - \dfrac{\beta_2}{\omega_2-\omega_3}\right)\overline{\overline{\overline{c}}}_2(0,\alpha,n,p) \\ -\dfrac{\beta_2\beta_1}{\omega_2-\omega_3}\cdot\dfrac{1}{\left(b_2^+-b_2^-\right)\left(b_2^- - b_3^+\right)}\overline{\overline{\overline{c}}}_1(0,\alpha,n,p)\end{array}\right]\exp\left\{b_3^- x\right\} \qquad \text{(B44)} \\ &+ \frac{\beta_2}{\omega_2-\omega_3}\left[\overline{\overline{\overline{c}}}_2(x,\alpha,n,p) + \frac{\beta_1\overline{\overline{\overline{c}}}_1(x,\alpha,n,p)}{\left(b_2^+-b_2^-\right)\left(b_2^- - b_3^+\right)}\right]\end{aligned}$$

$$\omega_2 = \omega_1, \omega_3 \neq \omega_1, \omega_2 \neq \omega_3$$

Finally, if $\omega_1 = \omega_2 = \omega_3$

$$\begin{aligned}\overline{\overline{\overline{c}}}_3 &= A\exp\left\{b_3^- x\right\} + B\exp\left\{b_3^+ x\right\} \\ &- \frac{\beta_2}{b_3^+-b_3^-}\left[\frac{1}{b_3^+-b_3^-} + x\right]\left[\frac{c_{p_2}}{p+\gamma_2} + \frac{\gamma_1}{p+\gamma_2}\overline{\overline{\overline{c}}}_1(0,\alpha,n,p)\right]\exp\left\{b_3^- x\right\} \qquad \text{(B45)} \\ &- \frac{\beta_2\beta_1}{\left(b_3^+-b_3^-\right)^2}\left[\frac{1}{b_3^- - b_3^+}\left(x - \frac{1}{b_3^- - b_3^+}\right) - \frac{x^2}{2}\right]\overline{\overline{\overline{c}}}_1(x,\alpha,n,p)\end{aligned}$$

Now, making use of the boundary conditions for $\overline{\overline{\overline{c}}}_3$ gives $B = 0$ and

$$A=\frac{c_{p_3}\zeta_3(\alpha)\kappa_3(n)}{p+\gamma_3}+\frac{\gamma_2}{p+\gamma_3}\overline{\overline{\overline{c}}}_2(0,\alpha,n,p)$$
$$+\frac{\beta_2}{\left(b_3^+-b_3^-\right)^2}\left[\frac{c_{p_2}}{p+\gamma_2}+\frac{\gamma_1}{p+\gamma_2}\overline{\overline{\overline{c}}}_1(0,\alpha,n,p)\right] \tag{B46}$$
$$-\frac{\beta_1\beta_2}{\left(b_3^+-b_3^-\right)^2}\frac{1}{\left(b_3^--b_3^+\right)^2}\overline{\overline{\overline{c}}}_1(0,\alpha,n,p)$$

Finally, substituting for *A* and *B* in (B45) gives

$$\overline{\overline{\overline{c}}}_3=\left[\begin{array}{l}\dfrac{c_{p_3}\zeta_3(\alpha)\kappa_3(n)}{p+\gamma_3}+\dfrac{\gamma_2}{p+\gamma_3}\overline{\overline{\overline{c}}}_2(0,\alpha,n,p)\\ +\dfrac{\beta_2}{\left(b_3^+-b_3^-\right)^2}\left\{\dfrac{c_{p_2}}{p+\gamma_2}+\left(\dfrac{\gamma_1}{p+\gamma_2}\dfrac{\beta_1}{\left(b_3^+-b_3^-\right)^2}\right)\overline{\overline{\overline{c}}}_1(0,\alpha,n,p)\right\}\end{array}\right]\exp\left\{b_3^-x\right\}$$
$$-\frac{\beta_2}{b_3^+-b_3^-}\left[\frac{1}{b_3^+-b_3^-}+x\right]\left[\frac{c_{p_2}}{p+\gamma_2}+\frac{\gamma_1}{p+\gamma_2}\overline{\overline{\overline{c}}}_2(0,\alpha,n,p)\right]\exp\left\{b_3^-x\right\} \tag{B47}$$
$$-\frac{\beta_1\beta_2}{\left(b_3^+-b_3^-\right)^2}\left[\frac{1}{b_3^--b_3^+}\left(x-\frac{1}{b_3^--b_3^+}\right)-\frac{x^2}{2}\right]\overline{\overline{\overline{c}}}_1(x,\alpha,n,p)$$

Or, upon simplifying (B47):

$$\overline{\overline{\overline{c}}}_3=\left[\begin{array}{l}\dfrac{c_{p_3}\zeta_3(\alpha)\kappa_3(n)}{p+\gamma_3}+\dfrac{\gamma_2}{p+\gamma_3}\overline{\overline{\overline{c}}}_2(0,\alpha,n,p)\\ -\dfrac{\beta_2\beta_1}{\left(b_3^+-b_3^-\right)^2}\overline{\overline{\overline{c}}}_1(0,\alpha,n,p)\end{array}\right]\exp\left\{b_3^-x\right\}$$
$$-\frac{\beta_2}{b_3^+-b_3^-}\left[x\left(\frac{c_{p_2}}{p+\gamma_2}+\frac{\gamma_1}{p+\gamma_2}\overline{\overline{\overline{c}}}_1(0,\alpha,n,p)\right)\right]\exp\left\{b_3^-x\right\} \tag{B48}$$
$$-\frac{\beta_2\beta_1}{\left(b_3^+-b_3^-\right)^2}\left[\frac{1}{b_3^--b_3^+}\left(x-\frac{1}{b_3^--b_3^+}\right)-\frac{x^2}{2}\right]\overline{\overline{\overline{c}}}_1(x,\alpha,n,p)$$

The inverse transform of $\overline{\overline{\overline{c}}}_3$ is given by substituting either (B38), (B41b), (B44) or (B48) into:

$$c_3(x,y,z,t)=\mathscr{L}^{-1}\left[\frac{1}{\pi B}\int_0^\infty\left[\overline{\overline{\overline{c}}}_3\left(x,\alpha,n=0,p\right)+2\sum_{n=1}^{\infty}\overline{\overline{\overline{c}}}_3(x,\alpha,n,p)\cos\left(\frac{n\pi z}{B}\right)\right]\cos(\alpha y)\,d\alpha\right] \tag{B49}$$

Species 4:

$$R_4\frac{\partial c_4}{\partial t}+v\frac{\partial c_4}{\partial x}-D_x\frac{\partial^2 c_4}{\partial x^2}-D_y\frac{\partial^2 c_4}{\partial y^2}-D_z\frac{\partial^2 c_4}{\partial z^2}+\lambda_4R_4c_4-\lambda_3R_3c_3=0 \tag{B50}$$
$$c_4(x,y,z,0)=0 \tag{B51a}$$

$$\frac{\partial c_4}{\partial t}(0,y,z,t)+\gamma_4 c_4(0,y,z,t)-\gamma_3 c_3(0,y,z,t)=0 \tag{B51b}$$

$$c_4(0,y,z,0)=c_{p_4}\varpi_4(y)\cdot\left[H(z-H_1)-H(z-H_2)\right] \tag{B51c}$$

$$c_4(\infty,y,z,t)=0 \tag{B51d}$$

$$c_4(x,\pm\infty,z,t)=0 \tag{B51e}$$

$$\frac{\partial c_4}{\partial z}(x,y,0,t)=0 \tag{B51f}$$

$$\frac{\partial c_4}{\partial z}(x,y,B,t)=0 \tag{B51g}$$

Application of the transformations $\mathscr{T}$, $\mathscr{T}_c$, and $\mathscr{L}$ to the system (B50) and (B51) leads to

$$\frac{d^2\overline{\overline{\overline{c}}}_4}{dx^2}-\phi\frac{d\overline{\overline{\overline{c}}}_4}{dx}-\omega_4(\alpha,n,p)\overline{\overline{\overline{c}}}_4=\beta_3\overline{\overline{\overline{c}}}_3 \tag{B52}$$

$$\overline{\overline{\overline{c}}}_4(0,\alpha,n,p)=\frac{c_{p_4}\zeta_4(\alpha)\kappa_4(n)}{p+\gamma_4}+\frac{\gamma_3}{p+\gamma_4}\overline{\overline{\overline{c}}}_3(0,\alpha,n,p) \tag{B53a}$$

$$\overline{\overline{\overline{c}}}_4(\infty,\alpha,n,p)=0 \tag{B53b}$$

where:

$$\omega_4(\alpha,n,p)=\frac{1}{D_x}\left[R_4(p+\lambda_4)+\alpha^2 D_y+\frac{n^2\pi^2 D_z}{B^2}\right]$$

$$\beta_3=-\frac{\lambda_3 R_3}{D_x}$$

$$\zeta_4(\alpha)=\begin{cases}(2\pi)^{1/2}S_4\exp\left(-\dfrac{S_4^2\alpha^2}{2}\right) & \text{Gaussian type}\\ \dfrac{2}{\alpha}\sin(\alpha y_0) & \text{Rectangular patch type}\end{cases}$$

$$\kappa_4(n)=\begin{cases}(H_2-H_1) & n=0\\ \dfrac{B}{n\pi}\left[\sin\left(\dfrac{n\pi H_2}{B}\right)-\sin\left(\dfrac{n\pi H_1}{B}\right)\right] & n>0\end{cases}$$

Upon substituting (B38) for $\overline{\overline{\overline{c}}}_3$ in (B52) and (B28a) for $\overline{\overline{\overline{c}}}_2$ in (B38), the general solution to (B52) is:

$$\begin{aligned}\overline{\overline{\overline{c}}}_4 &= A\exp\left\{b_4^- x\right\} + B\exp\left\{b_4^+ x\right\} \\ &+ \frac{\beta_3}{\omega_3-\omega_4}\left[\begin{array}{l}\dfrac{c_{p_3}\zeta_3(\alpha)\kappa_3(n)}{p+\gamma_3} + \dfrac{\gamma_2}{p+\gamma_3}\overline{\overline{\overline{c}}}_2(0,\alpha,n,p) \\ -\dfrac{\beta_2}{\omega_2-\omega_3}\left(\dfrac{c_{p_2}\zeta_2(\alpha)\kappa_2(n)}{p+\gamma_2} + \left\{\dfrac{\gamma_1}{p+\gamma_2} - \dfrac{\beta_1}{\omega_1-\omega_2}\right\}\overline{\overline{\overline{c}}}_1(0,\alpha,n,p)\right) \\ -\dfrac{\beta_1\beta_2}{(\omega_1-\omega_2)(\omega_1-\omega_3)}\overline{\overline{\overline{c}}}_1(0,\alpha,n,p)\end{array}\right]\exp\left\{b_3^- x\right\} \\ &+ \frac{\beta_2\beta_3}{(\omega_2-\omega_3)(\omega_2-\omega_4)}\left[\frac{c_{p_2}\zeta_2(\alpha)\kappa_2(n)}{p+\gamma_2} + \left\{\frac{\gamma_1}{p+\gamma_2} - \frac{\beta_1}{\omega_1-\omega_2}\right\}\overline{\overline{\overline{c}}}_1(0,\alpha,n,p)\right]\exp\left\{b_2^- x\right\} \\ &+ \frac{\beta_1\beta_2\beta_3}{(\omega_1-\omega_2)(\omega_1-\omega_3)(\omega_1-\omega_4)}\overline{\overline{\overline{c}}}_1(x,\alpha,n,p)\end{aligned} \tag{B54}$$

for the case

$$\omega_1 \neq \omega_2 \neq \omega_3 \neq \omega_4$$

Boundary condition (B53b) gives $B = 0$ and (B53a) yields:

$$\begin{aligned}A &= \frac{c_{p_4}\zeta_4(\alpha)\kappa_4(n)}{p+\gamma_4} + \frac{\gamma_3}{p+\gamma_4}\overline{\overline{\overline{c}}}_3(0,\alpha,n,p) \\ &- \frac{\beta_3}{\omega_3-\omega_4}\left[\begin{array}{l}\dfrac{c_{p_3}\zeta_3(\alpha)\kappa_3(n)}{p+\gamma_3} + \dfrac{\gamma_2}{p+\gamma_3}\overline{\overline{\overline{c}}}_2(0,\alpha,n,p) \\ -\dfrac{\beta_2}{\omega_2-\omega_3}\left(\dfrac{c_{p_2}\zeta_2(\alpha)\kappa_2(n)}{p+\gamma_2} + \left\{\dfrac{\gamma_1}{p+\gamma_2} - \dfrac{\beta_1}{\omega_1-\omega_2}\right\}\overline{\overline{\overline{c}}}_1(0,\alpha,n,p)\right) \\ -\dfrac{\beta_1\beta_2}{(\omega_1-\omega_2)(\omega_1-\omega_3)}\overline{\overline{\overline{c}}}_1(0,\alpha,n,p)\end{array}\right] \\ &- \frac{\beta_2\beta_3}{(\omega_2-\omega_3)(\omega_2-\omega_4)}\left[\frac{c_{p_2}\zeta_2(\alpha)\kappa_2(n)}{p+\gamma_2} + \left\{\frac{\gamma_1}{p+\gamma_2} - \frac{\beta_1}{\omega_1-\omega_2}\right\}\overline{\overline{\overline{c}}}_1(0,\alpha,n,p)\right] \\ &- \frac{\beta_1\beta_2\beta_3}{(\omega_1-\omega_2)(\omega_1-\omega_3)(\omega_1-\omega_4)}\overline{\overline{\overline{c}}}_1(0,\alpha,n,p)\end{aligned} \tag{B55}$$

Substituting (B55) for A into (B54) and letting $B = 0$ yields the final solution for $\overline{\overline{\overline{c}}}_4$ for the case $\omega_1 \neq \omega_2 \neq \omega_3 \neq \omega_4$. Due to the large number of combinations of special case solutions for $\omega_4 = \omega_3$, etc., these solution will not be derived here. Finally using the inversion formula, we can write:

$$c_4(x,y,z,t) = \mathscr{L}^{-1}\left[\frac{1}{\pi B}\int_0^\infty\left[\overline{\overline{\overline{c}}}_4(x,\alpha,n=0,p) + 2\sum_{n=1}^\infty \overline{\overline{\overline{c}}}_4(x,\alpha,n,p)\cos\left(\frac{n\pi z}{B}\right)\right]\cos(\alpha y)\,d\alpha\right] \tag{B56}$$

Steady-state solutions:

For any species c_i, the steady-state solution follows from the final-value theorem for the Laplace transformation given by:

$$c_i(x,y,z) = \lim_{p\to 0} p\bar{c}_i(x,y,z,p)$$
$$= \frac{1}{\pi B}\int_0^{\infty}\left[\lim_{p\to 0}\left(p\cdot\bar{\bar{\bar{c}}}_i(x,\alpha,n=0,p)\right) + 2\sum_{n=1}^{\infty}\cos\left(\frac{n\pi z}{B}\right)\lim_{p\to 0} p\cdot\bar{\bar{\bar{c}}}_i(x,\alpha,n,p)\right]\cos(\alpha y)\,dx \quad \text{(B57)}$$

Note that the contributions of a decaying boundary condition at $x = 0$ for any of the parents leading to c_i is zero, including the concentration of c_{p_i} if it decays also. The limits appearing in (14) are easily written down.

Solution for simple splitting chains:

Consider the parent-daughter splitting reaction as illustrated in Figure 4.3.2b. Here, η_{1j} is a splitting factor with $j = 2, 3, 4,...$ and

$$\sum_{j=1}^{ND}\eta_{1j} = 1$$

where *ND* is the number of daughters. We have

$$\bar{\bar{\bar{c}}}_1 = \frac{c_{p_1}\zeta_1(\alpha)\kappa_1(n)}{p+\gamma_1}\exp\left(b_1^{-}x\right) \quad \text{(B58)}$$

as usual (e.g., see B13).

For the case shown here, the solution for $\bar{\bar{\bar{c}}}_1$ is:

$$\bar{\bar{\bar{c}}}_i = \left[\frac{c_{p_i}\zeta_i(\alpha)\kappa_i(n)}{p+\gamma_i} + \left\{\frac{\gamma_{1i}}{p+\gamma_i} - \frac{\beta_{1i}}{\omega_1+\omega_i}\right\}\bar{\bar{\bar{c}}}_1(0,\alpha,n,p)\right]\exp\left(b_i^{-}x\right)$$
$$+ \frac{\beta_{1i}}{\omega_1+\omega_i}\bar{\bar{\bar{c}}}_1(x,\alpha,n,p) \quad \text{(B59)}$$

provided that

$$\omega_1 \neq \omega_i,\ i = 2, 3,...$$

The assumption of unequal coefficients ω_i is the same as before (see B28a). For the special case where $\omega_1 = \omega_i$, where $i = 2, 3,...$, the solution becomes (see B29a).

$$\bar{\bar{\bar{c}}}_i = \left[\frac{c_{p_i}\zeta_i(\alpha)\kappa_i(n)}{p+\gamma_i} + \frac{\gamma_{1i}}{p+\gamma_i}\bar{\bar{\bar{c}}}_1(0,\alpha,n,p)\right]\exp\left(b_i^{-}x\right)$$
$$+ \frac{\beta_{1i}x}{b_i^{+}-b_i^{-}}\bar{\bar{\bar{c}}}_1(x,\alpha,n,p) \quad \text{(B60)}$$

if

$$\omega_i = \omega_i, \text{ where } i = 2, 3,\ldots$$

In the above, we have defined $\gamma_{1i} = \eta_{1i}\gamma_1$, $\beta_{1i} = \eta_{1i}\beta_1$ and normally we would use $\gamma_1 = \lambda_1$.

Solution for simple converging chains:

Consider the parent-daughter converging reaction as illustrated in Figure 4.3.2c. Here, η_{1j} is a splitting factor with j = 2, 3, 4,...and

$$\overline{\overline{\overline{c}}}_i = \frac{c_{p_i}\zeta_i(\alpha)\kappa_i(n)}{p+\gamma_i}\exp\left(b_i^- x\right) \qquad i = 1, 2, \ldots N-1 \tag{B61}$$

$$\begin{aligned}\overline{\overline{\overline{c}}}_N = &\left[\frac{c_{p_N}\zeta_N(\alpha)\kappa_N(n)}{p+\gamma_N} + \sum_{i=1}^{N-1}\left(\frac{c_{p_i}\gamma_i}{p+\gamma_N} - \frac{\beta_i}{\omega_i-\omega_N}\right)\overline{\overline{\overline{c}}}_i(0,\alpha,n,p)\right]\exp\left(b_N^- x\right)\\ &+\sum_{i=1}^{N-1}\frac{\beta_i x}{\omega_i-\omega_N}\overline{\overline{\overline{c}}}_i(x,\alpha,n,p)\end{aligned} \tag{B62}$$

for the case $\omega_i \neq \omega_N$ and

$$\begin{aligned}\overline{\overline{\overline{c}}}_N = &\left[\frac{c_{p_N}\zeta_N(\alpha)\kappa_N(n)}{p+\gamma_N} + \sum_{i=1}^{N-1}\frac{\gamma_i}{p+\gamma_N}\overline{\overline{\overline{c}}}_i(0,\alpha,n,p)\right]\exp\left(b_N^- x\right)\\ &-\frac{x}{b_N^+ - b_N^-}\sum_{i=1}^{N-1}\frac{\beta_i}{\omega_i-\omega_N}\overline{\overline{\overline{c}}}_i(x,\alpha,n,p)\end{aligned} \tag{B63}$$

for the case $\omega_i = \omega_N$. Equations (B62) and (B63) for $\overline{\overline{\overline{c}}}_N$ are simply based on superposition using (B28a) and (B29a).

Solution for a seven-member branching chain:

Consider the seven-member branching chain as shown in Figure 2e:

Member 1: as equation (B17) with $\overline{\overline{\overline{c}}}(x,\alpha,n,p)$ given by (B13)

Member 2: as equation (B28a) or (B28), but with β_1 replaced by β_{12} where $\beta_{12} = \eta_{12}\beta_1$. Because the mass from the decay of member 1 splits at x = 0 also, then the term $\frac{\gamma_1}{p+\gamma_2}$ in (B28a) must be replaced by $\frac{\eta_{12}\gamma_1}{p+\gamma_2}$.

Member 3: as equation (B28a) or (B28), but with β_1 replaced by β_{13} where $\beta_{13} = \eta_{13}\beta_1$. Also, replace $\frac{\gamma_1}{p+\gamma_2}$ by $\frac{\eta_{13}\gamma_1}{p+\gamma_2}$ noting that all subscripts involving "2" now become "3" to denote member 3 in (B28a).

Member 4: same as (B38) but replace $\frac{\gamma_2}{p+\gamma_3}$ by $\frac{\eta_{24}\gamma_2}{p+\gamma_3}$, β_2 by $\eta_{24}\beta_2$, $\frac{\gamma_1}{p+\gamma_2}$ by $\frac{\eta_{12}\gamma_1}{p+\gamma_2}$, and β_1 by $\eta_{12}\beta_1$. Note that all subscripts "3" will become "4" to denote member 4.

Member 5: same as (B38) but replace $\frac{\gamma_2}{p+\gamma_3}$ by $\frac{\eta_{25}\gamma_2}{p+\gamma_3}$, β_2 by $\eta_{25}\beta_2$, $\frac{\gamma_1}{p+\gamma_2}$ by $\frac{\eta_{12}\gamma_1}{p+\gamma_2}$, and β_1 by $\eta_{12}\beta_1$. Note that all subscripts "3" will become "5" to denote member 5.

Member 6: same as (B38) but replace $\frac{\gamma_2}{p+\gamma_3}$ by $\frac{\eta_{36}\gamma_2}{p+\gamma_3}$, β_2 by $\eta_{36}\beta_2$, $\frac{\gamma_1}{p+\gamma_2}$ by $\frac{\eta_{13}\gamma_1}{p+\gamma_2}$, and β_1 by $\eta_{13}\beta_1$. Note that all subscripts "3" will become "6" to denote member 6 and all subscripts "2" will refer to member 3 which is the parent of 6.

Member 7: same as (B38) but replace $\frac{\gamma_2}{p+\gamma_3}$ by $\frac{\eta_{37}\gamma_2}{p+\gamma_3}$, β_2 by $\eta_{37}\beta_2$, $\frac{\gamma_1}{p+\gamma_2}$ by $\frac{\eta_{13}\gamma_1}{p+\gamma_2}$, and β_1 by $\eta_{13}\beta_1$. Note that all subscripts "3" will become "7" to denote member 7 and all subscripts "2" will refer to member 3 which is the parent of 7.

Appendix C: Analytical inversion of $\overline{\overline{\overline{c}}}_1(x,\alpha,n,p)$

From equation (B13) and using the definitions of $\omega(\alpha,n,p)$, ϕ, $\zeta_1(\alpha)$ and $\kappa_1(n)$, (B13) can be expressed as

$$\overline{\overline{\overline{c}}}_1 = c_{p_1}\zeta_1(\alpha)\kappa_1(n)\exp\left(\frac{vx}{2D_x}\right) \cdot\frac{1}{p+\gamma_1}\exp\left[-\left\{p+\lambda_1+\frac{v^2}{4R_1D_x}+\frac{\alpha^2D_y}{R_1}+\frac{n^2\pi^2D_z}{R_1B^2}\right\}^{1/2}\left(\frac{R_1}{D_x}\right)^{1/2}x\right] \tag{C1}$$

Where

$$\zeta_1(\alpha)=\begin{cases}(2\pi)^{1/2}S_1\exp\left(-\dfrac{S_1^2\alpha^2}{2}\right) & \text{Gaussian type}\\ \dfrac{2}{\alpha}\sin(\alpha y_0) & \text{Rectangular patch type}\end{cases}$$

$$\kappa_1(n)=\begin{cases}(H_2-H_1) & n=0\\ \dfrac{B}{n\pi}\left[\sin\left(\dfrac{n\pi H_2}{B}\right)-\sin\left(\dfrac{n\pi H_1}{B}\right)\right] & n>0\end{cases}$$

Now define the following inverse Laplace transforms:

$$\mathcal{L}^{-1}\left[\exp\left\{-a\left(p+b\right)^{1/2}\right\}\right]=\frac{a}{2\pi^{1/2}t^{3/2}}\exp(-bt)\exp\left(-\frac{a^2}{4t}\right)\qquad a>0 \tag{C2}$$

$$\mathcal{L}^{-1}\left[\frac{1}{p+a}\right]=\exp(-at) \tag{C3}$$

And the convolution theorem:

$$\mathcal{L}^{-1}\left[\overline{f}_1(p)*\overline{f}_2(p)\right]=\int_0^t f_1(\tau)\cdot f_2(t-\tau)\,d\tau \tag{C4}$$

Using (C2) - (C4) we get:

$$\overline{\overline{\overline{c}}}_1(x,\alpha,n,t)=\frac{c_{p_1}R_1^{1/2}x}{2(\pi D_x)^{1/2}}\cdot\zeta_1(\alpha)\cdot\kappa_1(n)\exp\left(\frac{vx}{2D_x}\right) \cdot\int_0^t\frac{1}{\tau^{3/2}}\exp\left\{-\left(\frac{v^2}{4R_1D_x}+\frac{\alpha^2D_y}{R_1}+\frac{n^2\pi^2D_z}{R_1B^2}+\lambda_1\right)\tau-\frac{R_1x^2}{4D_x\tau}\right\} \cdot\exp\left\{-\gamma_1(t-\tau)\right\}d\tau \tag{C5a}$$

Depending on the source types, (C5a) can be expressed as two types. If $\zeta_1(\alpha)$ is the Gaussian source type, then:

$$= \frac{c_{p_1} S_1 R_1^{1/2} x}{\left(2D_x\right)^{1/2}} \cdot \exp\left(\frac{vx}{2D_x}\right) \cdot \kappa_1(n) \exp\left(-\gamma_1 t\right)$$
$$\cdot \int_0^t \frac{1}{\tau^{3/2}} \exp\left\{-\left(\frac{v^2}{4R_1 D_x} + \frac{n^2\pi^2 D_z}{R_1 B^2} + \lambda_1 - \gamma_1\right)\tau - \frac{R_1 x^2}{4D_x \tau}\right\} \tag{C5b}$$
$$\cdot \exp\left\{-\alpha^2\left(\frac{D_y \tau}{R_1} + \frac{S_1^2}{2}\right)\right\} d\tau$$

or if $\zeta_1(\alpha)$ is the rectangular patch source type, then:

$$= \frac{c_{p_1} R_1^{1/2} x}{2\left(\pi D_x\right)^{1/2}} \cdot \exp\left(\frac{vx}{2D_x}\right) \cdot \kappa_1(n) \exp\left(-\gamma_1 t\right)$$
$$\cdot \int_0^t \frac{1}{\tau^{3/2}} \exp\left\{-\left(\frac{v^2}{4R_1 D_x} + \frac{n^2\pi^2 D_z}{R_1 B^2} + \lambda_1 - \gamma_1\right)\tau - \frac{R_1 x^2}{4D_x \tau}\right\} \tag{C5c}$$
$$\cdot \frac{2}{\alpha} \sin(\alpha y_0) \cdot \exp\left(-\frac{\alpha^2 D_y \tau}{R_1}\right) d\tau$$

We can use the following inverse Fourier transform $\mathscr{F}^{-1}$:

$$\mathscr{F}^{-1}\left[\exp\left\{-a\alpha^2\right\}\right] = \frac{1}{2\left(\pi a\right)^{1/2}} e \exp\left(-\frac{y^2}{4a}\right) \tag{C6a}$$

$$\mathscr{F}^{-1}\left[\frac{2}{\alpha}\sin\left(\alpha y_0\right)\right] = H\left(y + y_0\right) - H\left(y - y_0\right) \tag{C6b}$$

And the convolution theorem:

$$\mathscr{F}^{-1}\left[\overline{f}\left(\alpha\right) * \overline{g}\left(\alpha\right)\right] = \int_{-\infty}^{\infty} f\left(\xi\right) \cdot g\left(y - \xi\right) d\xi \tag{C6c}$$

To invert the Fourier transform involving α. For (C5b), making use of (C6a) yields

$$\overline{c_1}\left(x, y, n, t\right) = \frac{c_{p_1} S_1 R_1^{1/2} x}{2\left(2\pi D_x\right)^{1/2}} \exp\left(\frac{vx}{2D_x}\right) \exp\left(-\gamma_1 t\right) \kappa_1\left(n\right)$$
$$\cdot \int_0^t \frac{1}{\tau^{3/2}\left(D_y \tau / R_1 + S_1^2/2\right)^{1/2}} \exp\left\{\begin{array}{l} -\dfrac{R_1 x^2}{4D_x \tau} - \dfrac{y^2}{4\left(D_y \tau / R_1 + S_1^2/2\right)} \\ -\left(\dfrac{v^2}{4R_1 D_x} + \dfrac{n^2\pi^2 D_z}{R_1 B^2} + \lambda_1 - \gamma_1\right)\tau \end{array}\right\} d\tau \tag{C7a}$$

Similarly, using (C6b) and (C6c), (C5c) can be transformed:

$$\bar{c}_1(x,y,n,t) = \frac{c_{p_1} R_1^{1/2} x}{4(\pi D_x)^{1/2}} \exp\left(\frac{vx}{2D_x}\right) \exp(-\gamma_1 t)\kappa_1(n)$$
$$\cdot \int_0^t \frac{1}{\tau^{3/2}} \left[erfc\left\{\frac{y-y_0}{2(D_y\tau)^{1/2}}\right\} - erfc\left\{\frac{y+y_0}{2(D_y\tau)^{1/2}}\right\}\right] \quad \text{(C7b)}$$
$$\cdot \exp\left\{-\left(\frac{R_1 x^2}{4D_x\tau} + \frac{v^2}{4R_1 D_x} - \frac{n^2\pi^2 D_z}{R_1 B^2} + \lambda_1 - \gamma_1\right)\tau\right\} d\tau$$

Finally making use of the inverse Fourier cosine transform (B14) to obtain:

A. Case for Gaussian source type:

$$c_1(x,y,z,t) = \frac{c_{p_1} S_1 R_1^{1/2} x}{2B(2\pi D_x)^{1/2}} \exp\left(\frac{vx}{2D_x}\right) \exp(-\gamma_1 t)$$
$$\cdot \int_0^t \left[(H_2 - H_1) + \frac{2B}{\pi} \sum_{n=1}^{\infty} \frac{1}{n} \left\{\sin\left(\frac{n\pi H_2}{B}\right) - \sin\left(\frac{n\pi H_1}{B}\right)\right\} \cos\left(\frac{n\pi z}{B}\right) \exp\left\{-\frac{n^2\pi^2 D_z \tau}{R_1 B^2}\right\}\right] \quad \text{(C8a)}$$
$$\cdot \frac{1}{\tau^{3/2}\left(D_y\tau/R_1 + S_1^2/2\right)^{1/2}} \exp\left\{-\frac{R_1 x^2}{4D_x\tau} + \left[\frac{y^2}{4\left(D_y\tau/R_1 + S_1^2/2\right)} + \frac{v^2}{4R_1 D_x} + \lambda_1 - \gamma_1\right]\tau\right\} d\tau$$

B. Case for Rectangular patch source type:

$$c_1(x,y,z,t) = \frac{c_{p_1} R_1^{1/2} x}{4B(\pi D_x)^{1/2}} \exp\left(\frac{vx}{2D_x}\right) \exp(-\gamma_1 t)$$
$$\cdot \int_0^t \left[(H_2 - H_1) + \frac{2B}{\pi} \sum_{n=1}^{\infty} \frac{1}{n} \left\{\sin\left(\frac{n\pi H_2}{B}\right) - \sin\left(\frac{n\pi H_1}{B}\right)\right\} \cos\left(\frac{n\pi z}{B}\right) \exp\left(-\frac{n^2\pi^2 D_z \tau}{R_1 B^2}\right)\right] \quad \text{(C8b)}$$
$$\cdot \frac{1}{\tau^{3/2}} \exp\left\{-\left(\frac{R_1 x^2}{4D_x\tau} - \frac{v^2}{4R_1 D_x} + \lambda_1 - \gamma_1\right)\tau\right\} \left[erfc\left\{\frac{y-y_0}{2(D_y\tau)^{1/2}}\right\} - erfc\left\{\frac{y+y_0}{2(D_y\tau)^{1/2}}\right\}\right] d\tau$$

Equation (C8a) and (C8b) are the final form of the solution for c_1 with Gaussian and rectangular patch source types, respectively.

Appendix D: Solution to the nonhomogeneous ordinary differential equation

Given the nonhomogeneous ordinary differential equation:

$$\frac{d^2\overline{\overline{\overline{c}}}_i}{dx^2} - \phi\frac{d\overline{\overline{\overline{c}}}_i}{dx} - \omega_i(\alpha,n,p)\overline{\overline{\overline{c}}}_i = \beta_k\overline{\overline{\overline{c}}}_k \qquad i \geq 2 \tag{D1}$$

we seek a general solution of the form:

$$\overline{\overline{\overline{c}}}_i = A\exp\left\{b_1^-(\alpha,n,p)x\right\} + B\exp\left\{b_1^+(\alpha,n,p)x\right\} + \overline{\overline{\overline{c}}}_i^p(x,\alpha,n,p) \tag{D2}$$

where

$$b_1^{\pm}(\alpha,n,p) = \frac{\phi}{2}\left[1 \pm \left\{1 + \frac{4\omega_i}{\phi^2}\right\}^{1/2}\right]$$

and $\overline{\overline{\overline{c}}}_i^p$ is the particular solution arising from the nonhomogeneous term $\beta_k\overline{\overline{\overline{c}}}_k(x,\alpha,n,p)$.

The solution for $\overline{\overline{\overline{c}}}_i^p$ is given by:

$$\overline{\overline{\overline{c}}}_i^p = \beta_k\int^x \frac{\left[\exp\left(b_i^-\zeta\right)\exp\left(b_i^+x\right) - \exp\left(b_i^+\zeta\right)\exp\left(b_i^-x\right)\right]}{W(\zeta)}\overline{\overline{\overline{c}}}_k(\zeta,\alpha,n,p)\,d\zeta \tag{D3}$$

where the Wronskian W(x) is given by

$$W(x) = \begin{vmatrix} e^{b_i^-x} & e^{b_i^+x} \\ b_i^-e^{b_i^-x} & b_i^+e^{b_i^-x} \end{vmatrix} = \left(b_i^+ - b_i^-\right)\exp\left\{\left(b_i^- + b_i^+\right)x\right\} \tag{D4}$$

We note that the solution for $\overline{\overline{\overline{c}}}_k$ will be of the form:

$$\overline{\overline{\overline{c}}}_k = F\exp\left\{b_k^-x\right\} \tag{D5}$$

where F is some function (usually independent of x). Substitution of (D4) and (D5) into (D3) yields, after minor algebra:

$$\overline{\overline{\overline{c}}}_i^p = F\beta_k\cdot\frac{1}{b_i^+ - b_i^-}\int^x\left[\exp\left(b_i^+(x-\zeta)\right) - \exp\left(b_i^-(x-\zeta)\right)\right]\exp\left(b_k^-\zeta\right)d\zeta$$

$$= F\beta_k\frac{1}{b_i^+ - b_i^-}\left[\exp\left(b_i^+x\right)\int\left[\exp\left(\left(b_k^- - b_i^+\right)\zeta\right)d\zeta\right] - \exp\left(b_i^-x\right)\int\exp\left(\left(b_k^- - b_i^+\right)\zeta\right)d\zeta\right]$$

$$= F\beta_k\frac{1}{b_i^+ - b_i^-}\left[\frac{1}{b_k^- - b_i^+} - \frac{1}{b_k^- - b_i^-}\right]\exp\left(b_k^-x\right) \qquad if\ b_k^- \neq b_i^- \tag{D6a}$$

$$= F\beta_k\frac{1}{\left(b_k^- - b_i^+\right)\left(b_k^- - b_i^-\right)}\exp\left(b_k^-x\right) \qquad if\ b_k^- \neq b_i^- \tag{D6b}$$

Upon writing b_k^-, b_i^-, and b_i^+ in the denominator of (D6) in terms of ϕ, ω_i, and ω_k, (D6) can be simplified to:

$$\overline{\overline{\overline{c}}}_i^p = F\beta_k\frac{1}{\omega_k - \omega_i}\exp\left(b_k^-x\right) \tag{D7}$$

if we have

$$b_k^- \neq b_i^- \qquad \left(i.e., R_k\lambda_k \neq R_i\lambda_i\right)$$

If, however $\omega_k = \omega_i$ $\left(i.e., R_k\lambda_k = R_i\lambda_i\right)$, we must use:

$$\begin{aligned}
\overline{\overline{\overline{c}}}_i^p &= F\beta_{i-1}\frac{1}{b_i^+ - b_i^-}\left[\frac{\exp\left(b_k^- x\right)}{b_k^- - b_i^+} - \exp\left(b_i^- x\right)\int^x d\zeta\right] \\
&= F\beta_{i-1}\frac{1}{b_i^+ - b_i^-}\left[\frac{\exp\left(b_k^- x\right)}{b_k^- - b_i^+} - x\exp\left(b_i^- x\right)\right] \\
&= -F\beta_{i-1}\left[\frac{1}{b_i^+ - b_i^-} + x\right]\frac{1}{b_i^+ - b_i^-}\exp\left(b_i^- x\right) \\
b_k^- &= b_i^- \quad \left(x\exp\left(b_i^- x\right) \quad R_k\lambda_k = R_i\lambda_i\right)
\end{aligned} \tag{D8}$$

We can also have the case where $\overline{\overline{\overline{c}}}_k$ is the form:

$$\overline{\overline{\overline{c}}}_k = Fx\exp\left\{b_k^- x\right\} \tag{D9}$$

For which we need to evaluate:

$$\begin{aligned}
\overline{\overline{\overline{c}}}_i^p &= F\beta_k\frac{1}{b_i^+ - b_i^-}\left[\exp\left(b_i^+ x\right)\int^x \zeta\exp\left(\left(b_k^- - b_i^+\right)\zeta\right)d\zeta\right. \\
&\qquad \left. -\exp\left(b_i^- x\right)\int^x \zeta\exp\left(\left(b_k^- - b_i^-\right)\zeta\right)d\zeta\right] \\
&= F\beta_k\frac{1}{b_i^+ - b_i^-}\left[\exp\left(b_i^+ x\right)\left\{\frac{1}{b_k^- - b_i^+}\left(x\exp\left(\left(b_k^- - b_i^+\right)x\right) - \int^x \exp\left(\left(b_k^- - b_i^+\right)\zeta\right)d\zeta\right)\right\}\right. \\
&\qquad \left. -\exp\left(b_i^- x\right)\left\{\frac{1}{b_k^- - b_i^-}\left(x\exp\left(\left(b_k^- - b_i^-\right)x\right) - \int^x \exp\left(\left(b_k^- - b_c^-\right)\zeta\right)d\zeta\right)\right\}\right] \\
&= F\beta_k\frac{1}{b_i^+ - b_i^-}\left[\frac{1}{b_k^- - b_i^+}\left(x - \frac{1}{b_k^- - b_i^+}\right)\exp\left(b_k^- x\right) - \frac{1}{b_k^- - b_i^-}\left(x - \frac{1}{b_k^- - b_i^-}\right)\exp\left(b_k^- x\right)\right. \\
&= F\beta_k\frac{1}{b_i^+ - b_i^-}\left[\frac{1}{b_k^- - b_i^+}\left(x - \frac{1}{b_k^- - b_i^+}\right) - \frac{1}{b_k^- - b_i^-}\left(x - \frac{1}{b_k^- - b_i^-}\right)\right]\exp\left(b_k^- x\right)
\end{aligned} \tag{D10}$$

if

$$b_k^- \neq b_i^-$$

but:

$$\frac{1}{b_i^+ - b_i^-}\left[\frac{1}{b_k^- - b_i^+} - \frac{1}{b_k^- - b_i^-}\right] = \frac{1}{\omega_k - \omega_i}$$

in which case (D10) can be written as:

$$\overline{\overline{\overline{c}}}_i^p = F\beta_k\frac{1}{\omega_k - \omega_i}\left[x - \frac{1}{b_k^- - b_i^+}\right]\exp\left(b_k^- x\right) \tag{D11}$$

for the case when

$$b_k^- \neq b_i^-, \quad \left(i.e., \omega_k \neq \omega_i\right)$$

If $\overline{\overline{\overline{c}}}_k$ is of the form of (D9) and $b_k^- = b_i^-$

, then:

$$\overline{\overline{\overline{c}}}_i^p = \frac{F\beta_k}{b_i^+ - b_i^-}\left[\frac{1}{b_k^- - b_i^+}\left(x - \frac{1}{b_k^- - b_i^+}\right)\exp\left(b_k^- x\right) - \frac{x^2}{2}\exp\left(b_k^- x\right)\right] \qquad \text{(D12)}$$

Appendix E: Supplementary figures for section 4.8.2

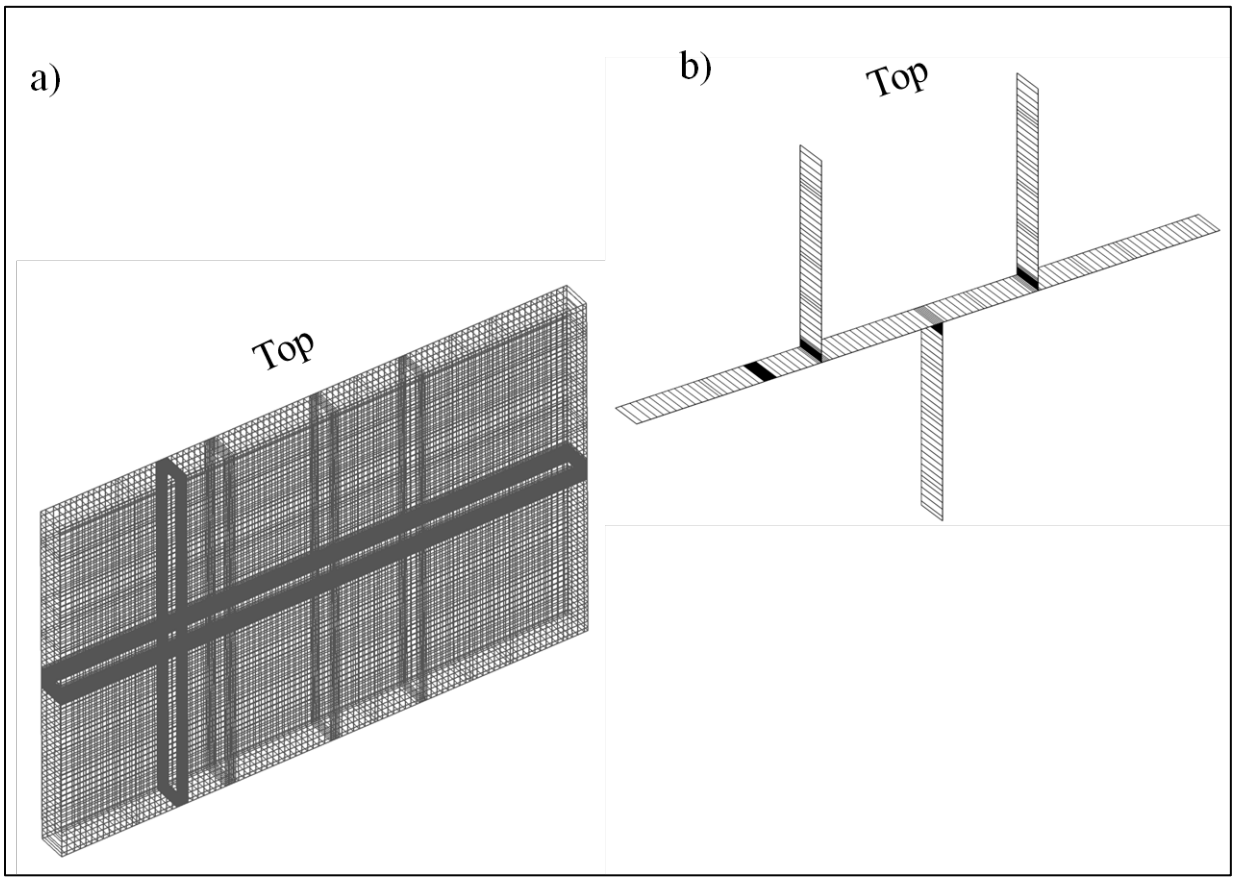

Figure E1: a) Mesh used for forward simulation of pumping tests and b) fracture faces.

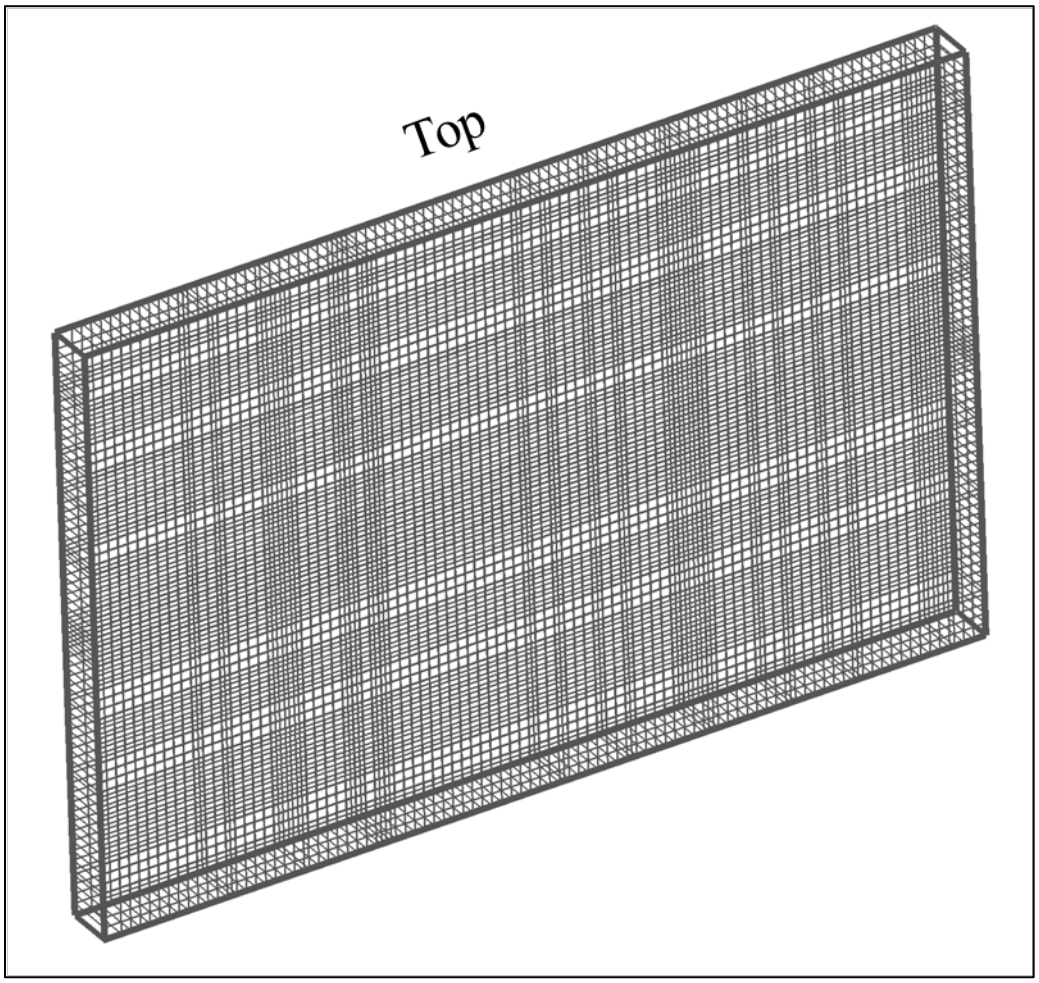

Figure E2: Computational grid used for THT analysis.

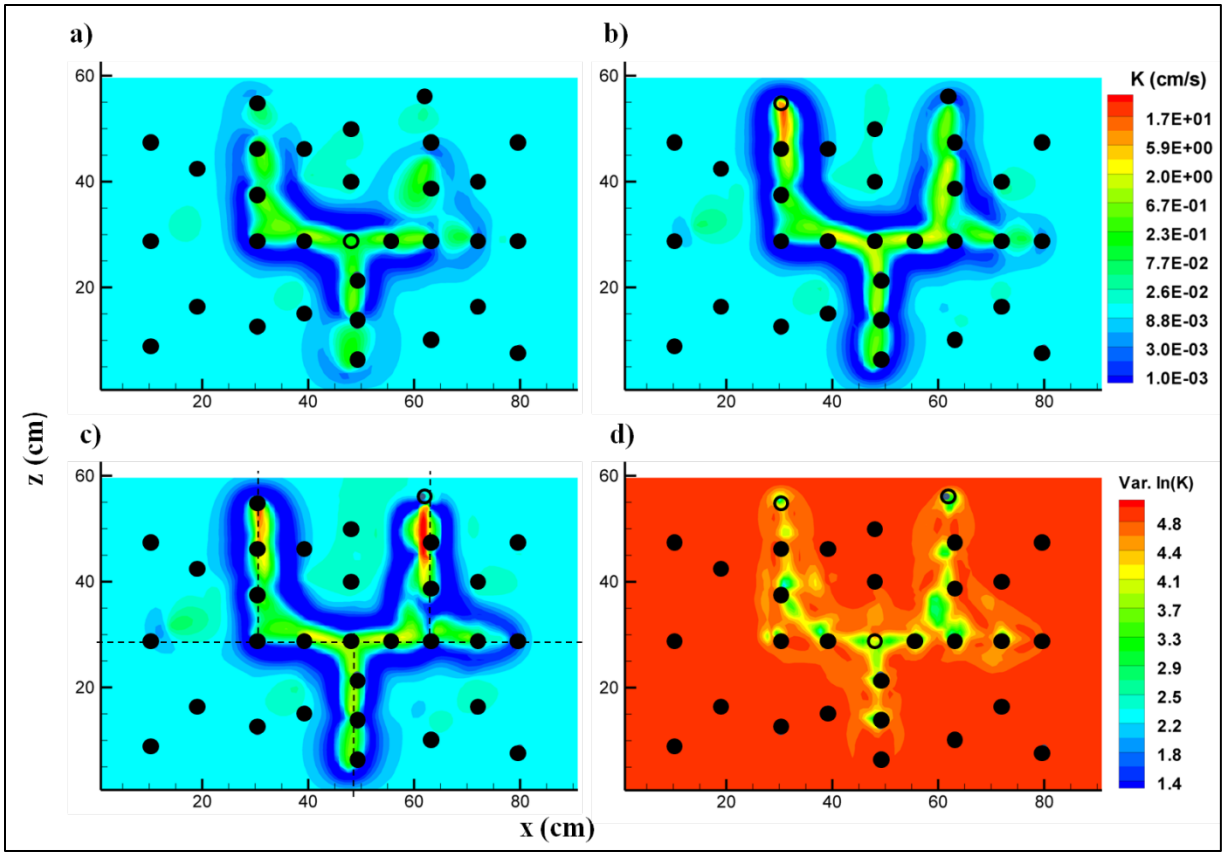

Figure E3: Case 2 *K* tomograms (cm/s) computed using real data from (a) one pumping test (port 5); (b) two pumping tests (ports 5, 16); (c) three pumping tests (ports 5, 16, 19); while (d) is the estimated ln *K* variance map associated with (c). Pumped locations are indicated by the open black circles, while observation intervals are indicated by solid black circles. Thin dashed lines on Figure S3c indicate the locations of the horizontal and vertical fractures. The image in each figure represents the x-z plane through the middle of the domain thickness.

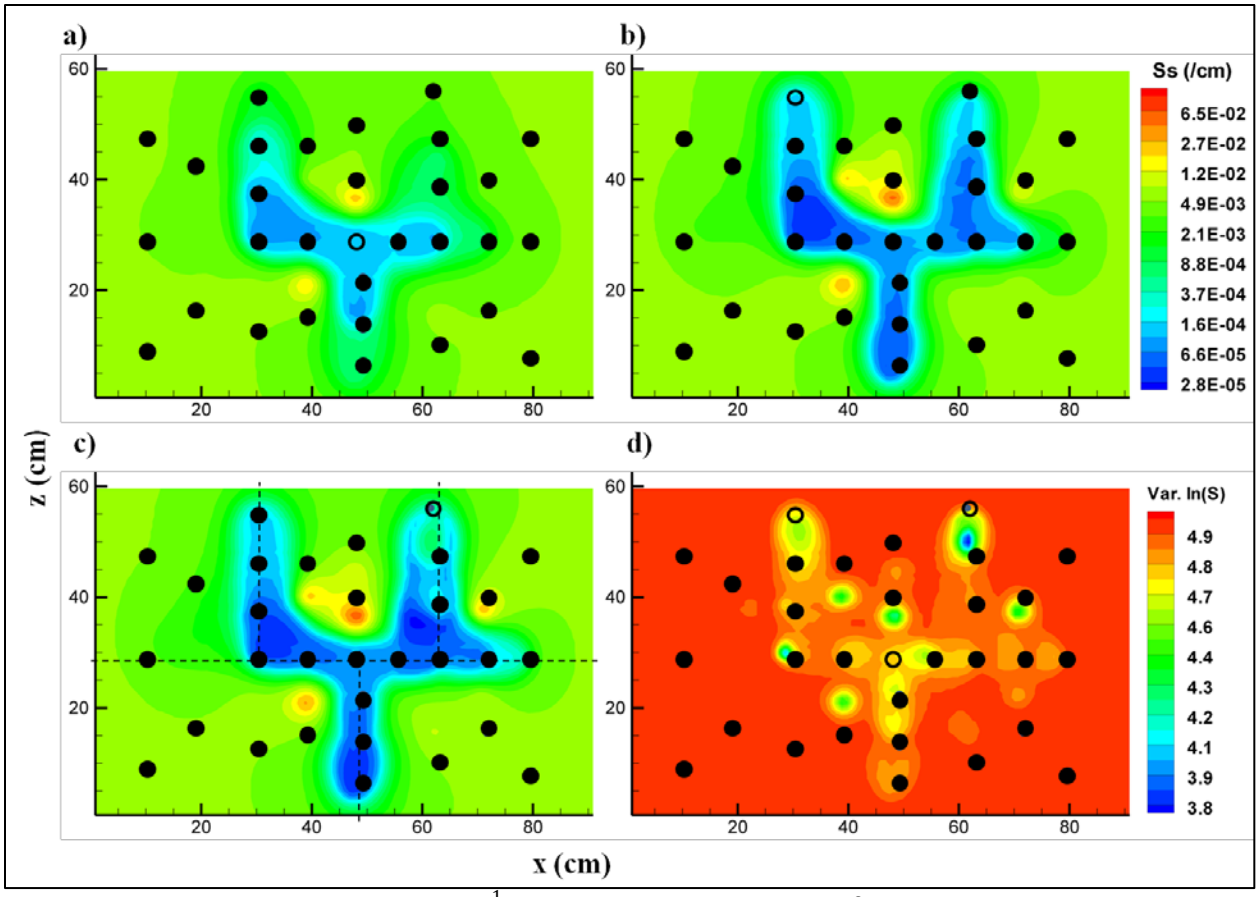

Figure E4: Case 2 S_s tomograms (cm^{-1}) computed using real data from (a) one pumping test (port 5); (b) two pumping tests (ports 5, 16); (c) three pumping tests (ports 5, 16, 19); while (d) is the estimated ln S_s variance map associated with (c). Pumped locations are indicated by the open black circles, while observation intervals are indicated by solid black circles. Thin dashed lines on Figure S4c indicate the locations of the horizontal and vertical fractures. The image in each figure represents the x-z plane through the middle of the domain thickness.

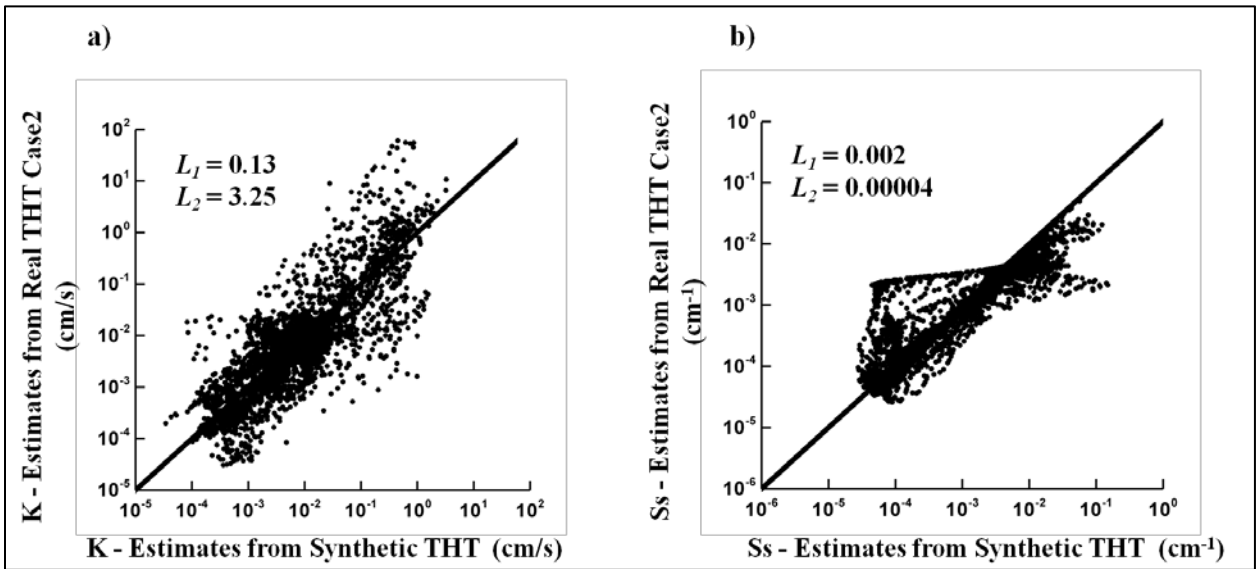

Figure E5: Scatter plots of (a) K and (b) S_s values from the inversion of real THT Case 2 and synthetic data.

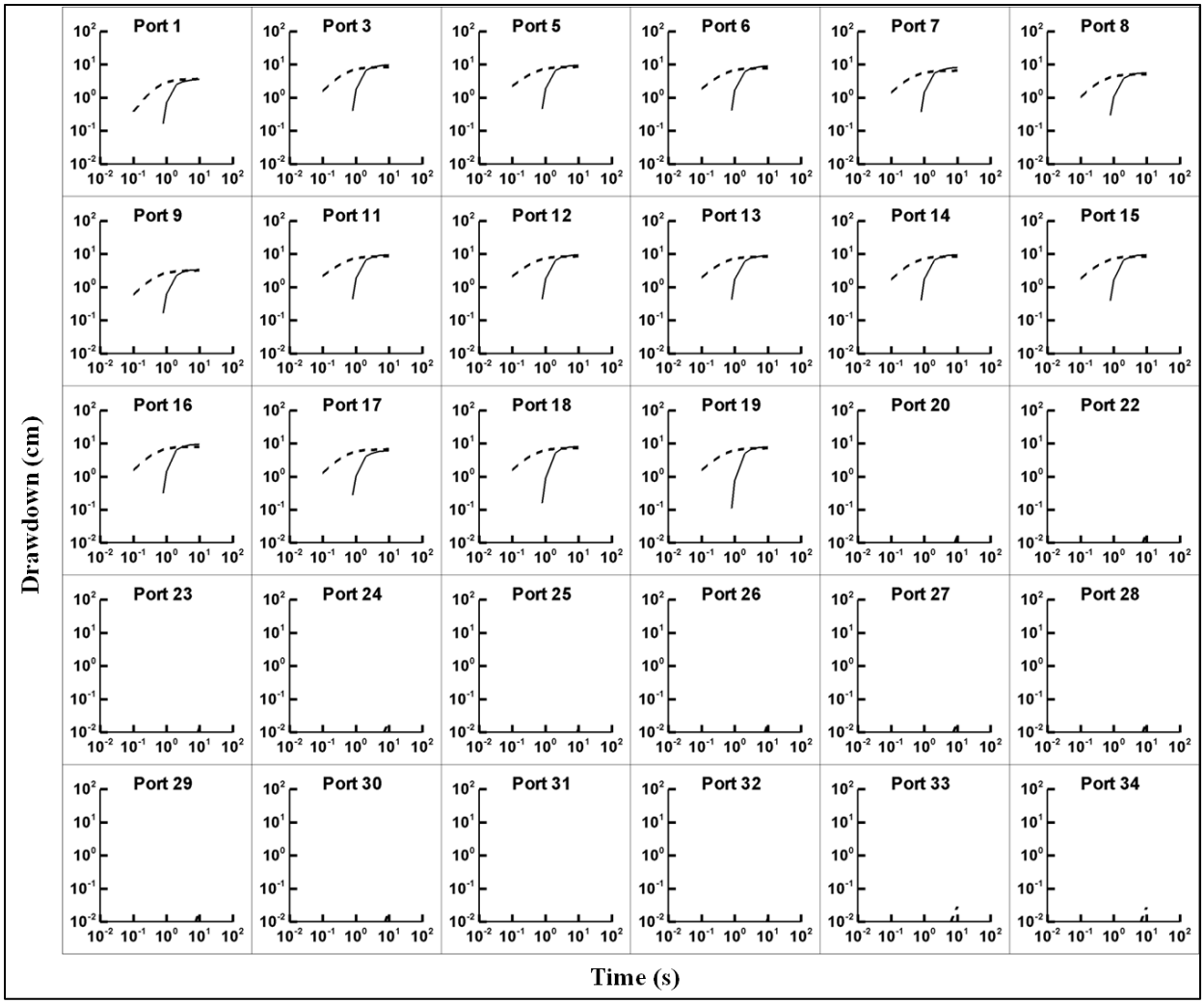

Figure E6: Drawdown versus time at the monitoring ports during the pumping test at port 4. The solid curve represents the observed drawdown curve while the dashed curve represents the predicted drawdown curve using the final K and S_s tomograms from case 1.

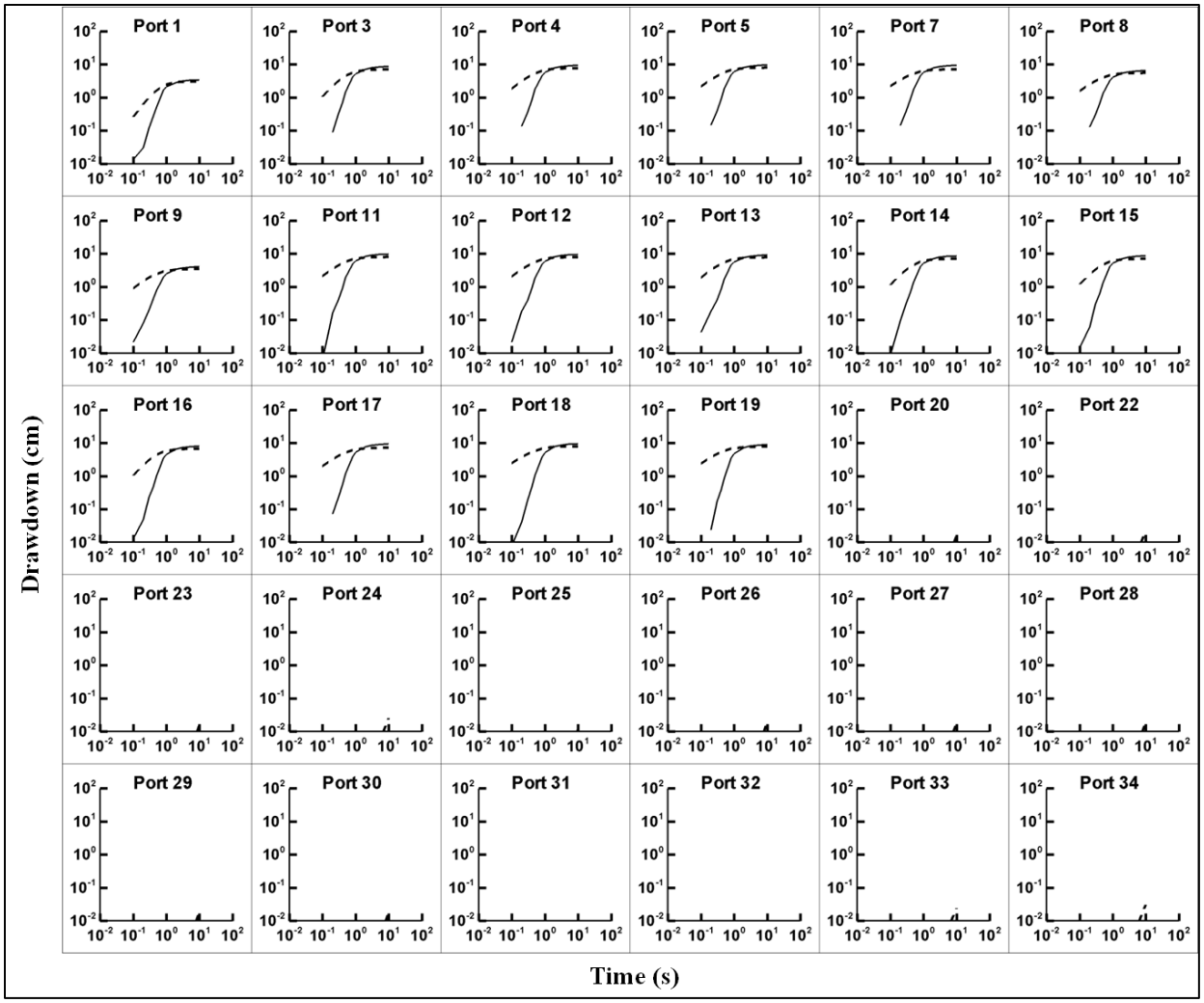

Figure E7: Drawdown versus time at the monitoring ports during the pumping test at port 6. The solid curve represents the observed drawdown curve while the dashed curve represents the predicted drawdown curve using the final K and S_s tomograms from case 1.

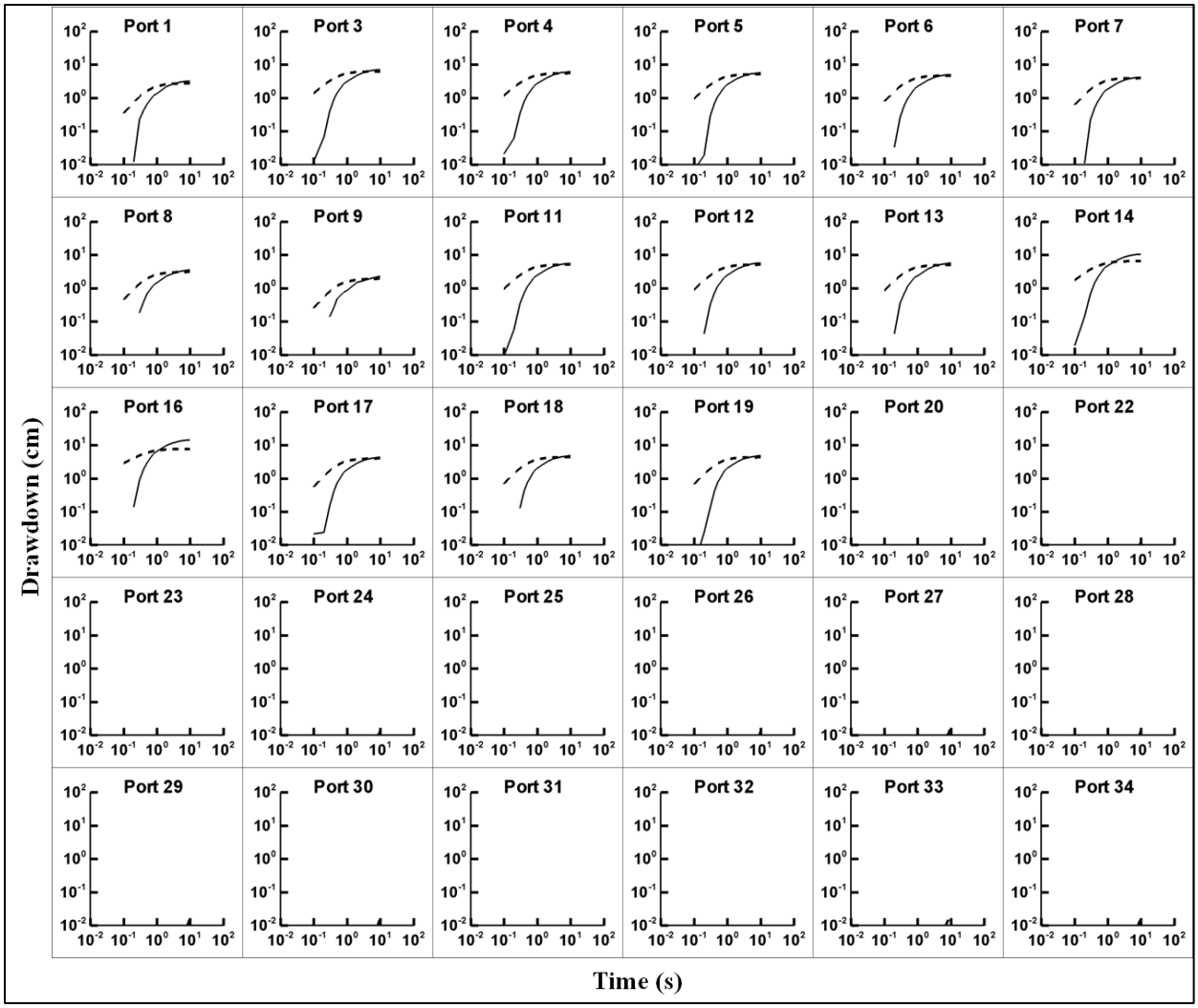

Figure E8: Drawdown versus time at the monitoring ports during the pumping test at port 15. The solid curve represents the observed drawdown curve while the dashed curve represents the predicted drawdown curve using the final K and S_s tomograms from case 1.

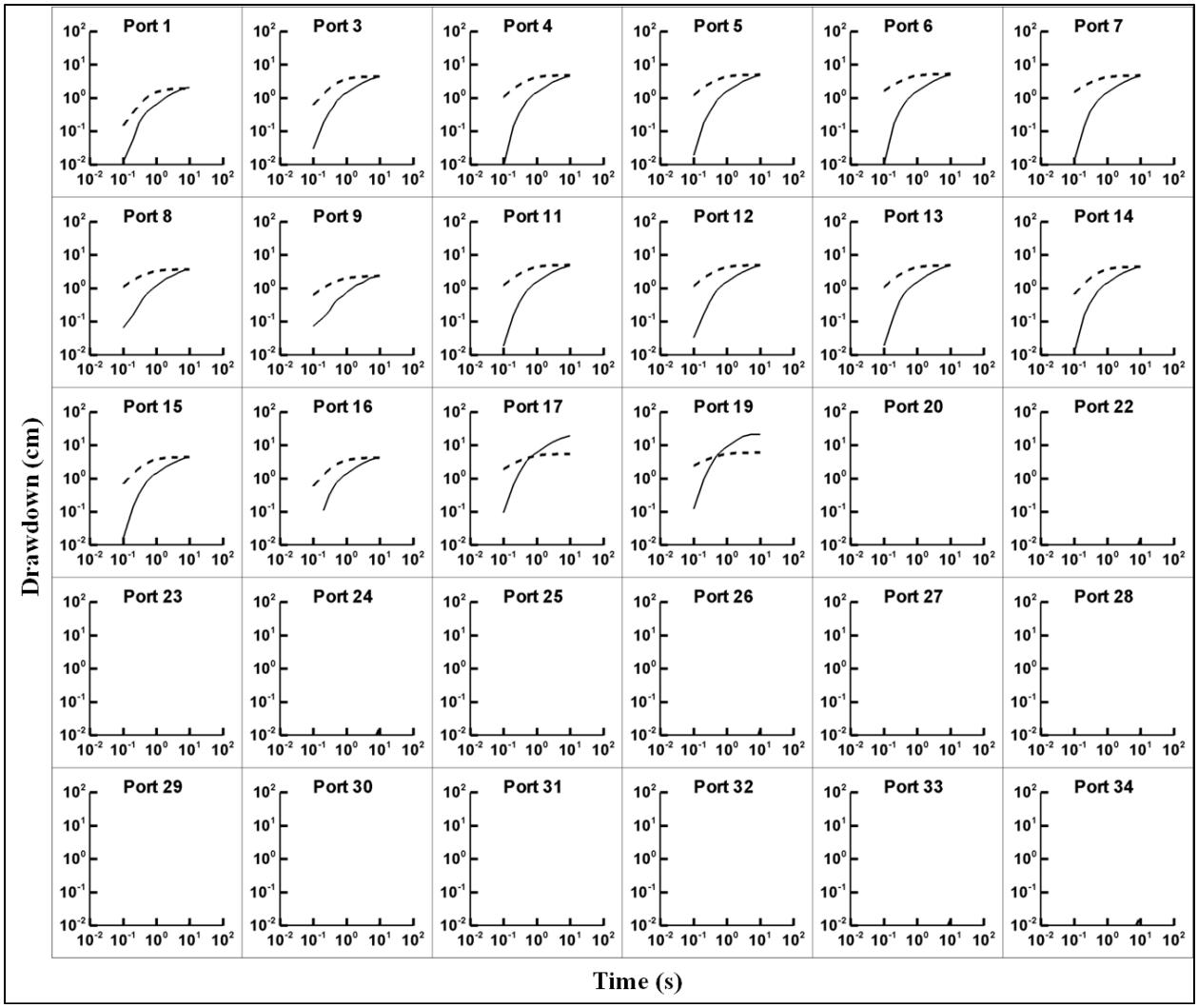

Figure E9: Drawdown versus time at the monitoring ports during the pumping test at port 18. The solid curve represents the observed drawdown curve while the dashed curve represents the predicted drawdown curve using the final K and S_s tomograms from case 1.

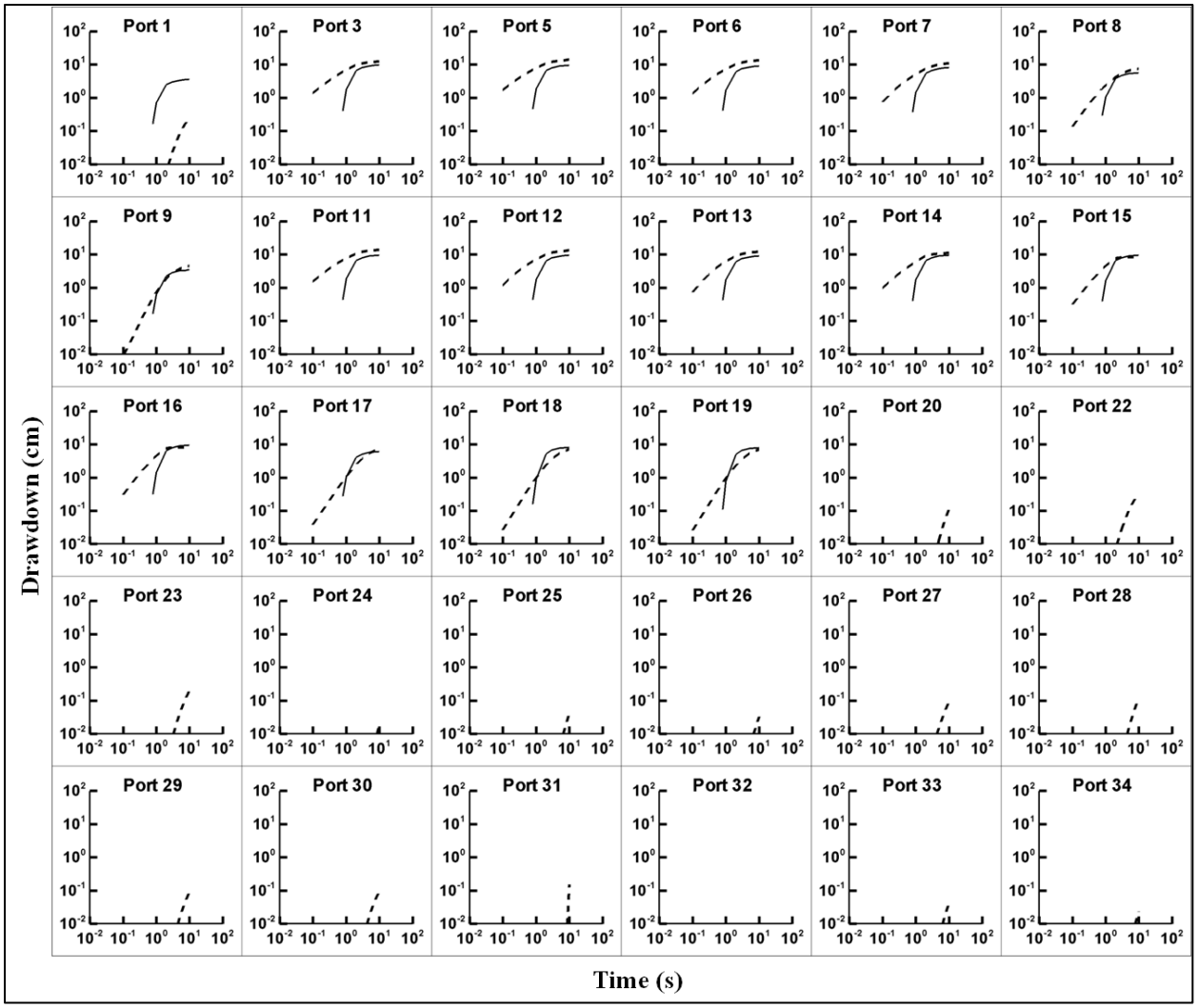

Figure E10: Drawdown versus time at the monitoring ports during the pumping test at port 4. The solid curve represents the observed drawdown curve while the dashed curve represents the predicted drawdown curve using the final K and S_s tomograms from case 2.

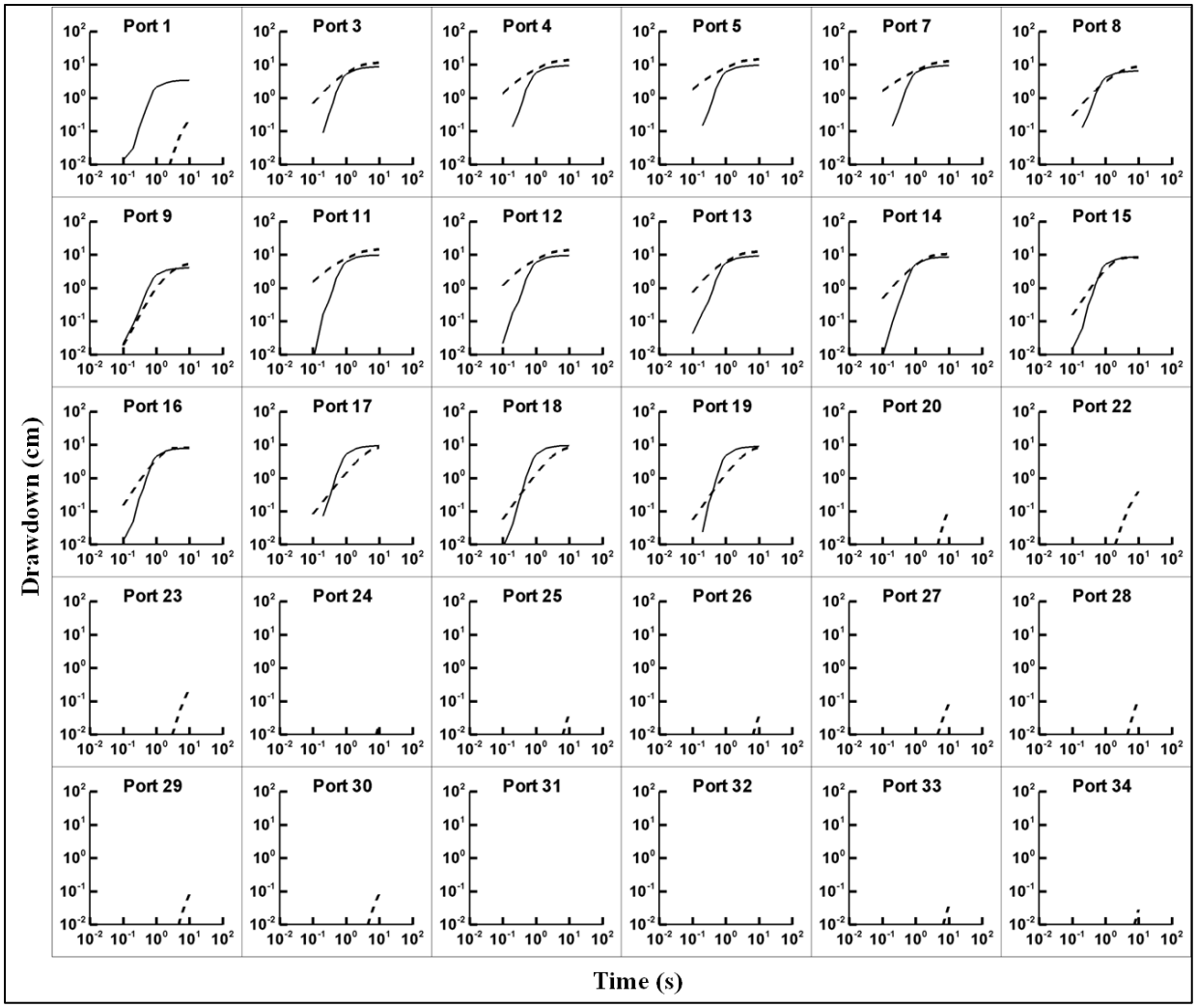

Figure E11: Drawdown versus time at the monitoring ports during the pumping test at port 6. The solid curve represents the observed drawdown curve while the dashed curve represents the predicted drawdown curve using the final K and S_s tomograms from case 2.

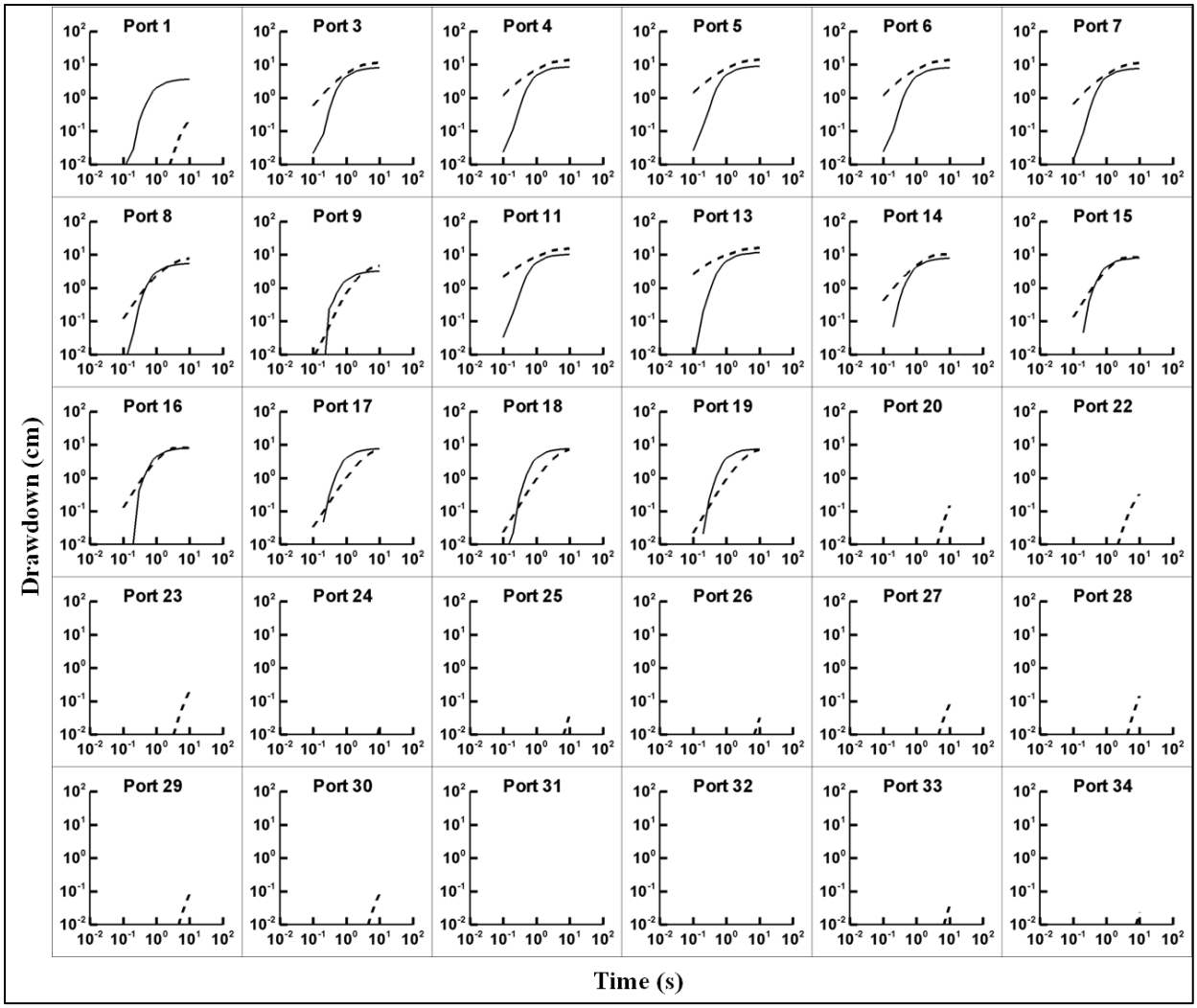

Figure E12: Drawdown versus time at the monitoring ports during the pumping test at port 12. The solid curve represents the observed drawdown curve while the dashed curve represents the predicted drawdown curve using the final K and S_s tomograms from case 2.

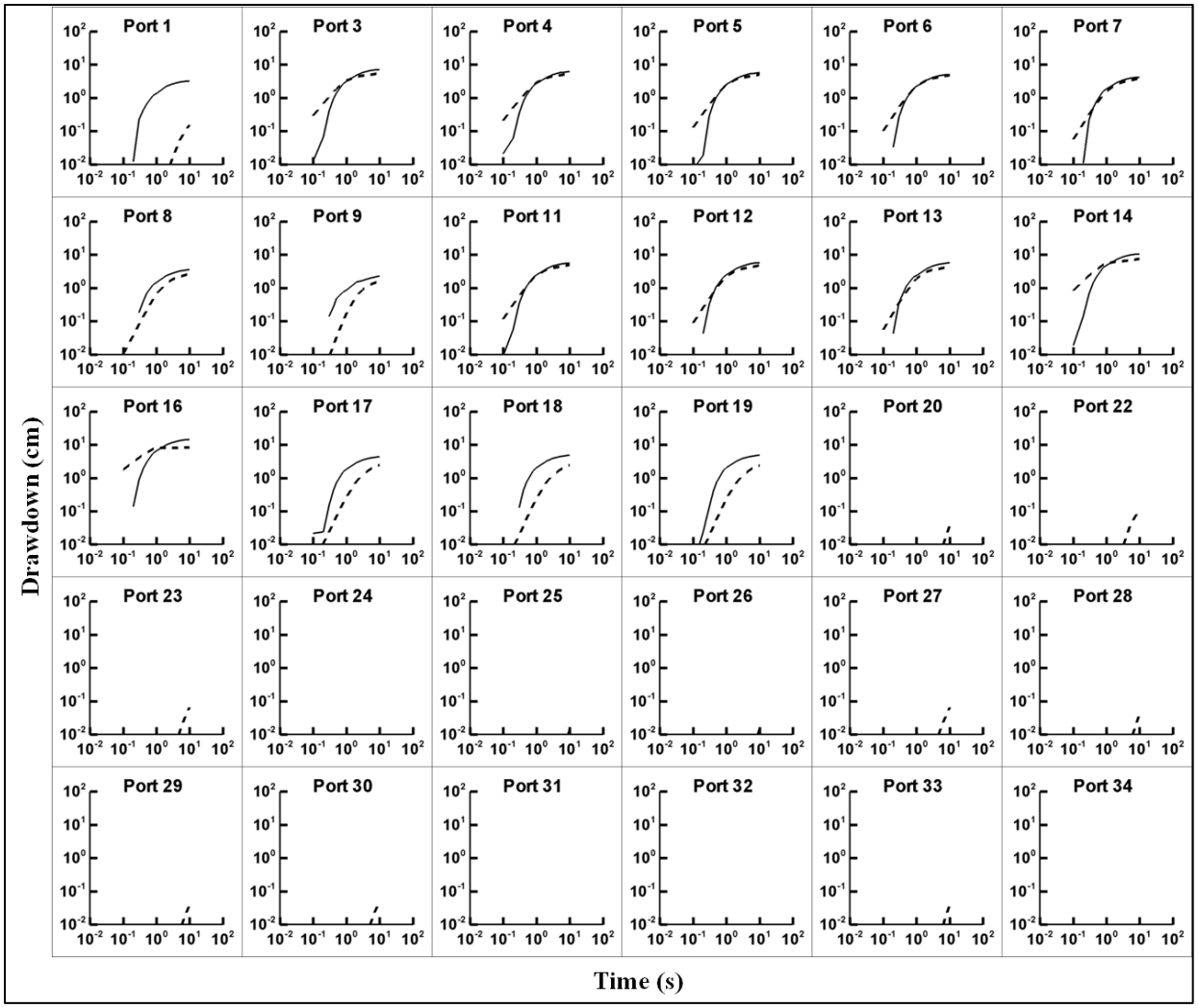

Figure E13: Drawdown versus time at the monitoring ports during the pumping test at port 15. The solid curve represents the observed drawdown curve while the dashed curve represents the predicted drawdown curve using the final K and S_s tomograms from case 2.

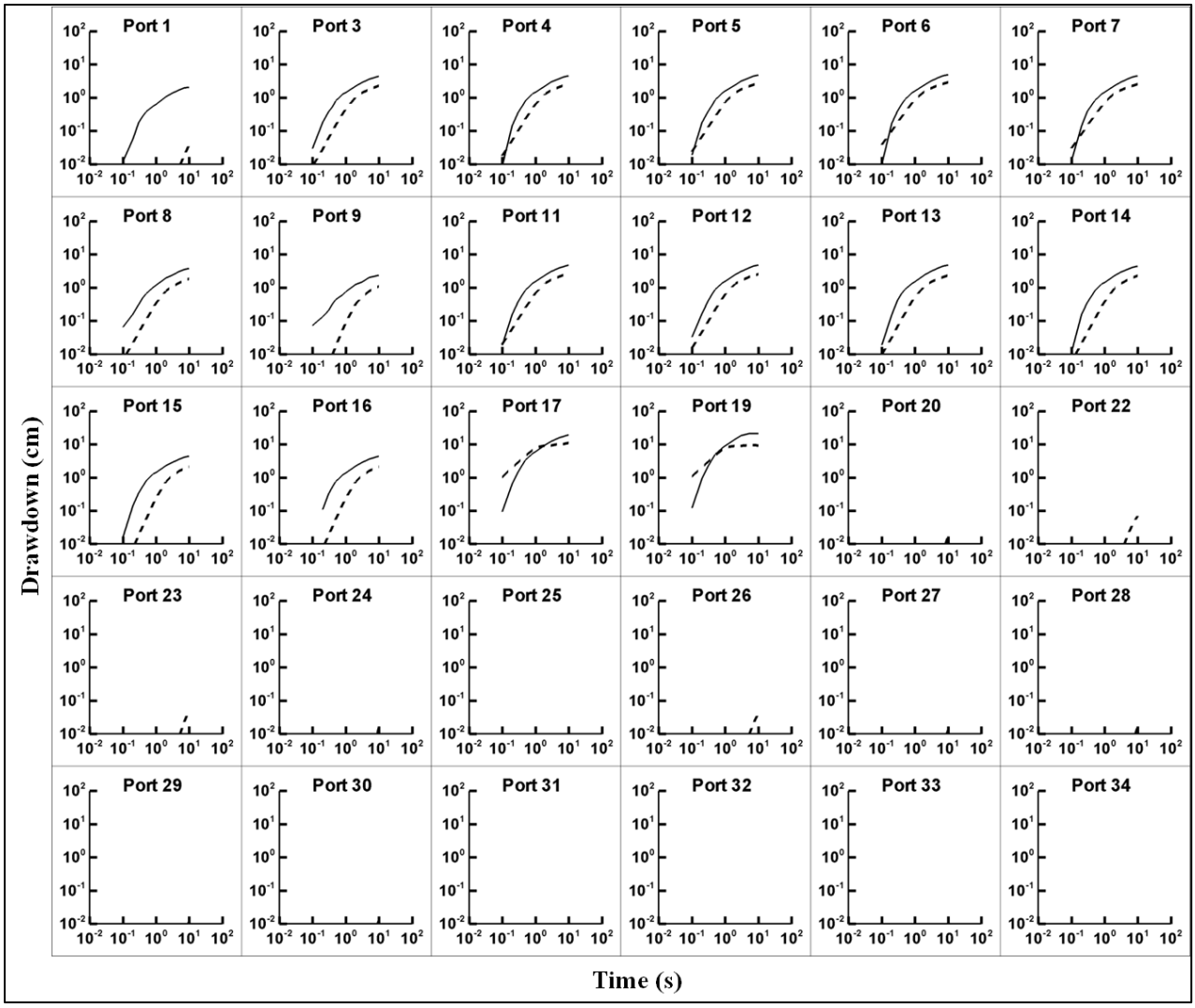

Figure E14: Drawdown versus time at the monitoring ports during the pumping test at port 18. The solid curve represents the observed drawdown curve while the dashed curve represents the predicted drawdown curve using the final K and S_s tomograms from case 2.

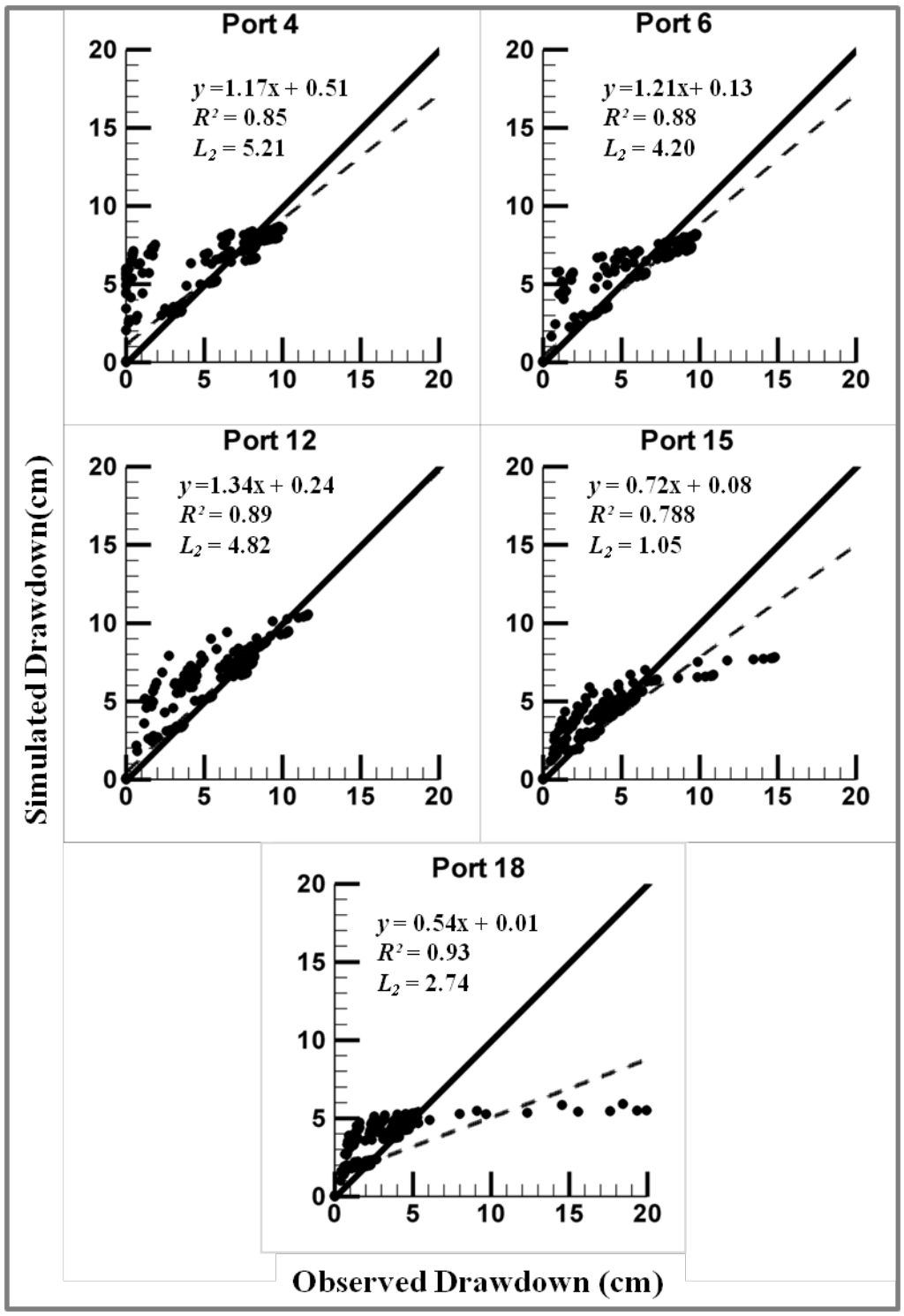

Figure E15: Scatter plots 5 pumping tests using the estimated K and S_s tomograms from the THT analysis (case 2). The solid line is a 1:1 line indicating a perfect match. The dashed line is a best fit line, and the parameters describing this line as well as L_2 norm for the corresponding tests are on each plot.